



HAL
open science

Development of Overhauser-enhanced magnetic resonance imaging in vivo : application to molecular imaging of proteolysis.

Neha Koonjoo

► **To cite this version:**

Neha Koonjoo. Development of Overhauser-enhanced magnetic resonance imaging in vivo : application to molecular imaging of proteolysis.. Imaging. Université de Bordeaux, 2015. English. NNT : 2015BORD0157 . tel-01314752

HAL Id: tel-01314752

<https://theses.hal.science/tel-01314752>

Submitted on 11 May 2016

HAL is a multi-disciplinary open access archive for the deposit and dissemination of scientific research documents, whether they are published or not. The documents may come from teaching and research institutions in France or abroad, or from public or private research centers.

L'archive ouverte pluridisciplinaire **HAL**, est destinée au dépôt et à la diffusion de documents scientifiques de niveau recherche, publiés ou non, émanant des établissements d'enseignement et de recherche français ou étrangers, des laboratoires publics ou privés.

THÈSE PRÉSENTÉE
POUR OBTENIR LE GRADE DE
DOCTEUR DE
L'UNIVERSITÉ BORDEAUX

MENTION : SCIENCE DE LA VIE ET DE LA SANTÉ
OPTION : BIOIMAGERIE

PRÉSENTÉE ET SOUTENUE PUBLIQUEMENT
LE 8 OCTOBRE 2015

PAR NEHA KOONJOO
NÉE LE 28 SEPTEMBRE 1986 AUX SEYCHELLES - MAHÉ

TITRE DE LA THÈSE

DEVELOPMENT OF OVERHAUSER-ENHANCED
MAGNETIC RESONANCE IMAGING *IN VIVO* –
APPLICATION TO MOLECULAR IMAGING OF PROTEOLYSIS

MEMBRES DU JURY :

Dr. Matthew S. ROSEN	Harvard University	Rapporteur
Dr. Frank KOBER	CRMBM - UMR7339	Rapporteur
Dr. Emmanuel BARBIER	Grenoble Institut des Neurosciences (GIN)	Président
Pr. Sylvain MARQUE	Université de Marseille – UMR 7273	Examinateur
Pr. Jean-Michel FRANCONI	Université de Bordeaux–UMR 5536	Examinateur
Pr. Eric THIAUDIÈRE	Université de Bordeaux – UMR 5536	Directeur de thèse

“a good theory is characterized by the fact that it makes a number of predictions that could in principle be disproved or falsified by observation.”

by STEPHEN HAWKING, A Brief History of Time

Acknowledgement

Of course, it was three years of TEAMWORK...

First and foremost, I will thank the two Philippes of my life – Philippe Massot & Philippe Mellet. They have been by my side everyday – be it for guidance in my project, for scientific reflections or a helping hand in my experiments. Their views of the science world have always motivated me to go ahead and do my best. Thank you both. Together with the Philippes, I'll always be thankful to her being there each time I needed her – Elodie Parzy. We have shared nice moments watching the weather forecasts and drinking tea in our small 0.2 T MRI workspace.

My PhD director – Pr Eric Thiaudière – how can I express my gratitude? Sir, I recently came across a quote that made me think of you. It goes as -“Quiet people have the loudest minds.” You have been the only reason for me liking the basics of NMR in my third year of Bachelor's and the courses of Quantum Mechanics in my Masters. You are a great teacher and of course my Model teacher ever. During these three years of thesis, I think that you have been proud of what we have achieved together... Thank you, Sir.

I have to say a big thanks to our laboratory director – Pr Jean Michel Franconi. He has always congratulated me for my achievements and has always pushed me to go further in my work.

My colleague first, then my dear friend – Damien Moncelet. I will not thank you for being by my side and sharing lots of philosophical thoughts as you are my friend. I will just be grateful that I have come across you in my life.

Besides Damien, I shared my workplace with two other mad people – Aurélien Trotier & Charles Castets. They are both smelly people who barely share the same views. They made my days so memorable in the lab together with the one and only uninvited person – William Lefrançois. In spite of their unique personalities, I do have a soft corner for them all as they do bring a smile on my face each and every time of my life.

Finally to all the members of the laboratory and especially to – Véronique Bouchaud,

Sabine Merliot, Marion Wagnies, Mazet Muriel, Yoann Millerioux, Marc Biran, Sylvain Miraux and Emeline Ribot. I would like to add one line for Pr Pierre Voisin. He has always been my good listener and good advisor in the enzymatic world.

Last but not least, I have a bunch of close ones to thank. First I am grateful to have the full support of my husband, Daniel and my one in a million papa, Shiv. The two men of my life have always been there on a daily basis for controlling my mood swings, my impatience and my stubbornness. My mama, Sheilah has been the person who has always cared about my meals and my ongoing focus in my studies. Of course, to my brother, Nirmal who always has his pieces of advice for me.

To my friends – Nalini Ramdhane, Fatma Marie Rose, Anusha Ramdhane, Andreea Hertanu, Virginie Sorbadere, and Anite Ramdhane – I love you so much. You have all been there for me.

I would like to pen off and say thank you to my belated grandfather (“TATA”)...

Contents

<i>Preface</i>	v
<i>Summary of Thesis</i>	ix
<i>Résumé de la Thèse</i>	xi
1 General Introduction	1
1.1 The need for Proteolytic Activity Detection	4
1.1.1 Introduction	4
1.1.2 Proteolytic activity related to diseases	7
1.1.3 Proteolytic activity Detection Strategies	14
A. Current clinical status	14
B. Current experimental <i>in vivo</i> strategies	15
i) Optical Imaging	15
ii) Nuclear Imaging	19
iii) Magnetic Resonance Imaging	21
1.2 State of Art of different techniques in enhanced MRI	22
1.2.1 The Principle of NMR imaging	22
1.2.2 Enhanced MRI Techniques for Proteolytic Detection	29
A. Chemical Exchange Saturation Transfer - CEST imaging	29
B. Gadolinium based MR imaging	31
C. Hyperpolarisation-based MR imaging	33
i) d-DNP – dissolution Dynamic Nuclear Polarization	33
ii) PHIP – Parahydrogen Induced Polarization	34
1.3 Overhauser-enhanced MRI Approach	37
1.3.1 History	37
1.3.2 Theory	39
1.3.3 OMRI contrast agents	44
2 Materials and Methods	47
2.1 Instrumental pre-requisite for OMRI experiments	48
2.2 Implementation of a new MRI sequence	51

2.2.1	TrueFISP sequence implementation	51
2.2.2	Acceleration Method – Keyhole Approach	54
2.2.3	Image reconstruction using raw data	56
2.3	OMRI contrast agents as proteolytic activity detectors	57
2.3.1	Nitroxide molecules	57
	A. PCA	58
	B. β -phosphorylated nitroxides	59
2.3.2	Nitroxide-labeled elastin	60
2.3.3	β -phosphorylated nitroxide radical with an acetyl group	63
2.4	Experimental Procedures	66
2.4.1	<i>In vitro</i> analysis	66
	A. Nitroxide-labeled elastin	66
	i) Kinetic Assays with purified enzymes	66
	ii) Kinetic Assays with living neutrophil cells	68
	B. β -phosphorylated nitroxide	70
	i) pH assessment	70
	ii) Enzyme specificity Assays	71
	iii) Kinetic Assays with Subtilisin A using EPR	72
	iv) OMRI frequency sweep	74
	v) Kinetic Assays with Subtilisin A using OMRI	75
2.4.2	<i>In vivo</i> experiments	76
	A. Animal Gavage Protocol	76
3	Results	77
3.1	<i>In vitro</i> proteolytic activity detection	77
3.1.1	Aims of this study	77
3.1.2	Article 1	78
3.2	<i>In vivo</i> proteolytic activity detection	86
3.2.1	Aims of this study	86
3.2.2	Article 2	86
3.3	Characterization of the β -phosphorylated nitroxide	96
3.3.1	Aims of this study	96
3.3.2	Article 3	96
4	Discussion and Perspectives	115
4.1	Discussion	115
4.1.1	OMRI acquisition advances - before and after	115
4.1.2	Elastolytic activity detection	117
4.1.3	Double substrate-product detection upon proteolysis	118
4.2	Perspectives	121
4.2.1	Disease related protease activity imaging in small animals	121

CONTENTS	iii
4.2.2 Very low Magnetic field & OMRI technique	122
Bibliography	125
<i>Annexes</i>	139

Preface

**DEVELOPMENT OF OVERHAUSER-ENHANCED MAGNETIC
RESONANCE IMAGING *IN VIVO*
APPLICATION TO MOLECULAR IMAGING OF PROTEOLYSIS**

This work relates the continuity and advances in the implementation of the Overhauser-enhanced Magnetic Resonance Imaging technique on a 0.2 T scanner. Briefly, OMRI technique is based on polarization transfer of saturated electronic spins from free nitroxide radicals to proton spins of surrounding water molecules in the aim to drastically enhance proton NMR signal. To this technique, our research team has merged specific strategies for proteolytic activity detection.

The first strategy relies on a 3D visualization of proteolytic activity happening in intact living cells or *in vivo* in healthy mice. With an Overhauser switch based upon changes in molecular tumbling time, high Overhauser enhancements of 10-fold were observed in the intestinal tract of mice after that elastolytic activity of our probe : the nitroxide-labeled elastin macromolecule took place. In addition, MRI developments - TrueFISP sequence implementation, undersampling Keyhole method and data reconstruction were carried out for imaging these rapid biological processes.

A second exquisite strategy is also described using nitroxides with shifting resonant peaks. Here, a β -phosphorylated nitroxide molecule was specifically detected at two distinct frequencies: one for its substrate and the other for its product once hydrolysis took place. This hydrolysis was imaged in 3D in the stomach of living mice with Overhauser enhancements of more than 400% and with a good spatiotemporal resolution. The perspectives of this work lie on a future detection of a pathological proteolytic activity *in vivo* and eventually and development of very low magnetic field OMRI.

Keywords: Overhauser effect, Overhauser-enhanced Magnetic Resonance Imaging (OMRI), Molecular Imaging, 0.2 T, Electron Paramagnetic Resonance (EPR), Resonant TE011 EPR cavity, Proteolysis, Enzymatic activity, phosphorylated nitroxide radicals, TrueFISP sequence, Keyhole method, Mice models, In vivo

**DÉVELOPPEMENT DE L'IMAGERIE PAR RÉSONANCE MAGNÉTIQUE
REHAUSSÉE PAR L'EFFET OVERHAUSER *IN VIVO*
APPLICATION À L'IMAGERIE MOLÉCULAIRE DE LA PROTÉOLYSE**

Ce travail fait l'objet d'une avancée scientifique dans le développement de la technique d'IRM rehaussée par l'effet Overhauser dans la souris à 0,2 T. Cette dernière repose sur le transfert de polarisation des spins électroniques saturés d'un radical libre vers les spins des protons (généralement de l'eau) voisins pour rehausser le signal RMN du proton. Notre équipe a développé cette technique pour détecter une activité protéolytique au travers de deux stratégies.

La première partie de la thèse a été de détecter pour la première fois une activité protéolytique *in situ* dans des souris saines et *in vitro* sur cellules vivantes. L'efficacité du rehaussement par effet Overhauser repose sur le temps de corrélation des spins des électrons non-appariés. Un radical nitroxyde greffé à l'élastine a été utilisé comme substrat. La protéolyse de ce dernier par des élastases pancréatiques a conduit l'observation en 3D d'un rehaussement du signal RMN de plus de 10 fois dans le tube digestif de souris vivantes. De plus des développements méthodologiques, tels que l'implémentation de la séquence TrueFISP, le sous-échantillonnage par la méthode "Keyhole", et la reconstruction des données en 3D ont été faits.

La deuxième stratégie repose sur des molécules de nitroxyde ayant l'unique propriété de pouvoir décaler leurs pics de résonance après hydrolyse. Un nitroxyde phosphorylé en position β pouvant être détecté à deux fréquences spécifiques différentes avant et après hydrolyse d'un groupement chimique a été synthétisé par des chimistes à Marseille. L'hydrolyse de cette macromolécule a été observée *in vivo* dans l'estomac de souris saines avec des rehaussements de plus de 400% et imagée en 3D avec une bonne résolution spatio-temporelle.

Ainsi, une prochaine étape serait de poursuivre ce travail sur un model pathologique et développer cette technique à un champ magnétique plus bas.

Mots clés: L'effet Overhauser, Overhauser-enhanced Magnetic Resonance Imaging (OMRI), Imagerie Moléculaire, 0,2 Tesla, Résonance Paramagnétique Electronique (RPE), Cavité RPE en mode TE011, Protéolyse, Activité enzymatique, Nitroxydes phosphorylés, séquence d'IRM - TrueFISP, Sous-échantillonnage "Keyhole", souris, In vivo

Summary of Thesis

Introduction

My dissertation will relate about a promising molecular imaging modality – the Overhauser-enhanced Magnetic Resonance Imaging (OMRI); also known as PEDRI (Proton Electron Double Resonance Imaging) or DNP (Dynamic Nuclear Polarization) in liquids. The first images acquired in 1990 by Dr Grucker D. by this approach demonstrated that free radicals, for instance Fremy's salt could be detected in living rats. Since then, several *in vivo* studies have been carried out mainly on the field of free radical bio-distribution, pH mapping and redox state evaluation. In our laboratory, we have developed this technique with the aim of detecting biological processes in intact organisms. Therefore, my thesis work will be divided into two projects – 1) how OMRI has been applied for the detection of enzymatic activity *in vivo* and 2) the characterization of a new type of OMRI probe also designed for visualizing proteolytic activity.

The Overhauser Effect

OMRI is based on the Overhauser effect occurring between unpaired electrons and proton nuclei. It combines two techniques : EPR (Electron Paramagnetic Resonance) and NMR. Unpaired electrons present in the medium (either in a solution or inside the living organism) are placed in a static magnetic field. The electronic transitions of unpaired electrons are saturated using a selective hyper-frequency wave. Through dipole-dipole interactions between the saturated unpaired electrons and the surrounding water proton nuclei, polarization transfer takes place; leading to the increase in the population spin difference of the protons. MRI of those enhanced protons will result in a bright signal at the site of the unpaired electrons.

1) Detection of a proteolytic activity *in vivo*

In this section, we synthesized an OMRI probe based on its modified tumbling time upon proteolytic activity. This probe consisted of a macromolecule grafted to a nitroxide molecule, here a nitroxide-labeled elastin molecule. It was first characterized *in vitro* in presence of pancreatic elastase and also with elastase-secreting human neutrophils. For the *in vivo* part, new MRI sequence implementation with an accelerated data acquisition was performed on the 0.2T Siemens magnet so as to image and follow biological processes *in vivo* and also to limit the heating effect coming from the electronic spin saturation. Hereafter, the nitroxide-labeled elastin was orally administered in mice and its digestion was observed in the intestinal tract.

2) New OMRI probe characterization

In the second part of my work, a particular nitroxide which has its resonant frequency shifted upon proteolytic action (i.e. a change in its hyperfin coupling constant) was tested *in vitro*. This synthesized 6-peak nitroxide has an ester bond that is targeted to proteolytic activity (synthesis done in collaboration with the team of Pr Marque R.A.S, Marseille, France). Kinetic assays in presence of the Subtilisin A (a serine peptidase) were conducted using the EPR spectrometer as well as OMRI. Being a frequency-specific imaging method, the advantage of having a shifting resonance, is that both the substrate and the product are detectable through OMRI. Distinct substrate and product frequencies were established through frequency swept OMRI experiments. Eventually, this probe design was orally administered in mice for the detection of the substrate form and of the product form after digestive enzyme action.

Conclusion

This work brings about new ideas for future pathological *in vivo* models for which new probes should be synthesized. The latter would possess specific peptide sequence and target specific protease. Even if instrumental improvements need to be done for a better image quality and faster acquisition, this technique has been proved to have a great potential in *in vivo* research. Proteolytic activity detection in deep-seated organs is a challenging field of study today and can be made possible with OMRI. Upgrading this technique to larger animals, is discussed in the complete version of the dissertation.

Résumé de la Thèse

Introduction

Le travail effectué durant ma thèse a porté sur l'étude d'une technique d'imagerie par résonance magnétique (IRM) rehaussée par l'effet Overhauser effectuée en milieu biologique. Cette technique est qualifiée d'OMRI pour Overhauser-enhanced Magnetic Resonance Imaging. Elle est aussi connue sous l'appellation de PEDRI (Proton Electron Double Resonance Imaging) ou encore la PDN (Polarisation Dynamique Nucléaire) dans les liquides. Avec les premières images *in vivo* obtenues en 1990 par Dr Grucker D, cette méthode d'imagerie a pu montrer que des radicaux libres, ici des sels de Frémy pouvaient être imagés dans des rats. Dans la littérature, plusieurs travaux ont été réalisés sur la bio-distribution des radicaux, la cartographie du pH et la quantification de la pression partielle en dioxygène dans le but d'observer une activité métabolique ou une fonction particulière dans l'organisme intact. Dans notre laboratoire, notre équipe a développé cette méthode d'imagerie dans le but de faire de l'imagerie de la protéolyse *in vivo* en utilisant des agents spécialement conçus à cet effet. Ainsi, cet ouvrage sera composé de deux projets effectués sur un modèle murin— 1) la première détection d'une activité protéolytique *in vivo* en utilisant l'OMRI et 2) la caractérisation d'un nouveau agent de contraste ayant des propriétés uniques.

L'effet Overhauser en IRM (OMRI)

Le principe de l'OMRI repose sur l'effet Overhauser décrit en 1953 [Overhauser A.W, 1953] et couple deux techniques : la RPE (Résonance Paramagnétique Electronique) et la RMN. L'idée est de saturer à l'aide d'une onde hyperfréquence (HF) de l'ordre du GHz les transitions de spin des électrons non-appariés (radical libre) présents dans une solution ou dans un organisme vivant placés dans un champ magnétique. Un transfert de polarisation des électrons libres aux protons (généralement de l'eau) voisins va s'effectuer. A l'état liquide, le mécanisme de transfert de polarisation est essentielle-

ment dipolaire. Pendant l'état polarisé du proton, une expérience de RMN est réalisée dans le domaine des MHz. Dans le cas de l'IRM, les images obtenues sont caractérisées par un fort signal dans les zones où sont présents les radicaux libres.

1) Détection d'une activité protéolytique *in vivo* par OMRI

La première partie de ma thèse a consisté à tester un agent de contraste (un macromolécule greffé à un nitroxyde) *in vitro* en présence soit d'un enzyme purifié soit de neutrophiles humains sécrétant naturellement un cocktail d'enzymes dont celui étudié. Ici la macromolécule substrat testée était l'élastine et l'enzyme ciblé pour détecter sont activé, l'élastase.

Pour la partie *in vivo*, une nouvelle séquence d'IRM a été implémentée sur la machine IRM utilisée pour l'étude avec une méthode d'accélération pour l'acquisition des données. Ces modifications ont permis d'améliorer la résolution spatiale et temporelle des images ce qui a permis d'observer et de suivre des processus biologiques dans l'organisme intact. En outre, des effets de réchauffement due à la saturation des spins électroniques ont été minimisés. Par la suite, un nitroxyde couplé à l'élastine a été introduit par gavage chez des souris et la protéolyse de ce substrat a été détectée dans les intestins.

2) Caractérisation d'un nouvel agent de contraste par OMRI

Dans la seconde partie de ma thèse, un nouvel agent de contraste a été synthétisé en collaboration avec l'équipe de recherche de Pr Marque R.A.S de Marseille. Cet agent de contraste est un nitroxyde qui a la particularité de décaler sa constante de couplage hyperfine lors de la protéolyse d'une liaison ester présente sur ce dernier. Ainsi, sachant que l'OMRI est réalisée à une fréquence électronique spécifique, cette propriété permet la visualisation sélective soit du substrat soit du produit de la réaction enzymatique. Des expériences *in vitro* avec/ou sans enzymes ont été réalisées par RPE ainsi que des cinétiques. Un balayage en fréquence a été réalisée en OMRI et par la suite des expériences de gavage *in vivo* ont été effectuées pour valider cette approche unique.

Conclusion

Ce travail de thèse a permis de détecter en 3D une activité protéolytique à l'aide d'agents de contraste spécifiques avec une bonne résolution spatiotemporelle dans les intestins d'une souris. De plus, un agent de contraste unique en son genre a été aussi caractérisé *in vivo*. En perspective, ces travaux pourront être transposés sur des modèles pathologiques ciblant des protéases spécifiques. Sachant que l'imagerie des protéases dans les tissus profonds *in vivo* est un vrai défi, l'OMRI est une approche qui pourra rendre atteignable ces objectifs. Le palier supérieur de cette approche sera de transposer cette méthode chez les gros animaux ; ceci sera discuté dans la thèse.

List of Figures

1.1	Proteolytic activity	4
1.2	Classification of proteases	5
1.3	Roles of Proteases in organisms	6
1.4	Classification of cathepsin proteases	9
1.5	Various roles of cysteine cathepsins in physiological and pathological conditions	11
1.6	Activatable cell-penetrating peptide (ACCP)	20
1.7	Principle of NMR	24
1.8	From MRI pulse sequence to Image formation	28
1.9	Principle of CEST imaging	29
1.10	Gadolinium-based contrast agents for enzymatic activity detection	31
1.11	Principle of Parahydrogen Induced Polarization	35
1.12	Energy level diagram for an electron-nucleus system	39
1.13	Examples of triarylmethyl/trityls radicals	44
2.1	Experimental OMRI setup	48
2.2	EPR resonant cavity – TE011 configuration	49
2.3	A typical 3D TrueFISP MRI pulse sequence	51
2.4	3D TrueFISP pulse sequence synchronized with EPR irradiation	53
2.5	Principle of the “Keyhole” method	54
2.6	The chemical structures of the two nitroxides used: PCA & β -phosphorylated nitroxide	58
2.7	EPR spectrum of PCA nitroxide	58
2.8	EPR spectrum of the β -phosphorylated nitroxide	59
2.9	EPR signatures of the digested and undigested nitroxide-labeled elastin	61
2.10	Evolution of the rotational correlational times with increasing nitroxide concentrations – in the digested form or the undigested form	62
2.11	Synthesis of β -phosphorylated nitroxide	63
2.12	EPR spectrum of the acetate & ketone forms of the β -phosphorylated nitroxide	64
2.13	Enzymatic kinetic experiment with purified enzymes performed by EPR or OMRI	67

2.14	Enzymatic kinetic experiment with induced neutrophils performed by EPR or OMRI	68
2.15	pH assessment of the β -phosphorylated nitroxide	70
2.16	Experimental procedure to evaluate enzyme specificity towards the β -phosphorylated nitroxide	71
2.17	Experimental procedure to evaluate the catalytic efficiency of Subtilisin A enzyme towards β -phosphorylated nitroxide	73
2.18	Experimental procedure of the OMRI frequency sweep experiment . .	74
2.19	Results of the OMRI frequency sweep experiment	75

List of Tables

1.1	Characteristics of Various Molecular Imaging techniques	16
2.1	Measured EPR line-widths of the nitroxide-labeled elastin before and after enzymatic action for varying concentrations	61
2.2	EPR parameters of both forms of the phosphoryl nitroxide molecules.	64

General Introduction

The complexity in studying the function of proteases within their natural cellular habitat has been an all-time compelling research area, including biochemistry, cell biology or animal physiology. With about 2% of the human or mouse genome being protease-encoded genes and representing over 500 in number, these molecular moieties undergo a set of controls that tightly regulate their activity within the cell and the extracellular matrices [Turk 2006]. These controlled mechanisms consist of spatial and temporal expression, binding to small molecules, protein cofactors and post-translational modification. Until recently, most of the studies on the understanding of functional regulation of proteases have been carried out *in vitro*. However due to organelle and fine compartments disruption leading to activators or inhibitors release and altered enzymatic activity, *in vitro* studies remain quite irrelevant and misleading compared to the real physiological processes [Baruch et al. 2004; Neefjes et al. 2004]. Therefore, the ultimate goal during these few years has been to develop new technological advances; be it through novel imaging tools to detect and monitor enzymatic activity within intact cells [Blum et al. 2005] and eventually *in vivo* [Ntziachristos et al. 2002].

Apart from understanding the functional regulation of proteases happening *in vivo* during physiological processes, there is also a need to understand how the properties of these proteases are altered in a disease state. Deregulated proteolytic activities are associated with a wide variety of pathological conditions, notably diabetes, inflammation, hypertension, cystic fibrosis, certain tumors, pancreatitis, arthritis and more. As a matter of fact, proteases are not only described as catabolic proteins having non specific substrates, but as enzymes that possess a highly selective cleavage of specific substrates which can influence cell behavior (such as in activation, growth, cell division,

differentiation, migration, signaling and so on). They are also involved in specific processes like in blood clotting, apoptosis, extracellular matrix degradation, cleavage of transmembrane proteins and precursor processing in the secretory pathway [Neefjes et al. 2004]. Our view of the proteolytic world has certainly expanded and above all, it has brought in a new developing field on the use proteases as biomarkers or for drug targeting.

Patients' blood sample are to-date the most widely used specimens for diagnosing, prognosing or therapeutic monitoring of different diseases. Even if blood testing remains an all-time cost effective way for screening pathologies in a population, further validating analysis is required as it is known that serum and plasma have high intrinsic proteolytic activity that is related to diverse exopeptidases as well as different endoproteases. Therefore when it comes to the most reliable method by which diseases can be detected unambiguously, surgical interventions and imaging techniques are put forward. Here, our concern is to better understand and detect biological processes taking place in pathophysiological cases with a minimum perturbation.

An emerging field resulting from the need to monitor enzymatic activity is the field of Molecular Imaging.

"The term molecular imaging can be broadly defined as the in vivo characterization and measurement of biological processes at the cellular and molecular level. In contradistinction to "classical" diagnostic imaging, it sets forth to probe the molecular abnormalities that are the basis of disease rather than to image the end effects of these molecular alterations." [Weissleder et al. 2001]

Since the past 10 years, this field has been explored in all its splendor, be it in the optical, nuclear or magnetic discipline. Nevertheless, it has to be mentioned that the major technological developments in activity-based substrate imaging is well established with Optical Imaging : FRET for Förster-Resonance Energy Transfer, NIRF for Near Infra Red Fluorescence, BRET for Bioluminescence Resonance Energy Transfer, or Photo-acoustic Imaging. The reason behind such a growing interest for this particular technique is the availability of fluorophores, their ease in designing new activity-based probes and the high sensitivity. However, the low depth penetration of light is one feature that hinders Optical techniques. On the contrary, a technique that remains the only means by which soft tissues can be imaged with high contrast, correct spatial resolution, without invasiveness, and without any depth limitations is low- and middle- field – Magnetic Resonance Imaging (MRI). Among the methods used in MRI to generate a specific activity-based contrast, the most common approach today is PARACEST for Paramagnetic Chemical Exchange Saturation Transfer. However, there is another uncommon but unique approach known as Overhauser Enhanced MRI (OMRI) that is very sensitive with signal enhancements reaching up to 1000% (up to 10 fold). The potential of this technique to excel in the field of Molecular Imaging is

currently explored.

Established as an enhanced imaging technique and originally named as PEDRI for **Proton Electron Double Resonance Imaging** by Lurie D.J in 1988, OMRI is based on the Overhauser effect between unpaired electrons and water molecules at room temperature, more precisely on the polarization transfer of saturated unpaired electrons with a larger spin polarisability onto the nuclear protons of the surrounding water molecules which is commonly imaged using MRI [Lurie et al. 1988]. This principle was developed in the laboratory "Centre de Resonance Magnetique des Systemes Biologiques" for the first time in 2005 and the proof-of-concept for OMRI spotting of proteolytic activity was proposed *in vitro* in 2009 [Mellet et al. 2009].

The aims of my PhD research work were to implement efficient OMRI methodologies in view to facilitate and optimise *in vivo* detection. We validated and visualized the proteolytic activity *in vitro* and within intact organisms. Another set of work was also carried out using a new probe-design strategy destined to the same imaging technique and to study its feasibility as substrate for proteolysis for *in vitro* as well as *in vivo* studies.

My dissertation will be divided into four chapters: The first chapter will begin with the biological context surrounding proteolytic activity imaging. Then a full description of the current achievements in the different enzyme-based imaging strategies will be discussed, which will take us to enhanced MRI as a suitable molecular imaging approach. Finally, the last section in this chapter will entirely deal with OMRI and how it will be explored for detecting enzymatic reactions.

The second chapter will focus on the OMRI pre-requisites – equipments, MRI sequence development and image reconstruction along with the experimental protocols. The different OMRI contrast agents will also be discussed.

Afterwards, in the third and fourth chapters, I will describe how *in vitro* and *in vivo* proteolytic activity detection were achieved using firstly an OMRI probe based on its tumbling time and secondly another OMRI probe based on its resonant frequency.

To finish, a proper discussion and perspectives chapter shall be developed.

1.1 The need for Proteolytic Activity Detection

1.1.1 Introduction

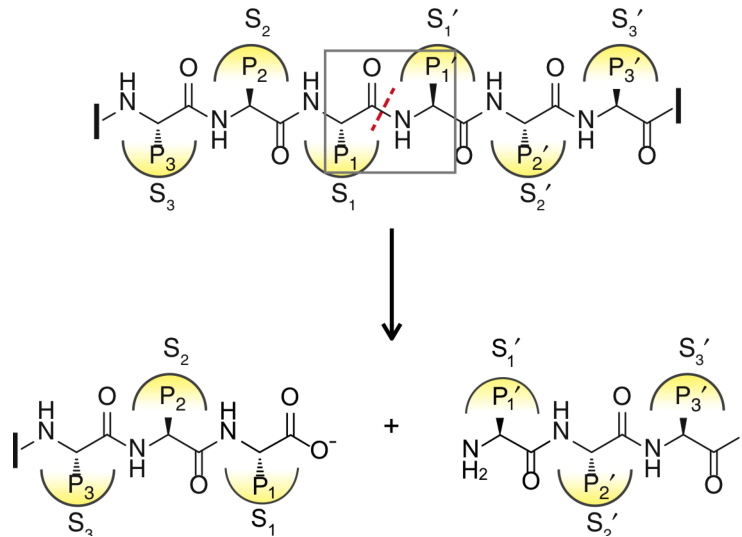


Figure 1.1: This figure illustrates the hydrolysis of a peptide/amide bond. This chemical reaction can take place spontaneously in the presence of water molecules, but is a very slow process. To catalyze this hydrolytic reaction in living organisms, enzymes are used.

Proteolysis is a biochemical reaction taking place constantly inside a cell as well as in the extracellular space. The entity responsible for this reaction is known as Enzyme, Protease or Peptidase. Practically all enzymes are proteins. Its role is to catalyse the hydrolytic cleavage of a peptide bond (see Figure 1.1), more precisely an amide functional group found between two amino acids and which are themselves the building blocks of a macromolecule or protein. So, the purpose of disassembling macromolecules can either be for the digestion of nutrients, the constant protein turnover in cells, for protein maturation during their biosynthesis (such as for insulin) or even for signal transduction (like cell death, blood coagulation and other more). In return, proteases have to be strictly regulated so that there is no auto-cellular damages occurring.

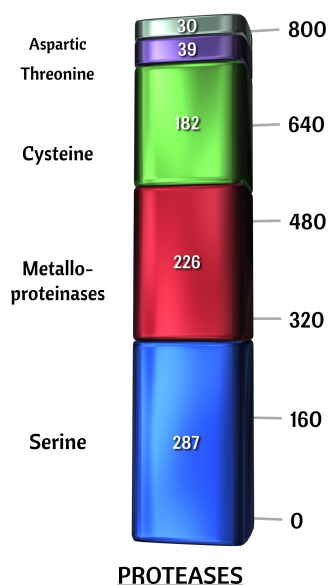


Figure 1.2: The different classes of proteases based on their catalytic mechanisms

After sequencing the human genome and other model organisms an impressive and diverse number of protease functions with different structures and catalytic mechanisms were unearthed. The complete set of human proteases consists of at least 764 proteases and homologues dispatched in five classes namely 226 metalloproteinases, 287 serine, 182 cysteine, 39 threonine and 30 aspartic proteases (see Figure 1.2) [Rawlings et al. 2014].

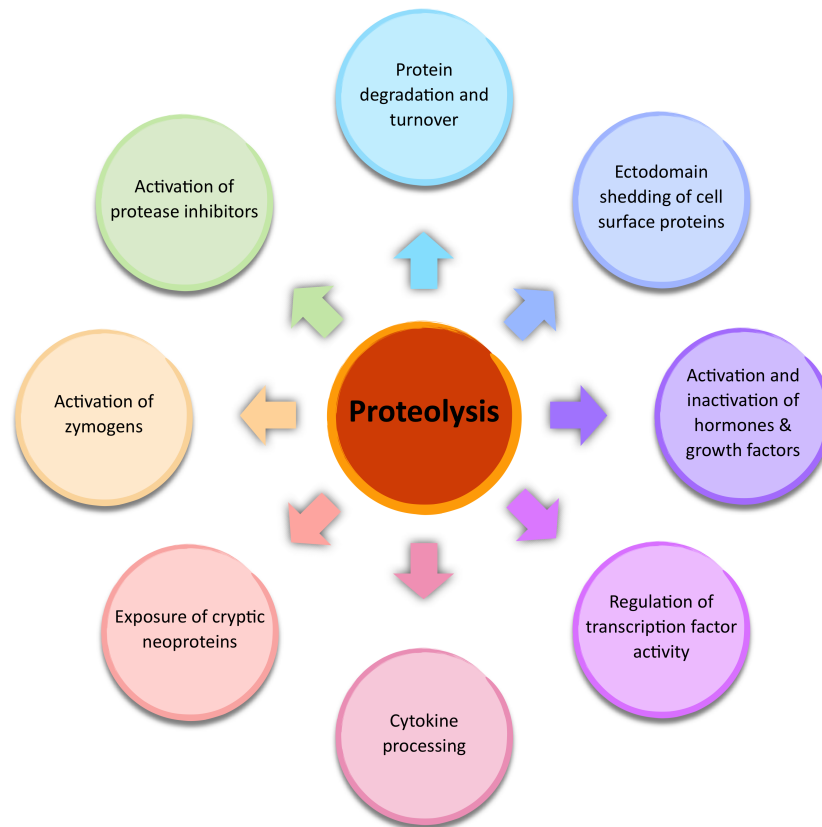


Figure 1.3: The main roles of proteases in living organisms. [Lai et al. 2015]

Originally, even if proteases were recognised as the central executioners of nonspecific protein catabolism present in the pancreatic juice, today, our view of proteases has considerably widened. With their participation in the catalysis of specific proteolytic activities, their highly selective and limited cleavage of specific substrates, proteases have proven to be essential in every cell and organism. Actually, there is a number of important processes that is strictly dependent on proteolytic processing events summarized in the figure above (Figure 1.3).

Protease-mediated processing events, which are distinct from nonspecific protein degradation reactions, are vital in the control of essential biological processes such as DNA replication, cell-cycle progression, cell proliferation, differentiation and migration, morphogenesis and tissue remodeling, immunological reactions, ovulation, fertilization, neuronal outgrowth, angiogenesis, homeostasis, and apoptosis [Lai et al. 2015]. However, any alteration in the structure and expression patterns of these proteases would unfortunately underlie abnormalities, thus giving rise to pathological conditions.

1.1.2 Proteolytic activity related to diseases

Occasionally, deregulation of proteolytic activities can come about and it is associated to pathological conditions. Ample evidence exist showing that deregulation of proteolytic activities plays a role in the etiology and/or progression of inflammation, cystic fibrosis, certain tumors, pancreatitis, arthritis, atherosclerosis, stroke and heart disease, multiple sclerosis and so on.

Matrix metalloproteinases (MMPs) are the third most important class of proteases and are members of the metzincin group of protease, which are named after the zinc ion and the conserved methionine residue in the active site. [Bode et al. 1993]

Since the 1990s, MMPs (in particular MMP-9 or gelatinase B protease) have gained much attention when diseases targeting was concerned. But due to first failures in using broad-spectrum MMPs inhibitors for clinical trials, in-depth research was carried out on how its molecular structure and its mild varying domains define its implication in specific cellular pathway signaling. Known at first as an extracellular cellular matrix degradation enzyme allowing tumor invasiveness and cell proliferation, these macromolecules have recently been proved to be of a higher complexity. MMPs has shown to have important roles:

- ◆ in lung diseases
 - with an elevated level of MMP-9 notably for : hyperacute hypersensitivity reactions like asthma and acute respiratory distress syndrome (ARDS), chronic diseases like chronic obstructive pulmonary disease (COPD), common genetic disorders like cystic fibrosis, lung cancer or interstitial lung fibrosis [Vandooren et al. 2013; Galliera et al. 2015].
- ◆ in diabetes
 - MMP 2, 3, 9, 10, 14, 15 are expressed in kidney tissues of patients with diabetic nephropathy. Besides from extracellular matrix degradation, these MMPs are involved in the release and activation of several factors such as TGF, TNF, insulin-like growth factors and heparin-binding epidermal growth factor , thus contributing indirectly to tubular cell proliferation and renal fibrosis, leading to renal damage. [Thraikill et al. 2009]
 - Due to activated MMPs, diabetic wounds are unable to heal quickly. In the murine model, MMP 9 and 8 have been identified as valuable pharmacological targets.
- ◆ in cardiovascular diseases :

- The high amount of monocyte derived macrophages secreting MMP-1,8, 10, 12, 13 and TIMPs in the environment of atherosclerotic plaque accounts for enhanced plaque ruptures [Newby 2015].
 - Abdominal aortic aneurysm (AAA) is described as a permanent dilatation of the abdominal aorta. This pathology upregulates proteolytic pathways, loss of the arterial wall ECM, inflammation, oxidative stress and apoptosis, where especially MMP-9 and MMP-2 have been implicated [Siemianowicz 2012].
- ◆ in proliferative diseases
- It is believed that MMPs are secreted by tumor-associated macrophages and neutrophils for cell invasion and metastasis. However this inflammatory effect can be anti-tumoral or pro-tumoral. Depending on the cancers cells, proteases and their natural inhibitors can play a positive or negative role as these host cells have a high genetic instability. Studies have shown that MMP-9 is involved through the secretory pathway but the role of these proteases as beneficial components is still to be determined.
 - Specific cancer types which have been evaluated for MMP expression are : Breast cancer, skin and oral epithelial cancers, cancers of the digestive system, brain tumors, prostate cancer, laryngeal and nasopharyngeal cancers, bladder cancer, lung cancer [Galliera et al. 2015].
- ◆ in dentistry
- in periodontitis, the use of MMP inhibitors called chemically modified tetracyclines remains a successful clinical approach in preventing disease [Vandooren et al. 2013].

These disease-related examples with the MMP family particularly shows the varying behavior depending of the stimulated signalization pathway up-regulating or down-regulating its expression in pathological conditions.

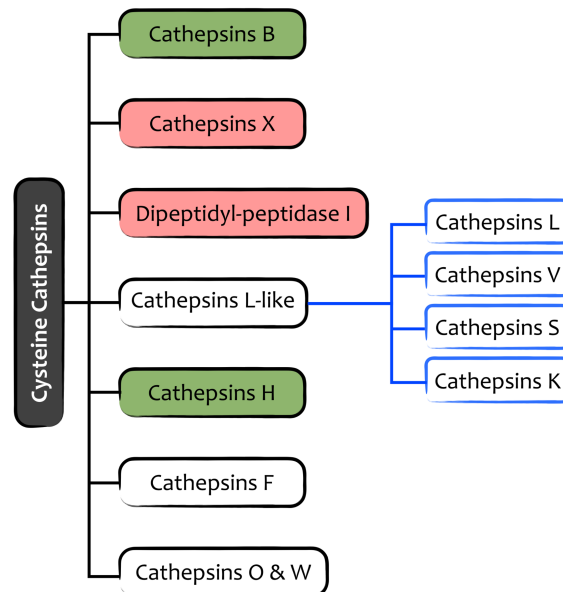


Figure 1.4: Classification of cathepsin proteases – the white boxes are exclusively endopeptidases, the red boxes are exclusively exopeptidases and the green ones are both endo- and exo-peptidases.

Another class of enzymes has also gained substantial interest in these later years: **cysteine cathepsins** which is classified into 7 groups as shown in the Figure 1.4. The majority of the cysteine cathepsins are endopeptidases, except for cathepsin B and H which are both endo and exopeptidases and cathepsins X and Dipeptidyl-peptidase I which are strictly exopeptidases (c.f Figure 1.4).

Today our perception of cysteine cathepsins has shifted from non-specific lysosomal scavenger to specialized processing enzymes. They have a broad sub-cellular distribution and are involved in numerous physiological as well as pathological processes. At first due to their intracellular lysosomal localization, these proteases were considered to be only involved in protein turnover. Contrary to this belief, cysteine cathepsins were also observed in the nucleus where they acted as important effectors of nuclear physiology [Fonović et al. 2014]. In diseases, cysteine cathepsins were found to be secreted in the extracellular environment. Natural inhibitors such as cystatins, thryopins and serpins were also present to fight against its destructive potential of the extracellular space. Hence, any imbalance between active cathepsins and their inhibitors would result into a variety of pathologies - cancer, arthritis, atherosclerosis, osteoporosis, neurodegeneration, and infectious diseases.

Below the web-like diagram (Figure 1.5) shows a summarized form of the various roles of human cysteine cathepsins in both physiological and pathological conditions

[Novinec et al. [2013](#)]. The major functions in the highlighted green shaded boxes are linked to different cell types. These cells were shown to express specific cysteine cathepsins in various situations. In turn these proteases expressions were related to different molecular processes for either physiological processes or pathological conditions.

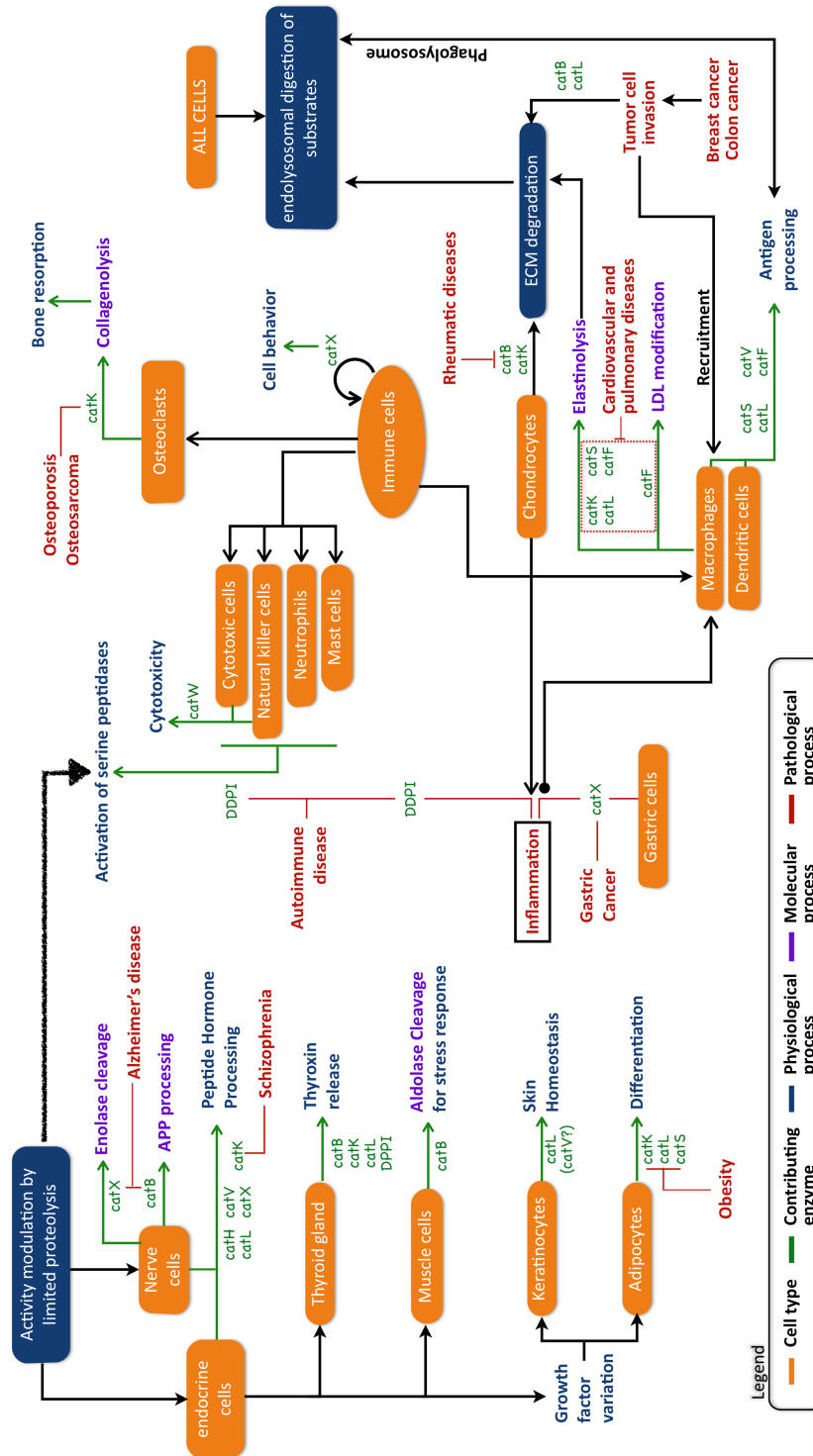


Figure 1.5: The figure illustrates an interconnected expression of the different cathepsin isoenzymes according to their cell type specificity, their physiological roles and also their implications in pathological conditions.

Focusing on the current clinical status, cysteine cathepsins play a major role [Novinec et al. 2013]:

- ◆ In the balance of bone resorption and bone formation
 - the hyperactivity of cathepsin K in osteoclasts enhances bone resorption causing osteoporosis. Odanacatib (Merck), a cathepsin K inhibitor, is already in phase III clinical trial for treating osteoporosis.
 - the cartilage destruction through the release of MMPs and cysteine cathepsins from various cell types - osteoclasts, chondrocytes, synovial fibroblasts and macrophages are of concern in arthritis (osteoarthritis and rheumatoid arthritis). The inhibitor MIV-711 (MedivivAB) is in phase I clinical trial for reducing the high level of cathepsin K expression in arthritis.
- ◆ In maintaining a healthy cardiovascular wall
 - Impairment in the degradation of the major constituents of the cardiovascular wall: collagen and elastin leads to myocardium, coronary, and valve diseases. Cathepsins K and S were upregulated in valve degradation.
 - Cathepsin S is involved in atherosclerotic plaques destabilisation and rupture. It has been shown that deficiency in this protease reduces the size and number of atherosclerotic plaques. Still studied on an animal model, a nitrile-based cathepsin S inhibitor has shown a significant effect on atherosclerosis.
- ◆ In the migration of primary cancer cells to form metastases
 - Cathepsins B, C, H, L, S, and X were shown to be implicated in breast, lung, brain, gastrointestinal, pancreatic, head and neck, and melanoma cancers. However their distinct roles still need to be elucidated.
 - Cathepsins have shown to weaken the chemotherapeutics response and their inhibition were found to significantly improve the efficiency of chemotherapy.

As it can be noticed in the web-like diagram, all molecular processes and the specific roles of each cathepsins remain unsolved.

For all pathologies, strategies in understanding the implications of specific proteases and in finding various targets to treat the disease are being studied. The ability to reduce tumor growth, invasion, metastasis, and angiogenesis or in limiting bone or cartilage destruction by increasing expression of the endogenous inhibitors or by administering a small inhibitors suggest that targeting specific enzymes will be of therapeutic benefit. The only small inhibitor shown to be effective so far was a broad-spectrum inhibitor; be it for metalloproteinases or for cathepsins proteases.

By far, targeting individual enzymes seems to be a wiser strategy, given the potential protective roles of enzymes and the deleterious effects observed in mice. Further work will be needed to define the appropriate target in the tumor cells, tumor-associated cells or both, and whether it is intracellular, secreted or membrane-associated. In this regard, imaging probes to detect proteolytic activities *in vivo* would be useful surrogate markers and would serve in enhancing the efficacy of enzyme inhibitors. Strategies aimed at imaging and detecting enzyme activity have substantial potential in aiding to diagnose and predict diseases.

1.1.3 Proteolytic activity Detection Strategies

For years till now, proteolytic activity has been vastly studied *in vitro* – their kinetic measurements, their substrate specificity, their potential inhibition activities using specific drugs, their 3D structure to understand their catalytic mechanism – are all the topics that are still being resolved for their better understanding in physiological processes as well as pathological ones. Even if *in vitro* studies are necessary, the biological system is entirely perturbed when measured out of its environment.

A. CURRENT CLINICAL STATUS

Clinically, the most widely used specimens to make up diagnosis, prognosis or therapeutic monitoring for a multitude of different diseases are patients' blood and blood-derived fluids. However, serum and plasma have high intrinsic proteolytic activity that is related to diverse exopeptidases and endopeptidases, for instance in the process of blood coagulation or the immune response. Nonetheless, studies are still ongoing and biomarkers are being identified in serum specimens for diagnosis. For all these *in vitro* analysis, biochemical approaches are being used either to detect the presence of the proteases and/or their activities. These techniques include:

- ◆ the zymography assays [Wilkesman et al. 2009] -
 - which is an electrophoretic technique commonly based on sodium dodecyl sulfate-polyacrylamide gel electrophoresis (SDS-PAGE) which contains a substrate copolymerised with the polyacrylamide gel matrix. After the electrophoretic run, and the successive steps, the areas of digestion are identified.
 - types of zymography analysis are 1-D zymography, 2-D zymography, 2-D zymography combined with mass spectrometer, in-situ zymography, real-time zymography, multiple layer substrate zymography and the reverse zymography [Lista et al. 2013].
- ◆ the enzyme-linked immunosorbent assay (ELISA), Western blotting and radioimmunoassays are commonly employed for quantification of the biomarkers.

A recent article of the team of Yepes showed that there are five synthetic reporter peptides that are being cleaved preferentially by tumor-associated proteases found in the serum of colorectal cancer patients and that are highly stable in the serum of healthy controls [Yepes et al. 2014]. The research group of Taylor JM et al. identified specific aminopeptidases activity, notably alanyl aminopeptidase and cathepsin C in the urine sample of bladder cancer patients [Taylor et al. 2014]. The alanyl aminopeptidase was seen to be downregulated, and on the other hand the cathepsin C was upregulated

in the cancer group. These two proteases may be a potential candidate as urinary indicator for the presence of bladder cancer.

However, great care should prevail upon sample choice and sample preparation when clinical diagnosis is concerned. In order to approve a clear-cut diagnosis in clinical practice based on upregulation or downregulation of a set of disease-associated proteases, further *in vitro* studies need to be carried out. Standardised protocols need to be established with a minimum of false positive and/or negative results and a specific proteolytic activity. Even if *in vitro* assays are more cost effective, studying and diagnosing pathology-related proteolytic activities *in vitro* is often misleading due to :

- ◆ organelle damages upon sample preparation which would lead to the release of activators or inhibitors, thus artificially affecting enzymatic activities and
- ◆ the incorrect *in vitro* assay model conditions which might not imitate the *in vivo* environment accurately.

B. CURRENT EXPERIMENTAL *IN VIVO* STRATEGIES

A second strategy is the *in vivo* imaging of proteolytic activities assigned to specific diseases. Based on *in vitro* studies, proteomic profiling have been performed for years identifying the over-expressed proteases' activities occurring in each disease. Three imaging techniques are currently used for imaging enzyme activity in small animal research. Their characteristics are briefly tabled below (see Table 1.1):

i) Optical Imaging

Optical Imaging is indubitably the most versatile visualization modality for imaging proteolytic activity *in vivo* mainly because of the availability of fluorescent reporters for tagging cellular and sub-cellular processes *in vivo*. Among the different optical imaging systems, there are :

– BIOLUMINESCENCE IMAGING - BLI

The principle of BLI is based on genetically modified cells which express constitutively a bioluminescent reporter gene commonly the luciferase encoding gene. The expressed bioluminescent enzyme then catalyses the oxidation of small molecules, here the luciferin into oxyluciferin and release photons of light. This light travels across tissue depths of several millimetres to centimetres. It is finally detected at its proper wavelength with charged-coupled device (CCD) cameras, converting the light photons

Table 1.1: Characteristics of Various Molecular Imaging techniques

Imaging technique		Resolu- tion	Sensitivity	Tissue Depth	Examination time
Optical	Bioluminescence Imaging (BLI)	several mm	< nM	≈ 1 cm	minutes
	Fluorescence Molecular Tomography (FMT)	1-2 mm	nM	< 10 cm	seconds/ minutes
	Photoacoustics Imaging	few cm	μM - nM	> 7 cm	minutes
Nuclear Imaging	Single photon emission computed tomography (SPECT)	1-2 mm	nM - pM	no limit	minutes/ hours
	Positron emission tomography (PET)				
Magnetic Resonance Imaging (MRI)	PARACEST MR Imaging non-biological nuclei MR imaging	200 μM	mM	no limit at regular fields	minutes/ hours

Source: [Weissleder 2002; Wang 2008; Razgulin et al. 2011]

into electrons. Two-dimensional (2D) images are acquired in around one-second. The dispersion of light is the biggest disadvantage for *in vivo* imaging as it enhances low spatial resolutions and limits depth penetration.

Nevertheless, imaging proteolytic activities using BLI for either *in vitro* assays or *in vivo* surface-based tissues have extensively been carried out. For example in living animals, β -galactosidase, caspases, furin, and β -lactamases activities have been demonstrated. It should be noted that BLI is linked to versatile probe-design strategies that are based upon either:

1. specific chemically modified luciferin substrates [Dragulescu-Andrasi et al. 2009; Godinat et al. 2013] – Dragulescu-Andrasi A. et al used an aminoluciferin tagged with an arginine-rich peptide sequence to detect furin activity in xenografted breast tumors in nude mice whereas Godinat A. et al chose to synthesize the luciferin molecule in-situ between 2-cyanobenzothiazole molecule and the freed D-Cysteine once a caspase3/7 peptide substrate Asp-Glu-Val-Asp-D-Cys (DEVD-(D-Cysteine)) is cleaved in transgenic luciferase mice with induced caspase activity.
2. distinguished bioluminescent reporter gene constructs [Fu et al. 2013] – Fu Q and colleagues built a specific plasmid ANLuc(DEVD)BCLuc which constitutes

the split N- and C-terminal fragments of luciferase, fused to interacting peptides, pepA and pepB, respectively, with an intervening caspase-3 cleavage motif. When apoptosis is induced, the reporter molecule is proteolytically cleaved by caspase-3 at the DEVD motif. Association of pepA and pepB brings inactive fragments of luciferase into close proximity, thereby producing bioluminescence activity. Thus the activity of caspase-3 was reflected by the activity of luciferase which could be detected by camera in whole animals.

The BLI technique has a limited and wavelength-dependent light transmission which highly attenuates the photon intensity for deep-seated tissues. Hence, this technique remains however limited to imaging surface tissues in living animals with low spatial resolutions. Above all, this technique requires the presence of luciferase encoding gene in the cells, which is definitely an incompatible translational imaging technique for patients' disease diagnosis.

– FLUORESCENCE MOLECULAR TOMOGRAPHY - FMT

Another optic-based approach is the fluorescence molecular tomography. Briefly, this technique relates the use of fluorophores *in vivo* with their own absorption and emission spectrum. The subject is illuminated uniformly at the appropriate wavelength to excite the fluorophore. The emitted fluorescence signal is then recorded by a CCD camera encoding spatially the intensity of the photons. The image is inherently one 2D projection of the emitted photons with no information on signal's depth. With FMT, the particularity is the reconstruction of series of images, acquired using a point excitation source with a number of source-detector pairs to produce several different projections through the subject, into a volume. Here the reconstruction of the volume is derived from an inversion algorithm relying on the behavioral models of light when traveling through tissue.

In regard to *in vivo* proteolytic activity imaging, FMT has added a third dimension to the images. Indeed, cathepsin-B activity was detected in orthotopic gliomas, stereotactically implanted into the brain of nude mice. Images were acquired in 5 minutes and only 2 nmol of Cyanine 5.5 (a poly-lysine based fluorochrome) were administered intravenously. This technique allowed somehow a correct localisation of the biological activity taking place inside the animal's brain [Ntziachristos et al. 2002]. Chen HH and his colleagues were able to perform non invasive imaging of rapamycin-induced autophagy at the apex of the heart with an ischemia-reperfusion injury. By injecting intravenously 5 nmol of cathepsin activable fluorochrome (Prosense 680 ®), cathepsin activity was clearly detected on the tomographic images with spatial resolution of $1 \times 1 \text{ mm}^2$ in plane and 0.5 mm of slice thickness and a marked difference of around 30-fold was observed between untreated and treated mice [Chen et al. 2013].

The major challenge of this technique is in the reconstruction algorithm of the im-

ages. Since light scattering and absorption depend on the physical properties of the tissues, the distance travelled and the wavelength of the light, correct simulations and probability calculations should be performed to find the most likely location of the fluorescent source. This estimation ultimately leads to a semi-quantification of the fluorescent signal. Another downside of this modality is about the anatomical information. FMT provides us with no morphology or anatomical structures of the subject. In most cases, this modality is therefore combined to another imaging technique, notably MRI or X-ray computed tomography (CT). Ultimately FMT suffers from high tissue autofluorescence caused by the excitation light which reduces signal-to-noise ratio (SNR)[Darne et al. 2014].

– PHOTOACOUSTIC IMAGING

This method also known as optoacoustic imaging combines light and sound. Nanosecond pulses of laser light are used for excitation, which are absorbed, turned into heat, and through thermal expansion generate a thermoelastic pressure wave. This wave propagates through the tissue at the corresponding speed of sound and can be detected using an array of ultrasound detectors, revealing the tomographic information of the absorber. Unlike fluorescence, this technique records absorption, retaining optical contrast by using excitation light, while providing the refraction-limited resolution of ultrasound, which is less scattered in tissues.

So far, among the optical-imaging techniques, the spatial resolution was limited by the penetration depth to only about a millimeter. The photoacoustic imaging works at a far greater depth (up to 3-5 cm) with a far better spatial resolution as the pressure waves are modestly scattered and attenuated by the tissue, leading to a faithful signal encoding. Here, for the first time an activatable oligomerizable photoacoustic imaging probe was established for a furin-like activity in living nude mice [Dragulescu-Andrasi et al. 2013]. Furin is one of the central regulators of tumor progression and metastasis and thus of high interest as a drug target. With a voxel size of $250\mu m$, photoacoustic images were acquired with a 7-fold enhanced signal at the xenografted site of furin-overexpressed human breast adenocarcinoma cells (MDA-MB-231) as compared to the controls. More recently, MMP13 activity was observed in xenograft tumor models (SCC7 breast cancer cells) *in vivo* using a near-infrared absorbing copper sulfide nano-probe conjugated to a black hole quencher via a MMP-cleavable peptide linker. Yang K and his colleagues clearly demonstrated a difference in the signal after proteolysis versus the situation where the activity was inhibited [Yang et al. 2014].

Despite its potential and its many advantages over other methods, there are some difficulties with photoacoustic imaging that have not yet been resolved. As light penetrates deeper into tissue, the resulting ultrasonic signal diminishes due to tissue light absorption and laser light dispersion / diffusion or back-scattering. Hence it limits

on just how deep photoacoustic imaging can delve. Bone tissue represents another obstacle to the technology. Laser light and sound do not easily pass through bone structures. The speed at which sound travels through bone is different from the speed at which it travels through soft tissue, and as the ultrasound passes from one medium to the next it gets reflected and refracted. Air cavities, many of which are found inside the human body, pose a similar problem.

ii) Nuclear Imaging

Nuclear Imaging is another field of bio-imaging that can assess pathophysiological cellular processes and in particular enzyme trafficking. This approach is based on detection of the decay of radioactive isotopes. In the case of proteolytic activity detection, the enzyme-catalysed reaction has to generate a product that is better trapped at the site of the abnormal proteolytic activity than the substrate probe. In this section we will specially talk about SPECT and PET and how they were able to reveal enzyme activity *in vivo*.

– SINGLE-PHOTON EMISSION COMPUTED TOMOGRAPHY - SPECT & POSITRON EMISSION TOMOGRAPHY - PET

Briefly, SPECT imaging consists of detecting specific gamma-emitting radioisotopes like ^{99m}Tc ($t_{\frac{1}{2}}$: 6.0 h), ^{111}In ($t_{\frac{1}{2}}$: 2.8 d), ^{123}I ($t_{\frac{1}{2}}$: 13.2 h), and ^{131}I ($t_{\frac{1}{2}}$: 8.0 d) using scintillation detectors. On the other hand, PET is based on positron-emitting isotopes decay leading to the emission of two diametrically oriented gamma rays. The most commonly used isotopes in PET are ^{18}F ($t_{\frac{1}{2}}$: 1.83 h), ^{64}Cu ($t_{\frac{1}{2}}$: 12.7 h), ^{11}C ($t_{\frac{1}{2}}$: 20.4 min), ^{13}N ($t_{\frac{1}{2}}$: 9.96 min), ^{15}O ($t_{\frac{1}{2}}$: 2.05 min), ^{68}Ga ($t_{\frac{1}{2}}$: 1.14 h), and ^{124}I ($t_{\frac{1}{2}}$: 4.18 d). Both techniques are known to be highly activity specific for radio-pharmaceuticals, together with a high detection sensitivity, non-invasiveness, and semi-quantitative or quantitative results. However recent literature has shown very little concern in developing radioactive labels for imaging proteolytic activity in living subjects.

In 2012, the team of Chuang C.H and his colleagues worked on a fluorine-18 labelled MMP2/9 substrate. This substrate releases a hydrophobic product upon enzymatic action. A 20 fold increase in signal from the MMP expressing tumor *in vivo* was observed as compared to breast adenocarcinoma induced tumor that did not express MMP proteases [Chuang et al. 2012]. This PET imaging strategy hinges on the retention of the cleaved hydrophobic product at the vicinity of the proteolytic activity through membrane interactions. Another strategy does exist - the activatable cell-penetrating peptide (ACCP) concept. Mostly used in optical imaging, ACCP is composed of a polycation peptide domain facilitating cell uptake and a polyanion peptide domain that are linked in-between by a protease substrate. (see Figure 1.6). An article published in

2011 and later on with further advances in 2015 [Duijnhoven et al. 2011; Duijnhoven et al. 2015] showed that the hairpin-like ^{177}Lu labelled to ACPP probe which was meant to be specifically cleaved by MMP2/9 *in vivo* in tumors was unselectively hydrolysed prior in the blood circulation and then accumulated in the tumor by retention. Further research need to be set up for a pathology-specific proteolysis using this peculiar probe strategy.

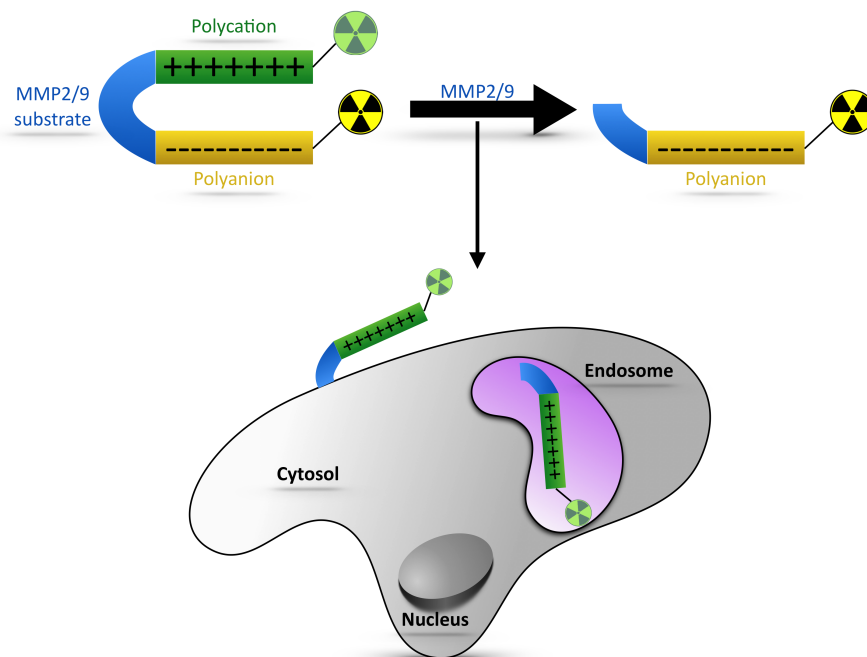


Figure 1.6: The cell-penetrating property of a polycationic peptide is masked by a polyanionic peptide. Cleavage of the linker by MMP-2/9 releases the polycationic cell-penetrating peptide, which will carry its radionuclide cargo (in green) across the cell membrane. The polyanionic peptide and its radionuclide cargo (in yellow) will be cleared from the target tissue. The ratio of the radionuclide cargoes (green-over-yellow) is a measure for local ACPP activation.

It should be noted that most of the *in vivo* SPECT or PET imaging has been favorable for protease imaging, more precisely not the detection of their activity but their presence through antibody labeled probes or by using radio-labeled inhibitors [Máté et al. 2015]. Furthermore, nuclear medicine is radiation based imaging modality and has a very low spatial resolution and very limited anatomic resolution. For these reason, most of the time, nuclear imaging is coupled to another imaging modality like Computed Tomography or MRI.

iii) Magnetic Resonance Imaging

Magnetic Resonance Imaging (MRI) can be depicted as a less ideal imaging modality for target-specific imaging due to its inherent low sensitivity (milli-molar). Nevertheless, today it is by far the only universal anatomic-to-functional imaging approach with its reasonable spatiotemporal resolution, natural imaging contrast of deeply seated soft tissues, the administration of non-radiative contrast agents, and also with a good molecular specificity behind that of optical imaging.

Various methods have been established in molecular MRI imaging to detect proteolytic activities specifically. Among them, there is the use of T_1 -weighted contrast agents which are able to alter their access to water molecules upon enzymatic action. T_2^* -weighted contrast agents have also been designed for protease sensing. Their molecular remodeling upon proteolytic activity relies on their aggregation process which modifies the T_2 relaxation time of the probe itself. The third interesting approach is the Chemical Exchange Saturation Transfer (CEST) technique which is a relatively recent mechanism for generation of functional MR contrast. CEST depends on the selective saturation of labile protons found on the contrast agent, that consequently diminishes the MR signal. Further explanations about this method will be given below. Last but not least, MR polarization transfer has also been utilized for the same purpose with compelling results which are to be further developed in the next section.

Hence, before looking at the different strategies used in MRI to assess a proteolytic activity *in vivo*, I would like to describe briefly the principle lying beneath this technique.

1.2 State of Art of the different techniques in enhanced MRI

1.2.1 The Principle of NMR imaging

NMR is based on an intrinsic property of matter – the “spin” which is a form of angular momentum denoted as \vec{p} . Assuming proton NMR, its spin angular momentum is characterized by a quantum number, with two orientations (generally known as the α and β states respectively). These possible orientations observed as z-components, can be quantized as (c.f. Figure 1.7) –

$$\|\vec{p}_z\| = \pm \frac{1}{2} \hbar \quad (1.1)$$

In classical physics, the spin of any elementary particle can be described as a sphere rotating about its own axis creating a magnetic moment, $\vec{\mu}$ which is collinear to \vec{p} and is expressed as –

$$\vec{\mu} = \gamma \vec{p} \quad (1.2)$$

,where γ is the gyromagnetic ratio of a given nucleus.

In absence of an applied magnetic field, all the proton nuclear spins are randomly positioned in the precessional orbit, i.e. there is no degeneracy in the proton spin states. The total magnetic moment is considered to be zero ($\sum \vec{\mu} = 0$) as all the vectors are statistically distributed at equilibrium.

When these nuclei are now placed in an intense external magnetic field, B_0 generated by a magnet, all the nuclear magnetic moments will orient themselves in one of two possible spin states, α and β . At equilibrium, the α state will be more favored as this state corresponds to the minimum energy state.

$$E = - \mu_z \cdot B_0 \quad (1.3)$$

$$E = \mp \frac{1}{2} \gamma \hbar B_0 \quad (1.4)$$

This system is said to be **polarized** (c.f. Figure 1.7), meaning that the nuclear spins will have a weak tendency to point along the field, B_0 and together the many nuclei form a total magnetization called the **net magnetization**, $\langle \mu_z \rangle$ or M_z . This net magnetization at room temperature is equivalent to only around 3 per million nuclear spins oriented along the direction of the field (3 ppm at 1 tesla) and is proportional

to the field i.e. a larger field will produce a large magnetization, thereby a better signal-to-noise ratio (SNR):

$$M_z \approx \frac{\hbar^2 \gamma^2 B_0}{4kT} \quad (1.5)$$

Concurrently, all the nuclear spins will start precessing about B_0 at a specific frequency known as the **Larmor frequency**, ω_0 . As only the M_{xy} component gives rise to a measurable signal, in order to measure M_z , it must be tilted away from B_0 or z-axis. M_{xy} being a time-dependent motion, the resonance condition needs to be satisfied. By using radio waves or radio-frequency (RF) pulses, 2 following conditions will have to be met:

1. the RF magnetic field should be perpendicular to B_0 ; and
2. it should oscillate at the same frequency as the Larmor frequency.

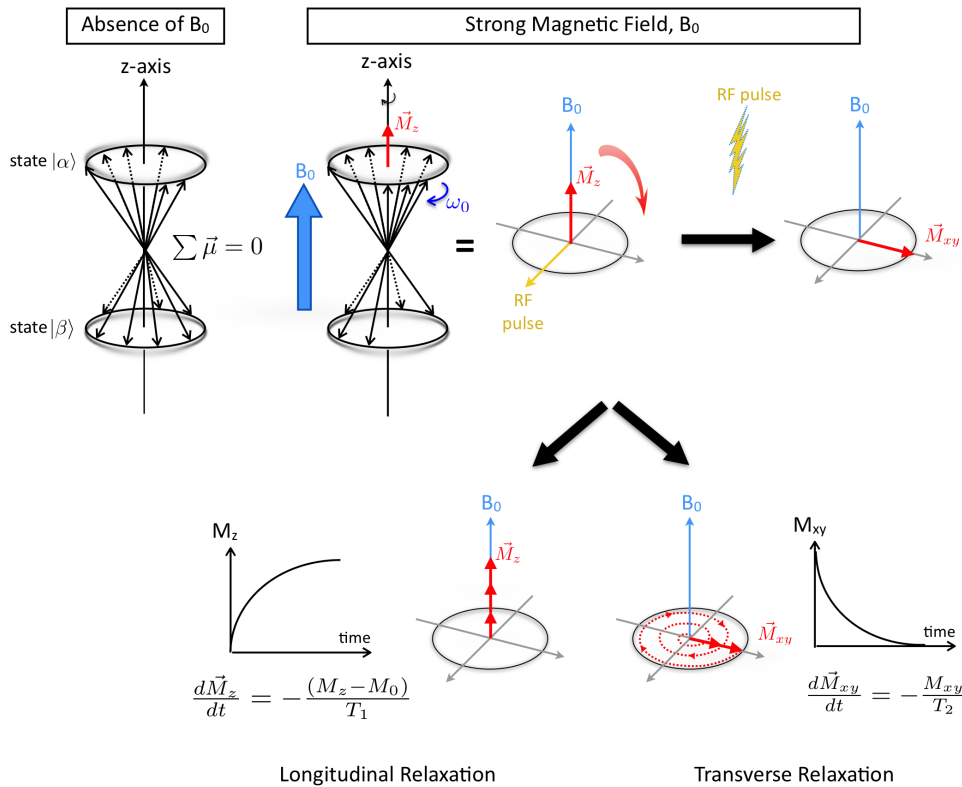


Figure 1.7: Principle of NMR: A) The spins are oriented randomly, with a uniform distribution over directions, meaning that there is about an equal number of spins pointing in both directions. The net magnetization is near zero and the nuclei do not precess. B) When a magnetic field B_0 is added, a degree of alignment is established and the spins precess about B_0 at their characteristic frequency, ω_0 . C) When a resonant radio frequency field (RF pulse) is applied, the net magnetization is rotated in the transverse plan. D) Afterwards the two relaxation time scales: T_1 for the longitudinal relaxation (M_z recovery) and T_2 for the transverse relaxation (M_{xy} decay) are illustrated.

After the net magnetization has been perturbed by the RF irradiation at the Larmor frequency, a number of interactions will result in a net magnetization approaching the equilibrium state, i.e. the return to alignment with B_0 . This is what we call **relaxation**.

Relaxation occurs on two different time scales : 1) the spin-lattice relaxation time, characterized by its constant T_1 – that involves the exchange of energy between the protons and the molecular environment and 2) the spin-spin relaxation time, characterized by its constant T_2 – in which the proton spins can exchange energy amongst themselves (also termed as phase de-coherence).

1. Spin-lattice relaxation takes place due to locally fluctuating magnetic fields which

are caused by physical processes like – dipolar interactions, electric quadrupole, chemical shift anisotropy, spin rotation and paramagnetic interactions. These interactions induce transitions between the two spin states. This process causes the total magnetic moment to realign itself over time with B_0 and can be expressed as –

$$\frac{d\vec{M}_z}{dt} = -\frac{(M_z - M_0)}{T_1} \quad (1.6)$$

$$M_z(t) = M_0 + (M_z(0) - M_0)e^{-\frac{t}{T_1}} \quad (1.7)$$

2. Spin-spin relaxation is about the de-phasing processes taking place in-between proton spins. Due to fluctuating fields, each individual proton will lose phase with each other and precess at different frequencies. This results in the extinction of the x-y component of the magnetic moment and is expressed by –

$$\frac{d\vec{M}_{xy}}{dt} = -\frac{M_{xy}}{T_2} \quad (1.8)$$

$$M_{xy}(t) = M_0(e^{-\frac{t}{T_2}}) \quad (1.9)$$

So globally, during realignment of the total magnetization, proton spins lose energy and emit a measurable signal in the x-y plane, referred as the **Free Induction Decay** (FID). The signal is measured by a conductive field coil, called the receiver coil placed around the object being imaged. It is then processed or reconstructed to obtain 3D grey-scale MR images.

The **IMAGING** part is based on the spatial localization of the magnetic resonance information. In short, it is the acquisition of spatial maps of proton densities. To produce MR 2D images with slice selection, the FID signal must be encoded in both directions by applying sequentially three pulsed magnetic gradient fields (G_z , G_y and G_x).

Knowing that the Larmor frequency is directly proportional to the field ($\omega_0 = -\gamma B_0$), an applied field gradient in a certain direction will urge the 1H spins to precess at distinct precession frequencies depending on their position in that same direction. As we move along the applied gradient, the proton spins will resonate either faster or slower depending on their position. The faster or slower precession is detected as higher or lower frequencies in the MR signal. The expression is as follows

$$B(x) = B_0 + G_x \cdot x \quad (1.10)$$

Before going further, all sequential events needed to obtain an image – such as the RF impulsions, the delays and the gradient impulsions, are formally illustrated in a

chronogram named as the “Pulse sequence” (as illustrated in Figure 1.8). A 2D MR image implies –

1. A slice selection step: for instance – a plane/slice perpendicular to B_0 can be selectively excited by applying a field gradient in the z-direction, G_z during the RF impulsion. In the presence of this gradient, the Larmor frequency becomes a function of z –

$$\omega(z) = -\gamma(B_0 + G_z \cdot z) \quad (1.11)$$

$$\Delta z = \frac{\Delta\omega}{\gamma G_z} \quad (1.12)$$

Thus, by exciting with an RF bandwidth of $\Delta\omega$ during the selection gradient, only spins about the magnet’s isocenter of slice thickness Δz will be nutated into the x-y plane.

2. A phase encoding step: Once the slice is selected, the frequency and phase of the precessing net magnetization are made to vary against its position within the slice. To encode the precessional phases of the rotating net magnetization, the y-gradient is immediately switched on after the slice selection gradient. The Larmor frequency now varies along the y-direction according to –

$$\omega(y) = -\gamma(B_0 + G_y \cdot y) \quad (1.13)$$

If the y-gradient is switched off after a time interval of T_y , then the rotating magnetization is brought back to the constant Larmor frequency, ω_0 , with a phase shift memory, $\phi(y)$ as a function of y –

$$\phi(y) = \gamma G_y \cdot y \cdot T_y \quad (1.14)$$

3. A frequency encoding step: Following this phase encoding step, all spins are rotating at the same Larmor frequency but at different phases in their precessional orbits. By applying a field gradient in the x-axis, the Larmor frequency becomes a function of x –

$$\omega(x) = -\gamma(B_0 + G_x \cdot x) \quad (1.15)$$

During the application of this gradient, the echo signal is recorded.

By using the phase and frequency encoding gradients, we have indexed each nutated net magnetization in the selected slice with a unique combination of Larmor frequency

and Larmor phase, i.e x and y positions in the selected slice are identified with an unique combination of ω and ϕ . The total FID signal is given by –

$$S(k_x, k_y) = \int \int \rho(x, y) e^{(-i\gamma G_x t x - i\gamma G_y T_y y)} dx dy \quad (1.16)$$

$$= \int \int \rho(x, y) e^{(-ik_x x - ik_y y)} dx dy; \quad (1.17)$$

Finally, the proton density map is obtained by the inverse 2D Fourier Transform (FT) of the FID. k_y is varied by stepping through different values of G_y whereas k_x is obtained by holding on the frequency encoding gradient and by sampling the echo. The k_x, k_y plane is called the ***k-space***.

The voxel intensity of a given tissue type depends on the proton density of the tissue; the higher the proton density, the stronger the FID signal. MR image contrast also depends on two other tissue-specific parameters : T_1 and T_2 . By varying timing parameters, MRI images can have different contrast weightings namely – T_1, T_2 or proton density (PD)-weighted images. For each pulse sequence, two main parameters are used for contrast : the echo time, TE – which is the period from which the magnetization is tilted into the transversal plane until the maximal signal is recorded; and the repetition time, TR – which defines the time taken to acquire one line of the k -space. For example T_1 -weighted images are obtained with short TR and short TE because with a short TR, T_1 contrast will be maximized and with a short TE, T_2 contrast is minimized.

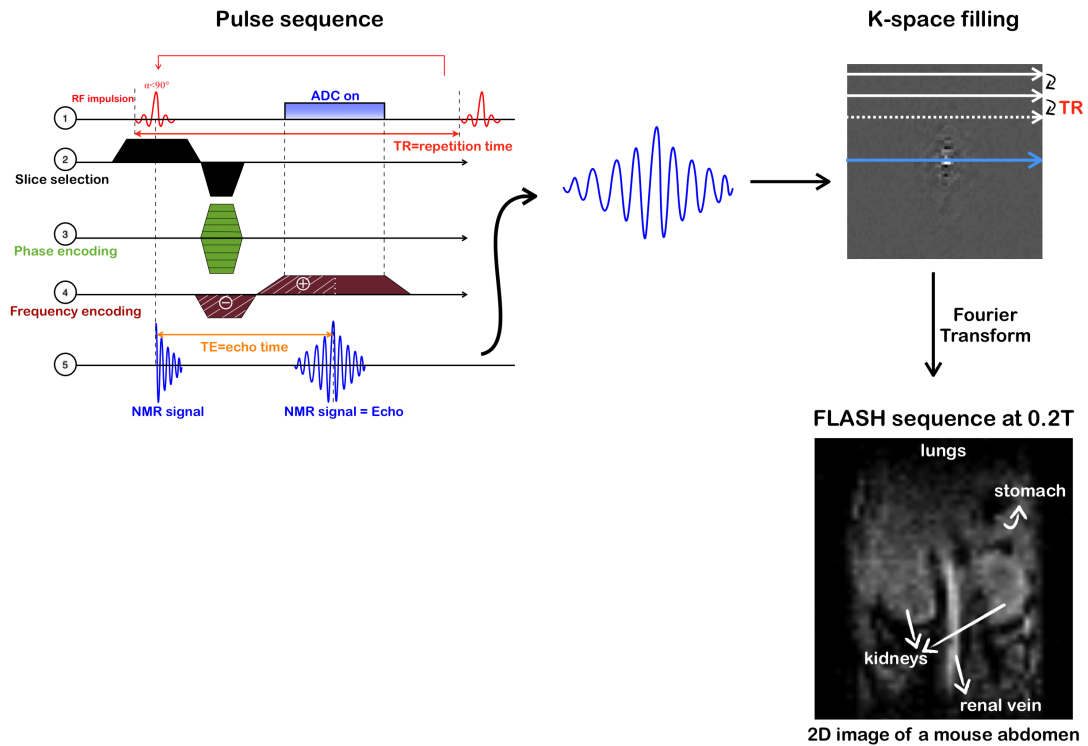


Figure 1.8: 2D Image formation in MRI – here is an example of a classic GRE sequence. After each RF pulse, an echo is recorded at the end of the TE. The signal intensities of the echo are collected in the matrix. Each line of the k -space is encoded with the slice selection gradient, the phase-encoding gradient and the frequency-encoding or read-out gradient, in a repeated manner during each TR, until the matrix is filled. The Fourier Transform of the k -space gives the image, here the abdomen of a mouse at 0.2 T.

1.2.2 Enhanced MR Imaging Techniques for Proteolytic Detection

Like other imaging techniques, the detection of proteolytic activity using MRI requires contrast agents to reveal the biological process. Exogenous contrast agents are used to provide enhanced image contrast as well as to improve the specificity of MRI. These contrast agents generally work by altering the water proton T_1 , T_2 , or both parameters and it includes paramagnetic chelated metal ions and diamagnetic ions in combination with super-paramagnetic ions. However, as stated earlier, MRI suffers from low sensitivity. For years, scientists and engineers have been working on the different ways to counteract this issue.

A. CHEMICAL EXCHANGE SATURATION TRANSFER - CEST IMAGING

One wide-spread strategy is high field magnets to increase the net magnetization. Due to a higher spectral resolution, the Proton Chemical Exchange dependent Saturation Transfer (CEST) technique, described in Figure 1.9, has been developed together with intense magnets to probe proteolytic activity. Lately, an increasing number of articles using this approach has been published, however most of them are only *in vitro* based [Yoo et al. 2007; Chauvin et al. 2008].

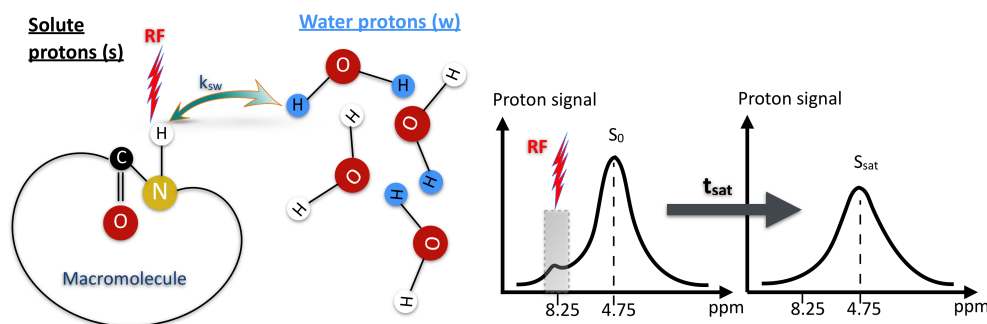


Figure 1.9: The underlying principles of CEST imaging are very simple : exchangeable solute protons (s) that resonate at a frequency different from the bulk water protons (w) are selectively saturated using radiofrequency (RF) irradiation. This saturation is subsequently transferred to bulk water when solute protons exchange the water protons and the water signal becomes slightly attenuated. If the solute protons have a sufficiently fast exchange rate (k_{sw}) and the saturation time (t_{sat}) is sufficiently long, prolonged irradiation leads to substantial enhancement of this saturation effect, which eventually becomes visible on the water signal, allowing the presence of low-concentration solutes to be imaged indirectly.

For instance, in the research team of Reddy Ravinder, cathepsin B activity has been revealed *in vivo* in intracranially implanted 9L gliosarcoma tumors using poly-L-glutamate (PLG) as CEST contrast agent [Haris et al. 2014]. This contrast agent happens to show no CEST contrast because of its low content in exchangeable amine protons. Upon enzymatic action, PLG is cleaved into glutamate (Glu) thus increasing the number of exchangeable amine protons, and thereby the CEST contrast. By selectively saturating these amine protons at 3 ppm, the net NMR signal of the bulk water protons is decreased through chemical exchange processes. This difference in signal is the origin of the CEST contrast. Here, in this work an average of 32% of GluCEST contrast increase was observed at a field of 7T in the tumor region in rat models.

The first complication in using diamagnetic CEST agents is the small shift difference ($\Delta\omega < 10$ ppm) between the resonances of the exchanging solute and the bulk water proton pools, which eventually interferes in the selectivity of the saturation pulse. The second issue is based on the upfield resonances' interferences in the CEST spectrum (i.e. those due to nuclear Overhauser effects in the 0 to -5 ppm range from mobile macromolecules). This inconvenience adds up a major difficulty in the asymmetry data analysis which presumably give the CEST contrast.

Apart from diamagnetic CEST agents, another interesting study was carried out *in vivo* by Yoo.B et al. in 2014 using CatalyCEST agents. These molecular probes are paramagnetic CEST agents that typically consist of lanthanide chelate ($\Delta\omega > 10$ ppm). This lanthanide ion shifts the MR frequencies of the chelate to unique values, thereby facilitating the selective saturation of one CEST agent in a mixture of agents. Yoo B. used Z-Gly-Gly-Arg- α -amino-(Tm-DOTA) as a proteolytic beacon *in vivo* ($\Delta\omega = 48$ ppm) at 7.05T. This probe targets the urokinase plasminogen activator (uPA). This molecule has a CEST effect via its amide group before uPA action. The cleavage of ZGGR peptidyl ligand by uPA converts the amide group into an amine group on the Tm-lanthanide chelate, resulting in the disappearance of CEST from the agent. Its selective saturation revealed a maximum of 15% CEST increase in the subcutaneous Capan-2 tumor implanted on the mouse's flank. As control assay, a second agent, Eu-DOTA-Gly4 ($\Delta\omega = -51$ ppm) was mixed up with the first one; the second giving a positive invariable CEST contrast at its saturation frequency. Each agent showed the same initial tumor uptake rates but the rates of CEST disappearance from the tumor were different for each agent. The faster disappearance from ZGGR- α -amino-(Tm-DOTA) was attributed to uPA activity. [Yoo et al. 2014]

Unfortunately, this global picture of CEST proteolytic activity imaging still needs improvement for *in vivo* studies. Data analysis is quite complex and demands statistical threshold evaluations for proper image interpretation and signal detection. In spite of the intense magnetic field, higher efficient saturating frequencies, larger chemical displacements of agents ($\Delta\omega$) and high temporal resolution MRI sequences (for e.g - 5

sec per image acquisition), small changes in the contrast (usually < 20% rise *in vivo*) were observed. Also, spatial resolution remained above $500 \mu\text{m} \times 500 \mu\text{m}$ with a slice thickness of 1 mm (i.e 2D images). It should also be noted that CEST imaging is based on a signal decrease approach. Last but not least, due to field inhomogeneities across the volume and different tissues, the MR frequencies are not the same everywhere (for e.g a difference of nearly +3 ppm was recorded between a tumor region and the bladder). These variations should be taken into consideration when interpreting and calculating the CEST contrast.

B. GADOLINIUM BASED MR IMAGING

A second type of contrast agents using MRI for enzymatic activity visualisation - are T_1 or T_2 relaxation based agents. Multiple molecular designs based on Gadolinium chelates have been largely synthesised for that purpose. The Gadolinium ion (Gd^{3+}) has a large spin of $7/2$ and seven unpaired electrons. As Gd^{3+} ion is toxic, its chelates were produced (such as DOTA, DPTA and so on) leaving a limited number of coordinated water molecules in the complex. These water molecules are able to exchange with the surrounding water molecules, hence showing excellent characteristics to decrease the T_1 relaxation time of water molecules that are near the Gadolinium metal ion.

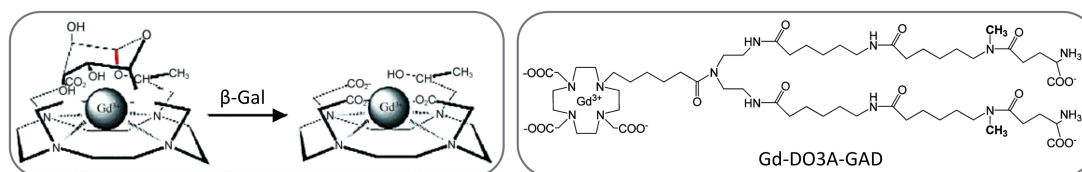


Figure 1.10: Here are represented two Gadolinium-based contrast agents which are able to probe enzymatic activity. On the left is a schematic diagram of the site-specific placement of the galactopyranosyl ring on the tetraazamacrocycle. Upon cleavage of the sugar residue by β -galactosidase, an inner sphere coordination site of the Gd^{3+} ion becomes more accessible to water. On the right it is a GAD responsive probe complex. Once the coordinated glutamate moieties are cleaved by the glutamic acid decarboxylase enzyme, the hydration of the Gd^{3+} center is increased. Peptide bond cleavage [Louie et al. 2000]

To be enzyme-responsive, a galactose molecule was introduced as a ligand in the Gd-chelate that left no space for any water coordination (refer to Figure 1.10, left). In so doing, the surrounding water molecules are not relaxed and no signal enhancement is observed on T_1 -weighted images. Upon cleavage of the sugar molecule by β -galactosidase enzyme, water molecules are exchanged continuously with the Gd-chelate and the relaxation time drops. This process results in a signal enhancement on

the images. This strategy has been first elaborated by Louie A. and her team [Louie et al. 2000]. Glutamic acid decarboxylase (GAD) enzyme was also used to assess enzymatic activity *in vitro*. Synthesis of this specific Gd³⁺-chelate (Figure 1.10, right) in presence of the GAD showed a nice signal enhancement of 60% [Napolitano et al. 2013]. No *in vivo* studies has yet appeared concerning this molecule.

Gd-complex was also used in enzyme-catalysed polymerisation process, meaning that when the Gd-complex polymerises due to an enzymatic action, there will be a decrease in its tumbling time, leading to a decrease in relaxation time. This strategy was used for other enzyme targets, for instance myeloperoxidase with a signal increase above 40% [Chen et al. 2006].

Last but not least, fluorine-19 atom has been grafted to a Gd-complex via a specific peptide sequence. In the same way that the strong r_1 and r_2 relaxivities of the Gd³⁺ ion shortens the T_1 and T_2 relaxation times of water protons, it will also shorten the T_1 and T_2 relaxation times of fluorine, making it undetectable. However, once the peptide is cleaved, the relaxation time is brought back, thereby revealing the enzymatic activity. This study is still undergoing further research in order to confirm enzymatic action [Keliris et al. 2012].

It should be noted that in all these Gd-based concepts, there exist two main properties that is responsible for the shorter T_1 relaxation time :

1. the number of coordinated water molecules in a Gd³⁺-complex
2. the chemical exchange rates of water molecules that are exchanged between the Gd³⁺ complex and bulk water surrounding the agent.

Based on the above factors, great care should be taken when assessing biological interpretations in presence of other endogenous metabolites that can perhaps modulate the behaviours of the contrast agents. As a matter of fact, certain endogenous macromolecules are able to interact with the Gd-complex, and thereby can modify its relaxivity, r_1 . Furthermore, the number of coordinated water molecules could be altered and thus contributing misinterpretations of the images.

T_2^* contrast agents were also explored. Based on the aggregation state of the superparamagnetic iron oxide nanoparticles, a change in the T_2^* relaxation times was accounted for enzymatic activity [Perez et al. 2002; Granot et al. 2011]. These results can be interpreted only for *in vitro* controlled experiments as biological environments are much more complex and no such deductions would be plausible.

In spite of the fact that enzymatic detection is not fully validated *in vitro* and merely in intact living organisms, this T_1 or T_2 imaging concept has to be carried out at high field. Long acquisition times are required and also signal enhancements observed in the *in vitro* experiments are not persistent in all cases.

C. HYPERPOLARISATION-BASED MR IMAGING

Due to the low NMR sensitivity which is a direct consequence of the small energy difference between nuclear spin states, different ways have been set up to enhance this signal. By far the most concluding technique – Hyperpolarization (HP) has been able to overcome this limitation. The term hyperpolarization refers to a procedure that drives nuclei, temporarily, into a significant redistribution of the ordinary population of energy levels. For $i = 1/2$ spins, the energy difference that determines the population of the two spins states α and β is $\Delta E = \gamma\hbar B_0$, where γ is the gyromagnetic ratio and B_0 is the magnetic field. This energy difference determines the population of the spin states. Polarisation is commonly defined as:

$$P = \frac{n_\alpha - n_\beta}{n_\alpha + n_\beta} = \tanh \frac{\gamma\hbar B_0}{2kT} \quad (1.18)$$

where n is the number of spins in each state, $\hbar = h/2\pi$, h is Planck's constant and T , the temperature.

For HP techniques, P is artificially increased well above its low thermal equilibrium level. Brought by Carver and Slichter in 1953, P was increased through the polarization transfer from free electrons to ^7Li nuclei and this increase was named hyperpolarization. Numerous HP methods and strategies are being developed and tested for biomedical applications but only dissolution Dynamic Nuclear Polarization (d-DNP), and parahydrogen induced polarization (PHIP) have been applied to *in vivo* studies of enzymatic processes.

i) d-DNP – dissolution Dynamic Nuclear Polarization

d-DNP is the most commonly used HP method, with $[1-^{13}\text{C}_1]$ pyruvate as the main substrate. In d-DNP also called DNP in the liquid phase, droplets of a liquid sample containing a substrate and a radical (either a nitroxyl or a trityl molecule) are rapidly frozen in liquid nitrogen then transferred to the DNP polarizer where the electrons are fully polarized at a low temperature (1.1-1.4 K) in a high and uniform magnetic field (3.35 T). Microwaves are then applied to the frozen sample for 30-120 min so as to transfer polarization to nuclear spins of the substrate. The latter is then quickly dissolved and injected in the animal model and NMR experiments are conducted.

This technique has allowed dynamic NMR spectra and MRI distribution maps to be evaluated in both pathological and physiological conditions. 1-min assays were carried out on healthy rat brain after injection of hyperpolarized pyruvate and the evolutions of the substrate, lactate, alanine and bicarbonate were evaluated [Mayer et al. 2011]. This study showed the distribution and conversion of the pyruvate occurring inside

the cells. Pyruvate can be consumed into lactate through lactate dehydrogenase (LDH) enzyme and then into alanine by alanine transaminase (ALT) enzyme. In this process, the carbon dioxide formed will also be in equilibrium with bicarbonate according to the pH of the tissue through another enzyme, the carbonic anhydrase (CA). Another typical *in vivo* illustration of this technique was conducted in the team of Kevin Brindle in 2015 [Dzien et al. 2015], showing the oxidation of carbon-13 hyper-polarized and perdeuterated ethanol by the aldehyde dehydrogenase (ALDH) enzyme activity into acetate in mice. This article shows *in vivo* the proteolytic formation of acetate by ALDH2 which is the mitochondrial isoform. Because of the rapid acetate visualization at around 30 s post injection, results implied a diffusion-based transport of ethanol into cells. This d-DNP approach is now in well-driven clinical trials using the $1\text{-}^{13}\text{C}_1$ pyruvate in the detection of prostate cancer through the higher lactate production in tumoral environment. The first-in-man imaging study was carried out in 2013 – where the action of lactate deshydrogenase (LDH) on hyperpolarized pyruvate produced polarized lactate [Nelson et al. 2013].

ii) PHIP – Parahydrogen Induced Polarization

d-DNP can hyperpolarize practically any biomolecule, however it does take hours to produce injectable hyperpolarized probes. In PHIP, which exploits the spin order of the parahydrogen singlet state while hyperpolarizing metabolites, the process lasts around seconds or minutes and free-radical doping agents are not required. As schematised in the Figure 1.11 below, this technique converts hydrogen gas into parahydrogen and then uses cis addition of the latter across alkene or alkyne bonds followed by the spin order transfer from nascent protons to ^{13}C or ^{15}N with a theoretical polarization limit of 100%. This technique is nevertheless hampered by the fact that the precursor should be hydrogenated. A recent alternative technique called SABRE for **S**ignal **A**mplification **B**y **R**eversible **E**xchange has been developed and in which hydrogenation is not required. Here the polarization is transferred in a low magnetic field from the parahydrogen to scalar coupled nuclei found in the target molecule. However, the biomedical applications of SABRE are still to come.

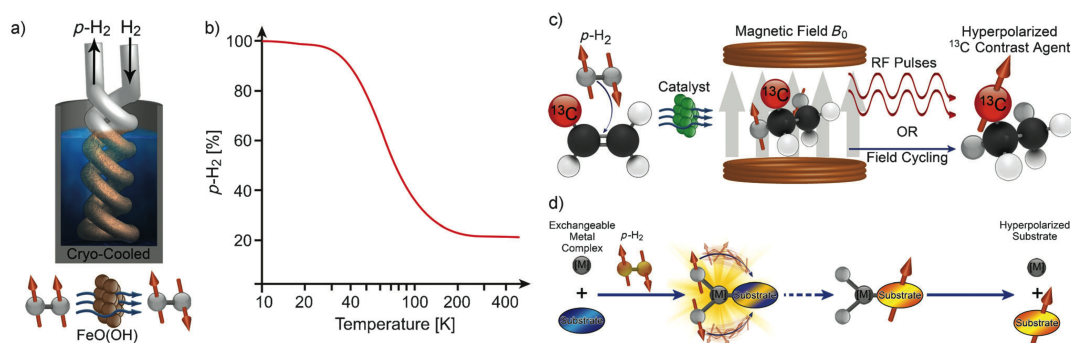


Figure 1.11: a) Schematic of a parahydrogen generator - the entering hydrogen gas is cooled to <77 K and is catalytically converted into parahydrogen under specific conditions. b) The temperature dependence curve shows that below 20 K gives almost a 100% parahydrogen conversion. c) PHIP step-by-step : the cis-addition of the parahydrogen to a molecular precursor across either an alkene or alkyne group adjacent to a ^{13}C or ^{15}N nucleus using a catalyst. The magnetically inequivalent protons on the precursor are then transferred to the ^{13}C nucleus (with a longer T_1) using either an RF pulse sequence or a field-cycling method. d) SABRE process : a spontaneous polarization transfer from the parahydrogen to the precursor through a metal complex. [Nikolaou et al. 2015]

Several PHIP contrast agents have been synthesized for *in vivo* imaging such as hyperpolarized succinate, 2-hydroxyl propionate and 2,2,3,3-tetrafluoropropyl [$1\text{-}^{13}\text{C}$, 2,2,3,3-d $_4$]propionate (TFPP). However all these compounds have physiological barriers. Bhattacharya P. and his team then found a strategy to divert those barriers with the synthesis of $1\text{-}^{13}\text{C}$ diethyl succinate [Zacharias et al. 2011]. They followed in real-time its biodistribution and its metabolic fate *in vivo* in the whole mouse after intravenous and intraperitoneal injections. The out-coming metabolites involved in Krebs tricarboxylic acid cycle (TCA) notably succinate, malate and aspartate were progressively observed on ^{13}C *in vivo* spectra over 3 minutes. The enzymatic activity of esterase on diethyl succinate was observed along with TCA enzymes such as succinate dehydrogenase activity. Another substrate, the $1\text{-}^{13}\text{C}$ -phospholactate where the phosphate group is a protective group was also injected in mice and its biodistribution was traced in different organs. This Chekmenev E.Y's work, even if it is an *ex vivo* study, demonstrated the enzymatic dephosphorylation of this contrast agent *in vivo* through the action of blood phosphatases, followed by the cellular uptake and metabolic outcome of the hyperpolarized lactate [Shchepin et al. 2014a; Shchepin et al. 2014b]. PHIP based molecular imaging in intact organisms suffers from large voxel size ^{13}C spectra resulting perhaps to misinterpretations at a cellular or even tissue level.

On a wider overview, the use hyperpolarization for imaging biological processes *in vivo* remains a transient effect. Slower pathological or physiological processes taking place in more than 10 minutes cannot be observed using this technique. Also, for the imaging part, low spatial resolution is achieved and proper data interpretation is missing for preclinical studies. On the other hand, clinical trials clearly show the potential of this technique to diagnose prostate cancers based on the glycolytic pathway of hyperpolarized pyruvate. Still and all, each cancer type has its own metabolic behavior and can be found unseen using the hyperpolarized pyruvate. Other probe design should be implemented regarding the targeted pathology

Besides all the above mentioned techniques which are currently the state-of-art in enzymatic activity imaging *in vivo*, there is another modality named the Overhauser-enhanced MRI technique which is uncommon but yet has great potential to excel in this field of work. For the rest of my dissertation, I will be focusing on the OMRI technique and I will clearly demonstrate through my work how it should be of growing interest in the field of molecular imaging for detecting active biological processes and eventually in the early detection of pathologies.

1.3 Overhauser-enhanced Magnetic Resonance Imaging Approach

The Overhauser effect is a so-called double resonance effect, in which one excites one resonant transition of a system while simultaneously monitoring a different transition. The method involves a family of energy levels whose populations are ordinarily held to thermal equilibrium by thermal relaxation processes. If one saturates one of the transitions, one so-to-speak transition clamps their populations together (i.e forces them to be equal). The thermal relaxation processes then repopulate all the levels, producing unusual population differences.

In the quest of describing this technique, several names have been used - Dynamic Nuclear Polarization in liquids, Proton Electron Double Resonance Imaging (PEDRI) and of course the one I am actually using - the Overhauser enhanced MRI.

So, before going in depth in this technique, I will relate a small history paragraph of the Overhauser effect and its evolution until *in vivo* imaging. Secondly, I will describe the principle of OMRI with a theoretical background and I will finish with OMRI contrast agents.

1.3.1 History

To begin in 1952, Overhauser A. W. invented a method that he claimed would transfer the large polarization of the conduction electrons in a metal, to the metal nuclei, thereby enhancing the nuclear polarization [Overhauser 1953]. The same effect occurring in non metals was first demonstrated in Carver's thesis in 1954 . He measured proton resonance signals from ammonia molecules in solutions of sodium in liquid ammonia versus applied magnetic field with and without saturation of the electron resonance. He found an increase in the proton absorption rate by a factor of 100. Again in 1957, Abragam A. proved this polarization transfer by using Fremy's salt, a nitroxide molecule in an aqueous solution [Abragam et al. 1957]. In his work, he explicitly evaluated all the energy levels within the spin system. To better understand the electronic relaxation mechanisms, in 1959, Andre Landesman showed that for the unpaired free electron, the relaxation mechanism was spin rotation [Landesman 1959]. On-going research exploring this Overhauser effect was carried out between 1960 and 1990; along with a variety of double resonance techniques [Slichter 2014]. During this era, MRI was first implemented, but it is only in 1988 that Lurie combined the imaging aspect to the Overhauser effect, which was clearly a stepping stone in visualizing free radicals *in vitro* [Lurie et al. 1988]. Later on in 1990, this concept was applied *in vivo* by Grucker's research group to image the bio-distribution of the free radicals in rats [Grucker 1990].

Further studies were carried out on the bio-distribution of free radicals in the aim of improving image quality and temporal resolution and of monitoring the evolution of the enhanced signal *in vivo* [Seimenis et al. 1997; Golman et al. 2000; Lurie et al. 2002; Li et al. 2002; He et al. 2002; Li et al. 2006; Sarracanie et al. 2014]. Most of these studies were carried out using the field-cycling technology or low-field imaging. Knowing that the EPR linewidth varies with the partial pressure of oxygen in blood arteries, Golman K proposed to map the redox state of an hypoxic region near the femoral artery of a rat [Golman et al. 2000]. pH mapping was another application of this OMRI method [Potapenko et al. 2006; Efimova et al. 2011; Takahashi et al. 2014].

Even if double resonance imaging has proven to be a powerful way to see exogenous radicals inside an organism, the *in vivo* biomedical application field remains largely unexplored with only a few world laboratories showing their interest. The need for designing useful OMRI probes have been illustrated in this thesis and in the future more specific probes need to be synthesized for later medical purpose or to understand the role of various unknown proteases.

1.3.2 Theory

In this sub-chapter, we will be talking about the theory of the Overhauser effect as far as free radicals in liquids are concerned. Numerous studies have already explored the theoretical principles of the Overhauser effect [Abragam et al. 1978; Guiberteau et al. 1993; Guiberteau 1994; Grucker et al. 1995; Guiberteau et al. 1996]. Nevertheless, it is always instructive to recall the fundamentals.

In an OMRI experiment, the Overhauser effect enhances the amplitude of the NMR signal of the solvent water protons while the EPR transitions of the dissolved free radical is saturated. Theoretically, for this two-spin system, the Overhauser phenomenon is described with the four energy-level diagram as shown in Figure 1.12, where the two spins I and S are coupled through dipolar and/or scalar interactions. Here the spin S will be the unpaired electron spin of a dissolved radical ($S=1/2$) and I , the nuclear water proton spin ($I=1/2$).

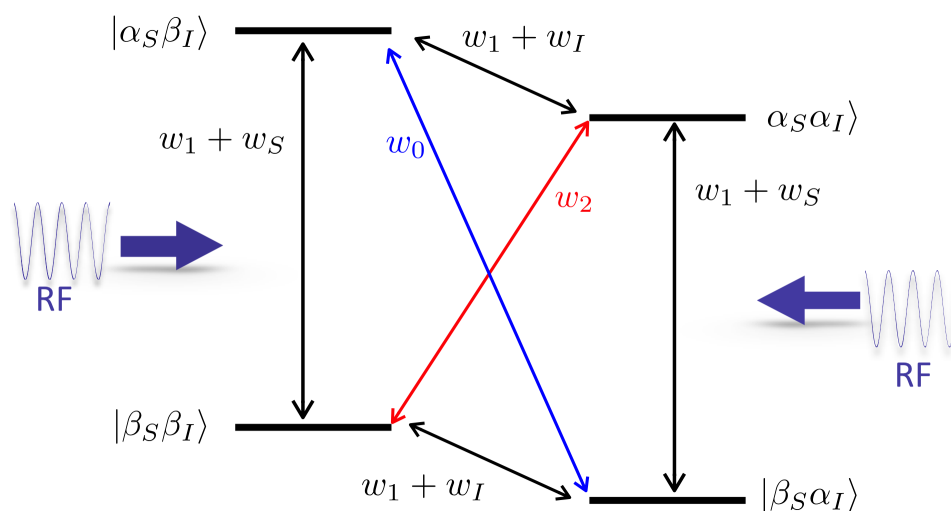


Figure 1.12: Energy level diagram for an electron-nucleus system – S and I represent the nucleus and electron spins respectively with both a spin number of $1/2$. It should be noted that the $\gamma_S < 0$ implying a change of sign for the electron energy level. The transitions are labeled with the respective transition probabilities: w_0 , w_1 , and w_2 represent respectively the zero, single and double quantum transitions probabilities accounting for the I-S cross relaxation. w_S , w_I represent the transition probabilities of the S-S and I-I spin-lattice relaxation respectively.

The Hamiltonian for the two coupled spins, **I** and **S**, in a magnetic field, B_0 is given by

$$\hat{H}_{total} = \hbar\gamma_s(S \bullet B_0) + \hbar\gamma_I(I \bullet B_0) + \hat{H}_{II} + \hat{H}_{SS} + \hat{H}_{IS}^s + \hat{H}_{IS}^d \quad (1.19)$$

$$\hat{H}_{IS}^s = \frac{\gamma_s\gamma_I\hbar^2 8\pi}{3} |\psi(0)|^2 (I \bullet S) \quad (1.20)$$

$$\hat{H}_{IS}^d = \gamma_s\gamma_I\hbar^2 \left[\frac{(I \bullet S)}{r^3} - \frac{3(I \bullet r)(S \bullet r)}{r^5} \right] \quad (1.21)$$

The first two terms of equation (1.19) describe the Zeeman interaction of each spin with the magnetic field, B_0 . The next two terms define respectively the spin-lattice interactions within each spin species, i.e I-I and S-S. The two end terms refer to the interactions between I and S spins. The fifth term \hat{H}_{IS}^s is the scalar interaction also known as the Fermi contact term. This term relies on the probability that the electron is present in the nucleus, $|\psi(0)|^2$ (c.f equation 1.20). The last term of the Hamiltonian, \hat{H}_{IS}^d is the dipolar term involving the magnetic moments of both spins. The strength of the dipolar interaction depends on r the distance between the two spins (c.f equation 1.21).

For free radicals dissolved in a solution, the coupling of the **I** and **S** has shown to be almost exclusively dipolar [Nicholson et al. 1994; Benial et al. 2006].

The irradiation of this system at the EPR frequency equalizes the electron spin populations of level 1 and 3, as well as 2 and 4 and saturates electron flip transitions $1 \leftrightarrow 3$ and $2 \leftrightarrow 4$. Consequently, relaxation occurs through transitions $1 \leftrightarrow 4$ and $2 \leftrightarrow 3$, i.e w_0 , for the flip-flop transitions and w_2 , for the flip-flip transitions. This cross relaxation process corresponding to the hamiltonian term, \hat{H}_{IS} enables the polarization transfer from the electron spins to the nuclear spins. As a result, the nuclear spin population is perturbed in such a way that –

$$\frac{\langle I_z \rangle - I_0}{I_0} = -\rho f \left(\frac{\langle S_z \rangle - S_0}{I_0} \right) \quad (1.22)$$

where I_0 and S_0 are the spin population of each spin at thermal equilibrium, ρ is the coupling factor, and f is the leakage factor.

- The coupling factor, ρ is expressed as follows –

$$\rho = \frac{w_2 - w_0}{w_0 + 2w_1 + w_2} \quad (1.23)$$

It is the contribution of the electron-nuclear spin cross relaxation over the nuclear spin relaxation rate caused by the electrons. It describes the efficiency of (dipolar or scalar) coupling between I and S. It ranges from -1 for pure scalar coupling ($w_0 \gg w_2$) between I and S to +1/2 for pure dipolar coupling ($w_2 \gg w_0$).

- The leakage factor, f is expressed as –

$$f = \frac{w_0 + 2w_1 + w_2}{w_0 + 2w_1 + w_2 + w_I} = 1 - \frac{T_1}{T_{10}} = \frac{rCT_{10}}{1 + rCT_{10}} \quad (1.24)$$

It measures the contribution of the electrons towards the relaxation of the nuclei. In other words it accounts for the loss of NMR polarization. It depends on the ratio of the longitudinal relaxation times of the proton spins in the presence (T_1) and in the absence (T_{10}) of unpaired electron spins, i.e f is sensitive to motion. Also expressed as a function of the concentration of radical, C and r the relaxivity constant, the leakage factor approaches 1 with increasing C. Its values ranges from 0, for no radical contribution to 1 for a relaxation controlled by the radicals.

By rearranging the expression (1.22) and replacing S_0/I_0 by γ_S/γ_I , we can define the achievable Overhauser enhancement, E in terms of –

$$E = \frac{\langle I_z \rangle}{I_0} = 1 - \rho f s \frac{|\gamma_S|}{\gamma_I} \quad (1.25)$$

where s, the saturation factor is given by–

$$s = \frac{S_0 - \langle S_z \rangle}{S_0} \quad (1.26)$$

The saturation factor, s ($0 < s < 1$) is the third key parameter in an OMRI experiment. It accounts for the effective polarisation transfer, and hence the high OMRI sensitivity as it determines the degree with which the electron transitions are saturated upon RF irradiation. When the electron transitions are fully saturated i.e $\langle S_z \rangle = 0$, s equals to 1.

In pursuit of this Overhauser theory, if unpaired electrons are interacting with water molecules through pure dipole-dipole interactions, the maximum theoretical Overhauser enhancement would be equal to -330 under ideal conditions of 100% saturation of the EPR transition and no NMR loss. However, experimentally, these enhancements remain unachievable.

Different reasons are responsible for the lower experimental Overhauser enhancement values.

The three parameters (ρ , f and s) are able to alter the enhancement, E . Ample publications illustrate the variation of the coupling constant according to the nature of the molecule and the magnetic field strength where ρ was shown to decrease at lower fields [Grucker et al. 1995; Höfer et al. 2008]. The leakage factor, f has also proven to vary linearly with the concentration of the radical when the condition $rcT_{10} \ll 1$ is satisfied [Türke et al. 2012; Dhas et al. 2015].

The saturation factor, s depends on the microwave power generating an oscillating magnetic field $B_{1,HF}$ and on the relaxation of the electrons, T_{1S} and T_{2S} , given by the expression 1.27 –

$$s = \frac{\gamma_S^2 B_{1,HF}^2 T_{1S} T_{2S}}{1 + \gamma_S^2 B_{1,HF}^2 T_{1S} T_{2S}} \quad (1.27)$$

These spin-spin electronic relaxation mechanisms rely to a large extent on intramolecular anisotropic interactions. Besides, it has been demonstrated that for radicals with several hyperfine lines such as nitroxide radicals, other mechanisms add up and shorten the relaxation times. The saturation effect is thus hampered.

Bates and Drozdowski have demonstrated that the electron spin exchange mechanism known as the Heisenberg spin exchange effect is enhanced at high concentrations of nitroxide radicals [Bates Jr et al. 1977]. This effect is defined as a process where two radical molecules with opposite spins, exchange during molecular collisions leading to the mixing of states. It arises in particular from the radicals having a hyperfine structure (hfs). Indeed, in nitroxide radicals, properly named nitroxyls, the unpaired electron spin, S is coupled to the nuclear spin of the nitrogen atom ($K=1$ for ^{14}N) and the energy levels are split into six, known as the **hyperfine splitting**. At high concentration of nitroxyl radicals, the saturation of one EPR transition will affect the population of the other states, leading to a significant EPR line broadening. The absorption linewidth, Γ is given by [Lingwood et al. 2010] –

$$\Gamma = \Gamma_0 + u \frac{k[R]}{|\gamma_S|} \quad (1.28)$$

where Γ_0 is the theoretical linewidth at zero concentration, k is the electron exchange rate and $[R]$ is the concentration of radicals. The constant, u relates to the probability of an exchange event occurring between two radicals with different hyperfine states, and $u=2/3$ at high magnetic fields and closer to 1 at low fields. In return, the efficiency in saturating one EPR transition is significantly decreased at high concentrations.

Further discussion on these nitroxide radicals at much lower fields and their corresponding saturation factor will feature in the discussion chapter.

Based on the assumptions made by Guiberteau T and Grucker D in 1993, where the saturation concerning nitroxide radicals with a spin, K of 1 and their three hyperfine

lines, we will pursue all our OMRI experiments admitting that there is no mixing of the individual hyperfine lines upon irradiation of one EPR transition.

In the next section, we will focus on the chemistry behind nitroxide radicals.

1.3.3 OMRI contrast agents

As mentioned above, to be able to produce the Overhauser effect in liquids, we need to have free radicals present. Free radicals are chemical moieties that possess an unsatisfied valence, i.e., an unpaired valence electron. The presence of this free valence imparts paramagnetism and in this view, the effective method to detect them, to measure their concentrations and to investigate the magnetic properties of free radicals is by using EPR – electron paramagnetic resonance.

The first free radicals with which man became acquainted were the paramagnetic oxides of nitrogen: NO^\bullet and NO_2^\bullet which are produced under natural conditions in lightning discharges for example. Free radicals have been classified according to their chemical structure. Among, we have mainly 2 groups of radicals – triarylmethyl radicals (in the Figure 1.13) and nitroxide radicals that have been both used *in vivo*.

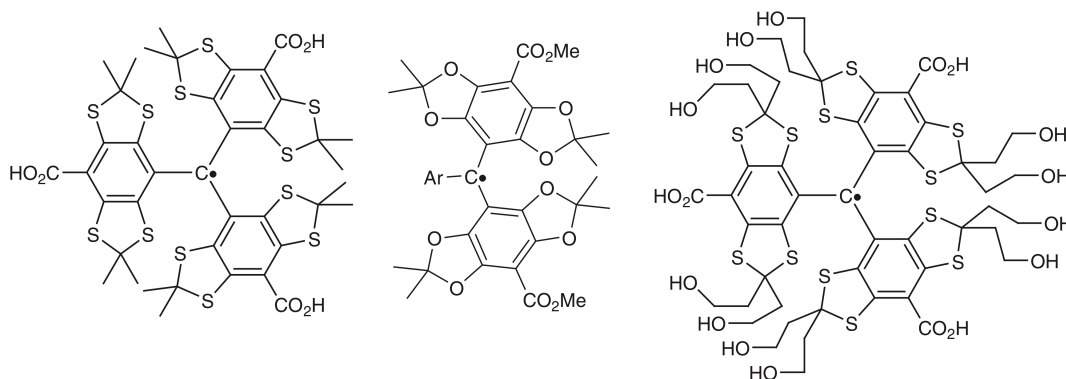


Figure 1.13: Examples of three triarylmethyl radicals or trityls used as contrast agents in OMRI experiments

Triarylmethyl radicals referred to as trityls (c.f. Figure 1.13) were the first free radicals used as contrast agents in OMRI for their high stability in biological fluids, their narrow line widths, absence of hyperfine splitting and enhanced sensitivity towards oxygen. These molecules with a high degree of unsaturation immediately adjacent to the radical carbon give a high degree of spin delocalization and stability to the molecule which result in very narrow line widths < 0.5 Gauss. The second reason for such fine line widths are the highly substituted aryl groups, resulting in farther hydrogen atoms and unresolved hyperfine splittings.

Regardless of these advantages, these free radicals are known to be toxic to living organisms. On the other hand, when a nitroxide radical (4-hydroxyTEMPO or TEMPOL) was compared to a trityl radical (triphenylmethyl radical known as TAM) in water,

the nitroxide radical showed considerably larger DNP enhancements up to 100 (9 GHz) using continuous microwave irradiation [Höfer et al. 2008]. The reason has been attributed to the smaller molecular size of the nitroxide radical which leads to a faster correlation governing the Overhauser effect (15-20 ps for TEMPOL vs 142 ps for the TAM).

In the OMRI field, these trityl molecules have been used to assess oxygen concentrations *in vivo* – oxymetry. Knowing that the EPR line of free radical varies with the oxygen content, coregistration of anatomical and oxygen status can be recorded *in vivo*. The presence of O₂ in tissues shortens the electron spin relaxation times and consequently reduces the saturation factor, *s*. The triphenylmethyl radical was utilized to perform oxygen imaging. In his work, Golman K and his team showed a significant change in the oxygen content of an experimentally induced ischemic region after a femoral artery clamping was made on a rat [Golman et al. 2000]. The oxygen content was also recorded in tumor hypoxia in mice by using Oxo63, a trityl-based contrast agent [Krishna et al. 2002]. The determination of the partial pressure of O₂ in tumors would eventually help in radiotherapy treatments.

Nitroxide radicals, on the other hand represent the most diverse class of stable organic radicals varying in stability, spectral properties and functionality. Known to have broader EPR line widths than trityls, that there is hyperfine splittings due to interactions between the unpaired electron and the nitrogen nucleus and that they are more prone to bio-reduction reactions than trityls, nitroxide radicals have been successfully used in EPR spectroscopic and OMRI applications. Also, nitroxides have not shown any toxicity up to millimolar concentrations [Couet et al. 1984].

Within the family of ‘nitroxides’, we will be talking about one sub-class of nitroxides, more exactly ‘nitroxyls’ with localized unpaired electron. Those free radicals are said to be stable radicals as the NO group does not take part in the formation of a conjugated system of multiple bonds. Therefore the unpaired electron is localized at the sterically protected NO group ($\rho^\pi O = 0.6$ and $\rho^\pi N = 0.4$). Moreover, the NO group is included in a cyclic five or six membered rings with the substituted adjacent carbon atoms, i.e., no α -hydrogen atoms. The substituted groups, often methyl group are protective groups and therefore increase the stability the nitroxide by steric hindrance of attack, thereby restraining degradation by reductive or oxidative enzymatic processes.

Nitroxide molecules have already been used in various OMRI applications involving – pH mapping and redox reaction imaging. Some nitroxides being prone to bio-reduction, were easily utilized for monitoring the redox status in tissues. They are directly reduced to corresponding hydroxylamines, resulting in EPR signal loss. The reduction of ¹⁵N-Carbamoyl PROXYL radical by ascorbic acid and oxidation of the hydroxylamine of ¹⁴N-Carbamoyl PROXYL by horseradish peroxidase enzyme were visualized simultaneously *in vitro* [Utsumi et al. 2006]. Another redox-sensitive contrast agent, methoxycarbonyl-

PROXYL was used to assess the redox status of the rat's brain [Yamato et al. 2009]. Indeed, the decrease in the signal decay rates in the ischemic hemisphere and not in the colateral hemisphere indicated that the reduction was due to the conversion from methoxycarbonyl-PROXYL to its hydrolamine form. pH mapping functional OMRI studies using pH-sensitive nitroxide radicals were also assessed. The protonation or deprotonation of these pH-sensitive nitroxide radicals showed EPR line shifting, resulting in two EPR lines for each protonated or deprotonated nitroxide species. *In vitro* studies at two different EPR irradiation frequencies allowed pH mapping of an imidazoline pH-sensitive radical [Efimova et al. 2011]. Intratumoral injection of the nitroxide probes revealed a broader pH distribution with an acidic mean of 6.8 in the tumor tissue [Samouilov et al. 2014].

In this dissertation, we have solely used nitroxide-based radicals for all the OMRI experiments.

This was a therefore a theoretical description of OMRI. The following chapter will now focus on the description of the imaging system, the data acquisition, the reconstruction proceedings and of course the OMRI probes that will be able to detect proteolytic activities. Last but not least the experimental protocols are described accordingly.

CHAPTER 2

Materials and Methods

All the experiments carried out during my thesis, were executed on a 0.194 T Siemens Magnetom Open Viva magnet. At this field, the Larmor frequency for the proton is 8.243 MHz and that for the unpaired electron is 5.435 GHz (which is 660 times higher).

Using this clinical magnet, a unique experimental set-up was established in 2005 by our team for OMRI applications. Since then, adapted MRI sequence was developed for optimized imaging acquisition. The next section will describe in detail the full montage needed.

2.1 Instrumental pre-requisite for OMRI experiments

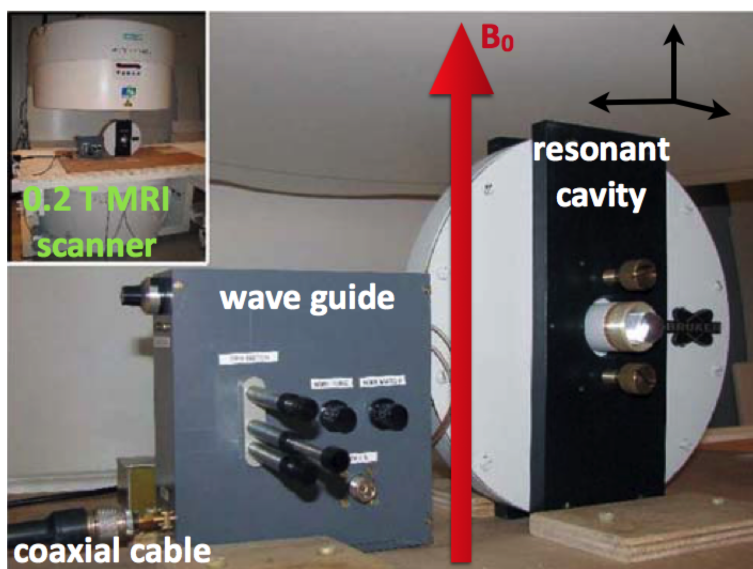


Figure 2.1: shows the EPR resonant cavity placed at the center of the MRI magnet bore (see inset view). The coaxial cable was used to transmit the HF electron frequency to the cavity via the wave guide component. The vertical field, B_0 is represented with the red arrow; the $B_{1,HF}$ was in the same direction as the sample and the $B_{1,RF}$ was orthogonal to both B_0 and $B_{1,HF}$.

The 0.2 T MRI scanner was a resistive whole body open magnet with a non-magnetic EPR cavity placed at the center of the magnet bore (40 cm in diameter). As seen in the Figure 2.1 above, the static magnetic field, B_0 is oriented vertically. This MRI system was used for the proton imaging part. The gradient coils had a maximum strength of 14 mT/m.

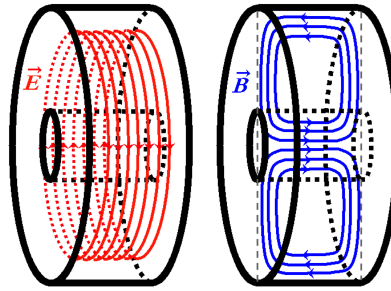


Figure 2.2: EPR cavity diagram – In red is represented the electric field component, \vec{E} which is mainly on the outer part of the cavity and in blue, the magnetic field component, \vec{B} which is concentrated on the sample.

The EPR set-up was used for specific electronic saturation of the OMRI nitroxide. It consisted of a cylindrical hollow resonant cavity coupled to a rectangular wave guide operating in the transverse electric (TE₀₁₁) mode. The purpose of using such a cavity was, first-of-all to be able to transfer electromagnetic HF waves of several gigahertz (around 5.4 GHz) from one point to another efficiently and secondly to hinder sample heating during wave propagation. This mode meant that there was mostly the magnetic field component in the central part, here in the direction of the sample and the electric field component was concentric and on the outer part of the cavity (see Figure 2.2). This particular geometry was designed to concentrate the magnetic component at the center of the cavity where a 2-sided opening allowed sample access. The sample imaging area was of 28 mm in diameter and 29 mm in length.

The resonant (HF) wave of intensity ~ 5.4 GHz was generated by a synthesizer and amplified with a cascade of two specific amplifiers (RFPA, Artigues-pres-Bordeaux, France). It was then fed with a coaxial cable to the wave guide. As shown in the picture of the set-up, the wave guide included matching and tuning devices. The cavity measured 240 mm in diameter and 29 mm thick. Its size, more precisely its thickness was matched to a specific resonance frequency according to the targeted EPR line of the OMRI nitroxide. This resonant frequency had an adjustable range of ± 50 MHz and was tuned and matched in the presence of the sample with the help of a network analyzer (Agilent Technologies, Santa Clara, CA, USA). The HF field, $B_{1,HF}$ was oriented in the same direction as the sample.

It should be noted that the original EPR cavity was redesigned to the present one in order to reduce eddy currents, which ultimately enabled the implementation of faster imaging sequences. Additional investigations about the true power deposition on the sample were evaluated by measuring the temperature rise in small animals with a rectal temperature probe. The temperature was seen to increase linearly with time. The slope was then used to estimate the amount of power absorbed by the animal at less than 1 W.

Theoretical power absorption calculations were also conducted. The quality factor, Q of the loaded (Q_L) and unloaded (Q_U) cavity revealed a 10% absorption of the incident power. Therefore, for all our experiments, the forward power was maintained at 60 W, with an absorbed power of 6 W or less. This value is indeed an overestimation due to power losses in the transmission line like in the co-axial cable and the tune-match circuit [Massot et al. 2012].

For small animal imaging, a home-made transmit-receive saddle-shaped coil of 26 mm inner diameter and length dedicated to mouse abdomen was fixed inside the cavity with the manual tuning circuitry placed apart. It was tuned at 8.243 MHz. The radio-frequency (RF) field of this magnetic resonance (MR) coil was oriented orthogonally to both $B_{0,staticfield}$ and $B_{1,HF}$. A transmit/receive switch device was placed in the RF control unit of the MRI equipment.

Together with this set-up, there was also a need for implementing a new MRI sequence at 0.2 T. The aim was to reduce the image acquisition time without compromising spatial resolution.

2.2 Implementation of a new MRI sequence on 0.2 T system

2.2.1 TrueFISP sequence implementation

There exist two main categories of sequences in MRI namely – 1) Spin Echo (SE) and 2) Gradient Echo (GRE). GRE-type sequences are classified in terms of 2 sub-categories :

1. In the 1st sub-category, the residual transverse magnetization after each elementary sequence impulsion is spoiled - called incoherent or spoiled GRE sequences for example the FLASH sequence – **F**ast **L**ow **A**ngle **S**Hot.
2. In the 2nd sub-category, the residual transverse magnetization after each elementary sequence impulsion is refocused to contribute to steady state – called coherent or steady-state GRE sequences for example the TrueFISP – **T**ru**e** **F**ast **I**maging with **S**teady **P**recession as illustrated in Figure 2.3.

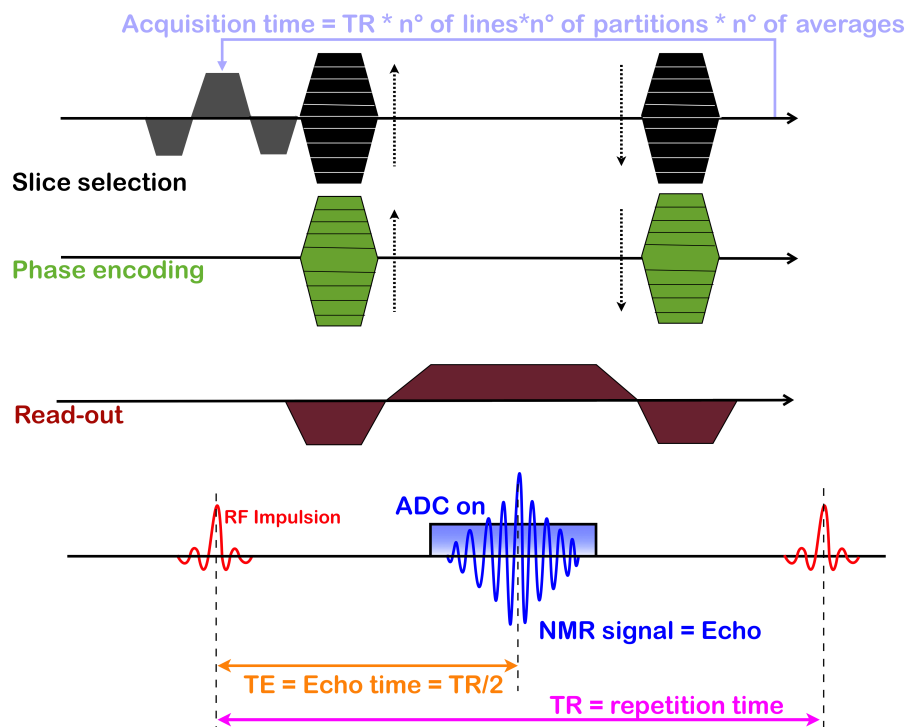


Figure 2.3: The pulse sequence of the TrueFISP MRI sequence

The 2nd sub-category of sequences exhibits a certain symmetry in their chronogram as in the diagram above. For the TrueFISP sequence, the residual transverse magnetization (TM) is rewound in all three directions, i.e. reset to zero by reversing the sign of the gradient pulses (indicated with up/down arrows in the diagram). The second characteristic of this sequence is that the TR is smaller than the T_2 [Scheffler et al. 2003]. The consequences are that:

1. The unused TM from the first RF pulse will superpose itself with the echo of the second RF pulse, as a stimulated echo. In so doing, the two accumulated echoes would continue adding up and hence increase the signal-to-noise ratio (SNR) as well as the contrast-to-noise ratio (CNR).
2. The small TRs will definitely reduce the total acquisition time of the image. Hence, the advantage of speed will reduce the motion artifacts from respirations and so on.

Since 2007 our laboratory was involved in the optimization of fully balanced steady-state free precession sequence to small animal MRI at high field in brain [Miraux et al. 2008] and heart [Miraux et al. 2009]. In parallel, undersampled acquisition using keyhole was successfully applied to monitor the biodistribution of contrast agents in mice [Bled et al. 2011]. Building on this strong experience, the team regarded as from 2011 the possible combination of k -space undersampling and balanced-SSFP at 0.2 T. Concomitantly and coincidentally, Sarraçanie M. and colleagues developed the same concept with the same purposes [Sarraçanie et al. 2014]. At that time, a FLASH sequence which was fully accessible and changeable on our 'PARGEN' system, was used as template. This GRE-type sequence was previously used in the work of Massot P. in 2D and 3D acquisitions [Massot et al. 2012]. However, from Massot's work, the 3D image acquisition time had to be shortened (around 5 minutes) for imaging rapid physiological processes. Moreover the EPR irradiation time which lasted for 1.5 minutes with compulsory 1-min intervals inbetween the acquisition time had to be minimized to reduce sample heating.

This 3D-FLASH sequence was therefore modified in several steps into a fully refocused sequence. The latter was then optimised and compressed to a maximum with a good compromise on SNR. The slice selection gradient pulses were also removed as the imaged volume fully occupied the duty volume of the resonant cavity. This manoeuvre further decreased the acquisition time. And finally a preparative module for the electronic saturation was integrated in the sequence. The duration of this module was optimised for a maximum NMR signal enhancement. Following this preparative module, the NMR image acquisition begun and was synchronized with the EPR irradiation for the entire acquisition time as shown in the pulse sequence, Figure 2.4.

The parameters of the sequence are as follows : TE = 6.64 ms; TR = 13.28 ms; flip angle = 30° , EPR preparation module = 800 ms and the reception bandwidth = 260 Hz/pixel. The pulse sequence is given below –

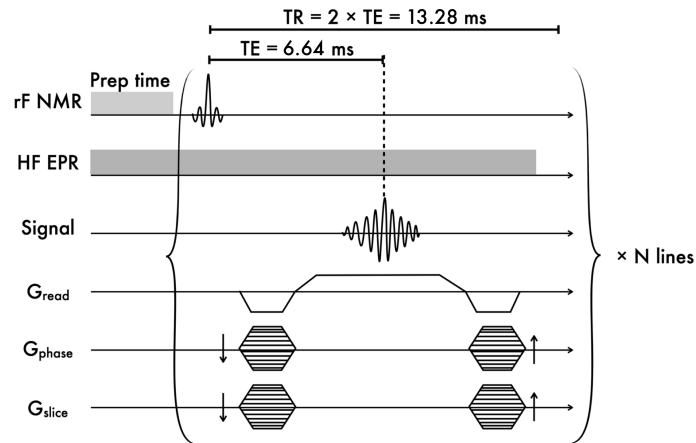


Figure 2.4: The pulse sequence of the 3D TrueFISP MRI sequence synchronized with the electronic saturation. Prep time = 800 ms

With this optimised sequence and for a matrix of $64 \times 64 \times 40$ and 2 averages, the time taken to obtain an image was 1 minute and 8 seconds. However, since our main objective is to image rapid biological processes taking place in small animals, the temporal resolution of the image should be even higher. Moreover, in an attempt to minimize the duration of the HF electronic irradiation, we applied an accelerating strategy regarding data acquisition.

2.2.2 Acceleration Method – Keyhole Approach

As per the understanding of the k -space and how data is acquired, the only way of reducing acquisition would be by decreasing the amount of data collected – down-sampling, of course at the price of poorer image quality. However, the reduction of matrix acquisition and zero-filling yield blurry images with sometimes ringing artifacts. As already demonstrated in several textbooks [McRobbie et al. 2006], the spatial frequencies in a k -space can be decomposed into –

- low frequency data found at the center of the k -space encoding the right brightness of the image but no detail.
- high frequency data found rather on the outer part of the k -space encoding the edges and sharp features of the image but the intensity is low elsewhere.

Here, we chose the “**keyhole**” method, a strategy designed by the team of van Vaals J.J in 1993 [Van Vaals et al. 1993]. This undersampling method has been well mastered in our laboratory since 2011 [Bled et al. 2011]. Hence, using our laboratory’s expertise, the Keyhole method was implemented on the Igor software and adapted for the raw data collected on the 0.2 T scanner in order to reconstruct the acquired OMR images.

This approach merges the low frequency data with high frequency data borrowed from a reference image to prevent blurring (c.f. Figure 2.5). As a result, this method allows a constant and rapid update/refresh of the central part of the k -space, through the acquisition of several down-sampled images along with the outline and sharpness of the reference image. The acquisition time is therefore significantly reduced for the same spatial resolution.

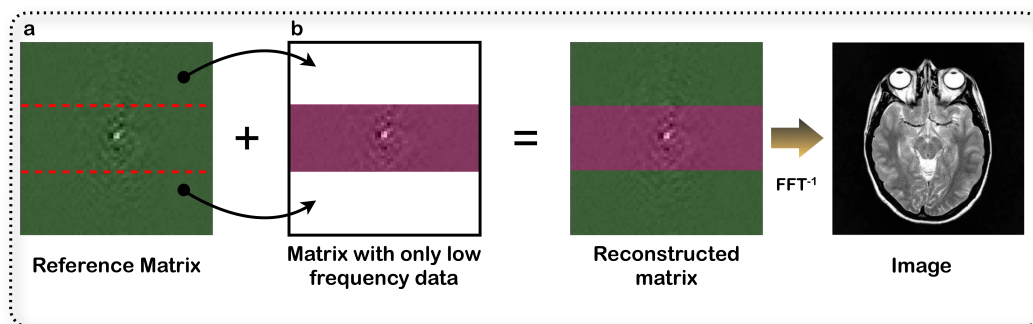


Figure 2.5: This figure illustrates the “keyhole” method. The first step (a) consists of acquiring a full matrix image named the reference matrix. Then in (b) a downsampled matrix is acquired with only the low frequency data (the center of the k -space). Finally the high frequency data from the reference matrix is merged into the downsampled one. Hence the reconstructed image will have the dynamic contrast and a preserved spatial resolution.

For our *in vivo* experiments, a partial matrix acquisition where both the number of partitions and lines were halved, the total acquisition time was only of 18 seconds for a matrix size of $64 \times 32 \times 20$. The reconstructed images were carried out posterior to the OMRI experiments.

2.2.3 Image reconstruction using raw data

All the keyhole algorithms have been developed by our team using the IGOR PRO software (Wavemetrics, Lake Oswego, USA). The raw data acquired on the 0.2 T scanner were first loaded in the software via built-in macros. They were correctly re-ordered from (k_x, k_y, Z) into (k_x, k_y, k_z) 3D matrices and then processed for keyhole reconstruction. A specific and detailed procedure file was implanted in the software. It was composed of a direct re-dimension of the partial matrix acquisition with the external lines of the reference matrix. The partial matrix was only 25% of the full matrix, i.e with a matrix size of $64 \times 32 \times 20$. Hence, after merging both matrices, the final image had a spatial resolution of $500 \mu m$ in all 3 dimensions for a matrix size of $64 \times 64 \times 40$. An Overhauser enhancement mapping macro was also integrated. It was based on the ratio of the full 3D matrix acquired with HF electronic saturation over the full 3D matrix acquired without HF electronic saturation –

$$\text{Overhauser Enhancement} = \frac{\text{3D enhanced image}}{\text{3D unenhanced image}} \quad (2.1)$$

Let us now figure out how the enhanced signal be related to the biological activity.

2.3 OMRI contrast agents as proteolytic activity detectors

Imaging proteolytic activity *in vivo* demands an unambiguous and well interpreted signal amplification upon proteolysis. In other words, the Overhauser enhanced signal need to be modulated by the targeted proteolytic activity for detection. To achieve this goal, our nitroxide OMRI contrast agents will have to be conditioned according to the peptide cleavage. There exists different ways to modulate the free radicals. The analysis of nitroxides, in general is based on the fact that their hyperfine structure of the EPR spectra relies on :

1. the orientation of the orbital of the unpaired electron in a constant magnetic field
2. their relative motion and
3. their exchange interaction with their surrounding.

Therefore, based on these parameters and how they are linked to efficient polarization transfer, we will now relate the two kinds of nitroxides used.

2.3.1 Nitroxide molecules

First of all, I will introduce the two nitroxides as free radicals. They are represented in Figure 2.6 and are named –

1. a commercially available nitroxide – PCA for 1-Oxyl-2,2,5,5-tetramethylpyrroline-3-carboxylic acid, and
2. a newly synthesised β -phosphonated nitroxide – acetate nitroxide form with the following chemical name – 2-Diethoxyphosphoryl-2,6,-trimethyl-1,2,3,6-tetrahydropyridin-4-yl-N-oxyl acetate

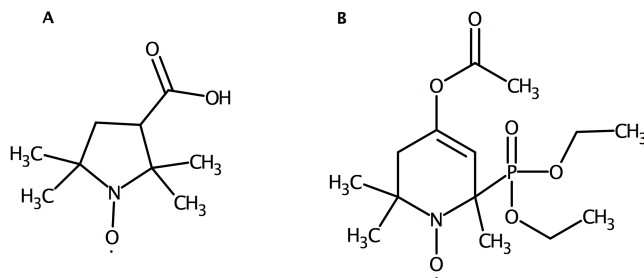


Figure 2.6: A) PCA or 1-Oxyl-2,2,5,5-tetramethylpyrroline-3-carboxylic acid and B) 2-(Diethoxyphosphoryl)-4-acetoxy-2,6,6-trimethyl-1-azacyclohex-3-enoxyl radical.

A. PCA

PCA has a typical 3-peak EPR spectrum due to the hyperfine splitting of the unpaired electron with the spin 1, nitrogen atom and the three permitted transitions (namely T_{16} , T_{25} and T_{34}) at high fields. The nitrogen hyperfine constant (hcc), a_N here is of 16.1 Gauss and line widths of 1.3 Gauss each (see Figure 2.7 below). Its longitudinal relaxivity, r_1 has been measured using T_1 values at different concentrations (0.5 mM to 50 mM) at $0.37 \pm 0.03 \text{ mM}^{-1}\text{s}^{-1}$. Due to its small molecular size, a correlation time of 17 ps was calculated, a value comparable to TEMPOL nitroxide measured at 15 - 20 ps [Höfer et al. 2008].

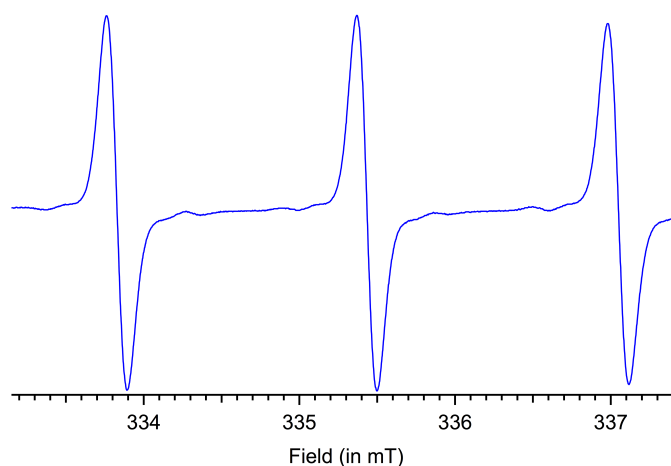


Figure 2.7: An EPR spectrum of an aqueous solution of PCA nitroxide acquired at 0.5mM. EPR acquisition parameters were as follows: $B_0 = 3353 \text{ G}$; sweep width = 43.16 G; sweep time = 60 s; number of passes = 1; modulation = 100 mG.

B. β -PHOSPHORYLATED NITROXIDES

β -phosphorylated nitroxides are commonly used for spin-trapping applications as they are highly sensitive to the nature of the trapped radical. In our case, we will be using this radical as an OMRI probe. This probe application will rely on the nitroxide properties related to the nitrogen hcc, a_N , phosphorus hcc, a_P and the interaction between the nitroxyl moiety and the solvent.

As seen in the Figure 2.8 below, the hyperfine structure (hfs) of the EPR spectrum of our β -phosphorylated nitroxide consists of six basic lines (a doublet of triplets pattern) of equal intensity. It is due to the interaction of the unpaired electron with the nucleus of the phosphorus atom, ^{31}P (spin $K=1/2$) with constant a_P at 38.7 G and with the nucleus of the nitrogen atom ^{14}N (spin $S=1$) with a_N at 15.6 G.

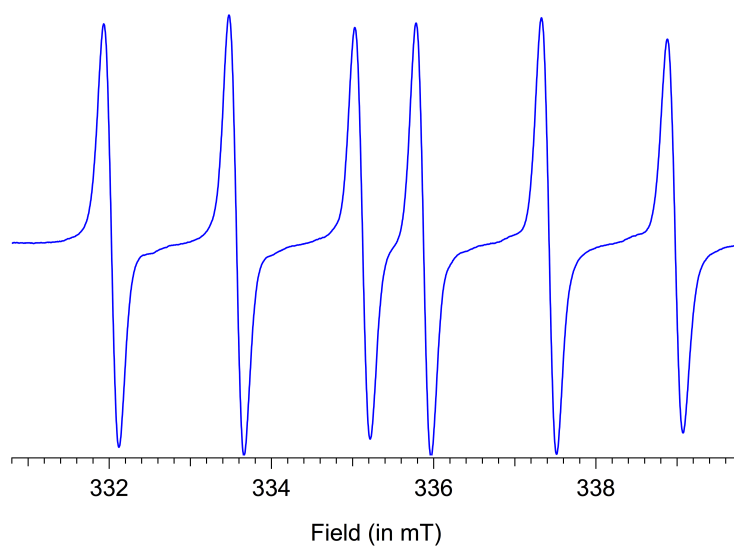


Figure 2.8: An EPR spectrum of an aqueous solution of 2-Diethoxyphosphoryl-2,6,-trimethyl-1,2,3,6-tetrahydropyridin-4-yl-N-oxyl acetate nitroxide acquired at 3mM. EPR acquisition parameters were as follows: $B_0 = 3353,55$ G; sweep width = 90.42 G; sweep time = 60 s; number of passes = 1; modulation = 300 mG.

It should also be pointed that even if the ^{31}P atom is in the β position, a strong phosphorus hyperfine coupling is observed. It is all because the C–P bond is predominantly orientated for a maximum overlapping between it and the radical center, thereby allowing the unpaired electron found in the $2p_z$ orbital of the nitrogen atom to interact strongly with the σ -bond of C–P. It is called the hyperconjugation mechanism. This predominant orientation certainly means steric hindrances (here the two ethoxyl substituents) which will favor a particular conformational state of the phosphorus atom

[Levin et al. 1975; Il'yasov et al. 1976; Audran et al. 2012; Le Breton et al. 2014].

These two nitroxides will now be conditioned for proteolytic activity detection.

2.3.2 Nitroxide-labeled elastin

A criterion of the mobility of the radicals is the rotational correlation time, τ_c which can be obtained from the expression (2.2) [Henry et al. 1971; Raison et al. 1971] –

$$\tau_c = K \times (W_{-1} - W_0) \quad (2.2)$$

where W_0 and W_{-1} are the widths of the central and high field lines on the EPR spectrum. K is a constant which depends on the anisotropic hyperfine coupling (a_N) values and the anisotropic g tensor values. Using the spectral values of Griffith, Cornell and McCornell [Griffith et al. 1965] for $K = 6.5 \times 10^{-10}$ s and assuming Lorentzian line shapes, the data reduction can be greatly facilitated by writing,

$$\frac{W_{-1}}{W_0} = \sqrt{\frac{h_0}{h_{-1}}} \quad (2.3)$$

where h refers to field line heights. Spectra in this tumbling range can, nevertheless, be analysed in terms of an empirical motion parameter –

$$\tau_c = 6.5 \times 10^{-10} \times W_0 \times \sqrt{\frac{h_0}{h_{-1}}} - 1 \quad (2.4)$$

Hence, based on the above motion properties, we synthesised a contrast agent composed of a known and commercialized nitroxide, PCA – 1-Oxyl-2,2,5,5-tetramethylpyrroline-3-carboxylic acid fixed on soluble elastin molecule of molecular weight greater than 30 000 kDa. When an activated form of the PCA nitroxide, 1-Oxyl-2,2,5,5-tetramethylpyrroline-3-carboxylate N-Hydroxysuccinimide ester was made to react with the amine bonds of the side chains amino acids present in the elastin macromolecule, the nitroxide radical formed an amino bond (CO–NH). Once grafted on the elastin macromolecule, the whole moiety was analyzed by EPR. This macromolecule was also subjected to pancreatic elastase, which enabled the cleavage of the macromolecule into smaller peptides.

A marked broadening and lower peak amplitudes of the EPR spectra were obtained when the nitroxide-labeled elastin was analyzed, as seen in Figure 2.9 in blue. The visible EPR lines observed with the undigested probe accounts merely for 5% of the total spectrum as far as the number of spins is concerned. The other 95% of the spectrum is spread over a larger range with large EPR line-widths (of more than 10 Gauss). Upon hydrolysis of the elastin macromolecule using the enzyme pancreatic porcine elastase,

a narrower line-width value was measured and a clear rise in the peak amplitudes was observed. The Table 2.1 describes the variation of the EPR line-widths as a function of the concentration of the nitroxide-labeled elastin before and after enzymatic action. Thirdly, the rotational correlational times were calculated for each concentration and plotted as in Figure 2.10.

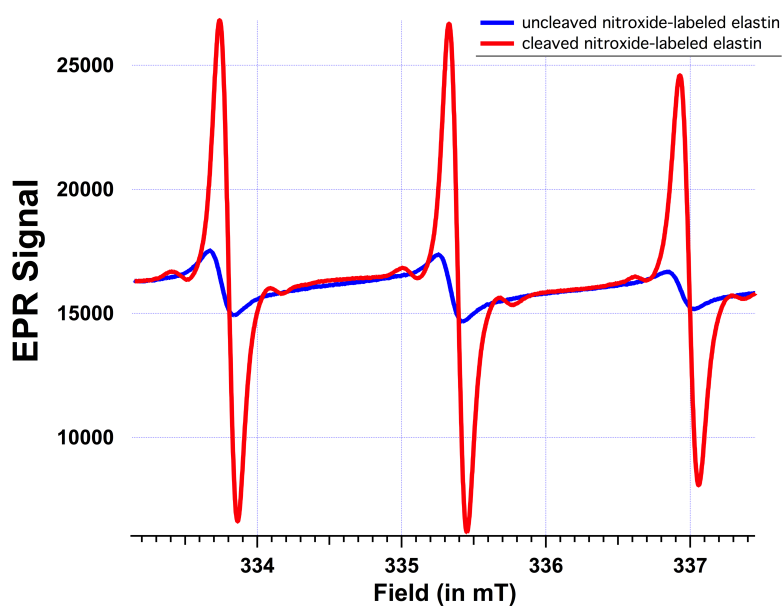


Figure 2.9: Here are the superimposed EPR spectra of the undigested nitroxide-labeled elastin in blue and the digested one in red. The estimated concentration of the nitroxide content was around 1.1 mM

Table 2.1: Measured EPR line-widths of the nitroxide-labeled elastin before and after enzymatic action for varying concentrations

Concentration (mM)	0.6	1.13	2.25	4.5	9	18
Peak-to-peak line-width for undigested nitroxide-labeled elastin (Gauss)	1.79	1.85	1.79	2.02	1.91	2.02
Peak-to-peak line-width for digested nitroxide-labeled elastin (Gauss)	1.00	1.00	1.02	1.14	1.54	2.02

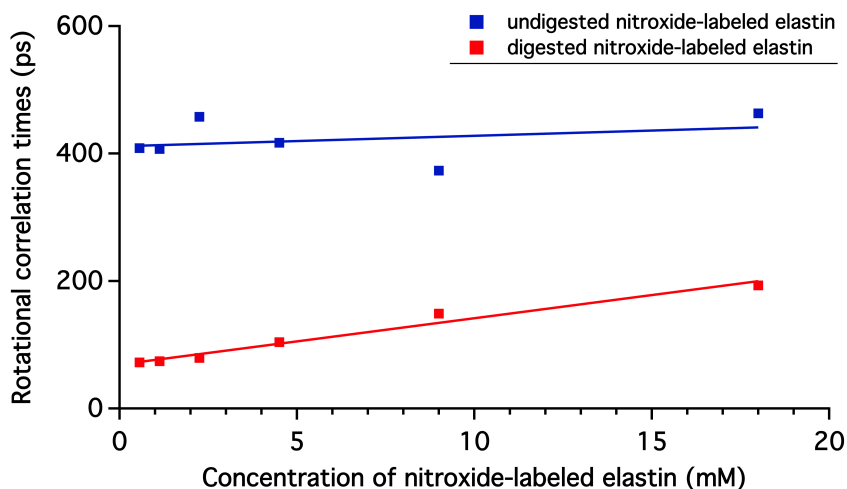


Figure 2.10: The calculated rotational correlational times as a function of its concentration obtained from a serial dilution. In blue: it is the relative motion of the undigested nitroxide-labeled elastin and in red : the digested nitroxide-labeled elastin using pancreatic porcine elastase. This experiment was carried out *in vitro* and their EPR spectra were analyzed. The different height amplitudes and linewidths of were measured and used to estimate τ_c .

As from all the EPR data collected on the nitroxide-labeled moiety, it can be discussed that:

1. At low concentrations, narrow line-width values and corresponding rotational correlation values for the digested elastin moiety account for the higher mobility of the unpaired electron as opposed to the a more restricted mobility for the undigested elastin moiety.
2. At high concentrations, the unchanged line-width values for the undigested nitroxide-labeled elastin shows that the unpaired electron is still contained within the macromolecule. However for the digested elastin moiety, the broadened linewidths and the high rotational correlation times were due to the dipolar and Heisenberg spin exchange interactions.

Our first OMRI proteolysis probe detector is based on a switch that is off when the unpaired electron is found on the bulky molecule with broad EPR lines, and is switched on when the bulky molecule is cleaved by protease. This results in lower saturation factor and an inefficient polarization transfer in the OMRI experiment when the probe is still uncleaved. It should be noted that for the electronic saturation frequency, the central EPR line of PCA was selected in all the OMRI experiments involving this nitroxide-labeled elastin.

2.3.3 β -phosphorylated nitroxide radical with an acetyl group

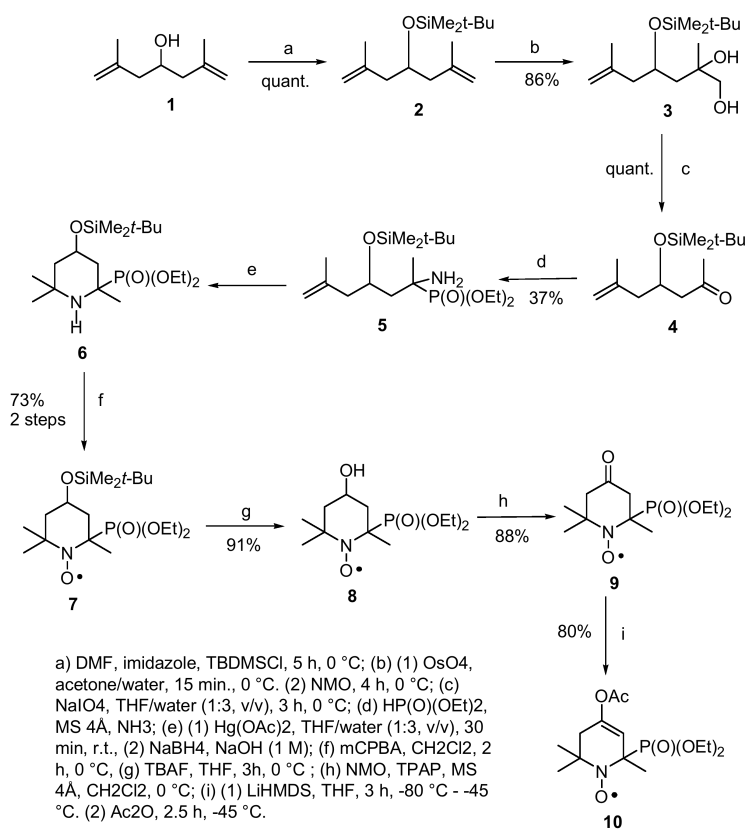


Figure 2.11: Synthesis of β -phosphorylated nitroxide

The β -phosphorylated nitroxide radical was synthesised by a chemistry research team, Pr Marquet S.A's team in the Institute for Radical Chemistry, in Marseille, France. This laboratory is specialized in the making of different types of nitroxide moieties. So the purpose was to design a unique type of proteolytic activity probe for OMRI applications. The complete synthesis of this nitroxide is illustrated in the Figure 2.11 above. The enzymatic action upon the nitroxide **10**, is targeting the keto-enol equilibrium by hydrolyzing the ester bond of the acetate functional group into a ketone functional group, i.e. **10**. into **9**.

As described earlier, the β -phosphorylated nitroxide radical has 6 hyperfine lines due to the additional coupling with the phosphorus atom of spin 1/2 in a β position. The strategy used for this molecule as an OMRI contrast agent is based on the conforma-

tional change of the entire molecule upon hydrolysis of functional group. The change in conformation after hydrolysis of the ester bond between the acetate functional group (**10.**) and the nitroxide ring definitely impacts and reorients the p^π orbitals the phosphorus and nitrogen atoms. The change in alignment of the p^π orbitals, in turn modifies the hyperfine couplings with the unpaired electron.

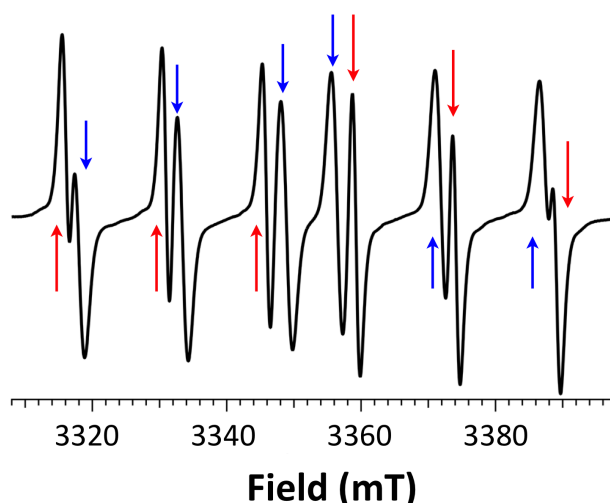


Figure 2.12: The EPR spectrum of solution containing both the 2-(Diethoxyphosphoryl)-4-acetoxy-2,6,6-trimethyl-1-azacyclohex-3-enoxyl radical acetate nitroxide form (**10.** is represented by blue arrows) and its 2-(Diethoxyphosphoryl) -2,6,6-trimethyl-4-oxypiperidin-N-oxyl radical ketone nitroxide form (**9.** is represented in red arrows) in a mixture of ratio 1:1. A shift of the phosphorus hyperfine coupling constant and of the nitroxide hyperfine coupling constant of 4.4 Gauss and 0.6 Gauss were observed respectively.

The EPR spectrum containing 50% of the acetate nitroxide form (**10.**) and 50% of the ketone nitroxide form (**9.**) is described above in Figure 2.12. The changes in the hyperfine coupling constants, a_N and a_P are reported in Table 2.2.

Table 2.2: EPR parameters of both forms of the phosphoryl nitroxide molecules.

Nitroxides	a_N (G)	a_P (G)	g-factor	Linewidths (G)
Acetate nitroxide form	15.0	43.1	2.0062	1.2
Ketone nitroxide form	15.6	38.7	2.0063	1.8

This EPR peak shifting nitroxide will therefore be evaluated as an on/off switch by saturating selectively one electronic EPR transition of either the substrate form or the product form. For all OMRI experiments done using the β -phosphorylated nitroxide,

the EPR cavity was tuned on the first high field EPR line of either the substrate form or the product form.

2.4 Experimental Procedures

For these types of OMRI contrast agent, a systematic *in vitro* analysis was carried out using both the EPR spectrometer and the OMRI setup.

2.4.1 *In vitro* analysis

A. NITROXIDE-LABELED ELASTIN

Elastin is a protein that is highly represented in connective tissues like skin, vascular smooth muscle cells and in lung tissue. It is mainly responsible for tissue flexibility and extensibility and this protein has a high tensile strength. Elastases are proteases that have the ability to digest insoluble elastin into soluble elastin peptide molecules. Besides these physiological processes, several pathological processes involve an elastolytic activity. Such processes are arteriosclerosis, diabetes, skin diseases and emphysema.

To start with, once this probe was synthesised, enzymatic activity tests were conducted in different conditions.

i) Kinetic Assays with purified enzymes

First, human neutrophil elastase, pancreatic porcine elastase, trypsin and chymotrypsin kinetic studies were performed for a fixed nitroxide content so as to evaluate the specificity of this probe. At different time intervals, the mixture was analyzed by EPR and the signal amplitude of the central EPR line was plotted against time (c.f Figure 2.13 left diagram). This experiment procedure tested the specificity of the enzymes towards the elastin molecule as substrate.

Secondly, the concentration of human neutrophil elastase was made to vary and after completion of the enzymatic activity (i.e an incubation of 24hrs), the EPR signal was plotted against the enzyme concentration (c.f Figure 2.13 middle diagram). EPR being a very sensitive method of detection, digestion of the elastin at very low concentrations showed how much the given enzyme was selective towards its substrate.

Thirdly, an OMRI experiment was setup at different concentrations of nitroxide-labeled nitroxide and after an incubation of 24 hr with human neutrophil elastase at a fixed concentration, the maximum OMRI signal was evaluated. Indeed for a given region of-interest in an acquired 2D image, the mean signal was collected and plotted against the nitroxide concentration (c.f Figure 2.13 right diagram). The purpose of this OMRI experiment was to establish to what extent proteolysis could be detected *in vitro* with high image contrasts.

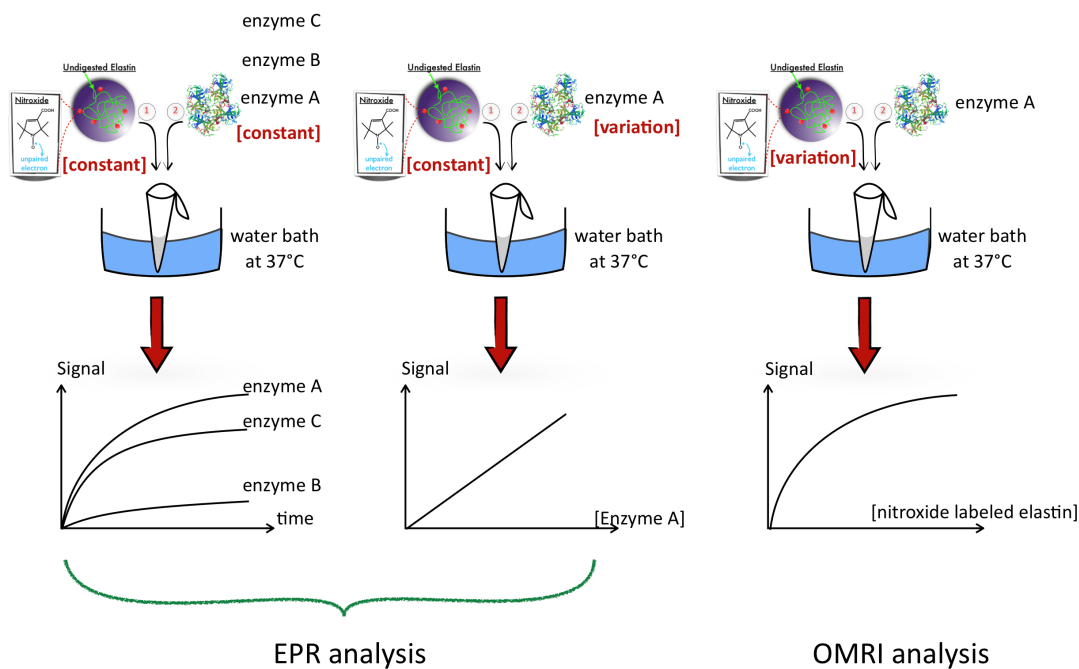


Figure 2.13: Diagram to illustrate the enzymatic kinetic experiment performed by EPR or OMRI. Here experiments were carried by mixing the OMRI probe with the purified enzyme(s). In the diagram to the left: different kinetic curve was measured by EPR according to the enzyme used. In the middle-placed diagram: the concentration of the enzyme was varied and the nitroxide probe was kept at a constant concentration. Measurements were achieved by EPR. In the right-sided diagram: an OMRI analysis by acquiring 2D images was conducted. The nitroxide probe concentration was varied and the concentration of the enzyme was kept constant.

ii) Kinetic Assays with living neutrophil cells

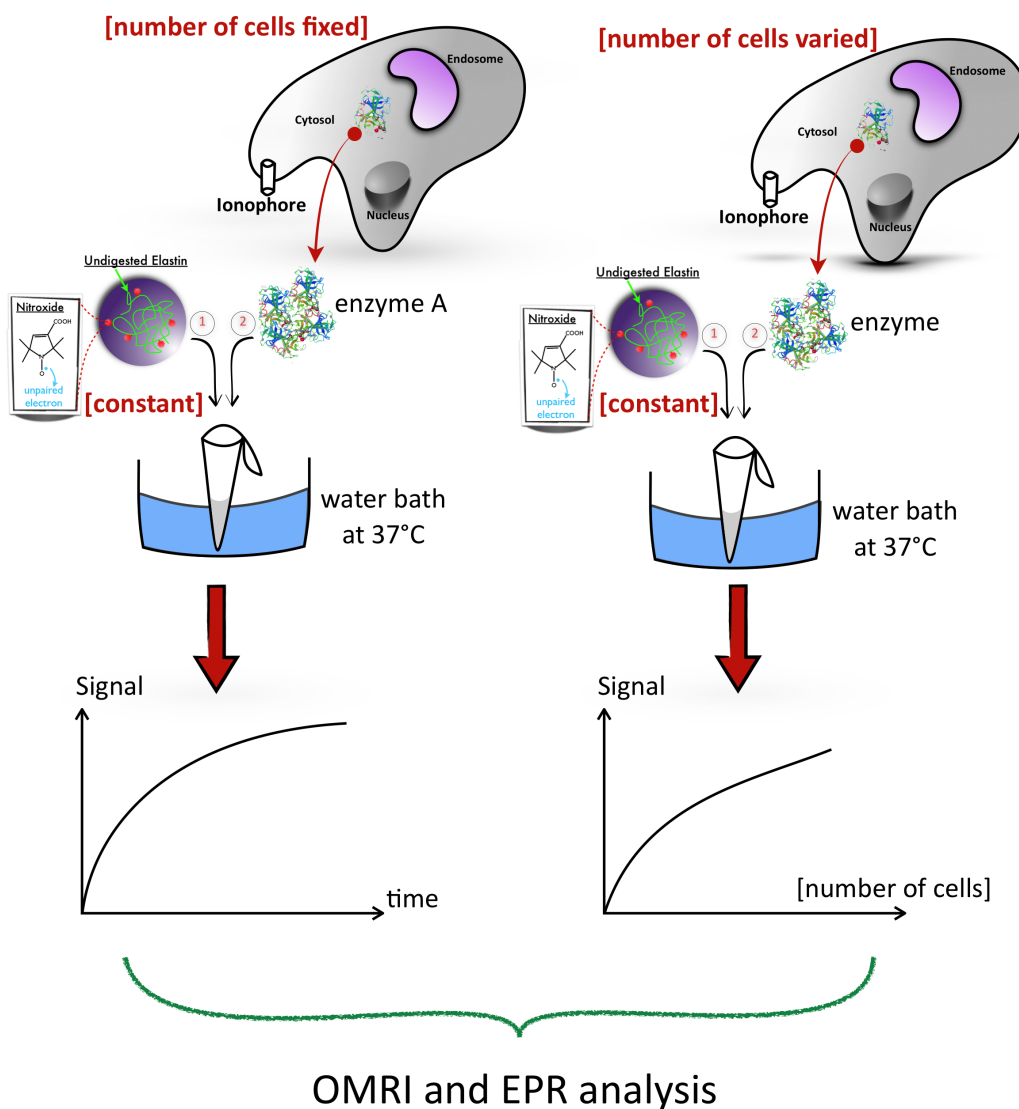


Figure 2.14: Diagram to illustrate the enzymatic kinetic experiment performed by EPR and OMRI. Here experiments were carried by mixing the OMRI probe with secreted enzyme(s) released by human neutrophil degranulation. The degranulation was initiated by a calcium ionophore and enzymatic activity was stopped using Eglin C inhibitor. In the left-diagram: a kinetic curve was obtained according to a fixed number of cells. In the right-sided diagram: The number of cells was varied and the concentration of the OMRI probe was kept constant. EPR and OMRI signal were gathered according to the both experimental conditions.

The next step *in vitro* was to use living cells, more precisely human neutrophils which are highly recruited *in vivo* during acute inflammations, emphysema, bacterial infections and other diseases, to assess proteolytic activity detection using both EPR and OMRI techniques (in Figure 2.14). So, isolated human neutrophils were used and activated using a calcium ionophore A23187. Upon activation of these cells, they will start secreting proteases in the extracellular matrix environment. Among the proteases releases, neutrophil elastase is also present and will be able to digest our OMRI probe. A proper kinetic curve was plotted at different time intervals till 5 hours to measure the elastolytic activity after degranulation. Afterwards the number of neutrophils was made to vary, meaning that the amount of elastase is varied with a constant concentration of OMRI probe. The plot evaluated the sensitivity of the technique upon enzymatic action. All these *in vitro* experiments form part of Article 1.

B. β -PHOSPHORYLATED NITROXIDE

The β -phosphorylated nitroxides **10**. and **9**. was first of all analyzed by EPR to validate the EPR parameters obtained by the Institute for Radical Chemistry laboratory.

i) pH assessment

Then its stability in different pH mediums was investigated by EPR. This experiment was carried out in four different buffers at pH1, pH3, pH7.4 and at pH9. To achieve pH1 and pH3, a buffer of glycine was prepared and EPR lines were acquired against time. The same procedure was undertaken for pH9 with a buffer of Tris (2-amino-2-hydroxymethyl,1-3 propanediol). For pH7.4, a saline phosphate buffer was used and the pH was correctly adjusted. The EPR lines were integrated and the areas were quantified. This spontaneous hydrolysis was followed for at least 100 minutes. This pH assay is given in the Figure 2.15 below. The nitroxide form **10**. is stable in acidic medium, though in the alkaline medium the nitroxide **10**. experiences a faster hydrolysis due to the nucleophilic attack of OH^- ion on the ester bond.

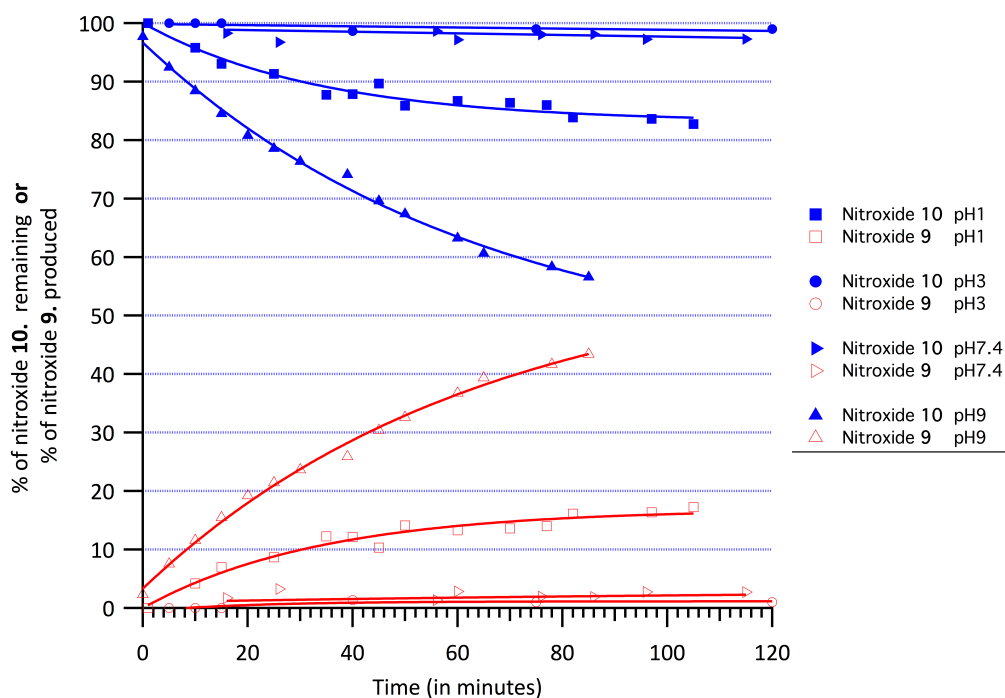


Figure 2.15: Percentage of nitroxide hydrolysis under acidic mediums, physiological pH and an alkaline medium when the nitroxide form **10**. is kept over about 100 minutes in their respective buffers.

ii) Enzyme specificity Assays

The next step was to search an enzyme specificity of this nitroxide in order to assess a kinetic study. In this view, we performed nitroxide hydrolysis by testing various enzymes – human neutrophil elastase, pancreatic porcine elastase, trypsin, chymotrypsin, thermolysin, collagenase, cathepsin B and Subtilisin A (c.f Figure 2.16). After a 5h-incubation time, EPR lines were acquired. The six peaks were integrated using the IGOR Pro software. A multippeak fitting module was applied for a deconvolution analysis. The area of the each peak were extracted and were plotted as a histogram for each enzyme used.

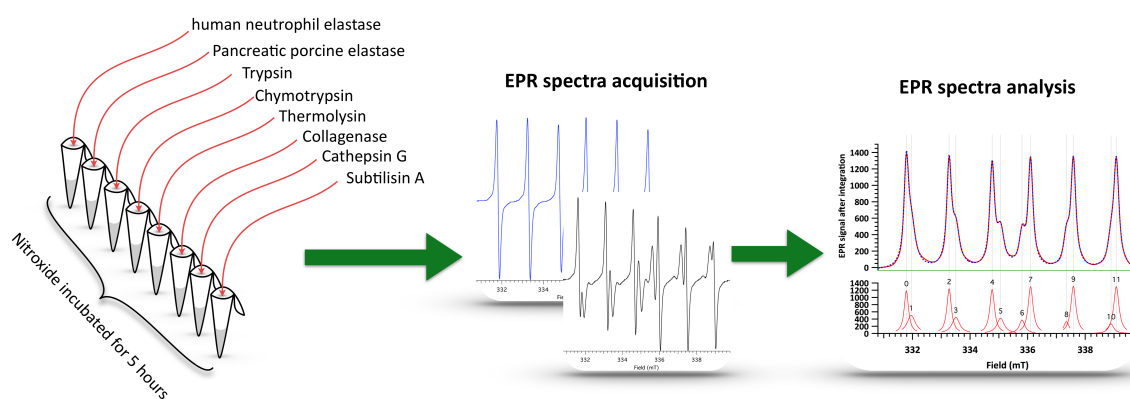


Figure 2.16: Experimental procedure illustrating the steps involved to evaluate enzyme specificity towards the β -phosphorylated nitroxide after a 5h-incubation time at 37°C.

iii) Kinetic Assays with Subtilisin A using EPR

Kinetic measurements were carried in view to determine the catalytic efficiency, $\frac{k_{cat}}{K_M}$. The simplest model which accounts for our experiment is:



where E is the enzyme, here Subtilisin A, S the substrate, here nitroxide **10.**, ES the enzyme-substrate complex, P is the product, here nitroxide **9.** of the reaction, k_1 the rate constant of the forward reaction of $E + S$, k_{-1} the rate of the reverse reaction, and k_2 the rate constant of the forward reaction of ES forming $E + P$. In this model, it is assumed that the global reaction velocity depends mainly upon the second rate constant and will be expressed as –

$$V = k_2[ES] \quad (2.6)$$

From the expression 2.6, and assuming that the concentration of the complex ES is always constant, i.e using the steady-state approximation, it can be deduced that –

$$[ES] = \frac{k_2[E][S]}{k_{-1} + k_2}; \text{ where } K_M = \frac{k_{-1} + k_2}{k_1} \quad (2.7)$$

Also, according to the law of conservation of mass and in the context where the enzyme concentration is very small ($[E] \ll [S]$): $[E] = [E_{total}] - [ES]$, the global reaction velocity can be written as –

$$V = \frac{k_2[E_t][S]}{K_M + [S]}; \text{ where } k_2 = k_{cat} \quad (2.8)$$

K_M is the Michaelis constant and in the case where $k_2 \ll k_{-1}$, K_M is reduced to $\frac{k_{-1}}{k_1}$, defined as the dissociation constant, K_d . k_{cat} is called the turnover number, which is equivalent to the unit time conversion of nitroxide molecules into its ketone form. In our study, the situation where $[S] \ll K_M$ was hypothesised, which reduces the expression 2.8 into –

$$V = \frac{k_{cat}}{K_M}[E_t][S] \quad (2.9)$$

Experimental EPR setup was therefore as follows (illustration in Figure 2.17):

1. The concentration of enzyme was kept constant and the concentration of nitroxide **10.** was made to vary.
2. EPR line evolution was determined by measuring the amount of the ketone nitroxide formed at each time interval.

3. The initial velocity was calculated as the tangent at the start of the reaction.
4. Then, for each nitroxide **10**. concentration, the initial velocity was evaluated and plotted.
5. A straight line was obtained and the slope of the line gave the catalytic efficiency of subtilisin A towards the nitroxide.

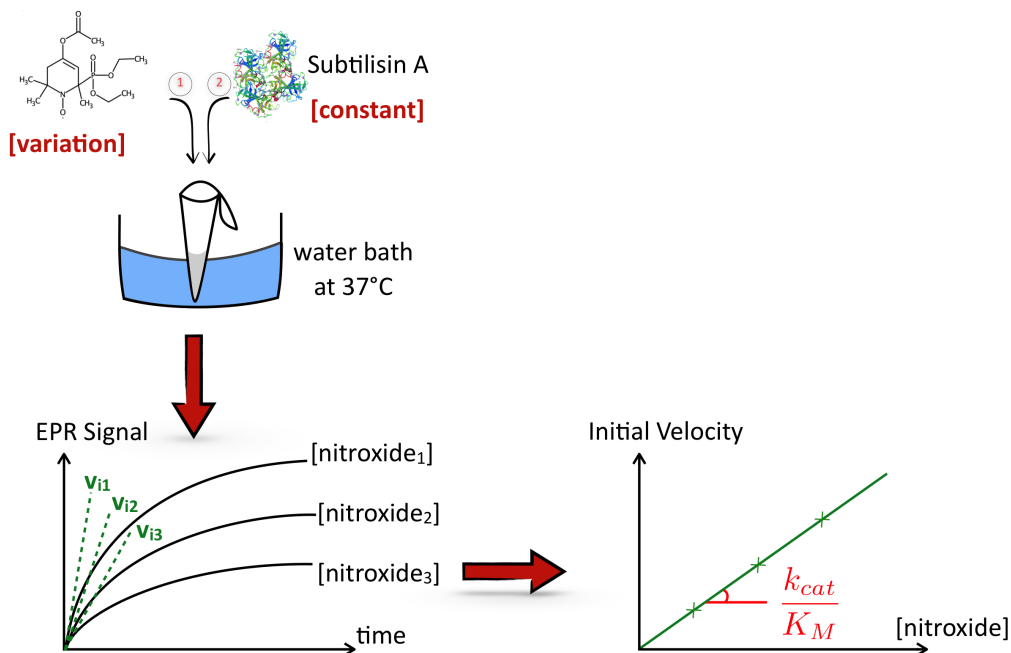


Figure 2.17: Experimental procedure illustrating the steps involved to evaluate the catalytic efficiency, $\frac{k_{cat}}{K_M}$ of Subtilisin A towards the β -phosphorylated nitroxide **10**. The EPR signal evolution is plotted for each concentration of the substrate. Afterwards, the initial velocity was determined and plotted against nitroxide **10**. concentration. The slope of the line was equal to the catalytic efficiency of subtilisin A.

iv) OMRI frequency sweep

This new OMRI probe had also to be evaluated using the OMRI approach. Before doing so, a frequency sweep experiment was performed to determine the optimum electronic saturation frequency and hence for an optimal detection of either the nitroxide **10**, or the nitroxide **9**. It consisted of varying the electronic saturating frequency about one EPR line and measuring the Overhauser signal enhancement. More explicitly, 2D images with and without electronic spin saturation were acquired at different equally-spaced EPR frequencies ranging (at each 0.5 MHz) from 5412.35 to 5429.85 MHz for nitroxides **9**, and **10**, for a proton frequency of 8.24264 MHz.

First, the EPR resonant cavity was successively tuned and matched at each given electronic saturating frequency by using a network analyzer (Agilent Technologies, Santa Clara, CA, USA). On the return loss spectrum as shown in Figure 2.18, the amplitude of the peak was maintained at around 50 dB. Afterwards the coaxial cable was reconnected to the amplifiers and the 2D images were acquired with and without the electronic saturation using a 2D NMR gradient echo sequence synchronized with electron saturation as in [Massot et al. 2012]. The NMR coil was tuned and matched only once at 8.243 MHz.

The acquisition parameters were: EPR pulse length = 260 ms; echo time (TE) = 10 ms; repetition time (TR) = 288 ms; flip angle = 70° ; receiver bandwidth = 52 Hz per pixel; matrix size = 64×64 ; field of view (FOV) = 22×22 mm; slice thickness = 7 mm; spatial resolution = $344 \times 344 \mu\text{m}^2$; and acquisition time = 22 s with one average.

A visual description is shown in Figure 2.18.

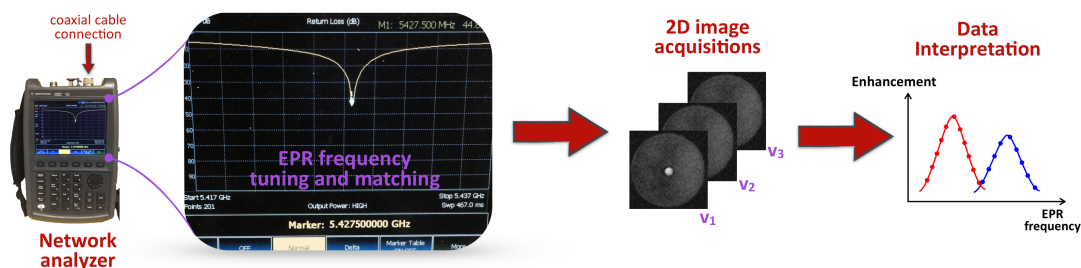


Figure 2.18: The steps involved in the frequency sweep experiments – For each EPR irradiation frequency, the resonant cavity was tuned, then enhanced and unenhanced 2D images were acquired. Finally, the signal enhancement was calculated for each set of frequency data and plotted against the range of frequencies.

An example of the data obtained for frequency sweep experiment for the nitroxide 9. and nitroxide 10. is shown in the Figure 2.19 below.

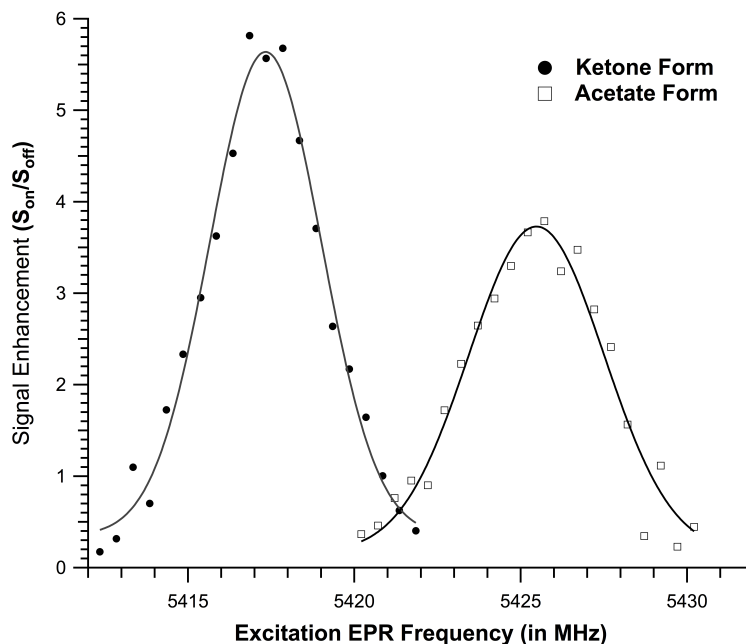


Figure 2.19: Frequency sweep results.

v) Kinetic Assays with Subtilisin A using OMRI

In the same manner as in EPR experiments, a kinetic study was carried out with the OMRI setup. Using a water tubing system around the center of the EPR cavity, the setup was kept at a temperature of 37°C. Immediately after adding the enzyme, Subtilisin A with the acetate nitroxide form at 1.8mM, the sample was placed at the center of the cavity. The latter was then tuned at the optimum frequency of the product formation (i.e at the detection frequency of the ketone nitroxide form) and 2D images were acquired as a function of time. Overhauser enhancements were calculated and the kinetic curve was plotted for 20 hours of enzymatic activity. These results were then compared to those obtained by the EPR experiments.

All the *in vitro* results carried out on the β -phosphorylated nitroxide formed part of Article 3.

2.4.2 *In vivo* experiments

The ultimate goal of proteolytic detection by OMRI was the *in vivo* visualization and the validation of this technique in molecular imaging.

A. ANIMAL GAVAGE PROTOCOL

Referring to Article 2 and Article 3, healthy mice (CB57/CRL, Charles River, L'Arbresle, France) weighing between 22 to 24 g were used for our *in vivo* experiments. All protocols included a thermostated bed at 37°C to maintain the animal's body temperature. For either of the OMRI probes used, the mice were orally administered with the nitroxide in the stomach. Anesthetization was performed for all the mice, at the time they were placed in the prone position inside the resonant EPR cavity.

1. For the experiments involving the nitroxide-labeled elastin probe, the cavity was adjusted to the proper electron frequency of the PCA nitroxide, only once. The following sequence of acquisitions is clearly illustrated in Article 2. Control experiments were also carried out with predigested nitroxide-labeled elastin administered in the mouse's stomach. The imaging protocol was the same as above.
2. For the experiments involving the β -phosphorylated nitroxide, as the OMRI on/off strategy lies in the frequency shifting, both substrate and product were detectable. Therefore, to validate this concept, the cavity was first adjusted to the corresponding first high field EPR line of the nitroxide **10**. 3D images of the acetate nitroxide form were acquired using the same MRI sequence as in Article 2 to confirm the presence of the nitroxide in the stomach.

Later on, the cavity was tuned to the corresponding first high field EPR line of the nitroxide **9**. Images were acquired and this time, the Overhauser signals were assigned to the product after hydrolysis of the acetate group.

The time scale of the experiments are described in Article 3. Control experiments were also performed by orally administrating the ketone form of the nitroxide, i.e nitroxide **9** in the stomach. OMR images were acquired using both EPR frequencies. This experiment procedure allowed to validate the specificity and selectivity of the OMRI signal according to the molecular species present *in vivo*.

Results

3.1 *In vitro* proteolytic activity detection using the OMRI technique

3.1.1 Aims of this study

The work presented in this dissertation is the first application of the OMRI technique in visualizing proteolytic processes in living intact organisms. The first step was therefore to detect this biological activity using purified enzymes and living immune cells capable of secreting enzymes upon induction. My contribution in this study was to conduct the OMRI experiments, collect and analyze the MRI data.

This *in vitro* as well as *ex vivo* proof-of-concept were by far an essential development for the OMRI technique. Through the synthesis of an appropriate OMRI probe that targets the elastolytic activity, we were able to demonstrate the specificity of the human neutrophil elastase enzyme towards the nitroxide-labeled elastin probe.

Also knowing that various pathologies like acute inflammation, emphysema, bacterial infection and so on, are associated with a recruitment of immune cells called neutrophils at the site of the disease, an *ex vivo* procedure was undertaken. Human neutrophil cells were extracted from human blood samples and upon activation of these cells using a calcium ionophore, a cocktail of enzymes was secreted in the interstitial environment. Kinetic studies evaluated the sensitivity of both EPR and OMRI methods and validated the OMRI method for spotting elastolytic activity.

The results of this study are presented in the following published article of the PLOS ONE journal in 2013.

3.1.2 Article 1

Overhauser-Enhanced MRI of Elastase Activity from In Vitro Human Neutrophil Degranulation

Elodie Parzy¹, Véronique Bouchaud¹, Philippe Massot¹, Pierre Voisin¹, Neha Koonjoo¹, Damien Moncelet¹, Jean-Michel Franconi¹, Eric Thiaudière¹, Philippe Mellet^{1,2*}

1 CRMSB, UMR 5536, University Bordeaux Segalen, CNRS, Bordeaux, France, **2** INSERM, Bordeaux, France

Abstract

Background: Magnetic resonance imaging can reveal exquisite anatomical details. However several diseases would benefit from an imaging technique able to specifically detect biochemical alterations. In this context protease activity imaging is one of the most promising areas of research.

Methodology/Principal Findings: We designed an elastase substrate by grafting stable nitroxide free radicals on soluble elastin. This substrate generates a high Overhauser magnetic resonance imaging (OMRI) contrast upon digestion by the target proteases through the modulation of its rotational correlation time. The sensitivity is sufficient to generate contrasted images of the degranulation of neutrophils induced by a calcium ionophore from 2×10^4 cells per milliliter, well under the physiological neutrophils concentrations.

Conclusions/Significance: These ex-vivo experiments give evidence that OMRI is suitable for imaging elastase activity from neutrophil degranulation. Provided that a fast protease-substrate is used these results open the door to better diagnoses of a number of important pathologies (cystic fibrosis, inflammation, pancreatitis) by OMRI or Electron Paramagnetic Resonance Imaging in vivo. It also provides a long-expected method to monitor anti-protease treatments efficiency and help pharmaceutical research.

Citation: Parzy E, Bouchaud V, Massot P, Voisin P, Koonjoo N, et al. (2013) Overhauser-Enhanced MRI of Elastase Activity from In Vitro Human Neutrophil Degranulation. PLoS ONE 8(2): e57946. doi:10.1371/journal.pone.0057946

Editor: Maria Rosaria Scarfi, National Research Council, Italy

Received: November 22, 2012; **Accepted:** January 28, 2013; **Published:** February 28, 2013

Copyright: © 2013 Parzy et al. This is an open-access article distributed under the terms of the Creative Commons Attribution License, which permits unrestricted use, distribution, and reproduction in any medium, provided the original author and source are credited.

Funding: This work was supported by the French Agence Nationale de la Recherche; grant number Blanc_09_434420. The funders had no role in study design, data collection and analysis, decision to publish, or preparation of the manuscript.

Competing Interests: The authors have declared that no competing interests exist.

* E-mail: philippe.mellet@mshb.u-bordeaux2.fr

Introduction

Although anatomical imaging methods like X-ray tomography, ultra-sound and MRI can give fine details many pathologies still escape diagnosis. Early transformations of healthy to pathological tissues are better characterized by their biochemistry than by their anatomy. Thus the trend has turned towards the molecular imaging approach to localize such processes. This branch potentially gives access to antigens and receptors targeting or to biochemical activities like the redox status [1,2] and enzyme activity [3,4].

Proteolytic activity is an interesting example of enzyme activity suitable for imaging. Protease activity is normally tightly regulated by a large excess of protease inhibitors. To the 500 protease sequences tagged in the human genome correspond about 100 protease inhibitors [5], some of them expressed at high concentration. Consequently the lifetime of an activated protease in normal tissues is very short. However an uncontrolled protease activity is associated with many diseases. In most situations this is the result of local secretion of a complex mixture of mutually activating proteases, each family of protease being able to inactivate the specific inhibitors of another family. Solid tumors, pancreatitis, rheumatoid arthritis, cystic fibrosis and inflammatory diseases of various origins are significant examples associated with a persistent

protease/inhibitor imbalance leaving uncontrolled proteolytic activity.

Acute neutrophil-mediated inflammation and cystic fibrosis have in common the role of neutrophils. These cells are the first white blood cells to migrate towards the damaged site. They organize the innate immune response at the early stage of inflammation [6] within minutes to hours. In the particular case of cystic fibrosis the lungs are partly infected with *Pseudomonas aeruginosa*. The bacteria trigger a massive recruitment of neutrophils which try to eliminate the bacteria by releasing the content of their granules and vesicles. However *Pseudomonas aeruginosa* colonies are surrounded by a mucus protecting them against neutrophil attack. Thus a chronic inflammation takes place and granules and vesicles content keep accumulating. Neutrophils carry three kinds of granules and one kind of vesicle. Each are able to release up to forty varieties of molecules [7]. Proteases secreted by the azurophilic granules and particularly the human neutrophil elastase (HNE) are the most deleterious molecules for the lungs. The term elastase defines a group of enzymes capable of the proteolytic release of soluble peptides from insoluble elastin [8]. Thus during cystic fibrosis elastin of the pulmonary alveoli is fragmented and the lungs progressively lose their function. As a result neutrophil proteases and particularly neutrophil elastase have long been therapeutic targets [9,10]. However, anti protease treatments have

failed so far to significantly improve the status of cystic fibrosis patients[11]. This can be attributed to the absence of any method to monitor the protease activity *in vivo* and to differentiate the pulmonary regions that are protected by the treatment from those that still undergo elastolytic activity. An imaging method of the elastolytic activity would thus be a great help to evaluate cystic fibrosis patients status and to develop new treatments.

The concept of taking advantage of the proteolytic activity for magnetic resonance imaging (MRI) has been explored by several authors either using gadolinium derivatives [12,13] or Overhauser magnetic resonance imaging (OMRI) [4]. OMRI is a double resonance experiment establishing a polarization transfer from the free electron of a stable free radical to the surrounding water protons. OMRI seems to be one of the most promising method for protease activity imaging for mainly two reasons. First, it can provide high contrasts and 3D well-resolved images as seen recently on tumor bearing mice [14]. Furthermore the involvement of a free radical is favorable to molecular imaging since the free electron is very sensitive to various changes in its environment: redox status [15], pH, molecular rotational correlation time [4]. In a previous paper we showed that the proteolytic hydrolysis of nitroxide-labeled bovine serum albumin could be followed *in vitro* by OMRI with the generation of high contrast[4].

In this paper we provide evidence that OMRI has the required sensitivity to follow a simple physiological event, neutrophil degranulation. A nitroxide-labeled elastin sample was used as a substrate for the human neutrophil elastase released upon the provoked degranulation. The induced reduction of the rotational correlation time was monitored by electronic paramagnetic resonance (EPR) spectroscopy and OMRI. The translation of this work towards *in vivo* protease imaging is discussed.

Results

Nitroxide-labeled elastin substrate characterization

The ability of nitroxide-labeled elastin to generate an EPR signal upon digestion by human neutrophil elastase (HNE) was probed with increasing concentrations of protease. The peak to peak height of the central line of the nitroxide was measured at several incubation times for each concentration. As shown in figure 1, one hour incubation easily discriminates HNE concentrations between 5 and 50 nM. As seen in the inset increasing EPR signal is still detectable in the 0.5 to 5 nM range. Thus EPR detection shows that nitroxide-labeled elastin is a sensitive elastase substrate. The most remarkable property of elastases is their unique capability to release soluble peptides from insoluble elastin[8]. This is due in part to their P1 specificity in the Schechter and Berger nomenclature[16] for valine and alanine which, respectively, constitute 13% and 26% of the amino acid composition of elastin. But the most selective feature is their ability to bind to the fibrous structure of elastin. Since our labeled elastin was made from a solubilized form it was interesting to search whether it has kept some of its elastase substrate specificity. Figure 2 shows the kinetics of hydrolysis by 50 nM human neutrophil elastase, porcine pancreatic elastase, bovine trypsin and chymotrypsin. Nitroxide-labeled elastin retains a good selectivity for both elastases while trypsin is nearly inactive. The slight activity of chymotrypsin is probably due to the chemical denaturation of soluble elastin which unveiled newly accessible cleavage sites.

The aim of this work is to generate high contrast images in the presence of elastase activity using Overhauser-enhanced MRI. Various concentrations of nitroxide-labeled elastin, corresponding to a range of 0.07 to 0.7 mM nitroxides, were thus incubated for 24 hours in the presence or absence of human neutrophil elastase.

Figure 3 shows that HNE produces a 3 to 5.6 times increase of the NMR signal due to the Overhauser effect for the whole range of concentrations. At 0.07 mM nitroxide concentration the signal is readily 3 times higher in the presence of HNE. Thus nitroxide-labeled elastin is able to generate high contrast images in the presence of HNE at low nitroxide concentration.

Application to neutrophil degranulation

To mimic a situation of inflammation human neutrophils were purified and incubated with the nitroxide-labeled elastin substrate. Degranulation was induced by adding A23187 calcium ionophore. The generated EPR signal intensities were compared to those from samples without ionophore. In figure 4a the EPR signal intensity clearly discriminates the samples with induced neutrophil degranulation from the samples with resting neutrophils at all times of observation. At each time point a faint signal increase without ionophore could be observed. This can easily be explained by some spontaneous cell death over time which triggers the release of granules. As seen in figure 4b at a given time of observation the EPR signal is strongly correlated to the number of neutrophils per well. Again, in the samples without ionophore spontaneous cell death generates a detectable signal however easily discriminated from the one in induced samples.

The potential capabilities of this substrate for imaging was probed using OMRI with the same neutrophil containing samples as in the previous EPR study. The kinetics shown in Figure 5a highlights a strong increase of the image intensity in the presence of the calcium ionophore, to be compared with the slow and moderate increase measured in the absence of ionophore. In figure 5b the image intensity versus the number of neutrophils undergoes a significantly steeper increase in the presence of calcium ionophore. In comparison to the EPR signal intensity curves OMRI intensity curves show less linearity at low enzymatic activity points which appear to be overestimated. This feature would be favorable to *in vivo* OMRI since low proteolytic activities would have a better chance to be detected.

The actual OMRI images used to produce figure 5b are shown in figure 5c. In the presence of ionophore the image intensity enhancement is visible from the first neutrophil concentration (1.12×10^4 cells/500 μ l). Interestingly, the signal enhancement due to elastase release from spontaneous cell death is also visible in the series without ionophore. In these examples of images the intensity enhancement produced by the elastase activity created a contrast equivalent to five times the basal intensity level of control images with nitroxide-labeled elastin but without adding neutrophils. Such an unusually high contrast, unattainable with conventional MRI, should facilitate image interpretation *in vivo*. Thus in an *ex vivo* system mimicking a situation of inflammation OMRI is sensitive enough to display high contrast images.

Discussion

Nitroxide-labeled elastin proves to be a sensitive elastase substrate for both EPR and OMRI. Moreover, this substrate was applied to detect a nearly physiological event, namely human neutrophils degranulation *ex vivo*, by EPR spectroscopy and to produce images of this event by OMRI. Significantly, the concentrations of cells in this experiment, 2.2×10^4 to 45×10^4 cells/ml, were well under the neutrophil concentration in normal blood (2×10^9 to 7.5×10^9 cells/ml). The target of our substrate, human neutrophil elastase, is an important enzyme in several pathologies. Chronic obstructive pulmonary disease[17], rheumatoid arthritis[18], atherosclerosis[19] or cystic fibrosis all involve HNE activity at some stage of the disease. For instance in the

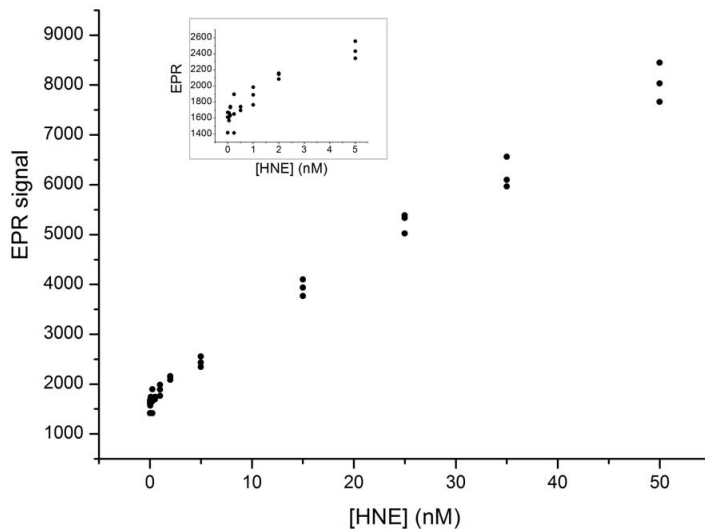


Figure 1. Human neutrophil elastase sensitivity test of nitroxide-labeled elastin substrate probed by EPR. The elastin substrate solution containing 0.36 mM nitroxide was incubated one hour at 37 °C with increasing elastase concentrations. Peak to peak heights of the nitroxide central line versus elastase concentration are plotted. The inset highlights the lowest elastase concentrations.
doi:10.1371/journal.pone.0057946.g001

pulmonary purulent sputum of the cystic fibrosis patients up to $5 \cdot 10^{-6}$ M active human neutrophil elastase has been found[11]. It is worth to notice that in the present work the sensitivity for active HNE was in the nanomolar range with EPR spectroscopy and OMRI imaging. Neutrophils are the first cells from the innate immune system to migrate towards an injured or infected site. For instance bronchoalveolar lavage fluid from young children with

cystic fibrosis may contain tens of million cells per ml[20]. Thus neutrophil elastase activity is a good marker of any kind of acute or chronic inflammation and an interesting target for imaging. Therefore the proposed imaging method based on elastolytic activity would favor progresses in basic research, diagnosis and treatment follow up.

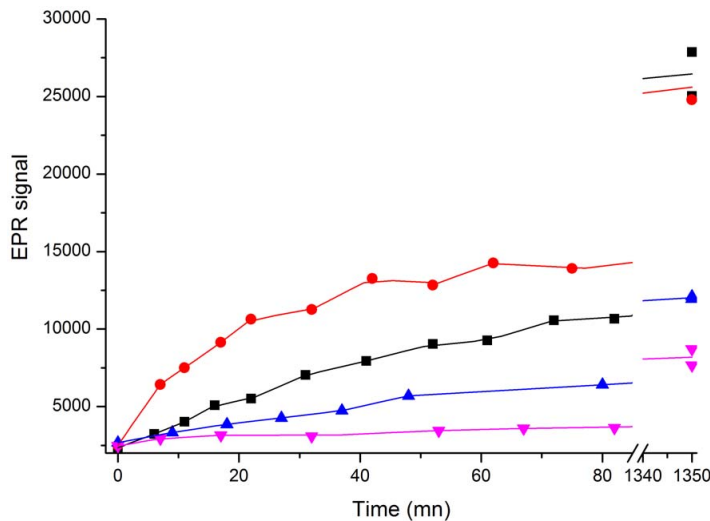


Figure 2. Comparative kinetics of hydrolysis of the elastin substrate by human neutrophil elastase (black squares), porcine pancreatic elastase (red circles), chymotrypsin (blue triangles) and trypsin (pink triangles) probed by EPR. 0.36 mM equivalent nitroxide substrate was incubated at 37°C with 50 nM of each enzyme.
doi:10.1371/journal.pone.0057946.g002

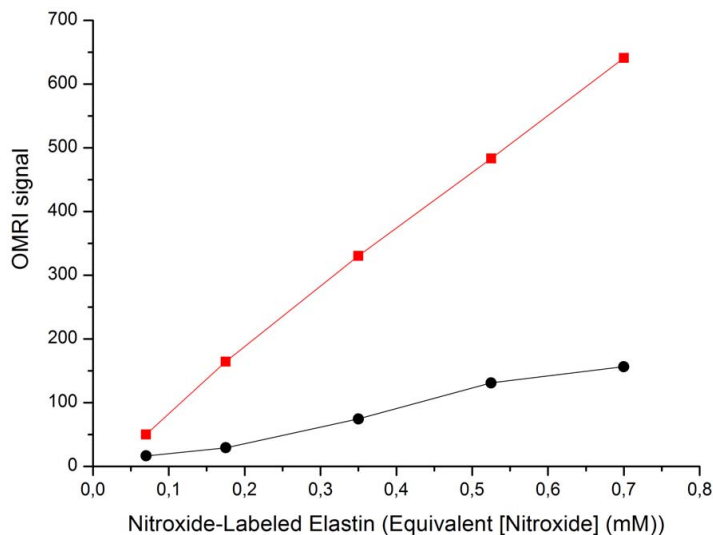


Figure 3. OMRI signal from increasing concentrations of native (black circles) or HNE-digested (red squares) nitroxide-labeled elastin. Complete elastin digestion was carried out during 24 hours with 50 nM HNE at 37°C. doi:10.1371/journal.pone.0057946.g003

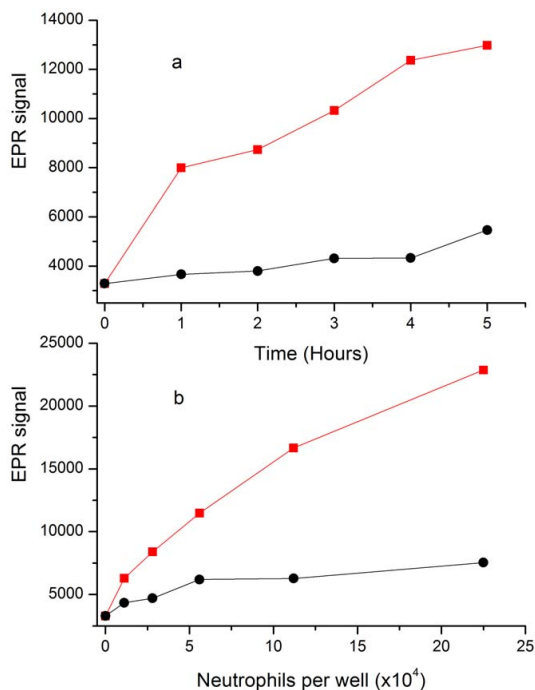


Figure 4. EPR detection of neutrophil degranulation in the presence of nitroxide-labeled elastin (1 mM equivalent nitroxide concentration). (a) EPR signal from 11×10^4 resting (black circles) or activated (red squares) neutrophils in 0.5 ml versus incubation time at 37°C. (b) EPR signal at five hours incubation at 37°C versus the number of resting (black circles) or activated (red squares) neutrophils. doi:10.1371/journal.pone.0057946.g004

The activity from pancreatic elastase can also be spotted by our method (see fig. 2). In pancreatitis this elastase is prematurely activated in the pancreas instead of being secreted as an inactive zymogen which is then activated in the duodenum. Pancreatitis can appear as a chronic or acute form and its etiology can either be gallstones, fat diet, alcohol or inherited zymogen defects. Understanding and evaluating the evolution of the disease during therapy, *e.g.* anti-protease treatments[21], would be made easier with a non-invasive whole-body protease imaging method, particularly in the early stages of chronic pancreatitis[22].

Mouse OMRI at 0.2 Tesla has proven to be an efficient method to follow nitroxide biodistribution in 3D at high resolution[14]. Thus *ex vivo* elastase imaging carried out with the same OMRI system opens the way to *in vivo* inflammation imaging, where protease activity is high enough to overcome the protection provided by protease inhibitors. To actually observe significant signal enhancement *in vivo* the free nitroxide concentration should remain in the range of 0.1 to 1 mM over several minutes. This requires both a good biodistribution of the substrate and a fast hydrolysis of the substrate by the enzyme to compensate for the diffusion of the free nitroxide and its renal clearance. In this paper we used a natural protein which undergoes a typical slow hydrolysis by the elastases thus limiting the chances for useful *in vivo* applications. It is however possible to use small nitroxide containing peptides including an elastase specific cleavage site. These peptides would then be linked to a protein or nanoparticle carrier to lower their rotational diffusion coefficient. The nitroxide would then be released from the carrier by the target enzyme hence providing OMRI contrast. In this way the kinetics of hydrolysis can be raised by several orders of magnitude.

Incidentally, nitroxide-labeled elastin is an excellent substrate to quantify elastase activity by EPR in opaque media where optical methods fail. Such substrates might consequently be used in EPR imaging (EPRI) of protease activity. However significant developments are needed to provide actual 3D EPR images at sub-millimeter spatial resolution within several minutes.

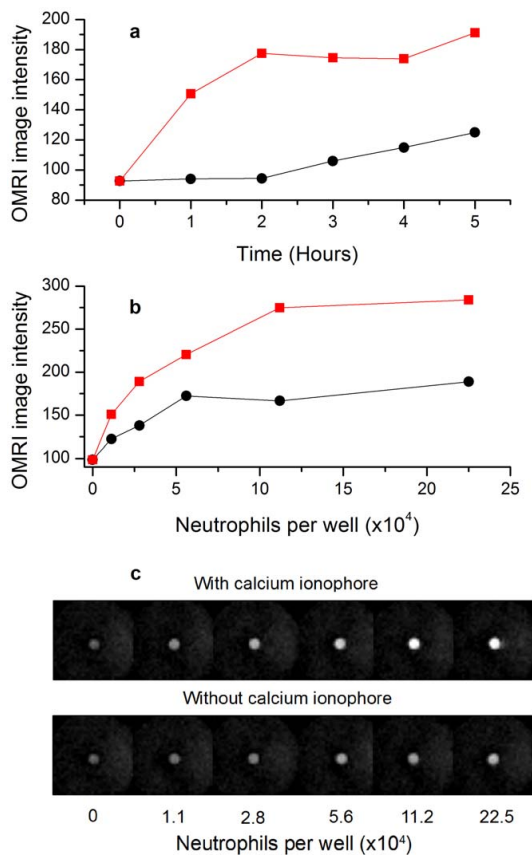


Figure 5. OMRI detection of neutrophil degranulation in the presence of nitroxide-labeled elastin (1 mM equivalent nitroxide concentration). (a) OMRI intensity from 11×10^4 resting (black circles) or activated (red squares) neutrophils in 0.5 ml versus time of incubation at 37 °C. (b) OMRI intensity at five hours incubation at 37 °C versus the number of resting (black circles) or activated (red squares) neutrophils. In (c) the images corresponding to plot (b) are displayed. Gradient Echo (Fast Low Angle SHot) trans-axial images were acquired with the following parameters: TR: 300 ms, TE: 10 ms, RF nutation angle: 70 degrees, Field of View (FOV): 22 mm*22 mm, acquisition matrix: 64*64, in plane resolution: 0.34 mm*0.34 mm, slice thickness: 3 mm, 2 averages. OMRI HF irradiation was applied for 260 ms out of 300 ms TR. doi:10.1371/journal.pone.0057946.g005

Materials and Methods

Enzymes

Human neutrophil elastase and porcine pancreatic elastase were purchased from Elastin Products company (Missouri, USA). Bovine trypsin and chymotrypsin were from Worthington (New Jersey, USA).

All experiments involving purified proteases were done in 0.1 M phosphate buffer pH 7.4 at 37 °C.

Nitroxide-labeled elastin

Elastin-soluble (Elastin Products Company, Missouri, USA) is bovine neck ligament elastin extracted and processed with hot

oxalic acid. The crude product is thus a mixture of peptides ranging from 3 kDa to 60000 kDa. In this paper the Overhauser switch relies on the initial high rotational correlation time of the substrate. Thus an initial molecular weight selection was done by centrifuging three times a 15 ml solution of 500 mg of elastin in 20 mM phosphate buffer at pH 7.2 on concentrating filters with a cut-off of 30000 kDa (Amicon Ultra 30 K, Millipore). The retained molecules were diluted in 15 ml of 20 mM phosphate buffer pH 8.3 and incubated overnight with 50 mg 1-Oxyl-2,2,5,5-tetramethylpyrroline-3-carboxylate N-Hydroxysuccinimide Ester (Toronto Research Chemicals, Canada). The mixture was then concentrated to 2 ml with the same type of filter. A second size selection was done by gel filtration through a Biosuite 250 21.5×300 mm HPLC column (Waters) at 4 ml/min in 0.1 M phosphate buffer with 0.15 M NaCl at pH 7.4. Fractions up to 20 minutes were collected and concentrated to 3.5 ml.

Characterization of nitroxide-labeled elastin: Figure 6 shows the EPR spectra of elastin before and after complete proteolysis with Human Neutrophil Elastase.

The concentration of nitroxide in the stock solution (18 mM) was measured by integrating the central line of the digested sample and comparing with a proxyl calibration line (not shown).

Neutrophil isolation and characterization

Neutrophils were isolated from a leukoreduction filter kindly provided by the French Blood Service (Bordeaux, France). The filter was back-flushed with 50 ml of DMEM (gibco) completed with BSA (40 g/l)(Sigma), Citrate-dextrose solution (10% vol/vol) (Sigma) and Pulmozyme, a dornase alpha commercial solution (10 µl/ml) at pH 7.4. The cells were diluted to 160 ml with the same solution and spun 20 mn at 110 g and 20 °C in four tubes. The pellets were re-suspended in 90 ml of DMEM with dornase, layered on six tubes containing 15 ml of Granulosep (Eurobio) and spun 20 minutes at 1500 g and 20 °C. The interface containing the white cells was harvested and washed in two times 50 ml of DMEM with dornase. Each pellet was resuspended in 20 ml DMEM with dornase, layered on 10 ml of Lymphocyte Separation Medium (Eurobio) and spun 40 mn at 400 g and 20 °C. The pellet was highly enriched in granulocytes but still contained red cells and a few lymphocytes as seen in figure 7. It was harvested and washed with DMEM and was used as such in further experiments since neither red cells nor lymphocytes are able to release elastase. Neutrophils counting was carried out from a sample diluted in red cells lysing solution (Becton Dickinson) washed in phosphate buffer saline solution and analyzed on a Guava easyCyte flow cytometer/counter (Millipore). The neutrophil population was identified and counted according to its forward scatter versus side scatter properties.

In all experiments neutrophils were incubated in DMEM without serum at 37 °C in 5% CO₂ atmosphere. Neutrophil degranulation was induced with 2.5×10^{-6} M calcium ionophore A23187 (Sigma). At the end of the incubation time eglin c, a rapid high affinity elastase inhibitor[23] was added in excess before sample freezing.

Electronic Paramagnetic Resonance

All EPR spectra were recorded with a MiniScope MS200 EPR spectrometer (Magnetech, Berlin, Germany). B0-field was set to 3350 G, sweep range to 45 G in 60 seconds, modulation to 100 mG. The gain was constant inside each series of spectra. The samples were loaded in 75 mm/60 µl capillaries (Hirschmann Laborgerate, Germany).

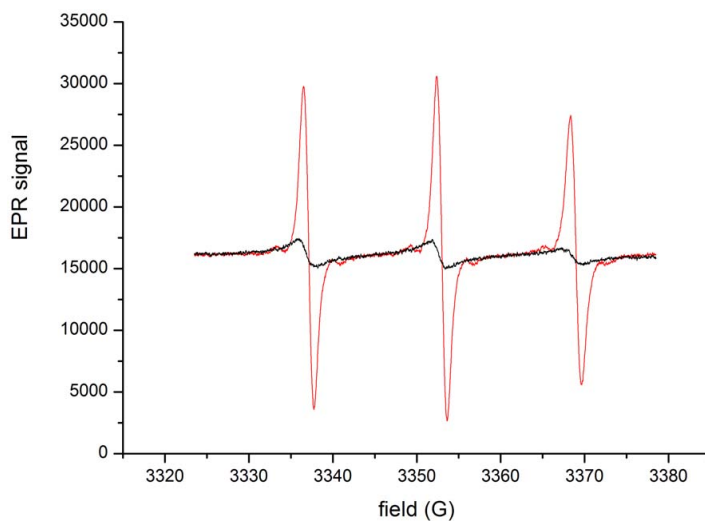


Figure 6. Typical EPR spectra of native (black line) and HNE digested (red line) nitroxide-labeled elastin (0.36 mM equivalent nitroxide).

doi:10.1371/journal.pone.0057946.g006

Dynamic Nuclear Polarization enhanced Magnetic Resonance Imaging

EPR Cavity and MRI devices. A C-shaped MRI system, Magnetom Open Viva operating at 0.194T (Siemens, Erlangen, Germany) was used. The proton frequency was 8.24 MHz. Gradients maximum intensity was 15 mT m^{-1} . Electron spin excitation was induced by a resonant hyperfrequency (HF) cylindrical cavity (Bruker, Wissembourg, France) running in

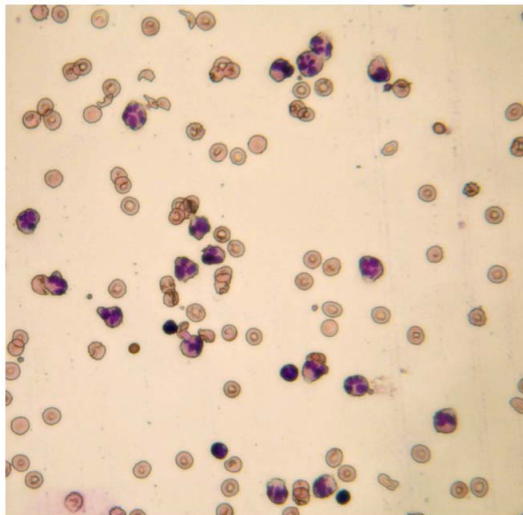


Figure 7. Representative optical microscope field from the May-Grünwald-Giemsa staining of the neutrophil-enriched preparation used for the degranulation experiments.

doi:10.1371/journal.pone.0057946.g007

TE011 mode, positioned at the center of the MRI magnet bore [4]. Its geometry (240 mm diameter, 29 mm width) was designed to reduce the electric component of the HF Field in its center, thus minimizing sample heating upon microwave emission. Actual power deposition was evaluated by measuring temperature elevation with a temperature probe placed in a phosphate-buffered saline phantom (25 mm in diameter). By neglecting conduction, a heat equation was used to fit the initial linear temperature changes upon microwave excitation. Peak power was estimated to be in the range of 4 W. Previous *in vivo* experiments in the same conditions were harmless to mice [14]. The usable magnetic component was concentrated at the center of this cavity where an opening from both sides allowed sample access. The sample area at the center of the cavity was 28 mm in diameter and 29 mm in length. The HF amplification channel and the cavity were fully described in a previous paper [4]. Modification for minimizing the Eddy currents in order to improve MRI image quality was described previously [14].

Each sample was loaded into a 1.6 mm internal diameter capillary mechanically sealed at both ends. Each capillary was then positioned at the center of a 12 mm plastic tube, filled with water in order to load the MRI coil.

Pulse sequences. Two-dimensional magnetic resonance images were obtained with a standard Gradient Echo sequence. MRI acquisition and HF pulses were synchronized by an external pulse generator (RFPA, Artigues-pres-Bordeaux, France), allowing modulation of HF pulse duration. The HF pulse duration was 260 ms to be compatible with the T_1 value of water in the presence of nitroxide in the millimolar range. It was immediately followed by the MRI sequence with an echo time (TE) of 10 ms and minimal TR of 27 ms. This scheme was repeated for each echo acquisition. The effective TR, including HF irradiation time, was then 300 ms. All MR adjustments were done manually, using the same fixed receiver amplification gain for both measurements, without and with HF irradiation, so that signals can be directly compared and Overhauser enhancements calculated.

Post processing. Post-processing evaluations were carried out with IGOR Pro (Wavemetrics, Lake-Oswego, OR, USA). All signal intensity measurements were done with ImageJ imaging software (ImageJ, National Institutes of Health, USA). Signal intensity was measured in a circular region of interest of 1 mm² positioned in the capillary area.

Acknowledgments

We thank A. Courtois, M. Dubois and B. Muller, (CRCTB, University Bordeaux Segalen) for their help and for access to the EPR spectrometer.

References

- Utsumi H, Yamada K, Ichikawa K, Sakai K, Kinoshita Y, et al. (2006) Simultaneous molecular imaging of redox reactions monitored by Overhauser-enhanced MRI with 14N- and 15N-labeled nitroxyl radicals. *Proc Natl Acad Sci U S A* 103: 1463–1468.
- Tu C, Louie AY (2012) Strategies for the development of gadolinium-based 'q'-activatable MRI contrast agents. *NMR Biomed.*
- Louie AY, Huber MM, Ahrens ET, Rothbacher U, Moats R, et al. (2000) In vivo visualization of gene expression using magnetic resonance imaging. *Nat Biotechnol* 18: 321–325.
- Mellet P, Massot P, Madelin G, Marque SR, Harte E, et al. (2009) New concepts in molecular imaging: non-invasive MRI spotting of proteolysis using an Overhauser effect switch. *PLoS One* 4: e5244.
- Southan C (2000) Assessing the protease and protease inhibitor content of the human genome. *J Pept Sci* 6: 453–458.
- Nathan C (2006) Neutrophils and immunity: challenges and opportunities. *Nat Rev Immunol* 6: 173–182.
- Faurschou M, Borregaard N (2003) Neutrophil granules and secretory vesicles in inflammation. *Microbes Infect* 5: 1317–1327.
- Bieth JG (2004) Leukocyte elastase. In: Barrett AJ, editor. *Handbook of Proteolytic Enzymes*. Second Edition ed: Elsevier pp. 1517–1523.
- Griese M, Kappler M, Gaggari A, Hartl D (2008) Inhibition of airway proteases in cystic fibrosis lung disease. *Eur Respir J* 32: 783–795.
- Korkmaz B, Horwitz MS, Jenne DE, Gauthier F (2010) Neutrophil elastase, proteinase 3, and cathepsin G as therapeutic targets in human diseases. *Pharmacol Rev* 62: 726–759.
- Elborn JS, Perrett J, Forsman-Semb K, Marks-Konczalik J, Gunawardena K, et al. (2012) Efficacy, safety and effect on biomarkers of AZD9668 in cystic fibrosis. *Eur Respir J* 40: 969–976.
- Jastrzebska B, Lebel R, Theriault H, McIntyre JO, Escher E, et al. (2009) New enzyme-activated solubility-switchable contrast agent for magnetic resonance imaging: from synthesis to in vivo imaging. *J Med Chem* 52: 1576–1581.
- Olson ES, Jiang T, Aguilera TA, Nguyen QT, Ellies LG, et al. (2010) Activatable cell penetrating peptides linked to nanoparticles as dual probes for in vivo fluorescence and MR imaging of proteases. *Proc Natl Acad Sci U S A* 107: 4311–4316.
- Massot P, Parzy E, Pourtau L, Mellet P, Madelin G, et al. (2012) In vivo high-resolution 3D overhauser-enhanced MRI in mice at 0.2 T. *Contrast Media Mol Imaging* 7: 45–50.
- Krishna MC, English S, Yamada K, Yoo J, Murugesan R, et al. (2002) Overhauser enhanced magnetic resonance imaging for tumor oximetry: coregistration of tumor anatomy and tissue oxygen concentration. *Proc Natl Acad Sci U S A* 99: 2216–2221.
- Schechter I, Berger A (1967) On the size of the active site in proteases. I. Papain. *Biochem Biophys Res Commun* 27: 157–162.
- Stockley RA (1999) Neutrophils and protease/antiprotease imbalance. *Am J Respir Crit Care Med* 160: S49–52.
- Luster AD, Alon R, von Andrian UH (2005) Immune cell migration in inflammation: present and future therapeutic targets. *Nat Immunol* 6: 1182–1190.
- Henriksen PA, Sallenaave JM (2008) Human neutrophil elastase: mediator and therapeutic target in atherosclerosis. *Int J Biochem Cell Biol* 40: 1095–1100.
- Peterson-Carmichael SL, Harris WT, Goel R, Noah TL, Johnson R, et al. (2009) Association of lower airway inflammation with physiologic findings in young children with cystic fibrosis. *Pediatr Pulmonol* 44: 503–511.
- Motou Y (2007) Antiproteases in the treatment of chronic pancreatitis. *JOP* 8: 533–537.
- Bilgin M, Bilgin S, Balci NC, Momtahan AJ, Bilgin Y, et al. (2008) Magnetic resonance imaging and magnetic resonance cholangiopancreatography findings compared with fecal elastase 1 measurement for the diagnosis of chronic pancreatitis. *Pancreas* 36: e33–39.
- Braun NJ, Bodmer JL, Virca GD, Metz-Virca G, Maschler R, et al. (1987) Kinetic studies on the interaction of eglin c with human leukocyte elastase and cathepsin G. *Biol Chem Hoppe Seyler* 368: 299–308.

We thank Z. Ivanovic and J. Chevalyre (french blood transfusion service, Bordeaux) for kindly providing leukodepletion filters and helpful advices with neutrophil purification from leukodepletion filters, respectively.

Author Contributions

Conceived and designed the experiments: P VB P. Massot PV NK DM JMF ET P. Mellet. Performed the experiments: EP VB P. Massot PV NK DM P. Mellet. Analyzed the data: EP VB P. Massot PV NK DM JMF ET P. Mellet. Wrote the paper: P. Mellet ET.

3.2 *In vivo* proteolytic activity detection using the OMRI technique

3.2.1 Aims of this study

Our team have implemented a MRI methodology in the aim of acquiring 3D OMRI images rapidly on small animals with continuous EPR transition saturation. A TrueFISP sequence was compiled on the 0.2T system. The sequence was tested *in vitro* on nitroxide-containing phantoms. All images were acquired with and without electronic saturation and in 3 dimensions for maximal SNR. A good spatial resolution was also one of our objectives.

Hence, to achieve good spatial resolution and rapidity in the acquisitions, partial k -space matrices were acquired. The Keyhole method was established. During the OMRI experiment, a reference full k -space matrix was acquired followed by multiple consecutive partial matrices. This strategy was less time consuming. Image reconstruction merging one partial matrix into the reference full matrix was done after the OMRI experiment, allowing images to regain a resolution like the reference matrix. Along with this MRI methodological development, the next step in proteolytic activity detection, was its *in vivo* application. Our goal was therefore to target elastase enzymes present in the digestive tract of normal healthy mice using the nitroxide-labeled elastin probe.

Specific localization of the proteolytic activity was made possible with technique. The results of this study are described in the next published article of the Contrast Media Molecular Imaging journal in 2013.

3.2.2 Article 2

In this *in vivo* proteolytic activity detection project, I conducted all *in vitro* and *in vivo* experiments. The development of the TrueFISP sequence on the 0.2 T MRI system, along with the reconstruction encoding on the Igor software was the work of Lepetit-coiffé M, Massot P and myself. I also had a large and main contribution in writing the article.

Full Paper

CONTRAST MEDIA &
MOLECULAR IMAGING

Received: 9 September 2013,

Revised: 21 October 2013,

Accepted: 31 October 2013,

Published online in Wiley Online Library: 14 April 2014

(wileyonlinelibrary.com) DOI: 10.1002/cmim.1586

In vivo Overhauser-enhanced MRI of proteolytic activity

Neha Koonjoo^a, Elodie Parzy^a, Philippe Massot^a, Matthieu Lepetit-Coiffé^{a,b}, Sylvain R. A. Marque^c, Jean-Michel Franconi^a, Eric Thiaudiere^a and Philippe Mellet^{a,d,*}

There is an increasing interest in developing novel imaging strategies for sensing proteolytic activities in intact organisms *in vivo*. Overhauser-enhanced MRI (OMRI) offers the possibility to reveal the proteolysis of nitroxide-labeled macromolecules thanks to a sharp decrease of the rotational correlation time of the nitroxide moiety upon cleavage. In this paper, this concept is illustrated *in vivo* at 0.2 T using nitroxide-labeled elastin orally administered in mice. *In vitro*, this elastin derivative was OMRI-visible and gave rise to high Overhauser enhancements (19-fold at 18 mM nitroxide) upon proteolysis by pancreatic porcine elastase. *In vivo* three-dimensional OMRI detection of proteolysis was carried out. A keyhole fully balanced steady-state free precession sequence was used, which allowed 3D OMRI acquisition within 20 s at 0.125 mm³ resolution. About 30 min after mouse gavage, proteolysis was detected in the duodenum, where Overhauser enhancements were 7.2 ± 2.4 (n=7) and was not observed in the stomach. Conversely, orally administered free nitroxides or pre-digested nitroxide-labeled elastin were detected in the mouse's stomach by OMRI. Combined with specific molecular probes, this Overhauser-enhanced MRI technique can be used to evaluate unregulated proteolytic activities in various models of experimental diseases and for drug testing. Copyright © 2014 John Wiley & Sons, Ltd.

Keywords: OMRI; *in vivo*; mouse; proteolytic activity

1. INTRODUCTION

In vivo molecular imaging is a promising tool in the field of early diagnosis of diseases. Novel imaging strategies are being developed to improve the sensitivity and the specificity of contrast agents with the goal of more accurate diagnosis and therapy follow-up (1,2). To the same extent, there is a strong need for new personalized molecular beacons capable of unveiling specific disease-related bio-reactions (3). Among the fundamental processes that can be investigated by molecular imaging, proteolysis plays a central role (4).

Proteolysis is essential for the activity of most, if not all, biological systems. Protease activity has to be kept strictly to a local and transient event by numerous intra- and extracellular protease inhibitors in order to maintain global inter/intracellular homeostasis. Interestingly, a local but persistent protease activity is associated with a variety of diseases. For instance, in solid tumours, inflammation, cystic fibrosis, rheumatoid arthritis and chronic obstructive pulmonary disease, the protease inhibitors are locally overwhelmed. With about 400 annotated proteases in the human genome, it has become a key target for future therapies (5,6). Thus, there is a true demand for visualizing and localizing proteolysis *in vivo* during abnormal activities so that, in the long run, better patient prognosis tools can be developed for monitoring treatments and disease progression. Technically, the detection of an enzymatic activity has the additional advantage of signal amplification through substrates turnover.

Molecular imaging approaches have already been developed for targeting protease activities *in vivo*, for example, cathepsin B in mouse brain tumors (7), the matrix metalloproteinase

(MMP) in tumor xenografts (8) and the neutrophil elastase in acute lung injuries of small animal models (9). Imaging modalities include optical imaging such as near-infrared fluorescence imaging and fluorescence molecular tomography (7,10), mainly because of the great advances in targeted fluorescent probe technology. This method is sensitive and proteolysis-sensitive fluorescent probes are easy to design, but it is hindered by the weak penetration of near-infrared light in living tissues. Alternatively, single-photon emission computed tomography (SPECT) and positron emission tomography (PET) imaging have been used for probing the presence of metalloprotease (11) with the advantage of sensitivity and the drawbacks of poor 3D localization and high cost.

* Correspondence to: Philippe Mellet, RMSB, UMR 5536, Case 93, University Bordeaux Segalen, 146 rue Leo Saignat, F33076 Bordeaux Cedex, France. E-mail: mellet@rmsb.u-bordeaux2.fr

a N. Koonjoo, E. Parzy, P. Massot, M. Lepetit-Coiffé, J.-M. Franconi, E. Thiaudiere, P. Mellet
Centre de Résonance Magnétique des Systèmes Biologiques, UMR 5536 CNRS
Université Bordeaux Segalen, Bordeaux, France

b M. Lepetit-Coiffé
Siemens France, Saint-Denis, France

c S. R. A. Marque
UMR 7273 Aix-Marseille Université, Marseille, France

d P. Mellet
INSERM, Université Bordeaux Segalen, France

An alternative visualization approach with a good potential in spatial resolution, three-dimensional anatomic localization and penetration depth can be used for molecular imaging of proteolysis. Indeed, Overhauser-enhanced Magnetic Resonance Imaging (OMRI) has been used to image proteolytic events *in vitro* (12,13). OMRI [also known as proton-electron double resonance imaging, PEDRI (14)] is based upon the Overhauser effect (15) occurring when unpaired electrons of a free radical species interact with surrounding water protons. Nuclear polarization can be increased by saturating the electron spin resonance, thereby revealing the presence of the unpaired electron in a magnetic resonance image. When covalently attached to proteins like bovine serum albumin or elastin, nitroxides could not generate Overhauser enhancement because long rotational correlation times induced a marked broadening of the EPR (electron paramagnetic resonance) lines, thus preventing electron spin magnetization saturation and lowering the electron-proton coupling factor (16). Upon proteolysis, the release of small nitroxide-labeled peptides restored the occurrence of narrow EPR lines and significant Overhauser enhancements. In this way, it has been demonstrated that an elastin-based substrate, labeled with nitroxides, could be efficiently cleaved by neutrophil elastase (13) and thus could reveal neutrophil degradation with high sensitivity and contrast. Moreover, OMRI detection of stable nitroxides was performed *in vivo* in mice at 0.2 T (17). This was possible with a dedicated EPR cavity operating at 5.43 GHz, which induced limited overheating in living systems.

In the present study, it is proposed to translate *in vivo* the proof-of-concept of OMRI proteolysis, as so far demonstrated *in vitro*. Three-dimensional OMRI of digestive proteolysis is described in healthy mice, after ingestion of nitroxide-labeled elastin. Prospects of this approach in molecular imaging of disease-associated proteolysis are discussed.

2. MATERIALS AND METHODS

2.1. Nitroxide-Labeled Elastin

The protein substrate has been partly described in a previous work (13). Soluble elastin (Elastin Products Company, Missouri, USA) containing variable peptide lengths was sorted to select peptides of long rotational correlation times. The initial 30 000 kDa cut-off selection was obtained from a 60 ml solution of 1 g of soluble elastin (Elastin Products Company, Missouri, USA) in 20 mM phosphate buffer at pH 7.2 using Amicon centrifugal filters. It was then incubated overnight with 100 mg 1-oxyl-2,2,5,5-tetramethylpyrrolidine-3-carboxylate-*N*-hydroxysuccinimide Ester (Toronto Research Chemicals, Canada) at pH 8.3. A second size selection was carried out by dialysis against 20 mM phosphate buffer. Dialysis was performed over two nights with one buffer exchange. The final product, free from unreacted nitroxides (total volume of 11 ml), was aliquoted and stored at -20°C . The nitroxide content was measured after a complete pancreatic porcine elastase digestion, by integrating the EPR spectra of the sample and comparing with a calibration curve made with 3-carboxy-proxyl standards (Sigma).

2.2. Animal Preparation

Mice ($n=7$, CB57/CRL, Charles River, L'Arbresle, France) weighing 22–24 g were orally administered with 200 μl of nitroxide-labeled

elastin at 18 mM (nitroxide concentration). Within 3 min, the mice were anesthetized with 1.5–2% isoflurane (Centravet, La Palisse, France) mixed with air. They were placed in a prone position, lying on a home-made thermostatic bed. Bed temperature was 37°C . Rectal temperature was measured with a temperature probe (model 1025 SA instruments, Inc., New York, USA). The mean temperature rise was $1.8 \pm 0.2^{\circ}\text{C}$ over a mean period of 50 ± 13 s and the mean body temperature was $36.6 \pm 1^{\circ}\text{C}$ during a 2.5 h experiment. A respiratory sensor was placed on the upper part of the abdomen to monitor animal state throughout the experiment. Throughout the *in vivo* assays, mouse position was constant, thus allowing correct image superimposition. This protocol was approved by the University Animal Ethics Committee. Oral gavage did not induce any animal loss.

2.3. EPR Spectroscopy

A Miniscope MS200 EPR instrument (Magnetech, Berlin, Germany) was used to characterize the undigested and digested nitroxide-labeled elastin and also to quantify the nitroxide concentration. Undigested and digested nitroxide-labeled elastin samples were loaded in 75 mm/60 μl capillaries (Hirschmann Laborgerate, Germany). The experiments were performed in the same manner as in a preceding article (13). EPR acquisition parameters were as follows: $B_0=3353$ G; sweep width = 43.16 G; sweep time = 60 s; number of passes = 1; modulation = 100 mG. The gain was kept constant between the undigested and digested elastin samples. EPR spectra processed using IGOR Pro (Wavemetrics, Lake Oswego, OR, USA) revealed a nitroxide-labeled elastin concentration of 18 mM (expressed as nitroxide concentration).

2.4. OMRI System

As previously described (13,17), the whole-body MRI system (Magnetom Open Viva, Siemens, Erlangen, Germany) was equipped with a resistive C-shaped magnet operating at 0.194 T (8.25 MHz proton frequency). Maximal field-gradient strength was 14 mT/m. A Transverse-Electric TE011-mode resonant cylindrical hyperfrequency (HF) cavity (5.43 GHz electron frequency, Bruker, Wissemburg, France) was positioned at the center of the magnet. This cavity was recast (removal of some metal parts) in order to limit eddy currents. An opening in the middle of the cavity enabled a home-made transmit-receive saddle-shaped coil (inner diameter and length of 26 mm) to be inserted and allowed sample/mouse positioning. Tuning and matching adjustments of the resonant cavity and the transmit-receive NMR coil were carried out with a network analyzer (Agilent Technologies, Santa Clara, CA, USA) by measuring the return loss spectrum in their respective frequency spans. The HF field was generated by a synthesizer preceding a two-stage amplification by two amplifiers (RFPA, Artigues-pres-Bordeaux, France), which were linked through a coaxial cable to a wave guide (consisting of matching and tuning stubs) then to the cavity. Regarding the power deposition, the limit was set to 6 W by fixing a 50 Ω load at the end of the second amplifier, and from the analog meters, the reflected power never exceeded 1 W. Also, the deposited energy was well below those published in a previous article (17), since the irradiation time was reduced from several minutes to about 20 s and were thus well in agreement with animal safety guidelines.

2.5. *In vitro* MRI Assessment of Nitroxide-Labeled Elastin

A sample of the stock solution of the nitroxide-labeled elastin was set aside for *in vitro* assays and then diluted with 2, 4, 8, 16 and 32 dilution factors. Each of the six samples was then mixed with 5.10^{-5} M porcine pancreatic elastase (Elastin Products company, Missouri, USA) in 0.1 M phosphate buffer pH 7.4 at 37 °C for complete digestion. Control experiments were carried out without elastase. Samples were loaded into 2.5 mm internal diameter capillaries sealed with paraffin. Proton longitudinal relaxation time (T_1) measurements were measured using the inversion–recovery sequence as already described (12).

OMRI experiments were carried out using a single slice using a 2D NMR gradient echo sequence synchronized with electron saturation as in (17). The acquisition parameters were: EPR pulse length = 260 ms; echo time (TE) = 10 ms; repetition time (TR) = 288 ms; flip angle = 70°; receiver bandwidth = 52 Hz per pixel; matrix size = 64 × 64; field of view (FOV) = 22 × 22 mm; slice thickness = 7 mm; spatial resolution = 344 × 344 μm^2 ; and acquisition time = 22 s with one average.

2.6. *In Vivo* MRI Assays

Post gavage, standard optimized positioning of mouse abdomen was assessed from scout views acquired with standard 2D multislices, multi-orientations and fast 3D gradient echo sequences. The 3D MRI pulse sequences used in this study are summarized in Table 1. A FLASH (fast low angle shot) (18) 3D anatomical image was acquired to confirm stomach location midway in the FOV and to visualize the nitroxide-labeled elastin orally introduced in the stomach, thanks to the positive contrast brought about by the longitudinal relaxivity, r_1 of nitroxide-labeled elastin (see 'FLASH 3D' in Table 1).

3D OMRI images were acquired with an implemented TrueFISP (true fast imaging with steady-state precession) (19) sequence as described in Fig. 1(A) and Table 1 as 'OMRI TrueFISP'. A keyhole acquisition scheme (20) was used in order to limit HF exposure. The undersampling ratio was 50% in the phase and slice directions. Acquisition time was 18 s. Electron saturation was initiated 800 ms before NMR acquisition and was kept constant throughout. OMRI TrueFISP was carried out with and without EPR saturation to calculate Overhauser enhancements. In order to fulfill the partial k -space matrices, the complete 3D True FISP dataset without electron spin excitation ('fully-resolved True FISP' in Table 1) was acquired: the peripheral k -pace lines were added to the truncated matrices prior to Fourier transformation.

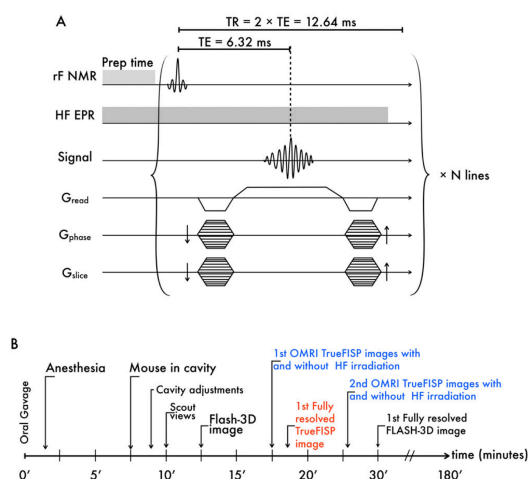


Figure 1. (A) True-FISP pulse program used for Overhauser-enhanced MRI (OMRI) experiments. 'Prep time' stands for 800 ms magnetization preparation without signal acquisition in order to establish the steady state for polarization transfer. The number of lines (N) was the product of the 32×20 phase encoding steps in the phase and slice directions, when the keyhole acquisition scheme was used. In this case, the acquisition duration was 18 s with two averages. For full matrix acquisition, the number of averages was eight, the number of lines was 64×40 , and no electron paramagnetic resonance (EPR) irradiation was applied. (B) Chronogram for *in vivo* protease imaging. The sequence acronyms are depicted in Table 1.

High-resolution anatomical images without electron spin excitation were also acquired with the 'fully-resolved FLASH 3D' gradient echo sequence (Table 1) with the same FOV parameters in order to allow image superimposition with OMRI images. These data were acquired either at the beginning or at the end of the experiment in case of slow or fast stomach-emptying rate, respectively.

Figure 1(B) displays the successive steps occurring in a complete Overhauser experiment with a mean duration time of about 3 h per mouse.

2.7. Image Reconstruction

In vitro signal intensities were measured with ImageJ imaging software (ImageJ, National Institutes of Health, USA) and then

Table 1. Parameters of the NMR pulse sequences used in this study

Sequence	FLASH-3D	OMRI TrueFISP	Fully resolved TrueFISP	Fully resolved FLASH-3D
TR/TE (ms)	200/20	12.64/6.32	12.64/6.32	200/20
Flip angle, α (deg)	50	30	30	50
Field of view (mm) ³	$32 \times 24 \times 20$	$32 \times 32 \times 20$	$32 \times 32 \times 20$	$32 \times 32 \times 20$
Matrix	$64 \times 54 \times 10$	$64 \times 32 \times 20$	$64 \times 64 \times 40$	$64 \times 64 \times 40$
Spatial resolution (μm) ³	$500 \times 600 \times 2000$	$500 \times 1000 \times 1000$	$500 \times 500 \times 500$	$500 \times 500 \times 500$
Number of averages	1	2	8	2
Acquisition time	3 min 38 s	18 s	4 min 37 s	17 min 06 s

transferred to IGOR Pro (Wavemetrics, Lake Oswego, OR, USA) for analysis. The region-of-interest (ROI) was 3 mm^2 . Signal amplifications were evaluated by dividing the mean signal intensity in the presence of EPR irradiation, S_{on} , by the mean signal intensity without EPR, S_{off} . The visualization software Amira (Konrad-Zuse-Zentrum Berlin, Germany) was used to display the 2D images of digested and undigested nitroxide-labeled elastin.

In vivo raw datasets were processed in IGOR Pro for keyhole 3D-reconstruction. Parametric images for signal amplification due to Overhauser effect were calculated as the ratio of signal intensity measured with and without EPR irradiation ($S_{\text{on}}/S_{\text{off}}$). These parametric images were used to evaluate the signal enhancement over a 2 mm^2 ROI in the region of the duodenum. Image superimposition was carried out with Amira.

3. RESULTS

3.1. Overhauser Switch Caused by the Nitroxide-Labeled Elastin Proteolysis

The concept of Overhauser switch has been described elsewhere (12). It is based upon OMRI-invisible nitroxide-labeled macromolecules that can generate strong Overhauser enhancements upon cleavage. Figure 2 and Table 2 display some characteristics of the undigested and the digested nitroxide-labeled elastin. The peak-to-peak linewidth of the observable EPR spectra in Fig. 2(A) revealed a measured value of 1.22 Gauss for the digested elastin, which was narrower compared with 1.77 Gauss for the undigested species. Furthermore, the peak-to-peak amplitudes were nearly 8-times increased upon peptide breakdown with porcine pancreatic elastase. Such a behavior was previously observed (13) and can be explained by a marked line broadening when the nitroxide is grafted on a slow rotating macromolecule (13). The observable EPR spectrum was probably due to some mobile nitroxides, although covalently bound to the elastin moiety. This observable fraction represented $<10\%$ of the total spectrum of the undigested nitroxide-labeled elastin. As seen from Fig. 2(B), at any concentration used (up to 18 mM nitroxide), the undigested nitroxide-labeled elastin was unable to generate any significant Overhauser enhancement (note that image windowing in Fig. 2B changed from left to right for a better reading). Inefficient dynamic nuclear polarization can be due to a very low saturation factor. Indeed, the microwave magnetic field amplitude used here was in the range of 0.4 Gauss. From an estimated electron T_1 -value of 350 ns, as already described (21) and a T_2 -value of 11 ns as estimated from a 10-Gauss EPR-linewidth for the non-mobile nitroxides, the saturation factor would be $<20\%$, compared with 60–70% for the free nitroxide. Moreover, a decrease in the coupling factor can be expected upon lowering the correlation time of the nitroxide (16), and can significantly contribute to low dynamic nuclear polarization.

Conversely, as observed in Fig. 2(B), Overhauser effect was significant after digestion by elastase. An Overhauser enhancement of 10.9-fold was triggered by the presence of elastase in the sample containing the stock solution, that is, 18 mM (corresponding to the blue circle number 1). These OMRI images showed beyond doubt that Overhauser enhancements were only due to proteolysis, validating the use of this substrate as a specific proteolysis probe. As a result, this Overhauser switch was then evaluated *in vivo* to visualize intestinal digestion.

3.2. *In Vivo* Imaging of Elastin Proteolysis

At about 10–15 min post oral gavage of 200 μl of nitroxide-labeled elastin titrated at 18 mM nitroxide, the first 3D gradient echo image was acquired, and the correct positioning of the mouse was confirmed by the positive T_1 -contrast owing to the presence of the substrate in the stomach. A keyhole 3D OMRI TrueFISP image with EPR irradiation was then acquired in 18 s. Intestinal proteolysis was detected via an Overhauser-enhanced signal, which delineated a high-contrast zone in the mouse's intestinal tract. Following this acquisition, an identical image without HF irradiation was obtained. It showed a normal T_1/T_2 contrast of the substrate in the stomach and no signal enhancement neither in the intestinal tract nor in the stomach. After keyhole reconstruction, fully resolved 3D OMRI images with a spatial resolution of $500 \times 500 \times 500 \mu\text{m}^3$ were computed. Highly resolved anatomical 3D FLASH images were also recorded in order to localize the enhanced NMR signal of the digested substrate. Actually, the T_1 -contrast provided by the nitroxides, allowed the delineation of the stomach and parts of the intestinal tract. The contrast-to-noise (CNR) ratio in the stomach compared to the liver was 6.2 ± 1.8 ($n=7$).

In Fig. 3, a series of partitions of reconstructed images are depicted for a particular mouse. The first and third rows (Fig. 3) show different slices of an anatomic 3D-FLASH image acquired in 17 min, 34 min post oral gavage with a spatial resolution of 0.5 mm in three dimensions. Here, the CNR of the stomach relative to the abdomen was 6.9. The second and fourth rows show the same partitions of the keyhole-reconstructed 3D OMRI image slices with HF irradiation, about 22 min after oral gavage. They revealed that the Overhauser signal enhancement originated from several regions corresponding to the intestinal tract and not from the stomach, strongly suggesting that proteolysis of the nitroxide-labeled elastin occurred through the action of the pancreatic proteases only. In the particular example shown in Fig. 3, the signal increase owing to the Overhauser effect was 5.7 ± 1.4 over an ROI of 2 mm^2 at the opening of the duodenum. The maximal enhancement value was 8.6 in this region. Further down the intestinal tract, Overhauser enhancements ranging from 3.1 ± 0.8 to 4.3 ± 0.4 were measured over 2 mm^2 ROIs.

In the seven-mouse cohort investigated, the maximum enhancements (7.2 ± 2.4) were found as expected at the opening of the duodenum where the pancreatic juice is first secreted by the exocrine pancreatic cells. An example is shown in Fig. 4(A), where the Overhauser enhancement was 7.3 ± 1.6 . In each case, 3D superimposed images were obtained from the anatomical 3D-FLASH images and the reconstructed 3D keyhole OMRI-TrueFISP images. This image overlay validated the correct localization of the Overhauser enhanced signal (Fig. 4A) within the digestive tract of the mouse. Furthermore, at various time intervals after gavage, OMRI images were acquired to observe the outcome of the digested elastin.

In control experiments, a typical free nitroxide, the 3-carboxyproxyl free radical was administered in the mouse's stomach (200 μl at 18 mM) and OMRI images were acquired at several time intervals. After data reconstruction, parametric mapping showed a maximum enhancement of 5.5 ± 0.2 in the stomach, 4.6 ± 0.1 in the duodenum and 5.6 ± 2.6 in the urinary bladder ($n=2$, data not shown). In one experiment, *in vitro* digested nitroxide-labeled elastin (200 μl at 18 mM, expressed as nitroxide concentration) was orally administered in a mouse and the Overhauser

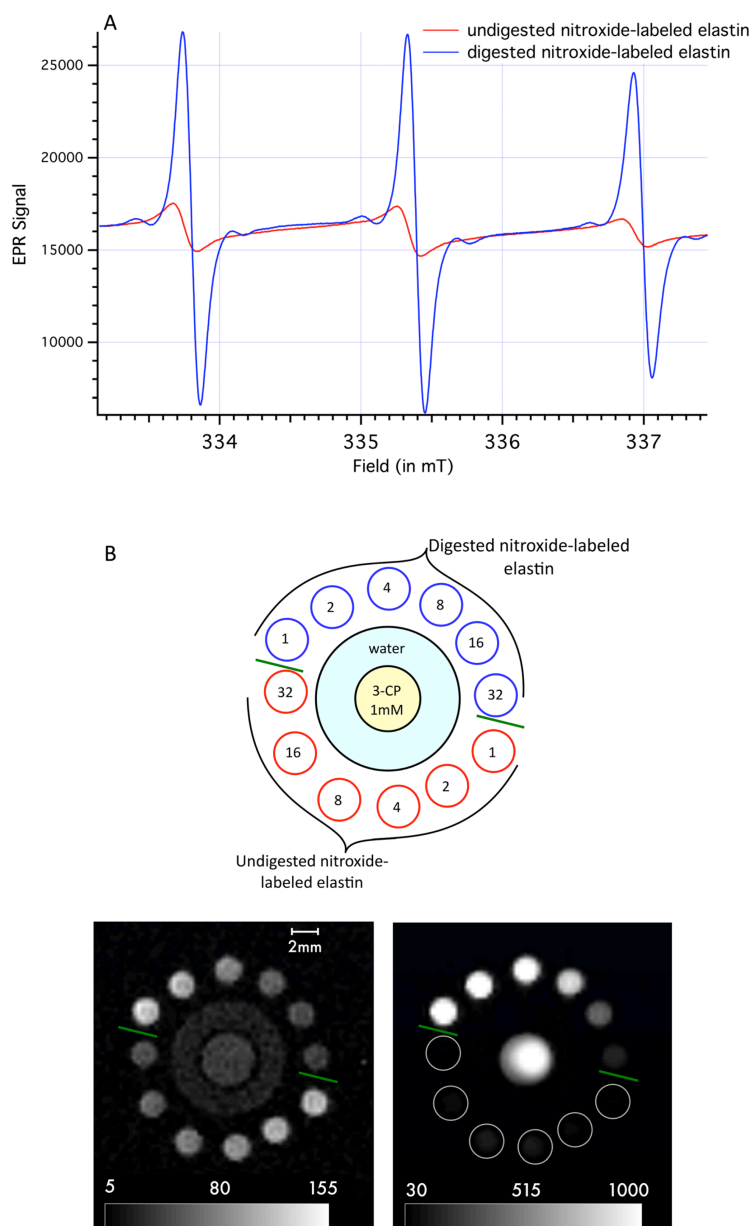


Figure 2. (A) EPR spectra of nitroxide-labeled elastin (18 mM nitroxide concentration) before (red) and after (blue) digestion by elastase. Both spectra were recorded with the same spectrometer adjustments. (B) *In vitro* Overhauser-enhanced MRI (OMRI) of proteolysis. Top: sketch of the 12 tubes containing nitroxide-labeled elastin at different dilutions factors (1,2,4,8,16,32) before (red tubes) and after (blue tubes) digestion by elastase. The central sample was a control tube with the protein-free nitroxide, 3-CP at 1 mM. Bottom: slices of 2D images recorded without (bottom left) and with (bottom right) EPR saturation. A different image windowing was used in the EPR-off image (from 5 to 155 without EPR saturation) and in the EPR-on (from 30 to 1000).

enhancement was of 10.9 in the stomach and 5.3 in the intestine (Fig. 4B). These results confirmed that the Overhauser effect could be observed in the stomach, the intestine and the bladder.

However, whenever nitroxide-labeled elastin was used *in vivo*, the Overhauser effect was visible only in the intestines highlighting a real specificity of the substrate.

	EPR		Water proton	OMRI
	Peak-to-peak line width of the central field lines (in Gauss)	Peak-to-peak amplitudes of the central/high field lines	Spin-lattice relaxivity, r_1 (in $s^{-1} mm^{-1}$)	Signal amplification = S_{on}/S_{off}
Undigested nitroxide-labeled elastin	1.77	2704/1504	0.49 ± 0.01	0.24
Digested nitroxide-labeled elastin	1.22	20496/16528	0.34 ± 0.01	10.9

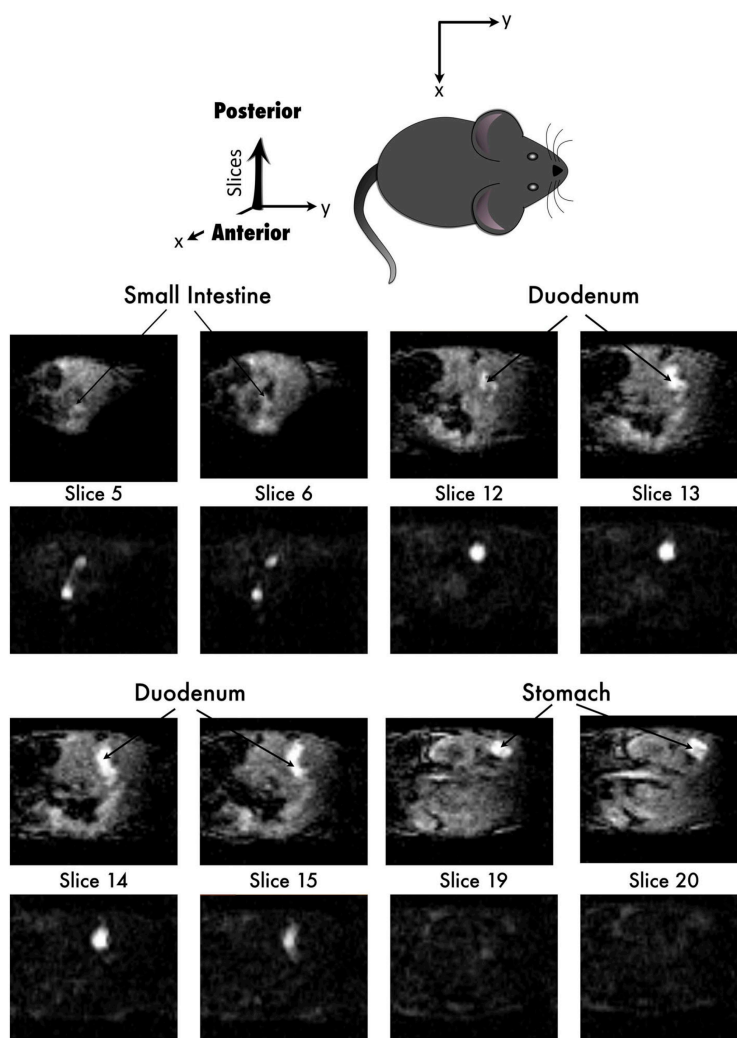


Figure 3. *In vivo* OMRI of proteolysis. On top, a sketch of a mouse viewed from the top in the xy -plane and a z -plane for the different image partitions going from anterior to posterior. Below, the partitions extracted from 3D-FLASH anatomical images (first and third rows, 34 min post gavage) and corresponding reconstructed 3D keyhole OMRI-TrueFISP images (second and fourth rows, 22 min post-gavage) of the same mouse. Note the positive T_1 -contrast in the FLASH images, denoting the presence of nitroxide and delineating the stomach and the duodenum.

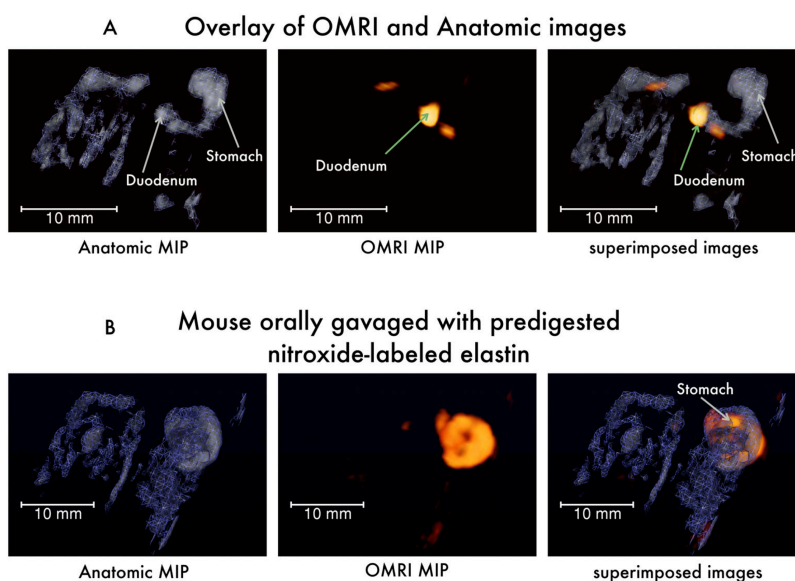


Figure 4. *In vivo* proteolysis localization. (A) Color maps of maximal-intensity-projections (MIP) of Overhauser signal amplification superimposed with MIP of anatomical 3D-FLASH images. (B) A control experiment on a mouse having pre-digested nitroxide-labeled elastin administered orally. Color map of the MIP of 3D-FLASH anatomical image (left), reconstructed 3D keyhole OMRI-TrueFISP of the same mouse (middle) 26 min post-gavage and superimposed MIPs (right).

4. DISCUSSION

The main goal of the present study was to translate *in vivo* the concept of DNP-enhanced MRI of proteolysis, initially demonstrated *in vitro* (12,13). This concept relies on the use of an Overhauser switch brought about by an EPR signature modulated by the tumbling correlation time and a double-resonance MRI system operating at 0.2 T, which is compatible with animal safety (17). In a more general context of molecular imaging of proteolysis and keeping in mind the importance of disease-associated protease as potential therapeutic target, the first step was to assess physiological proteolysis. An obvious candidate was digestive proteolysis occurring post oral gavage.

In this study, OMRI of the mouse's abdomen with a spatial resolution of $0.5 \times 0.5 \times 0.5 \text{ mm}^3$ in less than 20 s acquisition time was achieved, that is, five times quicker compared with our previous study (17). This time-efficiency was made possible by the use of the keyhole paradigm applied to the TrueFISP sequence. The sequential acquisition of partial k -space was shown to be quite useful for real-time contrast assessment in the whole body of rodents (22). Keyhole acquisition permitted 3D-OMRI to be performed over long periods without animal overheating. In literature OMRI has also been used for several biological applications (bio-distribution, pH or oxymetry measurements) with various free radicals, but with one exception (23), images of mouse or rats were acquired in two dimensions with slice thicknesses that were not lower than 5 mm (24–29).

Here, the Overhauser enhancement values are given as the ratio of signal intensities. However, taking into account the 180° phase shift in the case of electron–proton dipolar interaction, the signal amplitude enhancement values are in fact

negative, except for enhancements ranging from 0 to 1. Under such conditions, the ratio of signal intensities cannot be unambiguously interpreted, which could be problematic in pharmacokinetic studies. In this study, very low Overhauser effects were indeed not easily detectable *in vivo* and the work focused on significant, hence interpretable, Overhauser enhancements induced by proteolysis.

Although porcine pepsin is able to partially degrade and solubilize insoluble elastin (30), the murine gastric enzymes seem unable to degrade soluble elastin significantly *in vivo*. No Overhauser effect was detected in the stomach and positive effects were observed at the onset of duodenum and farther downstream. This result clearly indicated that neither gastric enzymes like pepsin nor an acidic medium was able to cleave the substrate. This is easily explained by the nature of the starting material of our substrate, which is a chemically and partially hydrolyzed elastine derivative with a size distribution going from 6000 to 60 000 kDa. Interestingly, proteolysis of elastin by porcine gastric pepsin yields peptides with a similar size distribution (31) and, unlike pancreatic or neutrophil elastase, it is not able to further hydrolyze elastin. Murine pepsin seems to act similarly *in vivo*. Consequently, our substrate happens to be specific for the pancreatic proteolytic activity. Most of the Overhauser enhancements were situated in a region corresponding to the junction of the pancreatic duct to the duodenum (Figs 3 and 4A). Among the proteolytic enzymes present in the pancreatic juice, mammal elastases are known to actively hydrolyze the elastin-based substrate and act synergistically with the other proteases (13). The digested elastin seemed to be quickly absorbed or diluted throughout the intestines since no enhanced signal was visualized farther away

in the intestinal tract and no sign of accumulation was seen in the urinary bladder. The presence of nitroxides induced no observable adverse effects on mouse behavior or mortality, emphasizing the intrinsic low toxicity of stable nitroxides previously observed (17).

Most studies preferentially exploit optical imaging when it comes to studying biological molecular processes *in vivo* (7,32–35). However, this imaging technique mainly offers shallow wave penetration and little anatomical information. Regarding sensitivity level, techniques like optical imaging, SPECT and PET are far ahead of MRI in micromolar-to-nanomolar detection. However, it is shown here that the Overhauser effect improved MRI sensitivity. Maximal signal increase in the duodenum was observed at the start of the digestion (about 20–30 min post oral administration), that is, at a period of very partial stomach emptying (36,37). Thus, small amounts of nitroxides were detected upon proteolysis. Signal amplification of ca. 7 would correspond to free nitroxide concentrations lower than 1 mM, as assessed from dose–response curves measured *in vitro* (not shown).

In conclusion, the proof-of-concept of protease imaging *in vivo* using an Overhauser switch has been successfully demonstrated. Work is in progress to translate this approach to disease-associated protease detection in mice. With the help of proper Overhauser switches, protease imaging could be used in the bio-medical field for diagnosis, drug-testing of protease inhibitors and therapy follow-up. Future advances in this domain would be the synthesis of molecular beacons made from a specific polypeptide sequence to target each of the numerous over-expressed disease-related proteases such as the matrix metalloproteinase MMP-9 and MMP-2 or the cysteine protease cathepsin B in solid tumours, and the serine proteases neutrophil elastase, cathepsin G and proteinase 3 in inflammation and cystic fibrosis. OMRI has the potential to be integrated into drug-development programs both to facilitate the functional validation of pharmaceutical targets and to monitor the spatial and temporal distribution of proteins and bioorganic molecules dynamically in whole animal, even if the transition of this technique to the treatment of human disease would require field-cycling (38,39) or low-field (40) approaches.

Acknowledgments

This study was supported by a public grant from the French 'Agence Nationale de la Recherche', grant number Blanc_09_434420, and within the context of the Investments for the Future Program, referenced ANR-10-LABX-57 and named TRAIL and with the support of the Regional Council of Aquitaine, France.

REFERENCES

- Kircher MF, Willmann JK. Molecular body imaging: MR imaging, CT, and US. Part I. principles. *Radiology* 2012; 263(3): 633–643.
- Kircher MF, Willmann JK. Molecular body imaging: MR imaging, CT, and US. Part II. Applications. *Radiology* 2012; 264(2): 349–368.
- Skotland T. Molecular imaging: challenges of bringing imaging of intracellular targets into common clinical use. *Contrast Media Mol Imag* 2012; 7(1): 1–6.
- Law B, Tung CH. Proteolysis: a biological process adapted in drug delivery, therapy, and imaging. *Bioconjug Chem* 2009; 20(9): 1683–1695.
- Southan C A genomic perspective on human proteases as drug targets. *Drug Discov Today* 2001; 6(13): 681–688.
- Choi KY, Swierczewska M, Lee S, Chen X. Protease-activated drug development. *Theranostics* 2012; 2(2): 156–178.
- Ntziachristos V, Tung CH, Bremer C, Weissleder R. Fluorescence molecular tomography resolves protease activity *in vivo*. *Nat Med* 2002; 8(7): 757–760.
- Waschkau B, Faust A, Schafers M, Bremer C. Performance of a new fluorescence-labeled MMP inhibitor to image tumor MMP activity *in vivo* in comparison to an MMP-activatable probe. *Contrast Media Mol Imag* 2013; 8(1): 1–11.
- Kossodo S, Zhang J, Groves K, Cuneo GJ, Handy E, Morin J, Delaney J, Yared W, Rajopadhye M, Peterson JD. Noninvasive *in vivo* quantification of neutrophil elastase activity in acute experimental mouse lung injury. *Int J Mol Imag* 2011; 2011: 581406.
- Graves EE, Weissleder R, Ntziachristos V. Fluorescence molecular imaging of small animal tumor models. *Curr Mol Med* 2004; 4(4): 419–430.
- Matusiak N, Waarde A, Bischoff R, Oltenfreiter R, Wiele C, Dierckx RA, Elsinga PH. Probes for non-invasive matrix metalloproteinase-targeted imaging with PET and SPECT. *Curr Pharm Des* 2013; 19(25): 4647–4672.
- Mellet P, Massot P, Madelin G, Marque SR, Franconi JM, Thiaudiere E. New concepts in molecular imaging: non-invasive MRI spotting of proteolysis using an Overhauser effect switch. *PLoS One* 2009; 4(4): e5244.
- Parzy E, Bouchaud V, Massot P, Voisin P, Koonjoo N, Moncelet D, Franconi JM, Thiaudiere E, Mellet P. Overhauser-enhanced MRI of elastase activity from *in vitro* human neutrophil degranulation. *PLoS One* 2013; 8(2): e57946.
- Lurie DJBD, Bell LH, Mallard JR. Proton-electron double resonance imaging of free radicals solutions. *J Magn Reson* 1988; 76: 366–370.
- Overhauser A. Polarization of nuclei in metals. *Phys Rev* 1953; 92(2): 411–415.
- Bennati M, Luchinat C, Parigi G, Törke MT. Water 1H relaxation dispersion analysis on a nitroxide radical provides information on the maximal signal enhancement in Overhauser dynamic nuclear polarization experiments. *Phys Chem Chem Phys* 2010; 12(22): 5902–5910.
- Massot P, Parzy E, Pourtau L, Mellet P, Madelin G, Marque S, Franconi JM, Thiaudiere E. *In vivo* high-resolution 3D overhauser-enhanced MRI in mice at 0.2 T. *Contrast Media Mol Imag* 2012; 7(1): 45–50.
- Oppelt AGR, Barfuß H, Fischer H, Hartl W, Schajor W. FISP – a new fast MRI sequence. *Electromedica (Engl Edn)* 1986; 54: 15–18.
- Haase A, Frahm J, Matthaei D, Hancike W, Merboldt KD. FLASH imaging: rapid NMR imaging using low flip-angle pulses. *J Magn Reson* 1986; 213(2): 533–541.
- van Vaals JJ, Brummer ME, Dixon WT, Tuithof HH, Engels H, Nelson RC, Gerety BM, Chezmar JL, den Boer JA. 'Keyhole' method for accelerating imaging of contrast agent uptake. *J Magn Reson Imag* 1993; 3(4): 671–675.
- Turke MT, Tkach I, Reese M, Hofer P, Bennati M. Optimization of dynamic nuclear polarization experiments in aqueous solution at 15 MHz/9.7 GHz: a comparative study with DNP at 140 MHz/94 GHz. *Phys Chem Chem Phys* 2010; 12(22): 5893–5901.
- Bled E, Hassen WB, Pourtau L, Mellet P, Lanz T, Schuler D, Voisin P, Franconi JM, Thiaudiere E, Miraux S. Real-time 3D MRI of contrast agents in whole living mice. *Contrast Media Mol Imag* 2011; 6(4): 275–281.
- Sarracanie M, Armstrong BD, Stockmann J, Rosen MS. High speed 3D Overhauser-enhanced MRI using combined b-SSFP and compressed sensing. *Magn Reson Med* 2013. doi: 10.1002/mrm.24705
- Golman K, Leunbach I, Ardenkjaer-Larsen JH, Ehnholm GJ, Wistrand LG, Petersson JS, Jarvi A, Vahasalo S. Overhauser-enhanced MR imaging (OMRI). *Acta Radiol* 1998; 39(1): 10–17.
- Grueter D. *In vivo* detection of injected free radicals by Overhauser effect imaging. *Magn Reson Med* 1990; 14(1): 140–147.
- Li H, Deng Y, He G, Kuppusamy P, Lurie DJ, Zweier JL. Proton electron double resonance imaging of the *in vivo* distribution and clearance of a triaryl methyl radical in mice. *Magn Reson Med* 2002; 48(3): 530–534.
- Li H, He G, Deng Y, Kuppusamy P, Zweier JL. *In vivo* proton electron double resonance imaging of the distribution and clearance of nitroxide radicals in mice. *Magn Reson Med* 2006; 55(3): 669–675.
- Lurie DJ, Li H, Petryakov S, Zweier JL. Development of a PEDRI free-radical imager using a 0.38 T clinical MRI system. *Magn Reson Med* 2002; 47(1): 181–186.
- Seimenis I, Foster MA, Lurie DJ, Hutchison JM, Whiting PH, Payne S. The excretion mechanism of the spin label proxyl carboxylic acid (PCA) from the rat monitored by X-band ESR and PEDRI. *Magn Reson Med* 1997; 37(4): 552–558.

30. Collins JF, Fine R. The enzymatic digestion of elastin at acidic pH. *Biochim Biophys Acta* 1981; 657(1): 295–303.
31. Hattori M, Yamaji-Tsukamoto K, Kumagai H, Feng Y, Takahashi K. Antioxidative activity of soluble elastin peptides. *J Agric Food Chem* 1998; 46(6): 2167–2170.
32. Weissleder R, Tung CH, Mahmood U, Bogdanov A Jr. *In vivo* imaging of tumors with protease-activated near-infrared fluorescent probes. *Nat Biotechnol* 1999; 17(4): 375–378.
33. Bremer C, Bredow S, Mahmood U, Weissleder R, Tung CH. Optical imaging of matrix metalloproteinase-2 activity in tumors: feasibility study in a mouse model. *Radiology* 2001; 221(2): 523–529.
34. Calton MA, Rosenthal A, Mallas G, Mauskopf A, Nudelman RN, Ntziachristos V, Jaffer FA. *In vivo* near infrared fluorescence (NIRF) intravascular molecular imaging of inflammatory plaque, a multimodal approach to imaging of atherosclerosis. *J Vis Exp* 2011; (54): 2257.
35. Mahmood U, Tung CH, Bogdanov A Jr, Weissleder R. Near-infrared optical imaging of protease activity for tumor detection. *Radiology* 1999; 213(3): 866–870.
36. Schwarz R, Kaspar A, Seelig J, Kunnecke B. Gastrointestinal transit times in mice and humans measured with 27Al and 19F nuclear magnetic resonance. *Magn Reson Med* 2002; 48(2): 255–261.
37. Watanabe J, Okabe H, Ichihashi T, Mizojiri K, Yamada H. Gastric emptying rate constants after oral administration of drug solution to mice, rats, and rabbits. *Chem Pharm Bull (Tokyo)* 1977; 25(9): 2147–2155.
38. Lurie DJ, Davies GR, Foster MA, Hutchison JM. Field-cycled PEDRI imaging of free radicals with detection at 450 mT. *Magn Reson Imag* 2005; 23(2): 175–181.
39. Krishna MC, English S, Yamada K, Yoo J, Murugesan R, Devasahayam N, Cook JA, Golman K, Ardenkjaer-Larsen JH, Subramanian S, Mitchell JB. Overhauser enhanced magnetic resonance imaging for tumor oximetry: coregistration of tumor anatomy and tissue oxygen concentration. *Proc Natl Acad Sci U S A* 2002; 99(4): 2216–2221.
40. Zotev VS, Owens T, Matlashov AN, Savukov IM, Gomez JJ, Espy MA. Microtesla MRI with dynamic nuclear polarization. *J Magn Reson* 2010; 207(1): 78–88.

3.3 Characterization of a new type of OMRI contrast agent – *in vitro* and *in vivo* studies

3.3.1 Aims of this study

A chemistry research team in the Institute for Radical Chemistry - UMR7273 in Marseille, France synthesised a new type of nitroxide in view for OMRI proteolytic activity detection. The main goal of this work was to validate the use of this nitroxide *in vitro* and also *in vivo* in small animals.

In so doing, the nitroxide was first characterized through EPR spectra and then subjected to a variety of enzymatic activities. Both EPR and OMRI were performed. Then through gavage administration in mice, the nitroxide was made to react with the enzymes found in the digestive tract.

With its unique resonant frequency shifting of its EPR lines upon hydrolysis of the nitroxide, both the substrate and the product were detectable on the EPR spectra. These simultaneous detection using OMRI was confirmed *in vitro* and *in vivo*.

Eventually, all the results were put together in the following paper in the *Angewandte Chemie International Edition Journal* this year. (Note : the article has already been accepted. However, the version below is not the final one as it is still under correction.)

3.3.2 Article 3

Finally for this final article, apart from the chemical nitroxide synthesis, I conducted all experiments *in vitro* as well as *in vivo*. I also largely contributed in the writing of the scientific article.

It may somehow be notified that *Angewandte Chemie International Edition Journal* is a well established chemistry journal and generally the authors are listed in alphabetical order.

In Vivo Imaging

International Edition: DOI: 10.1002/anie.201506267
German Edition: DOI: 10.1002/ange.201506267

Enzymatically Shifting Nitroxides for EPR spectroscopy and Overhauser-Enhanced Magnetic Resonance Imaging

Gérard Audran,* Lionel Bosco, Paul Brémond,* Jean-Michel Franconi, Neha Koonjoo, Sylvain R. A. Marque,* Philippe Massot, Philippe Mellet,* Elodie Parzy, and Eric Thiaudière*

In memory of J.-P. Finet

Abstract: *In vivo* investigations of enzymatic processes using non-invasive approaches are a long-lasting challenge. Recently, we showed that Overhauser-enhanced MRI is suitable to such a purpose. A β -phosphorylated nitroxide substrate prototype exhibiting keto–enol equilibrium upon enzymatic activity has been prepared. Upon enzymatic hydrolysis, a large variation of the phosphorus hyperfine coupling constant ($\Delta a_p = 4$ G) was observed. The enzymatic activities of several enzymes were conveniently monitored by electronic paramagnetic resonance (EPR). Using a 0.2 T MRI machine, *in vitro* and *in vivo* OMRI experiments were successfully performed, affording a 1200% enhanced MRI signal *in vitro*, and a 600% enhanced signal *in vivo*. These results highlight the enhanced imaging potential of these nitroxides upon specific enzymatic substrate-to-product conversion.

In recent years, dynamic nuclear polarization (DNP) has experienced a revival owing to bisnitroxide molecules as they can afford a dramatic OMR signal enhancement.^[1] However, its application *in vivo* is still severely limited owing to its lack of selectivity toward biological processes. Furthermore, because the resonance frequency of the free electron is 660 times higher than that of the proton, free electrons require irradiation with high frequencies. Those are hardly compatible with imaging in living animals because the energy

deposition is too high and wave penetration too shallow. In parallel, in the field of molecular imaging, anatomical magnetic resonance imaging (MRI) is growing into one of the most powerful non-invasive techniques for its high contrast in deeply-seated soft tissues, good spatial and temporal resolution, and its ability to diagnose pathological conditions. Nevertheless, the lack of sensitivity and non-selective contrasting agents hampers the use of MRI, particularly in the study of enzymatic processes occurring *in vivo*.

Proteases are a family of enzymes with a large variety of potential for diagnosis. Proteolytic activity is tightly regulated in space and time in normal tissues and thus is kept at low level and for short periods of time. However, they exhibit a persistent and specific activity in a number of diseases, such as solid tumors, pancreatitis, chronic obstructive pulmonary disease, cystic fibrosis, rheumatoid arthritis, and many inflammatory situations. Imaging these activities would offer an opportunity for early diagnosis independent of the anatomical alterations, which often appear later.^[2–5] Recently, our groups highlighted the potential of the OMRI technique^[6,7] at 0.2 T to detect and visualize a naturally occurring proteolytic activity in the digestive tract of living mice.^[8–10] Herein, our new approach requires a nitroxide probe exhibiting changes in the hyperfine coupling constant larger than one Gauss upon enzymatic hydrolysis. To our knowledge, no nitroxides exhibit such a large frequency shift upon chemical or biological changes at physiological pH and temperature.^[11–16] Previous reports of the use of nitroxides as probes relied on the changes in the nitrogen hyperfine coupling constant a_N or on the line width.^[17] On the other hand, β -hyperfine coupling constants are known to be highly sensitive to conformational changes.^[18] Thus, we chose to focus on the synthesis of β -phosphorylated nitroxides **9** and **10**, which exhibit exo- and intracyclic double bonds (Scheme 1). The EPR features of nitrogen and phosphorus hyperfine coupling constants (a_N and a_P , respectively) were investigated, as well as the kinetics of hydrolysis of **10** into **9** in the presence of various enzymes. The potential of **9** and **10** as polarizing agents was explored through *in vitro* and *in vivo* OMRI experiments (Figure 1).

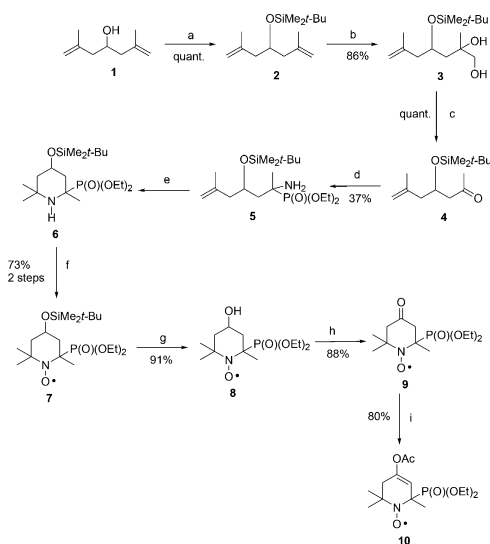
Nitroxide **9** was prepared in eight steps (Scheme 1) starting from the commercially available 2,6-dimethyl-4-hydroxy-hept-1,6-diene **1**. The regioselectivity of the formation of the intracyclic double bond to afford **10**^[19] was controlled by using a bulky base, potassium hexamethyldi-

[*] Prof. G. Audran, L. Bosco, Dr. P. Brémond, Prof. S. R. A. Marque
Aix-Marseille Université, CNRS, ICR, UMR 7273
Case 551, Avenue Escadrille Normandie-Niemen,
13397 Marseille Cedex 20 (France)
E-mail: g.audran@univ-amu.fr
paul.bremond@univ-amu.fr
sylvain.marque@univ-amu.fr

Prof. J.-M. Franconi, N. Koonjoo, P. Massot, Dr. P. Mellet,
Dr. E. Parzy, Prof. E. Thiaudière
Centre de Résonance Magnétique des Systèmes Biologiques,
UMR 5536 CNRS, Case 93,
University Bordeaux Segalen
146 rue Leo Saignat, 33076 Bordeaux Cedex (France)
E-mail: jean-michel.franconi@rmsb.u-bordeaux2.fr
eric.thiaudiere@rmsb.u-bordeaux2.fr

Dr. P. Mellet
INSERM
33076 Bordeaux Cedex (France)
E-mail: philippe.mellet@rmsb.u-bordeaux2.fr

Supporting information and experimental data for this article is available on the WWW under <http://dx.doi.org/10.1002/anie.201506267>.



Scheme 1. Preparation of **9** and **10**. a) DMF, imidazole, *tert*-butyldimethylsilyl chloride (TBDMSCl), 5 h, 0 °C; b) (1) OsO₄, acetone/water, 15 min, 0 °C; (2) *N*-methylmorpholine-*N*-oxide (NMO), 4 h, 0 °C. c) NaIO₄, THF/water (1:3, v/v), 3 h, 0 °C. d) HP(O)(OEt)₂, 4 Å M.S.. e) (1) Hg(OAc)₂, THF/water (1:3, v/v), 30 min, r.t.; (2) NaBH₄, NaOH (1 M). f) *meta*-chloroperoxybenzoic acid (mCPBA), CH₂Cl₂, 2 h, 0 °C. g) TBAF, THF, 3 h, 0 °C. h) NMO, TPAP, 4 Å M.S., CH₂Cl₂, 0 °C. i) (1) LiHMDS, THF, 3 h, -80 °C to -45 °C; (2) Ac₂O, 2.5 h, -45 °C.

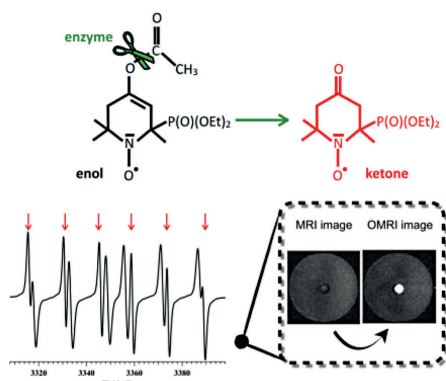


Figure 1. Nitroxides with different EPR signatures to target enzymatic processes with EPR and/or OMRI techniques *in vitro* and *in vivo*.

lazane (KHMDS), which reacted with the most acidic protons (see the Supporting Information).

EPR features are reported in Table 1 and Figure 2, and are in very good agreement with previously reported data.^[18] Interestingly, nitroxide **10** (intracyclic double bond) exhibits an a_p value 4.4 G smaller than the one of **9** (exocyclic double bond). Moreover, linewidths are narrow enough for OMRI

experiments.^[10] Owing to this difference in their a_p values, their spectra are sufficiently resolved to avoid peak overlapping, thus allowing individual quantification of the products in a 1:1 mixture of **9** and **10** (Figure 2).

Table 1: EPR parameters of nitroxides **9** and **10**.

Nitroxides	a_N [G] ^[a]	a_p [G] ^[a]	g ^[b]	ΔH_{pp} [G] ^[a,d]
9	15.0	43.1	2.0062	1.2
10	15.6	38.7	2.0063	1.8

[a] 1 G = 0.1 mT. [b] Landé's factor. [c] Linewidth peak to peak for the central lines.

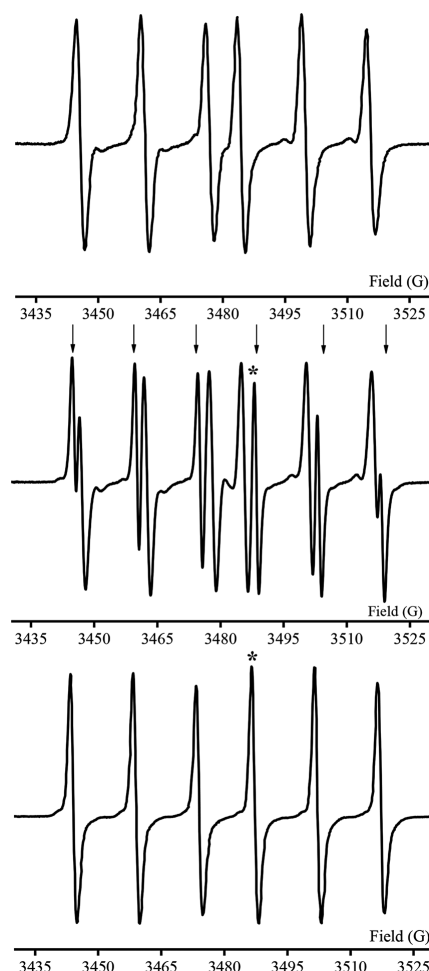


Figure 2. EPR signals of **10** (top) and **9** (bottom) and a 1:1 mixture of **9/10** (middle; arrows are for lines of **9**). The starred line in the EPR signal of **9** was used for electronic spin excitation for OMRI.

Enzymatic activity assays were carried out *in vitro* using the EPR technique to monitor the keto–enol hydrolysis. After an incubation time of 5 h and quantification of the third EPR line for **9**, out of 8 proteases of various specificities and origin, three were able to hydrolyze **10** into **9**, namely, porcine pancreatic elastase (PPE), human neutrophil elastase (HNE) and subtilisin A (Figure 3). Subtilisin A was selected for further experiments because of it displayed the highest activity (95 % hydrolysis in 5 h).

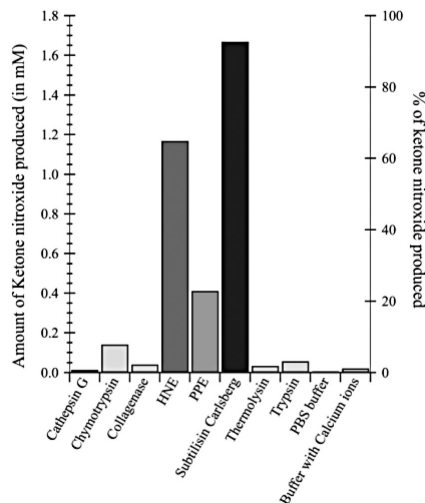


Figure 3. Efficiency of various enzymes as well as of PBS buffer and Ca^{2+} PBS buffer in hydrolysis of 1.8 mM of **10** into **9** for 5 h incubation. y-axis in mM (left) and % converted (right).

The kinetics of the consumption of substrate **10** consumption, and the formation of product **9** were monitored to complete hydrolysis (Figure 4). The half-life, $t_{1/2}$ was measured at 74 min with a substrate concentration of 1.1 mM and subtilisin A concentration of 2.8 μM . Given that the Michaelis–Menten condition of $[\text{S}] \ll K_m$ was fulfilled at substrate concentrations ranging from 0.3 to 1.1 mM, the catalytic constant, k_{cat}/K_m was $55 \text{ M}^{-1} \text{ s}^{-1}$ at 37°C in saline phosphate buffer pH 7.3. This low value is due to the very partial occupation of the enzyme active site by the small acetyl ligand.^[20] The spontaneous hydrolysis rate at 37°C and pH 7.3 (Figure 4) was not significant during the time of experiment. The rate of increase of **9** in the presence of Eglin C, a natural protease inhibitor from leeches, only showed a slow rate of transformation of **10** into **9** close to the rate of spontaneous hydrolysis, suggesting a complete inhibition of what appears to be a pure enzymatic process.

As already seen above in the EPR spectra, the substrate-to-product conversion revealed a significant coupling shift of about 4G without line overlapping. This molecular characteristic was then transposed into OMRI applications to monitor enzymatic reactions taking place either *in vitro* or *in vivo*. To check whether the non-overlapping condition is valid for

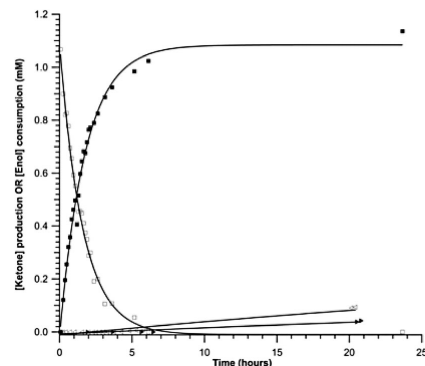


Figure 4. Kinetics for the decay of 1.1 mM of **10** (\square) and the generation of **9** (\blacksquare) in the presence of 2.8 μM of subtilisin A. The generation of **9** in the presence of subtilisin A plus the Eglin C inhibitor (\triangleleft), and spontaneous hydrolysis in PBS buffer solution (\blacktriangleright).

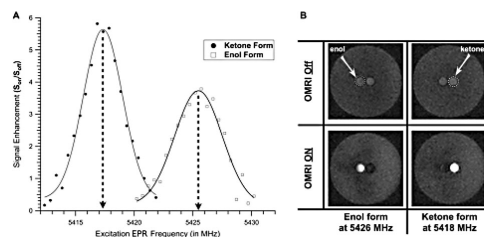


Figure 5. A) Optimal excitation EPR frequency (in MHz) determination and OMRI signal enhancements for **9** (\bullet) and for **10** (\square). B) *In vitro* spotting of **9** (left inserted tube labeled as enol) and (-)-**10** (right inserted tube labeled as ketone). The first row corresponds to the MRI images without electronic saturation and the second row with electronic saturation.

OMRI, the EPR irradiating frequency was swept for both the substrate and the product. The two spectra are shown in Figure 5a. 2D images with and without electronic spin saturation were acquired (data not shown) at different equally spaced EPR frequencies ranging from 5412.35 to 5429.85 MHz for **9** and **10** for a proton frequency of 8.24264 MHz. Thus, the maximal signal enhancements were observed at 5417.3 and 5425.3 MHz for **9** and **10**, respectively. As already seen in Table 1, the EPR line width was narrow enough to observe high signal enhancement on the OMRI images and the Δa_p (ca. 8 MHz, Figure 5a) between the third EPR line of **9** and that of **10** was sufficiently far apart for a selective and distinct electronic EPR saturation for OMRI experiment. *In vitro* experiments (Figure 5b) showed that nitroxides **9** and **10** were selectively spotted at 5417.9 MHz and of 5426.2 MHz, respectively. Consequently, OMRI experiments showed that each sample of **9** and **10** was lit up selectively (Figure 5b). It should be noted that the enhancements observed for **10** were poorer than those for **9**. This result is due to the larger line width of **10** (Table 1).

In vitro OMRI kinetic assays were then carried out to monitor the hydrolysis of (-)-**10** (1.8 mM) in phosphate buffer, pH 7.2 in the presence of subtilisin A (2.8 μ M). The rate of production of **9** from (-)-**10** monitored by irradiating the EPR line highlighted in Figure 6 yielded $t_{1/2} = 69$ min. at 37 °C, a value fairly close to the one obtained by EPR monitoring. The maximum signal enhancement was found to be 11.3 after 20 h of reaction time. These OMRI data agree with those obtained by EPR.

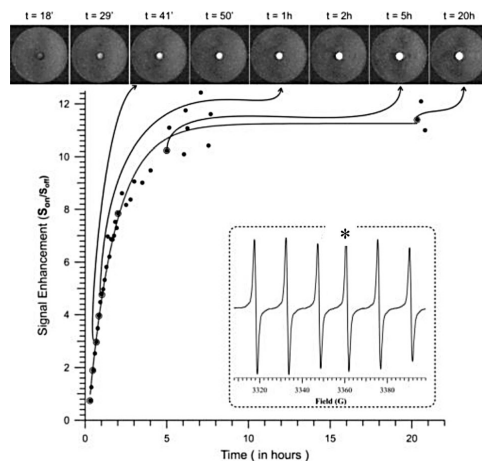


Figure 6. In vitro OMRI monitoring of the hydrolysis of (-)-**10** (1.8 mM) into **9** (bright spot) by subtilisin A (2.8 μ M) in phosphate buffer pH 7.2 at 37 °C. 2D images were acquired at various time intervals with/without EPR frequency saturation tuned at 5417 MHz. Inset: the starred line in the EPR signal of **9** was used for electronic spin excitation for OMRI.

To definitively highlight the potential of **9** and **10** in probing non-radical enzymatic activity, a mouse was fed with a solution of **10** at 24 mM (see the Supporting Information). Anatomical MRI was first performed and confirmed that the stomach was filled with the nitroxide solution (Figure 7A). Then, the first 3D OMRI images were acquired with and without electronic EPR saturation of the nitroxides found in the stomach. The saturation frequency was set at 5425.7 MHz and thereby specifically exciting one electronic transition of **10**. A hypersignal with a maximal signal amplification of 5.7 was visible in the stomach, highlighting the presence of the substrate at about 10 min post-gavage (Figure 7B).

Afterwards, 3D OMRI images were obtained again with and without electronic saturation at the frequency of 5417.5 MHz, corresponding to the equivalent EPR transition line of the product nitroxide **9**. The images revealed that some of the substrate was converted into the ketone product generating a specific high contrast with an 8.5-fold increase at 35 min post-gavage (Figure 7C). Mouse stomach and intestine pH have been measured at 3 and 5, respectively.^[21] The spontaneous hydrolysis of (+)-**10** nitroxide between pH 3 and 7 is not detectable while it is significant at pH of 1 or 9

(Supporting Information, Figure S1). Thus it is the digestive enzymes found in the stomach and/or in the intestine that were able to transform nitroxide **10** into **9**. Clearly, the conformational change from **10** to **9** plays the expected on/off role for selective OMRI experiments affording a powerful tool to investigate in vivo enzymatic processes.

These preliminary results in OMRI show the huge potential of the tautomeric equilibrium between **9** and **10** to investigate non-radical enzymatic processes in vivo using the non-invasive OMRI technique. The primary approach in activity-based molecular imaging has been optical imaging, mainly because of its high sensitivity. MRI is the only one that has high anatomical resolution in 3D, together with no depth limitations and no radiative issues. Furthermore, its poor sensitivity is being handled using the Overhauser effect of **9** and **10** onto the water molecules. In the present study, the signal was enhanced 8.5 times, thus affording a large specific contrast. Here, the in vivo validation was carried out at both substrate and product frequencies using the distinct signatures of each species. Although experiments were performed with only three mice (low statistical reproducibility) and despite that the acetyl nitroxide is a very poor protease substrate compared to usual peptidic substrates, our results confirm unambiguously the feasibility of this approach.

Improvements are still ongoing. Targeting specific disease-related enzymes by grafting enzyme-specific peptides on **10** is expected to enhance k_{cat}/K_M by several orders of magnitude, thus providing both sensitivity and protease specificity.^[22]

Proteases are tightly regulated biomolecules involved in many physiological events, and deregulations in their activities are correlated to various diseases, such as cancer with overwhelming matrix metalloproteinase (MMP) activity, pancreatitis with premature in situ pancreatic protease activation, cystic fibrosis, or chronic obstructive pulmonary disease (COPD) with overwhelming concentration of neutrophil proteases, and multiple sclerosis and rheumatoid arthritis with deleterious MMP activity. The specific nitroxides and imaging technique described here would certainly help for better understanding the function of those overexpressed proteases and their sustaining activities in vivo through monitoring and disease localization. Eventually, drug design against those proteases could also be tested accordingly.

Consequently, there is a need to develop such an application for humans. At 0.2 T Tesla, the 5.5 GHz waves corresponding to the resonance frequency of the electron is suitable for small animals but not for humans because of the poor penetration into tissues. However, it is possible at very low field. For instance, at earth field the electron resonance frequency is about 60 MHz, a usual frequency in clinical MRI. For connection to the anatomical images, two possibilities arise: a field cycling apparatus^[23] or more sensitive detectors.^[24] As a consequence much higher Overhauser enhancements are predicted^[25] and hence a much lower detection limit of the nitroxides.

These nitroxides are also suitable for a broad range of enzymes as the ester moiety can be designed for a particular enzyme, such as by using specific peptides, sugars, or lipids.

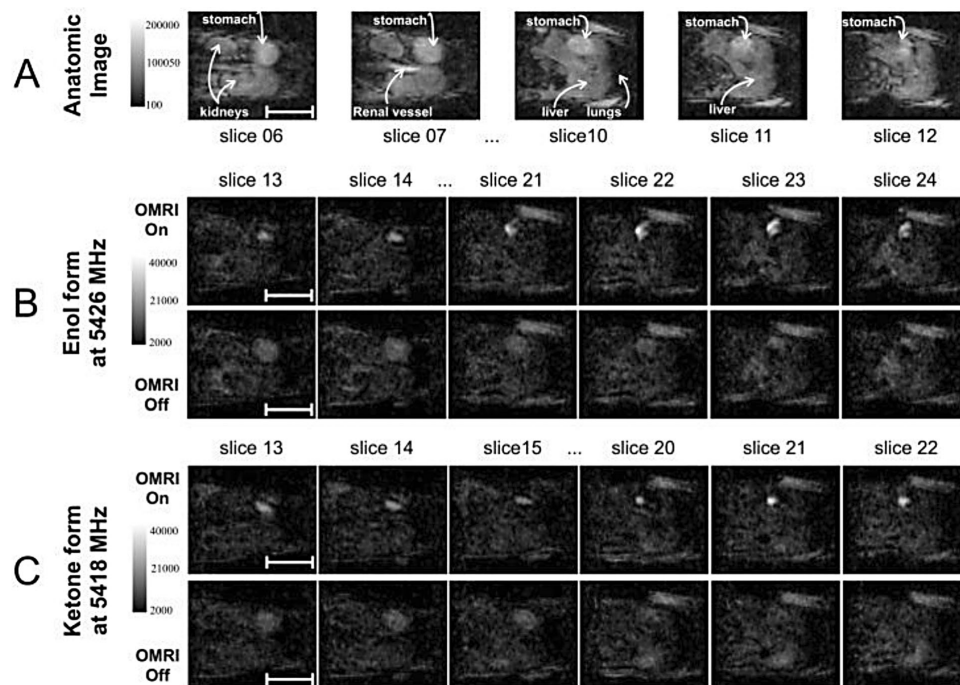


Figure 7. A) 3D anatomical MRI image of the stomach. B) The first row corresponds to the image with electronic saturation at 5425.7 MHz and the slices in the second row are the corresponding non-saturated electronic spins. C) The first row corresponds to the image with an electronic saturation of 5417.5 MHz (first row) and without (second row). All OMRI images were acquired in 18 seconds and then reconstructed into an isotropic spatial resolution of 0.5 mm in all three directions. The anatomical image has a spatial resolution of $0.5 \times 0.54 \times 1 \text{ mm}^3$ and a temporal resolution of about 3.5 min.

These non-exhaustive biomolecules, once grafted onto the nitroxide moiety, can be applied to several enzyme-specific studies including quantification, kinetic constant determination, and drug inhibition tests.^[22]

Acknowledgements

The authors thank CNRS, Aix-Marseille University for A*MIDEX grant (ANR-11-IDEX-0001-02) funded by the Investissements d'Avenir French Government program, managed by the French National Research Agency (ANR), University of Bordeaux 2 for the Labex TRAIL grant (ANR-10-LABX-57) funded by the French National Research Agency (ANR) in the frame of the Investments for the Future Program, within the Cluster of Excellence TRAIL. ANR was granted for funding this project (grants SonRadIs ANR-11-JS07-002-01 and NITROMRI ANR-09-BLA-0017-01). L.B. is thankful to ANR for the Ph.D. fellowship (grant SonRadIs).

Keywords: dynamic nuclear polarization · enzymes · nitroxides · NMR imaging · Overhauser effect

- [1] A. Zagdoun, G. Casano, O. Ouari, M. Schwarzwalder, A. J. Rossini, F. Aussenac, M. Yulikov, G. Jeschke, Ch. Copéret, A. Lesage, P. Tordo, L. Emsley, *J. Am. Chem. Soc.* **2013**, *135*, 12790–12797.
- [2] L. Zhu, J. Xie, M. Swierczewska, F. Zhang, Q. Quan, Y. Ma, X. Fang, K. Kim, S. Lee, X. Chen, *Theranostics* **2011**, *1*, 18–27.
- [3] P. Habibollahi, J. L. Figueiredo, P. Heidari, A. M. Dulak, Y. Imamura, A. J. Bass, S. Ogino, A. T. Chan, U. Mahmood, *Theranostics* **2012**, *2*, 227–234.
- [4] V. Catanzaro, C. V. Gringeri, V. Menchise, S. Padovan, C. Boffa, W. Dastrù, L. Chaabane, G. Digilio, S. Aime, *Angew. Chem. Int. Ed.* **2013**, *52*, 3926–3930; *Angew. Chem.* **2013**, *125*, 4018–4022.
- [5] N. Guyot, J. Wartelle, L. Malleret, A. A. Todorov, G. Devouassoux, Y. Pacheco, D. E. Jenne, A. Belaouaj, *Am. J. Pathol.* **2014**, *184*, 2197–2210.
- [6] D. Grucker, *Magn. Reson. Med.* **1990**, *14*, 140–147.
- [7] K. Golman, J. S. Petersson, J. H. Ardenkjaer-Larsen, I. Leunbach, L. G. Wistrand, G. Ehnholm, K. Liu, *J. Magn. Reson. Imaging* **2000**, *12*, 929–938.
- [8] E. Parzy, V. Bouchaud, P. Massot, P. Voisin, N. Koonjoo, D. Moncelet, J.-M. Franconi, E. Thiaudière, P. Mellet, *PLoS One* **2013**, *8*, 2.
- [9] N. Koonjoo, E. Parzy, P. Massot, M. Lepetit-Coiffé, S. R. A. Marque, J.-M. Franconi, E. Thiaudière, P. Mellet, *Contrast Media Mol. Imaging* **2014**, *9*, 363–371.

All the experimental details are presented as supporting information, SI as seen below
:



Supporting Information

Enzymatically Shifting Nitroxides for EPR spectroscopy and Overhauser-Enhanced Magnetic Resonance Imaging

Gérard Audran, Lionel Bosco, Paul Brémond,* Jean-Michel Franconi, Neha Koonjoo, Sylvain R. A. Marque,* Philippe Massot, Philippe Mellet,* Elodie Parzy, and Eric Thiaudière**

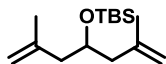
anie_201506267_sm_miscellaneous_information.pdf

All reactants were purchased to Aldrich. NMR analyses were performed on Bruker 300 and 400 Advance machines. Internal references (residual solvent peak) were used for ^1H and ^{13}C NMR shifts δ and ^{31}P NMR shifts δ were given from phosphoric acid (80% H_3PO_4 in water, as internal reference in a capillary). EPR experiments were performed on EMX Bruker machine. Cathepsin G, Collagenase from *Cl. Histolyticum*, Human Neutrophil Elastase (HNE) and Porcine Pancreatic Elastase (PPE) were purchased from Elastin Products company (Missouri, USA). Bovine Trypsin and Chymotrypsin were from Worthington (New Jersey, USA). Subtilisin Carlsberg (Subtilisin A) from *Bacillus licheniformis* and Thermolysin from *Bacillus thermoproteolyticus* were bought from Sigma-Aldrich

Preparation of nitroxides 9 and 10

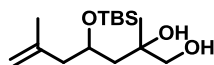
^1H nuclear magnetic resonance (NMR) spectra were recorded using an internal deuterium lock at ambient temperatures on the following instruments: Bruker AC400 (400 MHz) and Bruker AC300 (300 MHz). Data are presented as follows: chemical shift (in ppm), integration, multiplicity (s = singlet, d = doublet, t = triplet, m = multiplet, br means the signal is broad, dd = doublet of doublets, quint. = quintet), coupling constant (J in Hz) and integration. ^{31}P NMR spectra were recorded on a Bruker AC300 (122 MHz) and on a Bruker AC400 (162 MHz) spectrometers with complete proton decoupling. Chemical shifts (δ) were reported in ppm using residual non-deuterated solvents as internal reference. High-resolution mass spectra (HRMS) were performed on a SYNAPT G2 HDMS (Waters) spectrometer equipped with atmospheric pressure ionization source (API) pneumatically assisted. Samples were ionized by positive electrospray mode as follows: electrospray tension (ISV): 2800 V ; opening tension (OR): 20 V ; nebulization gas pressure (nitrogen): 800 L/h. The parent ion (M^+ , $[\text{M}+\text{H}]^+$, $[\text{M}+\text{Na}]^+$) is quoted. All experiments were performed under anhydrous conditions and an inert atmosphere of argon and, except where stated, using dried apparatus and employing standard techniques for handling air-sensitive materials. All reagents were weighed and handled in air at room temperature. For EPR measurements, samples with 0.5 mM concentration of nitroxide were prepared in non-degassed solvents. Experiments were performed indifferently on Elexsys, EMX or ER 100D

Bruker machines (a difference smaller than 0.1 G was noticed). EPR spectra were recorded with a gain of 2×10^5 (72 dB for Eleksys), a modulation amplitude of 1.0 G, a sweep width of 150 G, a sweep time of 21 s, and a power of 20 mW as parameters.



4-(*tert*-butyldimethylsilyloxy)-2,6-dimethylhept-1,6-diene (**3**)

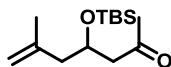
Alcohol **2** (11.5 g, 82.0 mmol) was dissolved in DMF (250 mL), then imidazole (16.7 g, 246 mmol, 3.0 equiv.) and *tert*-butyldimethylsilyl chloride (24.7 g, 164 mmol, 2.0 equiv.) were added, and the mixture was stirred at 0 °C for 5 h. The solution was then poured into water and extracted with Et₂O. The combined organic extracts were washed with water, brine, dried with MgSO₄, filtered, and concentrated under *vacuo*. Column chromatography of the residue gave **3** (20.6 g, 99%) as a colorless oil. ¹H NMR (400 MHz, CDCl₃): δ 4.77 (br s, 2H), 4.71 (br s, 2H), 3.93 (quint., $J = 6.3$ Hz, 1H), 2.20-2.11 (m, 4H), 1.73 (s, 6H), 0.87 (s, 9H), 0.04 (s, 6H). ¹³C NMR (75 MHz, CDCl₃): δ 143.0 (2 × C), 113.2 (2 × CH₂), 69.8 (CH), 46.0 (2 × CH₂), 26.1 (3 × CH₃), 23.2 (2 × CH₃), 18.3 (C), 4.4 (2 × CH₃). HRMS (ESI) calc for C₁₅H₃₀OSiNa⁺: 277.1958 [M+Na]⁺; found: 277.1959.



4-(*tert*-Butyldimethylsilyloxy)-2,6-dimethylhept-6-ene-1,2-diol (**4**).

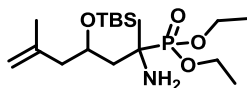
Alkene **3** (4.30 g, 16.9 mmol) was dissolved in acetone/water (200 mL, 3/1 v:v), then a catalytic amount of OsO₄ (1 mL, 4%wt in water) was added and the mixture was stirred for 15 min at 0 °C. Then, *N*-methylmorpholine-*N*-oxide (3.96 g, 33.8 mmol, 2.0 equiv.) was added and stirred for 4 h at 0 °C. The solution was poured into 10 % aqueous Na₂SO₃ and extracted with Et₂O. The combined

organic extracts were washed with water, brine, dried with MgSO_4 , filtered, and concentrated under *vacuo*. Column chromatography of the residue gave **3** (starting material, 3.38 g) and **4** (0.9 g, 86%) as a mixture of two diastereoisomers (2:1 ratio, determined by ^1H NMR). ^1H NMR (400 MHz, C_6D_6): δ 4.78 (br s, 1H, Maj), 4.76 (br s, 1H, Maj + min), 4.70 (br s, 1H, min), 4.26 (m, 1H, Maj + min), 3.78 (s, 1H, min), 3.45-3.28 (m, 3H, Maj + 2H, min), 2.37-2.27 (m, 1H, Maj + min), 2.22-2.07 (m, 1H Maj + 2H, min), 1.87-1.70 (m, 2H, Maj + 1H min), 1.65-1.50 (m, 4H, Maj + 4H, min), 1.18 (s, 3H, Maj), 1.14 (s, 3H, min), 0.94 (s, 9H, Maj + min), 0.11 (s, 3H, min), 0.09 (s, 3H, Maj), 0.05 (s, 3H, Maj + min). ^{13}C NMR (75 MHz, C_6D_6): δ 142.5 (C, Maj), 142.0 (C, min), 113.9 (CH_2 , min), 113.7 (CH_2 , Maj), 73.0 (C, min), 72.7 (C, Maj), 71.0 (CH_2 , min), 70.1 (CH_2 , Maj), 69.7 (CH, min), 69.6 (CH, Maj), 47.9 (CH_2 , Maj + min), 44.3 (CH_2 , Maj), 43.1 (CH_2 , min), 26.2 (CH_3 , Maj), 26.1 (CH_3 , min), 25.5 (CH_3 , Maj), 24.0 (CH_3 , min), 22.9 (CH_3 , Maj), 22.8 (CH_3 , min), 18.2 (C, Maj), 18.1 (C, min), -3.4 (CH_3 , min), -3.5 (CH_3 , Maj), -4.2 (CH_3 , Maj), -4.3 (CH_3 , min). HRMS (ESI) calc for $\text{C}_{15}\text{H}_{32}\text{O}_3\text{SiNa}^+$: 311.2013 $[\text{M}+\text{Na}]^+$; found: 311.2013.



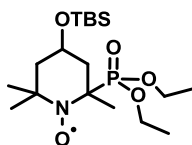
4-((*tert*-Butyldimethylsilyloxy)-6-methylhept-6-en-2-one (**5**))

Diol **4** (6.0 g, 20.8 mmol) was dissolved in THF/water (300 ml, 3/1 v:v), then NaIO_4 (11.1 g, 52.0 mmol, 2.50 equiv.) was added and the resulting mixture was stirred at 0 °C for 3 h. The solution was poured into water and extracted with Et_2O . The combined organic extracts were washed with water, dried with MgSO_4 , filtered, and concentrated under *vacuo*. Column chromatography gave **5** (5.11 g, 96%) as a yellowish oil. ^1H NMR (400 MHz, CDCl_3): δ 4.78 (br s, 1H), 4.70 (br s, 1H), 4.36-4.28 (m, 1H), 2.60-2.47 (m, 2H), 2.27-2.23 (dd, $J = 13.3$ Hz, $J = 5.3$ Hz, 1H), 2.16-2.11 (m, 1H), 2.15 (s, 3H), 1.74 (br s, 3H), 0.86 (s, 9H), 0.07 (s, 3H), 0.03 (s, 3H). ^{13}C NMR (75 MHz, CDCl_3): δ 207.9 (C), 142.3 (C), 113.7 (CH_2), 67.8 (CH), 50.5 (CH_2), 46.6 (CH_2), 31.8 (CH_3), 25.9 (3 CH_3), 23.0 (CH_3), 18.1 (C), -4.5 (CH_3), -4.8 (CH_3). HRMS (ESI) calc for $\text{C}_{14}\text{H}_{28}\text{O}_2\text{Si}^+$: 257.1931 $[\text{M}+\text{H}]^+$; found: 257.1930.



Diethyl (1-amino-3-((*tert*-butyldimethylsilyloxy)-1,5-dimethylhex-5-enyl)phosphonate (6)

Ketone **5** (1.0 g, 3.9 mmol) was dissolved in diethylphosphite (5 mL, 37.4 mmol, 9.6 equiv.), then 4 Å molecular sieves (1.0 g) were added and the mixture was stirred under an ammoniac atmosphere for 24 h. Then, the mixture was filtered and the excess of diethylphosphite was removed under vacuum (50 °C, 2.0 mmHg). Column chromatography gave **6** (550 mg, 37%) as a yellowish oil. ¹H NMR (400 MHz, CDCl₃): δ 4.77 (br s, 1H, Maj + min), 4.71 (br s, 1H, Maj + min), 4.42-4.32 (m, 1H, Maj), 4.27-4.20 (m, 1H, min), 4.19-4.07 (m, 4H, Maj + min), 2.33-2.26 (m, 1H, Maj + min), 2.23-2.15 (m, 1H, Maj + min), 1.95-1.85 (m, 1H, Maj + min), 1.80-1.55 (m, 6H, Maj + min), 1.37-1.28 (m, 9H, Maj + min), 0.88 (s, 9H, Maj + min), 0.13-0.10 (m, 6H, Maj + min). ³¹P NMR (162 MHz, CDCl₃): δ 31.7 (Maj), 30.9 (min). ¹³C NMR (75 MHz, CDCl₃): δ 142.5 (C, Maj), 142.0 (C, min), 113.4 (CH₂, min), 113.3 (CH₂, Maj), 67.6 (d, *J* = 12.7 Hz, CH, min), 67.5 (d, *J* = 10.5 Hz, CH, Maj), 62.3 (d, *J* = 5.5 Hz, CH₂, min), 62.2 (d, *J* = 5.5 Hz, CH₂, min), 62.1 (d, *J* = 7.7 Hz, CH₂, Maj), 62.0 (d, *J* = 7.7 Hz, CH, Maj), 51.9 (d, *J* = 154 Hz, C, min), 51.7 (d, *J* = 146 Hz, C, Maj), 48.0 (CH₂, Maj), 47.9 (CH₂, min), 42.5 (d, *J* = 3.9 Hz, CH₂, Maj), 41.8 (CH₂, min), 25.9 (3 CH₃, Maj + min), 23.7 (d, *J* = 1.1 Hz, CH₃, Maj), 22.7 (CH₃, min), 22.7 (CH₃, Maj), 22.5 (d, *J* = 2.2 Hz, CH₃, min), 17.9 (C, Maj), 17.8 (C, min), 16.5 (d, *J* = 5.5 Hz, CH₃, min), 16.5 (d, *J* = 5.0 Hz, CH₃, Maj), 3.7 (CH₃, min), 3.8 (CH₃, Maj), -4.2 (CH₃, min), 4.3 (CH₃, Maj). HRMS (ESI) calc for C₁₈H₄₁NO₄PSi⁺: 394.2537 [M+H]⁺; found: 394.2537.

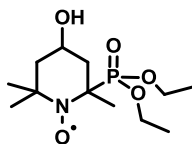


2-(Diethoxyphosphoryl)-4-((*tert*-butyldimethylsilyloxy)-2,6,6-trimethylpiperidin-*N*-oxyl radical (8).

Aminophosphonate **6** (400 mg, 1.02 mmol) was dissolved in THF/water mixture (50 mL, 3/1 v:v), then a solution of Hg(OAc)₂ (389 mg, 1.22 mmol, 1.20 equiv.) in THF/water (50 mL, 3/1 v:v) was slowly

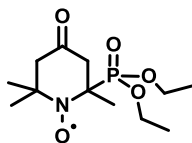
added and was stirred for 30 min at room temperature. The mixture was then poured on a solution of NaBH_4 (77 mg, 2.04 mmol, 2.0 equiv.) and NaOH (163 mg, 4.08 mmol, 4 equiv.) in ice-cold water (50 mL) and stirred for 5 min. After extraction with Et_2O , the combined organic extracts were washed with brine, dried with MgSO_4 , filtered, and concentrated to give piperidine **7** which was used in the next step without any further purification.

A solution of piperidine **7** (900 mg, 2.29 mmol) and *m*-CPBA (1.26 g, 4.58 mmol, 2.0 equiv.) in CH_2Cl_2 (90 mL) was stirred for 2 hours at 0 °C. The solution was then poured into 10 % aqueous $\text{Na}_2\text{S}_2\text{O}_3$ and extracted with CH_2Cl_2 . The combined organic extracts were washed with saturated aqueous solution of NaHCO_3 , dried with MgSO_4 , filtered, and concentrated under *vacuo*. Column chromatography gave **8** (685 mg, 73%) as a red oil. The two diastereoisomers were separated and the major diastereomer (*RR/SS*) was recrystallized from Et_2O . M.p. (Major) = 82 °C. EPR (Phosphate buffer $\text{NaH}_2\text{PO}_4/\text{Na}_2\text{HPO}_4$, 0.05 M, pH = 7.3): Major diastereomer, $a_N = 16.2$ G, $a_P = 24.0$ G; Minor diastereomer, $a_N = 15.0$ G, $a_P = 52.5$ G. HRMS (ESI) calc for $\text{C}_{18}\text{H}_{40}\text{NO}_5\text{P}^+$: 409.2408 $[\text{M}+\text{H}]^+$; found: 409.2408.



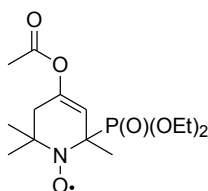
2-(Diethoxyphosphoryl)-4-hydroxy-2,6,6-trimethylpiperidin-*N*-oxyl radical (**9**)

To an ice-cold solution of silyl ether **8** (*RR/SS* + *RS/SR*) (400 mg, 0.979 mmol) in dry THF (4 mL) was added TBAF (1.0 M solution in THF, 1.47 mL, 1.47 mmol, 1.50 equiv.) dropwise under argon. The mixture was stirred for 3 hours. Concentration under *vacuo* followed by column chromatography gave **9** (262 mg, 91%) as a red oil. EPR (Phosphate buffer $\text{NaH}_2\text{PO}_4/\text{Na}_2\text{HPO}_4$, 0.05 M, pH = 7.3): Major diastereoisomer, $a_N = 16.2$ G, $a_P = 24.0$ G; Minor diastereoisomer, $a_N = 15.2$ G, $a_P = 49.8$ G. HRMS (ESI) calc for $\text{C}_{12}\text{H}_{26}\text{NO}_5\text{P}^+$: 295.1543 $[\text{M}+\text{H}]^+$; found: 295.1544; calc for $\text{C}_{12}\text{H}_{25}\text{NO}_5\text{PNa}^+$: 317.1363 $[\text{M}+\text{Na}]^+$; found: 317.1363.



2-(Diethoxyphosphoryl)-2,6,6-trimethyl-4-oxypiperidin-N-oxyl radical (10)

To a stirred ice-cold solution of **9** (RR/SS + RS/SR) (80 mg, 0.272 mmol) and powdered 4 Å molecular sieves (80 mg) in dry DCM (10 mL) was added *N*-methylmorpholine *N*-oxide (128 mg, 1.09 mmol, 4.0 equiv.) followed by a catalytic amount of tetrapropylammonium perruthenate under an argon atmosphere. The mixture was stirred for 20 minutes. Concentration under *vacuo* followed by column chromatography gave **10** (70 mg, 88%) as an orange solid. M.p. = 42 °C. EPR (Phosphate buffer NaH₂PO₄/Na₂HPO₄, 0.05 M, pH = 7.3): $a_N = 15.4$ G, $a_P = 44.2$ G. HRMS (ESI) calc for C₁₂H₂₄NO₅P⁺: 293.1387 [M+H]⁺; found: 293.1387; calc for C₁₂H₂₃NO₅PNa⁺: 315.1206 [M+Na]⁺; found: 315.1205.



2-(Diethoxyphosphoryl)-4-acetoxy-2,6,6-trimethyl-1-azacyclohex-3-enoxyl radical (11)

A solution of ketone **10** (100 mg, 0.342 mmol) in dry THF (5 mL) was slowly added to a –80 °C solution of KHMDS (1.0 M solution in THF, 513 μL, 0.513 mmol, 1.50 equiv.) in dry THF (5 mL). The mixture was stirred for 3 hours from –80 °C to –45 °C. Then, Ac₂O (65 μL, 0.684 mmol, 2.0 equiv.) was slowly added. The mixture was stirred for 2.5 hours, then it was poured on saturated aqueous NaCl solution and extracted with EtOAc. The combined organic extracts were dried with MgSO₄, filtered, and concentrated under *vacuo*. Column chromatography of the residue gave **11** (99 mg, 80%) as a red oil. EPR (Phosphate buffer NaH₂PO₄/Na₂HPO₄, 0.05 M, pH = 7.3): $a_N = 15.4$ G, $a_P = 38.6$ G. HRMS (ESI) calc for C₁₈H₄₁NO₄PSi⁺: 335.1492 [M+H]⁺; found: 335.1491.

Kinetic investigation

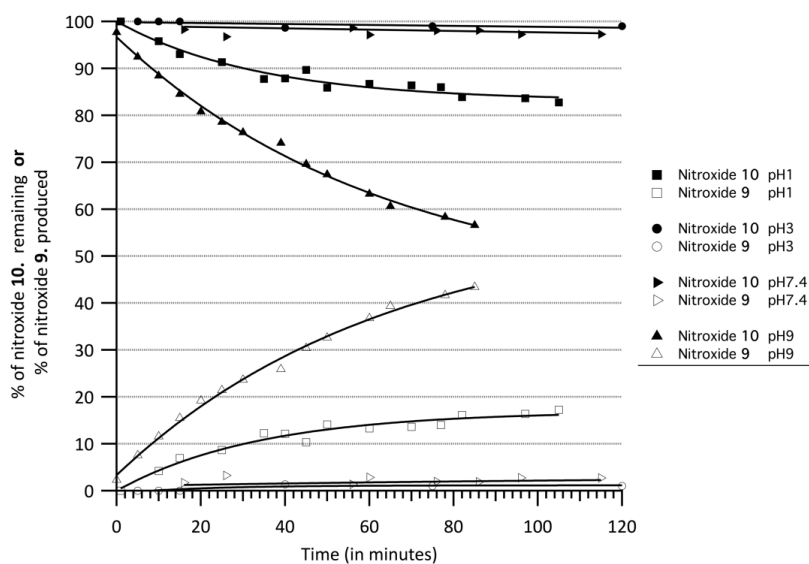


Figure 1S1. Kinetics of hydrolysis of **10+** affording **9** monitored by EPR at pH 1, pH 3, pH 7.4 and pH 9.

Enzymatic EPR kinetic investigations

A Miniscope MS200 EPR instrument (Magnettech, Berlin, Germany) was used for enzymatic reactions. Nitroxide samples were loaded in 75 mm/60 μ l capillaries (Hirschmann Laborgerate, Germany). The experiments were performed as previously reported.^[1] EPR acquisition parameters were as follows: $B_0 = 3353,55$ G; sweep width = 90.42 G; sweep time = 60 s; number of passes = 1; modulation = 300 mG. The gain was kept constant throughout the kinetic experiments. EPR spectra processed using IGOR Pro (Wavemetrics, Lake Oswego, OR, USA) enabled quantification of the third peak(s) during the required time course. After integrating the EPR peaks, the surface areas of the third peak were measured with a Lorentzian Curve fit. These data were then normalized to a final concentration of 1.8 mM.

A list of proteases was tested in pursuit of an effective proteolytic activity of the nitroxide **10**.

All experiments involving purified proteases were done in 0.1 M phosphate buffer, pH = 7.4 at 37 °C; except for collagenase, thermolysin and trypsin, for which CaCl_2 was added in the phosphate buffer for optimal activity.

All these enzymatic reactions were initiated by adding a small volume of enzyme solution between 5 to 20 μl at a concentration around 4 μM to the buffered substrate solution at a concentration of 1.8 mM and were left to incubate for 5 hours before EPR readings.

All kinetic measurements were carried out at pH = 7.4 (phosphate buffer) and sample temperature was kept at 37 °C. The enzymatic reactions were initiated by adding 20 μl of enzyme solution (Subtilisin A, E_0 at 2.8 μM , concentration determined by titrating a constant amount of enzyme with an increasing concentration of Eglin C inhibitor and a constant amount of Meo-Suc-Ala₃-pNA substrate) to the buffered nitroxide substrate solution at a concentration of 1.1 mM placed in a water bath at 37°C. At different time intervals, around 50 μl of the solution was taken for EPR acquisition. The reaction was followed for 20 hours discontinuously until completion. At low substrate concentrations ($[S]_0 \ll K_M$), the Michaelis-Menten equation simplifies to $v_i = k_{cat}/K_M \times [E]_0 \times [S]_0$ so that the release of product **9**, here the ketone form, with time is a pseudo first-order reaction described by $d[P]/dt = k_{obs}[S]$ where $k_{obs} = k_{cat}/K_M \times [E]_0$. The pseudo-first-order rate constant k_{obs} was also calculated using 0.3, 0.6 and 1.8 mM substrate concentrations with 2.8 μM E_0 . The progress curves were all first-order, and k_{obs} did not significantly change with $[S]_0$. This indicates that $[S]_0$ was indeed much lower than K_M . Curves were fitted with an exponential curve with the equation $y = y_0 + Ae^{-kt}$. Similar kinetic measurements were performed in the presence of Eglin C inhibitor at a concentration of 8 μM .

OMRI

1) Set-up

The OMRI setup was composed of a C-shaped 0.2 T MRI system (Magnetom Open Viva, Siemens, Erlangen, Germany) and a resonant TE011 transverse electric mode EPR cavity setup (Bruker, Wissembourg, France) as described in [2]. The EPR cavity placed at the center of the magnet was used to saturate one electron spin transition of the nitroxide. A homemade saddle-shaped MRI coil (28 mm in diameter and 29 mm in length) positioned in the center of the EPR cavity was used for imaging. MR imaging sequences were synchronized to an external pulse generator for electron spin saturation. For 2D sequences the EPR pulse time was 260 ms long followed immediately by the MRI pulse sequence whereas for 3D acquisition, continuous electron spin saturation was carried out. The proton frequency was 8.24 MHz.

2) Frequency sweep experiment

For a selective and an effective electron spin saturation, a frequency sweep experiment was carried out to characterize OMRI response of both nitroxide molecules (**9** and **10**) at 1.8 mM each. The EPR cavity was tuned and matched for each set of frequencies (5.420 - 5.430 GHz for the enol form; 5.412 - 5.427 GHz - for the ketone form). Each targeted peak corresponded to the third line starting from high field on the EPR spectrum (see Figure 6).

OMRI experiments were performed in NMR tubes: a 2 mm inner diameter tube containing 1.8 mM of either nitroxide **9** or nitroxide **10** in phosphate buffer saline; which was then placed in another 20 mm diameter water-filled tube. Two sets of 2D MRI images with a standard gradient echo sequence (with the same parameters reported in the literature) ^[3] were acquired for each tuned frequency with and without electron spin saturation. All MR adjustments were done manually, using the same fixed receiver amplification gain for both measurements, without (S_{off}) and with (S_{on}) electron spin saturation, so that signals can be directly compared and Overhauser enhancements ($S_{\text{on}}/S_{\text{off}}$) calculated.

A plot of the Overhauser enhancements against frequency was then plotted and distinct electron spin saturation frequencies were selected for each nitroxide species (Figure 5).

3) *In-vitro* MRI

An on/off assay was then carried out with two sample tubes (2 mm in diameter); one with the ketone form and the other with the enol form. Electron spin saturation was first set at 5.426 GHz, then at 5.417 GHz. For each frequency, 2D S_{off} and S_{on} images were acquired with the same parameters as before. Sample temperature was kept at 37 °C (Figure 5).

A kinetic assay was also performed over 20 hours and as from 18 minutes same 2D S_{off} and S_{on} images were acquired. Subtilisin A was at 2.8 μM and nitroxide **9** was at 1.8 mM. Here, the electron spin saturation frequency was set only at 5.417 GHz to follow the nitroxide **10** hydrolysis into its ketone form. The ketone nitroxide progression curve was then plotted with the Overhauser enhancements against time (Figure 6). The progress curve was also first-order and was fitted with an exponential curve with the following equation $y = y_0 + Ae^{-kt}$ where $y_0 = 11.3 \pm 0.2$; $A = -12.4 \pm 0.4$ and $k = 0.6 \pm 0.04 \text{ h}^{-1}$. The experimental half life, $t_{1/2}$ was 69 min.

4) *In-vivo* MRI

Mice (n=3, CB57/CRL, Charles River, l'Arbresie, France) weighing 22-24 g were orally fed with 200 μl of nitroxide **9** at 24 mM. Animal was prepared as previously reported.^[1] This protocol was approved by

Discussion and Perspectives

4.1 Discussion

In this thesis, new methodological developments, different specialized molecular beacons and *in vivo* small animals application have been achieved in the aim of detecting and localizing proteolytic activities using the OMRI modality. This work illustrates the first 3D visualization of a physiological process inside an intact organism. It also puts forward one original and unique strategy for detecting substrate-product enzymatic conversion of an OMRI contrast agent. To put all this work together, a proper methodology was developed.

4.1.1 OMRI acquisition advances - before and after

The OMRI setup in our laboratory has been developed on a 0.2 T magnet which gives a proton frequency at 8.24 MHz and an electron frequency at 5.43 GHz. The MRI gradient hardware available was limited to 14 mT/m. The 5.43 GHz electron irradiation allowed a wave penetration depth of around 10 mm, limiting our *in vivo* sample to small rodents. In addition, an electromagnetic wave of 5 GHz does have a heating side that should be controlled. The power at which the wave is transmitted through the cavity onto the sample should be kept as low as possible.

All our experiments were performed with an estimated effective power 6 W or less. Rough estimations of absorbed power were made from temperature elevation measurements during EPR irradiation in phosphate-buffered saline phantoms and *in vivo* in mice (rectal and buccal temperature). The results (unpublished data) *in vivo* showed

that a temperature elevation in the mouse with the buccal probe was 8°C for 150 seconds of EPR irradiation. Knowing that specific heat capacity of the animal is around 3600 J/kg/°C in most body parts [Hasgall et al. 2015] and that the irradiated mouse mass is around 10 g (half the body size), one may calculate a temperature elevation (assuming an initial linear regime and neglecting dissipation) of 0.16 degree/second for 6 W power (the maximal observed value in phantoms), 3-times larger than observed in mice. Thus the SAR value *in vivo* can be calculated as [Postow et al. 1996] : $SAR = c \Delta T / \Delta t = 180 \text{ W/kg}$ under EPR irradiation. This high value led us to divide the acquisition in several time-blocks in order to decrease the duty cycle. Another parameter that minimized the heating effect, was the use of a TE011 cavity configuration. Indeed the electric component of the hyperfrequency wave was set aside on the outer part of the resonant cavity. By far, the previous *in vivo* work conducted by our team on this OMRI setup had a total electronic saturation time of 90 seconds out of 5 minutes of total acquisition time [Massot et al. 2012]. In order to limit the temperature increase to 1-2 degrees, the 90 seconds were fragmented into 3 parts with a 1 minute rest between each part. Thirty seconds was defined to be the upper boundary for continuous *in vivo* EPR saturation. All these points assembled together, oriented the OMRI *in vivo* project towards the development of a new MRI sequence with a faster acquisition time of less than 30 seconds.

In this present work, the spatial resolution was also taken into consideration. From most of the past Overhauser-enhanced imaging applications, the spatial resolution was in two dimensions with slice thickness that were not lower than 5 mm [Seimenis et al. 1997; Golman et al. 1998; Grucker 1990; Golman et al. 2000; Li et al. 2002; Lurie et al. 2002; Li et al. 2006]. Even in the previous work of Massot P., the in-plane resolution was of 0.41 mm and the slice thickness was set at 1 mm [Massot et al. 2012]. So the second point here, was to attain isotropic resolution in the sub millimetric scale.

In this perspective, a fully balanced steady state MRI (TrueFISP) sequence was chosen so as to take advantage of its high SNR characteristics. Even if in 2014, Sarracanie M. successfully demonstrated for the first time the use of the TrueFISP MRI sequence applied to OMRI technique and also combined to an undersampling strategy [Sarracanie et al. 2014], our work on the TrueFISP sequence and the Keyhole strategy was already in progress. The ramp up gradients were at their maximum in order to decrease the acquisition time. The slice selection gradient was also removed for that same objective. A MRI sequence of 1 minute and 8 seconds for spatial resolution of 500 μm in all three dimensions was achieved. The next step was to accelerate this sequence by using the Keyhole approach. A partial acquisition with 50% reduction in 2 out 3 directions allowed an acceleration factor of 4. A final acquisition time of 18 seconds with or without continuous EPR saturation was attained. Consequently, taking into account the significantly reduced duty cycle achieved when acquiring OMRI images each 10 minutes interval (calculated as 3%), a SAR value of 5 W/kg (compared to 180 W/kg)

can be calculated.

4.1.2 Elastolytic activity detection

As per results obtained using the nitroxide-labeled elastin OMRI contrast agent, *in vitro*, *ex vivo* and *in vivo* proteolysis imaging were achieved. The modified correlation time of the OMRI probe upon cleavage of the elastin macromolecule from 330 ps to 170 ps allowed the design of an unambiguous on/off switch. EPR studies have shown a significant change in the linewidth of the electronic transitions from 10 Gauss to around 1.8 Gauss. Moreover, since the saturation factor depends on the EPR linewidth, a large difference in the saturation factor is observed. Taking electron $T_1 = 350$ ns and T_2 evaluated from the EPR linewidths, the saturation factor was about 0.7 for the digested elastin and an estimated 0.2 for the undigested elastin. Upon saturation of the central EPR transition of the nitroxide-labeled elastin, the high signal amplification obtained was directly associated to the digestion of the macromolecule. It should somehow be noted that the Overhauser enhancement is not directly proportional to the concentration of nitroxide especially at concentrations higher than 2 mM. Hence, to quantitatively link the Overhauser signal amplifications to the concentration of nitroxide would be unjustified and incorrect mainly for *in vivo* experiments. All enhancements obtained were qualitatively appreciated.

In vitro elastase activity (pancreatic elastase or neutrophil elastase) was followed continuously by OMRI. The sensitivity of the Overhauser signal was above 0.2 mM. Lower concentrations of nitroxides were rather imaged with enhancements between 0 and 1 and with as darker regions. *Ex vivo* human neutrophil elastase activity was also followed. Even though the sensitivity of the OMRI technique was fairly lower than that of the EPR spectroscopic technique, OMRI signal change was spotted on the 2D images upon secretion of the enzymatic pool out of the neutrophil cells. Signal amplifications obtained with neutrophil-induction was significantly different to those without neutrophil-induction. Specific elastolytic activity was detectable using the OMRI *ex vivo* [Parzy et al. 2013].

In vivo 3D OMRI images after an oral administration of 18 mM of nitroxide-labeled elastin in the mouse's stomach were obtained with a correct spatial resolution of $500\mu\text{m}$ in all 3 directions. High signal amplifications up to 10-fold were measured *in vivo*. As compared to the other MR imaging techniques like CEST, or Gadolinium-based contrast agents where the maximum increase in signal accounts for up to 20-30%, here, the OMRI approach shows a much higher sensitivity. The main advantage when compared to hyperpolarized technique is the *in situ* and non transient Overhauser effect in OMRI experiment. Indeed, with hyperpolarized approaches the signal of the enriched contrast agent decays within several minutes and hence all the enzyme-related signal can only

be followed in this small time interval. Also metabolic enzymatic activity is followed *in vivo* in large voxel-sizes of milimetric orders [Hurd et al. 2012; Eichhorn et al. 2013]. OMRI offers an enzymatic detection each time the EPR line are saturated. By using very stable nitroxides like PCA nitroxide, their presence can be observed for hours inside the organisms. Finally when compared to optical imaging techniques which are preferentially used for enzyme-activity detection *in vivo*, the major drawback is its low light penetration depths and no anatomical and morphological image acquisition. Most studies in this optic field deals a lot with surface tissue detection of enzymatic activity. The OMRI technique allows the imaging of deep seated tissues along with high anatomical images. Hence both morphological and functional imaging can be achieved with the OMRI technique. No other complementary techniques (as Computed Tomography) needs to be coupled. The results show a correct overlay of anatomical MRI acquisition and Overhauser enhanced acquisition was possible, which in turn delineated the Overhauser enhancement spots in deeply seated tissues.

On the other hand, the digestion of the nitroxide-labeled elastin was precisely located in the duodenum of the small intestines just at the opening of the pancreatic duct. No signal enhancements were seen in the stomach of the mouse. This anatomic location suggested that the various stomacal enzymes were not able to cleave the elastin and produce an Overhauser, but rather the pancreatic elastase enzyme present in the pancreatic juice was able to specifically cleave the elastin and produce a high Overhauser signal. The control experiment with orally administered predigested nitroxide-labeled elastin in the stomach showed a high signal amplification in the stomach itself. OMRI allowed a real specificity of the substrate towards its enzyme. The digestion was followed for at least 3 hours and no accumulation of the nitroxide in the urinary bladder was observed. These results suggest a quick absorption of the digested elastin by the intestinal cells [Koonjoo et al. 2014].

4.1.3 Double substrate-product detection upon proteolysis

Based upon the newly synthesized β -phosphorylated nitroxide, a unique substrate-to-product conversion was imaged using the OMRI approach. Upon hydrolysis of the ester bond, the nitroxide has its hyperfine coupling constant shifted due to a change in its conformational structure from a rigid cyclohexene structure-type to a more flexible cyclohexane one. This modification eventually brings about a different orbital overlapping of the 3-spin system (electron, nitrogen and phosphorus atom) which in fine creates two distinct non overlapping EPR frequencies characterizing each the substrate and the product. By selecting one of the particular EPR frequency for electronic saturation, either the substrate or the product has been selectively imaged.

To date such a molecule has never been synthesised for molecular imaging.

Nevertheless this molecular strategy resembles a lot to the deprotonation of free radicals which are often used for OMRI pH mapping. For instance, the team of Khramtsov VV in 2010 imaged an imidazole pH-sensitive radical with a EPR peak shift of 0.8 Gauss upon protonation of the nitroxide molecule [Khramtsov et al. 2010]. A second article described a trityl-based OMRI probe as a pH detector [Takahashi et al. 2014; Dhimitruka et al. 2013]. In this work, the deprotonation resulted in an increase of the phosphorus hyperfine coupling constant of 0.26 Gauss which implies an EPR frequency shift of only 0.3 MHz. These two examples show only a slight variation of the EPR frequency, and hence a higher probability of saturating both EPR frequencies at a time. Distinct protonated or deprotonated nitroxide form was less possible. Here with our β -phosphorylated nitroxide molecule, an EPR line shift of 4.4 Gauss was recorded corresponding to an EPR frequency shift of 8 MHz. Two non-overlapping EPR frequencies were obtained with the frequency sweep experiment.

Even if the acetyl functional group present on the nitroxide molecule is not a specific substrate towards specific enzymes for hydrolysis, a feasibility test was conducted. The β -phosphorylated nitroxide was made to react with different purified enzymes. Among all the enzymes used, the rate of hydrolysis was the fastest with Subtilisin A, a non-specific and broad spectrum serine peptidase. This reaction was proved to be enzymatic by addition of an inhibitor, Eglin C in the reaction mixture. On the contrary, the other enzymes needed more specific substrates for hydrolysis to take place. Hence, using Subtilisin A, all the kinetic studies undergone corroborated with the low substrate specificity of the acetate nitroxide form – with a kinetic constant, $\frac{k_{cat}}{K_M}$ of $55 \text{ M}^{-1}\text{s}^{-1}$.

The *in vivo* feasibility experiments carried out after orally administrating the acetate nitroxide form inside the stomach showed Overhauser enhancements of the substrate at 5.425 MHz and of the product at 5.417 MHz. The Overhauser amplifications were observed inside the stomach for the substrate and for the product, Overhauser signal was spotted in the stomach and down the intestinal tract. Knowing that the stomach has a very acidic environment, the stability of the nitroxide was evaluated and at pH = 1 a very slow and insignificant hydrolysis of the acetyl group was observed. The broad specificity catabolic proteases present in the mouse's stomach for instance esterases, pepsin, or gastrin, allowed a substrate-to-product enzymatic conversion. Control experiments with the administration of the ketone nitroxide form in the stomach, was also the proof that at each EPR frequency, transitions of only one nitroxide species were saturated. No accumulation of the nitroxide was obtained in the urinary bladder, suggesting a rapid absorption of the radical molecule into cells and eventually its bio-reduction into a non radical species which would be invisible by OMRI.

To sum up this discussion, we shall say that the OMRI approach has a great potential in the field of Molecular Imaging in detecting proteolytic activity. Eventually more research work need to be conducted on designing new OMRI contrast agents, which will in turn target more specific enzymes.

4.2 Perspectives

The upcoming future plans of our OMRI project in the laboratory, are :

1. first of all the detection of overly expressed protease activity that are directly associated to diseases – for example lung emphysema and pancreatitis animal models;
2. secondly the translational aspect of this OMRI technique at very low field and eventually at Earth's magnetic field.

4.2.1 Disease related protease activity imaging in small animals

The development of this project requires correct animal models and also specific OMRI probe designs in order to target specific pathologies. Taking the case of a lung emphysema animal model, new MRI methodological techniques should first be implemented so as to adapt the MRI sequence to lung imaging. In regard to the available TrueFISP sequence, preliminary results have shown no conclusive Overhauser enhanced signal in lung images when PCA nitroxide was intratracheally administered. Overhauser signals were diffused and small amplifications were observed. In order to optimize the MRI acquisition, spin-echo based or ultra-short TE sequences can be considered along with accelerated data acquisition methods.

In addition, the use of nitroxide-labeled elastin as substrate to target overexpressed neutrophil elastase would be somewhat inappropriate due to its slow cleavage rates towards neutrophil elastase. Indeed if correct peptide sequences that are specific to neutrophil elastase activity are grafted on the β -phosphorylated nitroxide, the chances for visualizing disease-related elastolytic activity would certainly increase. It should be noted that other enzymes that are overexpressed in this disease could also be targeted.

A second animal model based on a pancreatitis model can also be considered. Here also, OMRI substrates need to be specific and highly effective towards the targeted enzymes. The biodistribution of the OMRI substrate should also be taken into consideration as after an intravenous administration of the substrate, the on-site enzymatic activity visualization due to accumulation of the OMRI substrate would enable an early detection of the pathology. Eventually, inhibitors of these enzymatic reactions could be studied for a better understanding of the progression of the pathology.

4.2.2 Very low Magnetic field & OMRI technique

As stated earlier, at 5 GHz of EPR frequency transmission only small rodents can be studied due to the limiting wave penetration. Indeed, the maximum volume of the sample is constrained by the power of the EPR irradiation. In addition for *in vivo* OMRI applications, it is advisable to lower the power per unit volume as much as possible to avoid any excessive heating effect. Hence, in this view, the next logical step to attain large animal OMRI experiments is to decrease this EPR frequency, and thereby to decrease the amplitude of EPR magnetic field, so as increase the wave penetration depth. Lowering the field will hence enable longer continuous EPR irradiation sequences to be acquired without animal overheating. Another great advantage in implementing OMRI experiment at very low magnetic fields, is the exploration of other permitted electronic transitions of free radicals with a hyperfine structure (i.e nitroxide radical).

OMRI at low EPR frequency have been explored by Lurie D.J. since 1989 through Field-cycling [Lurie et al. 1989]. This approach consists of irradiating the unpaired electrons at a lower magnetic field and followed by NMR imaging data at a higher field. His most recent work using this approach *in vivo* was in 2005, where the EPR irradiation was carried out at 5 mT and then switched within 40 ms to 450 mT for MRI imaging [Lurie et al. 2005]. He was able to visualize the bio distribution of a nitroxide from the kidneys all the way down to the urinary bladder. Thus, by transposing this approach to enzymatic activity detection, larger samples can be imaged with a minimized heating effect.

Another possible approach is to conduct OMRI experiments at even lower magnetic fields. In recent years, there has been a growing interest in developing less costly MRI systems which operates at lower fields than present clinical MRI systems (commonly at 1.5 T). Suitable signal-to-noise and spatial resolutions of patients with metal implants have been achieved by prepolarizing proton spins at a higher magnetic field (0.4 T) than the magnetic field used for imaging (0.03 T) [Venook et al. 2006]. To overcome the enormous signal reduction at fields ranging in orders of $100\mu\text{T}$, a SQUID-based technology has been used to detect the signal with an untuned superconducting input circuit inductively coupled to a superconducting quantum interference device (SQUID) [Inglis et al. 2013]. Recently, the team of Zotev V.S in Los Alamos has taken advantage of this fine signal detectors to perform Overhauser enhanced MR imaging experiments on plants [Zotev et al. 2010]. An Overhauser enhancement of 24-fold was recorded with a 1-second EPR irradiation at 120 MHz and a 20-minute NMR image acquisition time at $96\mu\text{T}$. In the team of Rosen M.S, a low-field MRI scanner with a biplanar 6.5 mT electromagnet and biplanar gradients was customed built without the prepolarization step. Low-field OMRI experiments were conducted *in vitro* on large samples with an embedded EPR irradiation of 4-hydroxy TEMPO at 140.8 MHz into the MRI sequence. In this study, their aim was to achieve fast OMRI acquisitions [Sarracanie et al. 2014].

This team recently demonstrated the feasibility of *in vivo* low-field OMRI in the study of the brain's redox state in rat model of cerebral ischemia/reperfusion after administration of TEMPOL nitroxide [Rosen et al. 2014; Sarracanie et al. 2015].

The main interest to conduct OMRI experiments at very low magnetic fields, is based on the scalar Hamiltonian term when nitroxide radicals are concerned. The work of Guiberteau T in 1996 has shown the evolution of the Overhauser enhancement when the magnetic field intensity is reduced. At low magnetic fields (less than 2 Gauss), the scalar interaction of the unpaired electron with the nitrogen nucleus is fairly increased because the electronic spins experience a strong local magnetic field from the nitrogen spins. The Overhauser enhancement becomes inversely proportional to the applied magnetic field and tends towards absolute infinity [Guiberteau et al. 1996]. Hence, for microtesla-range OMRI experiments, the expected Overhauser enhancements would be even higher.

There is a lot of scope in OMRI imaging and more precisely the field of Molecular Imaging for proteolytic activity detection remains yet to be explored.

Bibliography

- Abragam, A, J Combrisson, and I Solomon (1957). “Nuclear Polarization by the Overhauser Effect in Solutions of Paramagnetic Ions”. In: *CR Acad. Sci* 246, p. 157.
- Abragam, A. and M. Goldman (1978). “Principles of dynamic nuclear polarisation.” In: *Reports on Progress in Physics* 41.3, pp. 395 –467. DOI: [10.1088/0034-4885/41/3/002](https://doi.org/10.1088/0034-4885/41/3/002). [Link](#).
- Audran, Gérard, Paul Brémond, Sylvain RA Marque, and Germain Obame (2012). “Hyperfine Coupling Constants of β -Phosphorylated Nitroxides: A Tool to Probe the Cybotactic Effect by Electron Paramagnetic Resonance”. In: *ChemPhysChem* 13.15, pp. 3542–3548. DOI: [10.1002/cphc.201200420](https://doi.org/10.1002/cphc.201200420). [Link](#).
- Baruch, Amos, Douglas A Jeffery, and Matthew Bogyo (2004). “Enzyme activity—it’s all about image”. In: *Trends in cell biology* 14.1, pp. 29–35. DOI: <http://dx.doi.org/10.1016/j.tcb.2003.11.002>. [Link](#).
- Bates Jr, Richard D and Walter S Drozdowski (1977). “Use of nitroxide spin labels in studies of solvent–solute interactions”. In: *The Journal of Chemical Physics* 67.9, pp. 4038–4044. DOI: <http://dx.doi.org/10.1063/1.435432>.
- Benial, A Milton Franklin, Kazuhiro Ichikawa, Ramachandran Murugesan, Ken-ichi Yamada, and Hideo Utsumi (2006). “Dynamic nuclear polarization properties of nitroxyl radicals used in Overhauser-enhanced MRI for simultaneous molecular imaging”. In: *Journal of Magnetic Resonance* 182.2, pp. 273–282. DOI: <http://dx.doi.org/10.1016/j.jmr.2006.06.025>. [Link](#).
- Bled, Emilie, Wadie Ben Hassen, Line Pourtau, Philippe Mellet, Titus Lanz, Dorothee Schüler, Pierre Voisin, Jean-Michel Franconi, Eric Thiaudière, and Sylvain Miraux (2011). “Real-time 3D MRI of contrast agents in whole living mice”. In: *Contrast Media & Molecular Imaging* 6.4, pp. 275–281. ISSN: 1555-4317. DOI: [10.1002/cmami.429](https://doi.org/10.1002/cmami.429). [Link](#).

- Blum, Galia, Stefanie R Mullins, Kinneret Keren, Marko Fonovič, Christopher Jedeszko, Mark J Rice, Bonnie F Sloane, and Matthew Bogyo (2005). “Dynamic imaging of protease activity with fluorescently quenched activity-based probes”. In: *Nature chemical biology* 1.4, pp. 203–209. DOI: [10.1038/nchembio728](https://doi.org/10.1038/nchembio728). [Link](#).
- Bode, Wolfram, Franz-Xaver Gomis-Rüth, and Walter Stöckler (1993). “Astacins, seralysins, snake venom and matrix metalloproteinases exhibit identical zinc-binding environments (HEXXHXXGXXH and Met-turn) and topologies and should be grouped into a common family, the ‘metzincins’”. In: *FEBS letters* 331.1, pp. 134–140. DOI: [http://dx.doi.org/10.1016/0014-5793\(93\)80312-I](http://dx.doi.org/10.1016/0014-5793(93)80312-I). [Link](#).
- Chauvin, Thomas, Philippe Durand, Michèle Bernier, Hervé Meudal, Bich-Thuy Doan, Fanny Noury, Bernard Badet, Jean-Claude Beloeil, and Éva Tóth (2008). “Detection of enzymatic activity by PARACEST MRI: a general approach to target a large variety of enzymes”. In: *Angewandte Chemie International Edition* 47.23, pp. 4370–4372. DOI: [10.1002/anie.200800809](https://doi.org/10.1002/anie.200800809). [Link](#).
- Chen, Howard H, Choukri Mekkaoui, Hoonsung Cho, Soeun Ngoy, Brett Marinelli, Peter Waterman, Matthias Nahrendorf, Ronglih Liao, Lee Josephson, and David E Sosnovik (2013). “Fluorescence tomography of rapamycin-induced autophagy and cardioprotection in vivo”. In: *Circulation: Cardiovascular Imaging* 6.3, pp. 441–447. DOI: [10.1161/CIRCIMAGING.112.000074](https://doi.org/10.1161/CIRCIMAGING.112.000074). [Link](#).
- Chen, John W, Manel Querol Sans, Alexei Bogdanov Jr, and Ralph Weissleder (2006). “Imaging of Myeloperoxidase in Mice by Using Novel Amplifiable Paramagnetic Substrates”. In: *Radiology* 240.2, pp. 473–481. DOI: [10.1148/radiol.2402050994](https://doi.org/10.1148/radiol.2402050994). [Link](#).
- Chuang, Chih-Hung, Kuo-Hsiang Chuang, Hsin-Ell Wang, Steve R Roffler, Jen-taie Shiea, Shey-Cherng Tzou, Ta-Chun Cheng, Chien-Han Kao, Shih-Yen Wu, Wei-Lung Tseng, et al. (2012). “In vivo positron emission tomography imaging of protease activity by generation of a hydrophobic product from a noninhibitory protease substrate”. In: *Clinical Cancer Research* 18.1, pp. 238–247. DOI: [10.1158/1078-0432.CCR-11-0608](https://doi.org/10.1158/1078-0432.CCR-11-0608). [Link](#).
- Couet, WilliamR., UlfG. Eriksson, ThomasN. Tozer, L. Dallas Tuck, GeorgeE. Wesbey, Danute Nitecki, and RobertC. Brasch (1984). “Pharmacokinetics and Metabolic Fate of Two Nitroxides Potentially Useful as Contrast Agents for Magnetic Resonance Imaging”. In: 1.5, pp. 203–209. DOI: [10.1023/A:1016317212601](https://doi.org/10.1023/A:1016317212601). [Link](#).
- Darne, Chinmay, Yujie Lu, and Eva M Sevick-Muraca (2014). “Small animal fluorescence and bioluminescence tomography: a review of approaches, algorithms and technology update”. In: *Physics in medicine and biology* 59.1, R1. DOI: [10.1088/0031-9155/59/1/R1](https://doi.org/10.1088/0031-9155/59/1/R1). [Link](#).

- Dhas, M Kumara, Hideo Utsumi, A Jawahar, and A Milton Franklin Benial (2015). “Dynamic Nuclear Polarization Properties of Nitroxyl Radical in High Viscous Liquid using Overhauser-enhanced Magnetic Resonance Imaging (OMRI)”. In: *Journal of Magnetic Resonance*. DOI: <http://dx.doi.org/10.1016/j.jmr.2015.05.009>. [Link](#).
- Dhimitruka, Ilirian, Andrey A Bobko, Timothy D Eubank, Denis A Komarov, and Valery V Khramtsov (2013). “Phosphonated trityl probes for concurrent in vivo tissue oxygen and pH monitoring using electron paramagnetic resonance-based techniques”. In: *Journal of the American Chemical Society* 135.15, pp. 5904–5910. DOI: [10.1021/ja401572r](https://doi.org/10.1021/ja401572r). [Link](#).
- Dragulescu-Andrasi, Anca, Gaolin Liang, and Jianghong Rao (2009). “In Vivo Bioluminescence Imaging of Furin Activity in Breast Cancer Cells Using Bioluminogenic Substrates”. In: *Bioconjugate Chemistry* 20.8. PMID: 19642690, pp. 1660–1666. DOI: [10.1021/bc9002508](https://doi.org/10.1021/bc9002508). [Link](#).
- Dragulescu-Andrasi, Anca, Sri-Rajasekhar Kothapalli, Grigory A Tikhomirov, Jianghong Rao, and Sanjiv S Gambhir (2013). “Activatable oligomerizable imaging agents for photoacoustic imaging of furin-like activity in living subjects”. In: *Journal of the American Chemical Society* 135.30, pp. 11015–11022. DOI: [10.1021/ja4010078](https://doi.org/10.1021/ja4010078). [Link](#).
- Duijnhoven, Sander MJ, Marc S Robillard, Klaas Nicolay, and Holger Grüll (2015). “In vivo biodistribution of radiolabeled MMP-2/9 activatable cell-penetrating peptide probes in tumor-bearing mice”. In: *Contrast media & molecular imaging* 10.1, pp. 59–66. DOI: [10.1002/cmml.1605](https://doi.org/10.1002/cmml.1605). [Link](#).
- Duijnhoven, Sander MJ van, Marc S Robillard, Klaas Nicolay, and Holger Grüll (2011). “Tumor targeting of MMP-2/9 activatable cell-penetrating imaging probes is caused by tumor-independent activation”. In: *Journal of Nuclear Medicine* 52.2, pp. 279–286. DOI: [10.2967/jnumed.110.082503](https://doi.org/10.2967/jnumed.110.082503). [Link](#).
- Dzien, Piotr, Mikko I Kettunen, Irene Marco-Rius, Eva M Serrao, Tiago B Rodrigues, Timothy J Larkin, Kerstin N Timm, and Kevin M Brindle (2015). “¹³C magnetic resonance spectroscopic imaging of hyperpolarized [1-¹³C, U-2H₅] ethanol oxidation can be used to assess aldehyde dehydrogenase activity in vivo”. In: *Magnetic Resonance in Medicine* 73.5, pp. 1733–1740. DOI: [10.1002/mrm.25286](https://doi.org/10.1002/mrm.25286). [Link](#).
- Efimova, Olga V, Ziqi Sun, Sergey Petryakov, Eric Kesselring, George L Caia, David Johnson, Jay L Zweier, Valery V Khramtsov, and Alexandre Samouilov (2011). “Variable radio frequency proton–electron double-resonance imaging: Application to pH mapping of aqueous samples”. In: *Journal of Magnetic Resonance* 209.2, pp. 227–232. DOI: <http://dx.doi.org/10.1016/j.jmr.2011.01.011>. [Link](#).

- Eichhorn, Tim R, Yuhei Takado, Najat Salameh, Andrea Capozzi, Tian Cheng, Jean-Noël Hyacinthe, Mor Mishkovsky, Christophe Roussel, and Arnaud Comment (2013). “Hyperpolarization without persistent radicals for in vivo real-time metabolic imaging”. In: *Proceedings of the National Academy of Sciences* 110.45, pp. 18064–18069. DOI: [10.1073/pnas.1314928110](https://doi.org/10.1073/pnas.1314928110). [Link](#).
- Fonović, Marko and Boris Turk (2014). “Cysteine cathepsins and their potential in clinical therapy and biomarker discovery”. In: *PROTEOMICS-Clinical Applications* 8.5-6, pp. 416–426. DOI: [10.1002/prca.201300085](https://doi.org/10.1002/prca.201300085). [Link](#).
- Fu, Qiuxia, Xiangguo Duan, Shaoduo Yan, Licui Wang, Yong Zhou, Shuaizheng Jia, Juan Du, Xiaohui Wang, Yuhua Zhang, and Linsheng Zhan (2013). “Bioluminescence imaging of caspase-3 activity in mouse liver”. In: *Apoptosis* 18.8, pp. 998–1007. DOI: [10.1007/s10495-013-0849-z](https://doi.org/10.1007/s10495-013-0849-z). [Link](#).
- Galliera, Emanuela, Lorenza Tacchini, and Massimiliano M Corsi Romanelli (2015). “Matrix metalloproteinases as biomarkers of disease: updates and new insights”. In: *Clinical Chemistry and Laboratory Medicine (CCLM)* 53.3, pp. 349–355. DOI: [10.1515/cclm-2014-0520](https://doi.org/10.1515/cclm-2014-0520).
- Godinat, Aurélien, Hyo Min Park, Stephen C Miller, Ke Cheng, Douglas Hanahan, Laura E Sanman, Matthew Bogyo, Allen Yu, Gennady F Nikitin, Andreas Stahl, et al. (2013). “A biocompatible in vivo ligation reaction and its application for noninvasive bioluminescent imaging of protease activity in living mice”. In: *ACS chemical biology* 8.5, pp. 987–999. DOI: [10.1021/cb3007314](https://doi.org/10.1021/cb3007314). [Link](#).
- Golman, K, I Leunbach, JH Ardenkjaer-Larsen, GJ Ehnholm, L-G Wistrand, JS Petersson, A Järvi, and S Vahasalo (1998). “Overhauser-enhanced MR imaging (OMRI)”. In: *Acta Radiologica* 39.1, pp. 10–17. DOI: [10.1080/02841859809172142](https://doi.org/10.1080/02841859809172142). [Link](#).
- Golman, Klaes, J Stefan Petersson, Jan-Henrik Ardenkjær-Larsen, Ib Leunbach, Lars-Göran Wistrand, Gösta Ehnholm, and Kecheng Liu (2000). “Dynamic in vivo oxymetry using overhauser enhanced MR imaging”. In: *Journal of Magnetic Resonance Imaging* 12.6, pp. 929–938. DOI: [10.1002/1522-2586\(200012\)12:6<929::AID-JMRI17>3.0.CO;2-J](https://doi.org/10.1002/1522-2586(200012)12:6<929::AID-JMRI17>3.0.CO;2-J). [Link](#).
- Granot, Dorit and Erik M Shapiro (2011). “Release activation of iron oxide nanoparticles:(REACTION) a novel environmentally sensitive MRI paradigm”. In: *Magnetic Resonance in Medicine* 65.5, pp. 1253–1259. DOI: [10.1002/mrm.22839](https://doi.org/10.1002/mrm.22839). [Link](#).
- Griffith, O Hayes, Douglas W Cornell, and Harden M McConnell (1965). “Nitrogen hyperfine tensor and g tensor of nitroxide radicals”. In: *The Journal of Chemical Physics* 43.8, pp. 2909–2910. DOI: <http://dx.doi.org/10.1063/1.1697233>. [Link](#).

- Grucker, D (1990). “In vivo detection of injected free radicals by Overhauser effect imaging”. In: *Magnetic resonance in medicine* 14.1, pp. 140–147. DOI: [10.1002/mrm.1910140113](https://doi.org/10.1002/mrm.1910140113). [Link](#).
- Grucker, Daniel, Thierry Guiberteau, Bernard Eclancher, Jacques Chambron, Robert Chiarelli, Andre Rassat, Guy Subra, and Bernard Gallez (1995). “Dynamic nuclear polarization with nitroxides dissolved in biological fluids”. In: *Journal of Magnetic Resonance, Series B* 106.2, pp. 101–109. DOI: <http://dx.doi.org/10.1006/jmrb.1995.1019>. [Link](#).
- Guiberteau, T. (1994). “Polarization Dynamique en Champ Magnétique Faible: Application à la Spectroscopie et à l’Oxymétrie”. Thèse de doctorat : PHYSIQUE. Université Louis Pasteur de Strasbourg.
- Guiberteau, T and D Grucker (1993). “Dynamic nuclear polarization of water protons by saturation of σ and π EPR transitions of nitroxides”. In: *Journal of Magnetic Resonance, Series A* 105.1, pp. 98–103. DOI: <http://dx.doi.org/10.1006/jmra.1993.1256>. [Link](#).
- Guiberteau, Thierry and Daniel Grucker (1996). “EPR spectroscopy by dynamic nuclear polarization in low magnetic field”. In: *Journal of Magnetic Resonance, Series B* 110.1, pp. 47–54. DOI: <http://dx.doi.org/10.1006/jmrb.1996.0006>. [Link](#).
- Haris, Mohammad, Anup Singh, Imran Mohammed, Ranjit Ittyerah, Kavindra Nath, Ravi Prakash Reddy Nanga, Catherine Debrosse, Feliks Kogan, Kejia Cai, Harish Poptani, et al. (2014). “In vivo Magnetic Resonance Imaging of Tumor Protease Activity”. In: *Scientific reports* 4. DOI: [10.1038/srep06081](https://doi.org/10.1038/srep06081). [Link](#).
- Hasgall, P.A., F. Di Gennaro, C. Baumgartner, E. Neufeld, M.C. Gosselin, D. Payne, A. Klingenberg, and N. Kuster (2015). *IT’IS Database for thermal and electromagnetic parameters of biological tissues*. Version 2.6, January 13th, 2015. [Link](#).
- He, Guanglong, Alexandre Samouilov, Periannan Kuppusamy, and Jay L Zweier (2002). “In vivo imaging of free radicals: applications from mouse to man”. In: *Molecular and cellular biochemistry* 234.1, pp. 359–367. DOI: [10.1023/A:1015994629341](https://doi.org/10.1023/A:1015994629341). [Link](#).
- Henry, Susan A and Alec D Keith (1971). “Membrane properties of saturated fatty acid mutants of yeast revealed by spin labels”. In: *Chemistry and physics of lipids* 7.4, pp. 245–265. DOI: [http://dx.doi.org/10.1016/0009-3084\(71\)90004-1](http://dx.doi.org/10.1016/0009-3084(71)90004-1). [Link](#).
- Höfer, Peter, Giacomo Parigi, Claudio Luchinat, Patrick Carl, Gisela Guthausen, Marcel Reese, Teresa Carlomagno, Christian Griesinger, and Marina Bennati (2008). “Field dependent dynamic nuclear polarization with radicals in aqueous solution”. In:

- Journal of the American Chemical Society* 130.11, pp. 3254–3255. DOI: [10.1021/ja0783207](https://doi.org/10.1021/ja0783207). [Link](#).
- Hurd, Ralph E, Yi-Fen Yen, Albert Chen, and Jan Henrik Ardenkjaer-Larsen (2012). “Hyperpolarized ¹³C metabolic imaging using dissolution dynamic nuclear polarization”. In: *Journal of Magnetic Resonance Imaging* 36.6, pp. 1314–1328. DOI: [10.1002/jmri.23753](https://doi.org/10.1002/jmri.23753). [Link](#).
- Il'yasov, A. V., Ya. A. Levin, A. Sh. Mukhtarov, and M. S. Skorobogatova (1976). “EPR spectra and structure of certain phosphorus-containing nitroxyl radicals”. In: 11.5, pp. 515–520. DOI: [10.1007/BF00524867](https://doi.org/10.1007/BF00524867). [Link](#).
- Inglis, Ben, Kai Buckenmaier, Paul SanGiorgio, Anders F Pedersen, Matthew A Nichols, and John Clarke (2013). “MRI of the human brain at 130 microtesla”. In: *Proceedings of the National Academy of Sciences* 110.48, pp. 19194–19201. DOI: [10.1073/pnas.1319334110](https://doi.org/10.1073/pnas.1319334110). [Link](#).
- Keliris, Aneta, Ilgar Mamedov, Gisela E Hagberg, Nikos K Logothetis, Klaus Scheffler, and Jörn Engelmann (2012). “A smart ¹⁹F and ¹H MRI probe with self-immolative linker as a versatile tool for detection of enzymes”. In: *Contrast media & molecular imaging* 7.5, pp. 478–483. DOI: [10.1002/cmml.1470](https://doi.org/10.1002/cmml.1470). [Link](#).
- Khrantsov, Valery V, George L Caia, Keerthi Shet, Eric Kesselring, Sergey Petryakov, Jay L Zweier, and Alexandre Samouilov (2010). “Variable field proton–electron double-resonance imaging: application to pH mapping of aqueous samples”. In: *Journal of Magnetic Resonance* 202.2, pp. 267–273. DOI: <http://dx.doi.org/10.1016/j.jmr.2009.11.017>. [Link](#).
- Koonjoo, Neha, Elodie Parzy, Philippe Massot, Matthieu Lepetit-Coiffé, Sylvain R. A. Marque, Jean-Michel Franconi, Eric Thiaudiere, and Philippe Mellet (2014). “In vivo Overhauser-enhanced MRI of proteolytic activity”. In: *Contrast Media & Molecular Imaging* 9.5, pp. 363–371. DOI: [10.1002/cmml.1586](https://doi.org/10.1002/cmml.1586). [Link](#).
- Krishna, Murali C, Sean English, Kenichi Yamada, John Yoo, Ramachandran Murugesan, Nallathamby Devasahayam, John A Cook, Klaes Golman, Jan Henrik Ardenkjaer-Larsen, Sankaran Subramanian, et al. (2002). “Overhauser enhanced magnetic resonance imaging for tumor oximetry: coregistration of tumor anatomy and tissue oxygen concentration”. In: *Proceedings of the National Academy of Sciences* 99.4, pp. 2216–2221. DOI: [10.1073/pnas.042671399](https://doi.org/10.1073/pnas.042671399). [Link](#).
- Lai, Zon W, Agnese Petrera, and Oliver Schilling (2015). “The emerging role of the peptidome in biomarker discovery and degradome profiling”. In: *Biological chemistry* 396.3, pp. 185–192. DOI: [10.1515/hsz-2014-0207](https://doi.org/10.1515/hsz-2014-0207).

- Landesman, André (1959). “Étude de la relaxation d’un ion paramagnétique par observation de signaux de résonance nucléaire”. In: *J. Phys. radium* 20.12, pp. 937–948. DOI: [10.1051/jphysrad:019590020012093700](https://doi.org/10.1051/jphysrad:019590020012093700). [Link](#).
- Le Breton, Nolwenn, Marlène Martinho, Kuanysh Kabytaev, Jérémie Topin, Elisabetta Mileo, David Blocquel, Johnny Habchi, Sonia Longhi, Antal Rockenbauer, Jérôme Golebiowski, et al. (2014). “Diversification of EPR signatures in site directed spin labeling using a β -phosphorylated nitroxide”. In: *Physical Chemistry Chemical Physics* 16.9, pp. 4202–4209. DOI: [10.1039/C3CP54816C](https://doi.org/10.1039/C3CP54816C). [Link](#).
- Levin, Ya. A., A. V. Il’yasov, I. D. Morozova, A. Sh. Mukhtarov, and M. S. Skorobogatova (1975). “The formation of phosphorus-containing nitroxyl radicals in the photolysis of 2-methyl-2-nitrosopropane in esters of unsaturated phosphonic acid”. In: 24.2, pp. 251–255. DOI: [10.1007/BF00925764](https://doi.org/10.1007/BF00925764). [Link](#).
- Li, Haihong, Yuanmu Deng, Guanglong He, Periannan Kuppusamy, David J Lurie, and Jay L Zweier (2002). “Proton electron double resonance imaging of the in vivo distribution and clearance of a triaryl methyl radical in mice”. In: *Magnetic resonance in medicine* 48.3, pp. 530–534. DOI: [10.1002/mrm.10222](https://doi.org/10.1002/mrm.10222). [Link](#).
- Li, Haihong, Guanglong He, Yuanmu Deng, Periannan Kuppusamy, and Jay L Zweier (2006). “In vivo proton electron double resonance imaging of the distribution and clearance of nitroxide radicals in mice”. In: *Magnetic resonance in medicine* 55.3, pp. 669–675. DOI: [10.1002/mrm.20804](https://doi.org/10.1002/mrm.20804). [Link](#).
- Lingwood, Mark D, Ivan A Ivanov, Alissa R Cote, and Songi Han (2010). “Heisenberg spin exchange effects of nitroxide radicals on Overhauser dynamic nuclear polarization in the low field limit at 1.5 mT”. In: *Journal of Magnetic Resonance* 204.1, pp. 56–63. DOI: <http://dx.doi.org/10.1016/j.jmr.2010.01.015>. [Link](#).
- Lista, Simone, Frank Faltraco, David Prvulovic, and Harald Hampel (2013). “Blood and plasma-based proteomic biomarker research in Alzheimer’s disease”. In: *Progress in Neurobiology* 101–102, pp. 1–17. ISSN: 0301-0082. DOI: <http://dx.doi.org/10.1016/j.pneurobio.2012.06.007>.
- Louie, Angélique Y, Martina M Hüber, Eric T Ahrens, Ute Rothbächer, Rex Moats, Russell E Jacobs, Scott E Fraser, and Thomas J Meade (2000). “In vivo visualization of gene expression using magnetic resonance imaging”. In: *Nature biotechnology* 18.3, pp. 321–325. DOI: [10.1038/73780](https://doi.org/10.1038/73780). [Link](#).
- Lurie, David J, David M Bussell, Lawrence H Bell, and John R Mallard (1988). “Proton-electron double magnetic resonance imaging of free radical solutions”. In: *Journal*

- of Magnetic Resonance (1969)* 76.2, pp. 366–370. DOI: [http://dx.doi.org/10.1016/0022-2364\(88\)90123-0](http://dx.doi.org/10.1016/0022-2364(88)90123-0). [Link](#).
- Lurie, David J, James MS Hutchison, Lawrence H Bell, Ian Nicholson, David M Bussell, and John R Mallard (1989). “Field-cycled proton-electron double-resonance imaging of free radicals in large aqueous samples”. In: *Journal of Magnetic Resonance (1969)* 84.2, pp. 431–437. DOI: <http://dx.doi.org/10.1016/j.jmr.2015.05.009>. [Link](#).
- Lurie, David J, Haihong Li, Sergey Petryakov, and Jay L Zweier (2002). “Development of a PEDRI free-radical imager using a 0.38 T clinical MRI system”. In: *Magnetic resonance in medicine* 47.1, pp. 181–186. DOI: [10.1002/mrm.10029](https://doi.org/10.1002/mrm.10029). [Link](#).
- Lurie, David J, Gareth R Davies, Margaret A Foster, and James MS Hutchison (2005). “Field-cycled PEDRI imaging of free radicals with detection at 450 mT”. In: *Magnetic resonance imaging* 23.2, pp. 175–181. DOI: <http://dx.doi.org/10.1016/j.mri.2004.11.051>. [Link](#).
- Massot, Philippe, Elodie Parzy, Line Pourtau, Philippe Mellet, Guillaume Madelin, Sylvain Marque, Jean-Michel Franconi, and Eric Thiaudiere (2012). “In vivo high-resolution 3D Overhauser-enhanced MRI in mice at 0.2 T”. In: *Contrast media & molecular imaging* 7.1, pp. 45–50. DOI: [10.1002/cmmi.464](https://doi.org/10.1002/cmmi.464). [Link](#).
- Máté, Gábor, István Kertész, Kata Nóra Enyedi, Gábor Mező, János Angyal, Nikolett Vasas, Adrienn Kis, Éva Szabó, Miklós Emri, Tamás Bíró, et al. (2015). “In vivo imaging of Aminopeptidase N (CD13) receptors in experimental renal tumors using the novel radiotracer 68 Ga-NOTA-c(NGR)”. In: *European Journal of Pharmaceutical Sciences* 69, pp. 61–71. DOI: <http://dx.doi.org/10.1016/j.ejps.2015.01.002>. [Link](#).
- Mayer, Dirk, Yi-Fen Yen, Atsushi Takahashi, Sonal Josan, James Tropp, BK Rutt, Ralph E Hurd, Daniel M Spielman, and Adolf Pfefferbaum (2011). “Dynamic and high-resolution metabolic imaging of hyperpolarized [1-13C]-pyruvate in the rat brain using a high-performance gradient insert”. In: *Magnetic Resonance in Medicine* 65.5, pp. 1228–1233. DOI: [10.1002/mrm.22707](https://doi.org/10.1002/mrm.22707). [Link](#).
- McRobbie, Donald W, Elizabeth A Moore, Martin J Graves, and Martin R Prince (2006). *MRI from Picture to Proton*. 2nd Edition. Cambridge university press.
- Mellet, Philippe, Philippe Massot, Guillaume Madelin, Sylvain R. A. Marque, Etienne Harte, Jean-Michel Franconi, and Eric Thiaudière (2009). “New Concepts in Molecular Imaging: Non-Invasive MRI Spotting of Proteolysis Using an Overhauser Effect Switch”. In: *PLoS ONE* 4.4, e5244. DOI: [10.1371/journal.pone.0005244](https://doi.org/10.1371/journal.pone.0005244). [Link](#).
- Miriaux, Sylvain, Philippe Massot, Emeline J. Ribot, Jean-Michel Franconi, and Eric Thiaudiere (2008). “3D TrueFISP imaging of mouse brain at 4.7T and 9.4T”. In:

- Journal of Magnetic Resonance Imaging* 28.2, pp. 497–503. ISSN: 1522-2586. DOI: [10.1002/jmri.21449](https://doi.org/10.1002/jmri.21449). [Link](#).
- Miriaux, Sylvain, Guillaume Calmettes, Philippe Massot, William Lefrançois, Elodie Parzy, Bernard Muller, Laurent M. Arzac, Véronique Deschodt-Arsac, Jean-Michel Franconi, Philippe Diolez, and Eric Thiaudière (2009). “4D retrospective black blood trueFISP imaging of mouse heart”. In: *Magnetic Resonance in Medicine* 62.5, pp. 1099–1105. ISSN: 1522-2594. DOI: [10.1002/mrm.22139](https://doi.org/10.1002/mrm.22139). [Link](#).
- Napolitano, Roberta, Giorgio Pariani, Franco Fedeli, Zsolt Baranyai, Markus Aswendt, Silvio Aime, and Eliana Gianolio (2013). “Synthesis and Relaxometric Characterization of a MRI Gd-Based Probe Responsive to Glutamic Acid Decarboxylase Enzymatic Activity”. In: *Journal of Medicinal Chemistry* 56.6. PMID: 23469759, pp. 2466–2477. DOI: [10.1021/jm301831f](https://doi.org/10.1021/jm301831f). [Link](#).
- Neefjes, Jacques and Nico P Dantuma (2004). “Fluorescent probes for proteolysis: tools for drug discovery”. In: *Nature Reviews Drug Discovery* 3.1, pp. 58–69. DOI: [10.1038/nrd1282](https://doi.org/10.1038/nrd1282). [Link](#).
- Nelson, Sarah J, John Kurhanewicz, Daniel B Vigneron, Peder EZ Larson, Andrea L Harzstark, Marcus Ferrone, Mark van Criekinge, Jose W Chang, Robert Bok, Ilwoo Park, et al. (2013). “Metabolic imaging of patients with prostate cancer using hyperpolarized [1-13C] pyruvate”. In: *Science translational medicine* 5.198, 198ra108–198ra108. DOI: [10.1126/scitranslmed.3006070](https://doi.org/10.1126/scitranslmed.3006070). [Link](#).
- Newby, Andrew C (2015). “Metalloproteinases promote plaque rupture and myocardial infarction: A persuasive concept waiting for clinical translation”. In: *Matrix Biology*. DOI: <http://dx.doi.org/10.1016/j.matbio.2015.01.015>. [Link](#).
- Nicholson, I, DJ Lurie, and FJL Robb (1994). “The application of proton-electron double-resonance imaging techniques to proton mobility studies”. In: *Journal of Magnetic Resonance, Series B* 104.3, pp. 250–255. DOI: <http://dx.doi.org/10.1006/jmrb.1994.1082>. [Link](#).
- Nikolaou, Panayiotis, Boyd M Goodson, and Eduard Y Chekmenev (2015). “NMR Hyperpolarization Techniques for Biomedicine”. In: *Chemistry-A European Journal* 21.8, pp. 3156–3166. DOI: [10.1002/chem.20140525](https://doi.org/10.1002/chem.20140525). [Link](#).
- Novinec, Marko and Brigita Lenarčič (2013). “Papain-like peptidases: structure, function, and evolution”. In: *Biomolecular concepts* 4.3, pp. 287–308. DOI: [10.1515/bmc-2012-0054](https://doi.org/10.1515/bmc-2012-0054).

- Ntziachristos, Vasilis, Ching-Hsuan Tung, Christoph Bremer, and Ralph Weissleder (2002). "Fluorescence molecular tomography resolves protease activity in vivo". In: *Nature medicine* 8.7, pp. 757–761. DOI: [10.1038/nm729](https://doi.org/10.1038/nm729). [Link](#).
- Overhauser, Albert W (1953). "Polarization of nuclei in metals". In: *Physical Review* 92.2, pp. 411–415. DOI: [10.1103/PhysRev.92.411](https://doi.org/10.1103/PhysRev.92.411). [Link](#).
- Parzy, Elodie, Véronique Bouchaud, Philippe Massot, Pierre Voisin, Neha Koonjoo, Damien Moncelet, Jean-Michel Franconi, Eric Thiaudière, and Philippe Mellet (2013). "Overhauser-enhanced MRI of elastase activity from in vitro human neutrophil degranulation". In: *PLoS ONE* 8.2, e57946 EP. DOI: [10.1371/journal.pone.0057946](https://doi.org/10.1371/journal.pone.0057946). [Link](#).
- Perez, J Manuel, Lee Josephson, Terrence O'Loughlin, Dagmar Högemann, and Ralph Weissleder (2002). "Magnetic relaxation switches capable of sensing molecular interactions". In: *Nature biotechnology* 20.8, pp. 816–820. DOI: [10.1038/nbt720](https://doi.org/10.1038/nbt720). [Link](#).
- Postow, Elliot and Charles Polk (1996). *Handbook of biological effects of electromagnetic fields*. Boca Raton: CRC Press.
- Potapenko, Dmitrii I, Margaret A Foster, David J Lurie, Igor A Kirilyuk, James MS Hutchison, Igor A Grigor'ev, Elena G Bagryanskaya, and Valery V Khramtsov (2006). "Real-time monitoring of drug-induced changes in the stomach acidity of living rats using improved pH-sensitive nitroxides and low-field EPR techniques". In: *Journal of Magnetic Resonance* 182.1, pp. 1–11. DOI: <http://dx.doi.org/10.1016/j.jmr.2006.06.002>. [Link](#).
- Raison, JK, JM Lyons, RJ Mehlhorn, and AD Keith (1971). "Temperature-induced phase changes in mitochondrial membranes detected by spin labeling". In: *Journal of Biological Chemistry* 246.12, pp. 4036–4040. [Link](#).
- Rawlings, Neil D, Alan J Barrett, and Alex Bateman (2014). "MEROPS: the peptidase database". In: *Nucleic acids research* 42.suppl 1, pp. D503–D509.
- Razgulin, Andrew, Nan Ma, and Jianghong Rao (2011). "Strategies for in vivo imaging of enzyme activity: an overview and recent advances". In: *Chem. Soc. Rev.* 40 (7), pp. 4186–4216. DOI: [10.1039/C1CS15035A](https://doi.org/10.1039/C1CS15035A). [Link](#).
- Rosen, Matthew S., Mathieu Sarraçanie, Brandon D. Armstrong, Fanny Herisson, Najat Salameh, and Cenk Ayata (2014). "Overhauser-Enhanced MRI as a Non Invasive Probe of BBB Breakdown and Redox State Following Ischemia/reperfusion". In: *Session : Moving Magnetization in Milano: NOE, APT & CEST – Program number : 0769*. Proc. Intl. Soc. Mag. Reson. Med. ISMRM – 22nd Meeting. [Link](#).

- Samouilov, Alexandre, Olga V Efimova, Andrey A Bobko, Ziqi Sun, Sergey Petryakov, Timothy D Eubank, Dmitrii G Trofimov, Igor A Kirilyuk, Igor A Grigor'ev, Wataru Takahashi, et al. (2014). "In vivo proton electron double-resonance imaging of extracellular tumor pH using an advanced nitroxide probe". In: *Analytical chemistry* 86.2, pp. 1045–1052. DOI: [10.1021/ac402230h](https://doi.org/10.1021/ac402230h). [Link](#).
- Sarracanie, Mathieu, Brandon D Armstrong, Jason Stockmann, and Matthew S Rosen (2014). "High speed 3D overhauser-enhanced MRI using combined b-SSFP and compressed sensing". In: *Magnetic Resonance in Medicine* 71.2, pp. 735–745. DOI: [10.1002/mrm.24705](https://doi.org/10.1002/mrm.24705). [Link](#).
- Sarracanie, Mathieu, Fanny Herisson, Najat Salameh, David Waddington, Cenk Ayata, and Matthew S. Rosen (2015). "Dynamic In Vivo Free Radical Imaging with Overhauser-Enhanced MRI". In: *Session : It's a Polarized World – Program Number 0320*. Proc. Intl. Soc. Mag. Reson. Med. ISMRM – 23rd Meeting. [Link](#).
- Scheffler, Klaus and Stefan Lehnhardt (2003). "Principles and applications of balanced SSFP techniques". In: *European radiology* 13.11, pp. 2409–2418. DOI: [10.1007/s00330-003-1957-x](https://doi.org/10.1007/s00330-003-1957-x). [Link](#).
- Seimenis, Ioannis, Margaret A Foster, David J Lurie, James Hutchison, Paul H Whiting, and Simon Payne (1997). "The excretion mechanism of the spin label proxyl carboxylic acid (PCA) from the rat monitored by X-band ESR and PEDRI". In: *Magnetic resonance in medicine* 37.4, pp. 552–558. DOI: [10.1002/mrm.1910370413](https://doi.org/10.1002/mrm.1910370413). [Link](#).
- Shchepin, Roman V., Wellington Pham, and Eduard Y. Chekmenev (2014a). "Dephosphorylation and biodistribution of 1-13C-phospholactate in vivo". In: *Journal of Labelled Compounds and Radiopharmaceuticals* 57.8, pp. 517–524. DOI: [10.1002/jlcr.3207](https://doi.org/10.1002/jlcr.3207). [Link](#).
- Shchepin, Roman V., Aaron M. Coffey, Kevin W. Waddell, and Eduard Y. Chekmenev (2014b). "Parahydrogen Induced Polarization of 1-13C-Phospholactate-d2 for Biomedical Imaging with >30,000,000-fold NMR Signal Enhancement in Water". In: *Analytical Chemistry* 86.12. PMID: 24738968, pp. 5601–5605. DOI: [10.1021/ac500952z](https://doi.org/10.1021/ac500952z). [Link](#).
- Siemianowicz, Krzysztof (2012). *The Role of Metalloproteinases in the Development of Aneurysm*. INTECH Open Access Publisher.
- Slichter, Charles P (2014). "The discovery and renaissance of dynamic nuclear polarization". In: *Reports on Progress in Physics* 77.7, p. 072501. DOI: [10.1088/0034-4885/77/7/072501](https://doi.org/10.1088/0034-4885/77/7/072501). [Link](#).

- Takahashi, Wataru, Andrey A Bobko, Ilirian Dhimitruka, Hiroshi Hirata, Jay L Zweier, Alexandre Samouilov, and Valery V Khramtsov (2014). "Proton-Electron Double-Resonance Imaging of pH Using Phosphonated Trityl Probe". In: *Applied magnetic resonance* 45.9, pp. 817–826. DOI: [10.1007/s00723-014-0570-2](https://doi.org/10.1007/s00723-014-0570-2). [Link](#).
- Taylor, Jennifer M., Mariana Yaneva, Kevin Velasco, John Philip, Hediye Erdjument-Bromage, Irina Ostrovnaya, Hans G. Lilja, Bernard H. Bochner, and Paul Tempst (2014). "Aminopeptidase activities as prospective urinary biomarkers for bladder cancer". In: *PROTEOMICS – Clinical Applications* 8.5-6, pp. 317–326. ISSN: 1862-8354. DOI: [10.1002/prca.201300118](https://doi.org/10.1002/prca.201300118). [Link](#).
- Thraillkill, Kathryn M, R Clay Bunn, and John L Fowlkes (2009). "Matrix metalloproteinases: their potential role in the pathogenesis of diabetic nephropathy". In: *Endocrine* 35.1, pp. 1–10. DOI: [10.1007/s12020-008-9114-6](https://doi.org/10.1007/s12020-008-9114-6). [Link](#).
- Turk, Boris (2006). "Targeting proteases: successes, failures and future prospects". In: *Nature reviews Drug discovery* 5.9, pp. 785–799. DOI: [10.1038/nrd2092](https://doi.org/10.1038/nrd2092). [Link](#).
- Türke, M-T and M Bennati (2012). "Comparison of Overhauser DNP at 0.34 and 3.4 T with Fremy's Salt". In: *Applied magnetic resonance* 43.1-2, pp. 129–138. DOI: [10.1007/s00723-012-0362-5](https://doi.org/10.1007/s00723-012-0362-5). [Link](#).
- Utsumi, Hideo, Ken-ichi Yamada, Kazuhiro Ichikawa, Kiyoshi Sakai, Yuichi Kinoshita, Shingo Matsumoto, and Mika Nagai (2006). "Simultaneous molecular imaging of redox reactions monitored by Overhauser-enhanced MRI with ¹⁴N- and ¹⁵N-labeled nitroxyl radicals". In: *Proceedings of the National Academy of Sciences of the United States of America* 103.5, pp. 1463–1468. DOI: [10.1073/pnas.0510670103](https://doi.org/10.1073/pnas.0510670103). [Link](#).
- Van Vaals, Joop J, Marijn E Brummer, W Thomas Dixon, Hans H Tuithof, Hans Engels, Rendon C Nelson, Brigid M Gerety, Judith L Chezmar, and Jacques A Den Boer (1993). "Keyhole method for accelerating imaging of contrast agent uptake". In: *Journal of Magnetic Resonance Imaging* 3.4, pp. 671–675. DOI: [10.1002/jmri.1880030419](https://doi.org/10.1002/jmri.1880030419). [Link](#).
- Vandooren, Jennifer, Philippe E Van den Steen, and Ghislain Opendakker (2013). "Biochemistry and molecular biology of gelatinase B or matrix metalloproteinase-9 (MMP-9): the next decade". In: *Critical reviews in biochemistry and molecular biology* 48.3, pp. 222–272. DOI: [10.3109/10409238.2013.770819](https://doi.org/10.3109/10409238.2013.770819). [Link](#).
- Venook, Ross D, Nathaniel I Matter, Meena Ramachandran, Sharon E Ungersma, Garry E Gold, Nicholas J Giori, Albert Macovski, Greig C Scott, and Steven M Conolly (2006). "Prepolarized magnetic resonance imaging around metal orthopedic implants". In: *Magnetic resonance in medicine* 56.1, pp. 177–186. DOI: [10.1002/mrm.20927](https://doi.org/10.1002/mrm.20927). [Link](#).

- Wang, Lihong V (2008). “Prospects of photoacoustic tomography”. In: *Medical physics* 35.12, pp. 5758–5767. DOI: [10.1118/1.3013698](https://doi.org/10.1118/1.3013698). [Link](#).
- Weissleder, Ralph (2002). “Scaling down imaging: molecular mapping of cancer in mice”. In: *Nature Reviews Cancer* 2.1, pp. 11–18. DOI: [10.1038/nrc701](https://doi.org/10.1038/nrc701). [Link](#).
- Weissleder, Ralph and Umar Mahmood (2001). “Molecular Imaging 1”. In: *Radiology* 219.2, pp. 316–333. DOI: [10.1148/radiology.219.2.r01ma19316](https://doi.org/10.1148/radiology.219.2.r01ma19316). [Link](#).
- Wilkesman, Jeff and Liliana Kurz (2009). “Protease analysis by zymography: a review on techniques and patents”. In: *Recent patents on biotechnology* 3.3, pp. 175–184. DOI: [10.2174/187220809789389162](https://doi.org/10.2174/187220809789389162). [Link](#).
- Yamato, Mayumi, Takeshi Shiba, Ken-ichi Yamada, Toshiaki Watanabe, and Hideo Utsumi (2009). “Noninvasive assessment of the brain redox status after transient middle cerebral artery occlusion using Overhauser-enhanced magnetic resonance imaging”. In: *Journal of Cerebral Blood Flow & Metabolism* 29.10, pp. 1655–1664. DOI: [10.1038/jcbfm.2009.84](https://doi.org/10.1038/jcbfm.2009.84). [Link](#).
- Yang, Kai, Lei Zhu, Liming Nie, Xiaolian Sun, Liang Cheng, Chenxi Wu, Gang Niu, Xiaoyuan Chen, and Zhuang Liu (2014). “Visualization of protease activity in vivo using an activatable photo-acoustic imaging probe based on CuS nanoparticles”. In: *Theranostics* 4.2, p. 134. DOI: [10.7150/thno.7217](https://doi.org/10.7150/thno.7217). [Link](#).
- Yepes, Diego, Victor Costina, Lothar R. Pilz, Ralf Hofheinz, Michael Neumaier, and Peter Findeisen (2014). “Multiplex profiling of tumor-associated proteolytic activity in serum of colorectal cancer patients”. In: *PROTEOMICS – Clinical Applications* 8.5-6, pp. 308–316. ISSN: 1862-8354. DOI: [10.1002/prca.201300103](https://doi.org/10.1002/prca.201300103). [Link](#).
- Yoo, Byunghee, Manu S Raam, Rachel M Rosenblum, and Mark D Pagel (2007). “Enzyme-responsive PARACEST MRI contrast agents: a new biomedical imaging approach for studies of the proteasome”. In: *Contrast media & molecular imaging* 2.4, pp. 189–198. DOI: [10.1002/cmml.145](https://doi.org/10.1002/cmml.145). [Link](#).
- Yoo, Byunghee, Vipul R Sheth, Christine M Howison, Matthew JK Douglas, Carlos T Pineda, Erin A Maine, Amanda F Baker, and Mark D Pagel (2014). “Detection of in vivo enzyme activity with CatalyCEST MRI”. In: *Magnetic Resonance in Medicine* 71.3, pp. 1221–1230. DOI: [10.1002/mrm.24763](https://doi.org/10.1002/mrm.24763). [Link](#).
- Zacharias, Niki M, Henry R Chan, Napapon Sailasuta, Brian D Ross, and Pratip Bhattacharya (2011). “Real-time molecular imaging of tricarboxylic acid cycle metabolism in vivo by hyperpolarized 1-¹³C diethyl succinate”. In: *Journal of the American Chemical Society* 134.2, pp. 934–943. DOI: [10.1021/ja2040865](https://doi.org/10.1021/ja2040865). [Link](#).

Zotev, Vadim S, Tuba Owens, Andrei N Matlashov, Igor M Savukov, John J Gomez, and Michelle A Espy (2010). “Microtesla MRI with dynamic nuclear polarization”. In: *Journal of Magnetic Resonance* 207.1, pp. 78–88. DOI: <http://dx.doi.org/10.1016/j.jmr.2010.08.015>. [Link](#).

Annexes

To complete my work, I am adding a fourth article which relates about the use of another type of nitroxide in theranostics – a field combining therapy and diagnosis. This theranostic agent named Alkoxyamine can spontaneously undergo homolysis producing an alkyl agent which in turn would target solid tumors and an nitroxide radical which would serve as the imaging contrast agent.

Here, this work illustrates the potential of this molecule *in vitro* and *ex vivo* on cancer cells. Biological studies as well as OMRI studies were conducted. My contribution is mainly related to the OMRI studies.

Alkoxyamines: Toward a New Family of Theranostic Agents against Cancer

Damien Moncelet,[†] Pierre Voisin,^{*,†} Neha Koonjoo,[†] Véronique Bouchaud,[†] Philippe Massot,[†] Elodie Parzy,[†] Gérard Audran,[‡] Jean-Michel Franconi,[†] Eric Thiaudière,[†] Sylvain R. A. Marque,[‡] Paul Brémond,^{*,‡} and Philippe Mellet^{*,†,§}

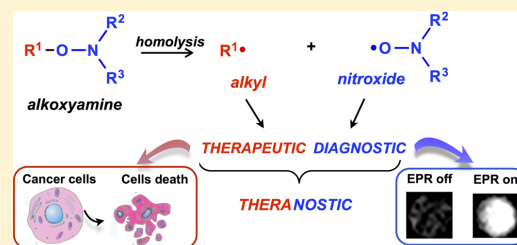
[†]CRMSB, CNRS-UMR-5536, Université Victor Segalen Bordeaux 2, 146 rue Léo Saignat, Case 93, 33076 Bordeaux Cedex, France

[‡]Aix Marseille Université, CNRS, ICR UMR 7273, 13397, Marseille, France

[§]INSERM, 146 rue Léo Saignat, Case 93, 33076 Bordeaux Cedex, France

ABSTRACT: Theranostics combines therapeutic and diagnostic or drug deposition monitoring abilities of suitable molecules. Here we describe the first steps of building an alkoxyamine-based theranostic agent against cancer. The labile alkoxyamine ALK-1 ($t_{1/2} = 50$ min at 37 °C) cleaves spontaneously to generate (1) a highly reactive free alkyl radical used as therapeutic agents to induce cell damages leading to cell death and (2) a stable nitroxide used as contrast agent for Overhauser-enhanced magnetic resonance imaging (OMRI). The ALK-1 toxicity was studied extensively *in vitro* on the glioblastoma cell line U87-MG. Cell viability appeared to be dependent on ALK-1 concentration and on the time of the observation following alkoxyamine treatment. For instance, the LC₅₀ at 72 h was 250 μ M. Data showed that cell toxicity was specifically due to the *in situ* released alkyl radical. This radical induced oxidative stress, mitochondrial changes, and ultimately the U87 cell apoptosis. The nitroxide production, during the alkoxyamine homolysis, was monitored by OMRI, showing a progressive MRI signal enhancement to 6-fold concomitant to the ALK-1 homolysis. In conclusion, we have demonstrated for the first time that the alkoxyamines are promising molecules to build theranostic tools against solid tumors.

KEYWORDS: theranostics, cancer, imaging, OMRI, alkoxyamines, alkyl radicals, nitroxides, apoptosis



INTRODUCTION

Although the number of available antitumoral drugs is continuously expanding, treatments still have a limited efficiency. This is mostly due to the general toxicity of the products in particular for the immune system that narrows the therapeutic range. Thus, the trend is to design less toxic, more selective, and preferably personalized treatments. To lower the side effects on nontargeted tissues *in situ*, activatable prodrugs are being developed. These drugs either are kept in cargoes which release their content at targeted sites or are activated only at targeted sites or in the presence of specific enzymatic activities. The specific activation steps add a safety lock that makes possible the use *in situ* of unspecific toxic products to induce tumor cell death. Among such drugs alkyl radicals are good candidates since they produce random alterations on proteins, lipids, and nucleic acids¹ inducing oxidative stress and ultimately apoptosis or necrosis.^{2,3} The random nature of their action makes drug resistance acquisition much less probable. Alkyl radical delivering drugs such as platinum derivatives or cyclophosphamides are currently used with some success in chemotherapy. These alkyl radicals are thought to act by targeting nucleic acids, but this is not a general case.⁴ These

families of drugs are now reconsidered in conjunction with new delivery/activation systems.⁵

Indeed, from these statements, we recently developed a concept describing the use and the requirements to apply alkoxyamines as theranostic agents.⁶ Alkoxyamines are a versatile family of molecules with the common structure R¹ONR²R³. They have the unique property of spontaneously homolyzing into a stable nitroxide and a highly reactive alkyl radical (Scheme 1A). These molecules are currently developed in polymer science as initiators and as controllers for radical polymerization.⁷ The activation energy for homolysis can be tuned by replacing the R¹, R², and R³ moieties.^{7,8} For instance, by methylating a pyridine moiety in the R¹ group of an alkoxyamine, the activation energy of homolysis decreases from 123 to 106 kJ/mol, thus shortening the homolysis half-time at 37 °C in water from 88 h to 50 min.^{9–11} Thus, alkoxyamines are interesting candidates for delivering alkyl radicals at tumor

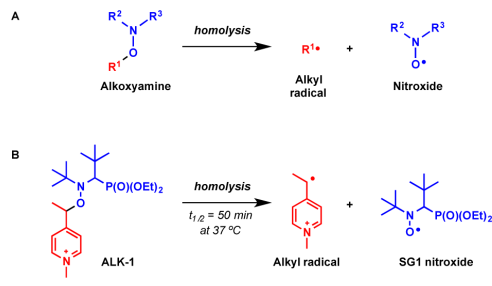
Received: February 17, 2014

Revised: April 15, 2014

Accepted: May 7, 2014

Published: June 17, 2014

Scheme 1. General Structures of Alkoxyamines (A); Structure and Homolysis Reaction of ALK-1 (B)



sites to trigger cell death throughout the above-mentioned processes.

Treatments have better chances to reach their goal, i.e., induce tumor cell death, if the concentration of the active product actually generated in the tumor environment could be monitored. This would allow treatment adjustments to exactly reach the optimal concentration of the drug as established *in vitro* independently of the delivery system, the weight of the patient, or the patient's metabolism. By generating a stable nitroxide at the same time as the alkyl radical, alkoxyamines offer the possibility to monitor the concentration and the location of drug delivery. Indeed the nitroxide free radical is detectable either by electron paramagnetic resonance imaging (EPRI)¹² or by Overhauser-enhanced magnetic resonance imaging (OMRI).¹³ OMRI (also called PEDRI for proton–electron double resonance imaging) is an emerging technique combining the high spatial resolution, speed, three-dimensional anatomic description, and depth of penetration of MRI with the higher sensitivity of EPR. The OMRI signal is enhanced by irradiating the free electron of the nitroxide at its Larmor frequency and simultaneously recording the ordinary MRI signals. Water protons on the vicinity of the nitroxide molecules which are coupled by dipole–dipole interaction receive a fraction of the higher electron polarization (658 times the polarization of the proton) and thus display a high contrast. This concept was applied *in vivo* by injecting various nitroxides in the bloodstream¹⁴ and was recently applied by us to reveal an experimental mouse glioma¹⁵ and the digestive elastolytic activity of a living mouse,¹⁶ both with unusually high contrast.

In this article, the effect of the treatment of U87 glioblastoma cell line with the alkoxyamine lead-compound ALK-1 (Scheme 1B) was investigated. The detection of the homolysis process by OMRI was also investigated in the context of a full theranostic approach. Propositions to develop future functional drugs with intelligent triggering and targeting will be discussed.

■ EXPERIMENTAL SECTION

Synthesis of Alkoxyamine ALK-1. ALK-1 was prepared as previously reported.^{9–11}

Cell Culture. Human glioblastoma cell lines U87 MG from the American Type Culture Collection (ATCC, LGC standards, Molsheim, France) was cultured in Dulbecco's modified Eagle's medium (DMEM, Gibco Corp) supplemented with 10% fetal calf serum (FCS, Gibco Corp), in a humidified atmosphere with 5% CO₂ at 37 °C.

Viability Test. The viability study of U87 cells treated or not with ALK-1 was carried out with measurements by the

LIVE/DEAD Viability/Cytotoxicity Kit (Molecular Probes, Invitrogen, Life Technologies). Briefly, the cells were allowed to grow during 24 h on 24 multiwell plates (Becton-Dickinson, 2 cm²/well). They were then treated with ALK-1 at concentrations ranging from 0.05 to 1.5 mM, left in this same medium at 37 °C, and tested for viability at distinct observation times (1, 3, 6, 24, or 72 h). To do this the adherent cells were dissociated from the plate using 0.05% trypsin (Invitrogen, Carlsbad, CA, USA) and pelleted by centrifugation. Then, the cells were resuspended at 10⁶ cells/mL on calcein-AM and ethidium homodimer-1 solution for 20 min at room temperature and analyzed on a Guava easyCyte flow cytometer/counter (Millipore, Billerica, MA). U87 cell viability was also measured after treatment with beforehand homolyzed ALK-1. For these experiments, ALK-1 was incubated in the culture medium during 72 h at 3 mM without the cells. U87 cells were then treated with different concentrations of this homolyzed ALK-1 for 1 or 72 h, and a viability test was performed as previously described. The viability test in the presence of the free radical scavenger was carried out with an ALK-1 concentration of 1.5 mM and an incubation time of 1 h. U87 cell viability was measured versus increasing concentrations of the nontoxic radical scavenger trihydroxyethylrutin (troxerutin, Santa Cruz Biotechnology, Inc.), namely, 20, 50, or 100 mM. These experiments were repeated at least three times.

Oxidative Stress Measurements. The cells were grown in a 24 multiwell plate as previously described. Then, cells were dissociated by trypsinization and suspended at a density of 10⁶ cells/mL in carboxy-H₂DCFDA (Molecular Probes, Invitrogen, Life Technologies) at 50 μM. This nonfluorescent intracellular probe becomes green-fluorescent in the presence of oxidizing species.

After 30 min at 37 °C, cells were washed with phosphate buffered saline (PBS). Cells were centrifuged and resuspended with medium containing or not 1.5 mM ALK-1 with or without troxerutin at 50 mM. Cells were also resuspended in a beforehand homolyzed ALK-1 solution at 1.5 mM. Treatment with H₂O₂ at 5 mM was used as positive control of oxidative stress. After washing, the cells were analyzed on a Guava easyCyte (Millipore) flow cytometer/counter. These experiments were repeated three times.

Mitochondrial Alterations Measurements. The red fluorescent dye tetramethylrhodamine ethyl ester (TMRE, Molecular Probes, Invitrogen, Life Technologies) was used to follow variations in mitochondrial membrane potential. This cationic probe accumulates in polarized mitochondria through the electrochemical gradient. Nonyl Acridine Orange (NAO, Molecular Probes, Invitrogen, Life Technologies) was then used as a complementary assay to assess the changes in mitochondrial morphology. Cells were plated on 24 multiwell plates (Becton-Dickinson, 2 cm²/well) during 24 h and treated with a range of ALK-1 concentrations (0.1; 0.25; 0.375; 0.5; 0.75; 1.0; and 1.5 mM). After 3, 24, or 72 h, cells were resuspended in TMRE (250 nM) or NAO (500 nM) and incubated 30 min at 37 °C, 5% CO₂. Incubation with 0.5 mM of carbonyl cyanide 3-chlorophenylhydrazone (CCCP, Sigma-Aldrich) was performed as positive control of the mitochondrial depolarization staining. Then, cells were washed and analyzed by flow cytometry. All the experiments were performed three times.

Cell Death Analysis by Annexin V/Propidium Iodide Staining. Cell death was detected by annexin V-FITC (Molecular Probes, Invitrogen, Life Technologies) binding to

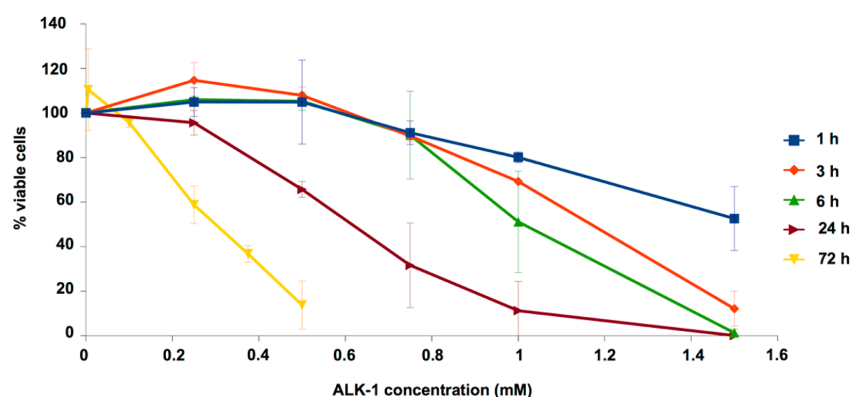


Figure 1. Viability of the U87 cells treated with ALK-1. U87 cells were treated with ALK-1 at several ranges of concentrations. The cell viability was measured, using calcein-AM and ethidium homodimer, by flow cytometry at 1, 3, 6, 24, or 72 h observation times ($n = 3$).

exposed phosphoserine (PS) residues at the surface of cells. Cells were treated with ALK-1 at concentrations ranging from 0.1 to 1.5 mM at 37 °C and tested at distinct observation times (3, 24, or 72 h). After treatment, cells were resuspended in staining buffer containing propidium iodide (PI, 2 $\mu\text{g}/\text{mL}$) and annexin V-FITC. Double-labeling was performed at room temperature for 15 min in darkness. Then, the percentage of viable (PI-/AV-), early apoptotic (PI-/AV+), and late apoptosis/necrotic cells (PI+/AV+) was quantified by flow cytometry. These experiments were performed twice.

Apoptosis Detection through Caspase-3/-7 Assay.

Quantitative assessment of apoptotic cells was also conducted by the detection of caspase activity using the vybrant FAM Caspase-3 and -7 Assay Kit (Molecular Probes, Invitrogen, Life Technologies). Briefly, cells were treated with the previously described ALK-1 concentrations during 3, 24, or 72 h. After the alkoxyamine treatment, the cells were dissociated from the support, washed, and incubated for 1 h at 37 °C in FLICA working solution. Then, the cells were washed and green fluorescence was measured by flow cytometry. These experiments were performed twice.

Overhauser-Enhanced Magnetic Resonance Imaging.

EPR Cavity and MRI Devices. The OMRI experiment were done in a C-shaped 0.2 T MRI system (Magnetom Open Viva, Siemens, Erlangen, Germany) and a resonant TE011 transverse electric mode EPR cavity setup (Bruker, Wissembourg, France) as described previously.¹⁷ The EPR cavity, placed at the center of the magnet, was used to saturate the electron spin transition of the nitroxide SG1 produced upon ALK-1 homolysis. A homemade saddle-shaped MRI coil (28 mm in diameter and 29 mm in length) in the EPR cavity was used for imaging.

Electron spin saturation was carried out at 5.4573 GHz, corresponding to the first line at high field from the center of the EPR spectrum. The proton frequency was 8.24 MHz. Sample temperature was kept at 37 °C.

OMRI experiments were performed in two NMR tubes (4 mm inner diameter): one containing 0.8 mM of SG1 nitroxide in phosphate buffer saline (not shown) and the other with 0.8 mM of ALK-1 in DMEM, 10% FCS. ALK-1 homolysis was followed for 48 h.

Pulse Sequences. 2D MRI images were acquired with a standard gradient echo sequence, which was synchronized to an external pulse generator for electron spin saturation. The EPR

pulse time was 260 ms long, followed immediately by the MRI sequence. This sequence had the following parameters: TE (echo time) = 10 ms; TR (repetition time) minimal = 27 ms; effective TR = 300 ms; field of view = 22 \times 22 mm; matrix size = 64 \times 64; slice thickness = 5 mm; spatial resolution = 0.34 \times 0.34 mm; number of averages = 2; and an acquisition time = 22 s. All MR adjustments were done manually, using the same fixed receiver amplification gain for both measurements, without (S_{off}) and with (S_{on}) HF irradiation, so that signals can be directly compared and Overhauser enhancements ($S_{\text{on}}/S_{\text{off}}$) calculated.

Postprocessing. All signal intensity measurements were made with ImageJ imaging software (ImageJ, National Institutes of Health, USA). Signal intensity was measured in a rectangular region of interest of 2 mm² positioned in the NMR tube area. Curve fitting and $t_{1/2}$ measurement were carried out with IGOR Pro (Wavemetrics, Lake Oswego, OR, USA).

RESULTS

Viability of U87 Cells Treated with ALK-1. The ALK-1 effect on U87 cell viability was characterized by flow cytometry with ranges of ALK-1 concentrations. The viability was assessed at several time points post ALK-1 treatment (later referred to as observation times). As shown in Figure 1, U87 cell viability decreased in a dose dependent manner after the alkoxyamine treatment. Moreover, the LC_{50} decreased while the observation time lengthened from approximately 1.5 mM at 1 h to 0.25 mM at 72 h. Similar results were observed after treatment on B16-F10 murine skin melanoma, CT26 colon carcinoma, and Jurkat T leukemia cell lines (data not shown). Interestingly, keeping in mind that the half-time of homolysis is about 50 min, 5 h after the beginning of treatment the ALK-1 residual concentration was only ca. 1% of the initial concentration. These results suggest that, when the toxic effect is engaged, it follows an irreversible process still observed at 72 h for the lowest alkoxyamine concentrations. Then, the alkoxyamine moiety affording the cell toxicity was investigated.

Contribution of Homolysis-Derived Species to Cell Toxicity. ALK-1 was left to homolyze 72 h at 37 °C in complete culture medium. As a result, the highly reactive alkyl radical was depleted by reacting with the culture medium. Then, U87 cells were treated with this beforehand homolyzed ALK-1 at a concentration range from 0.05 mM to 1.5 mM for 1

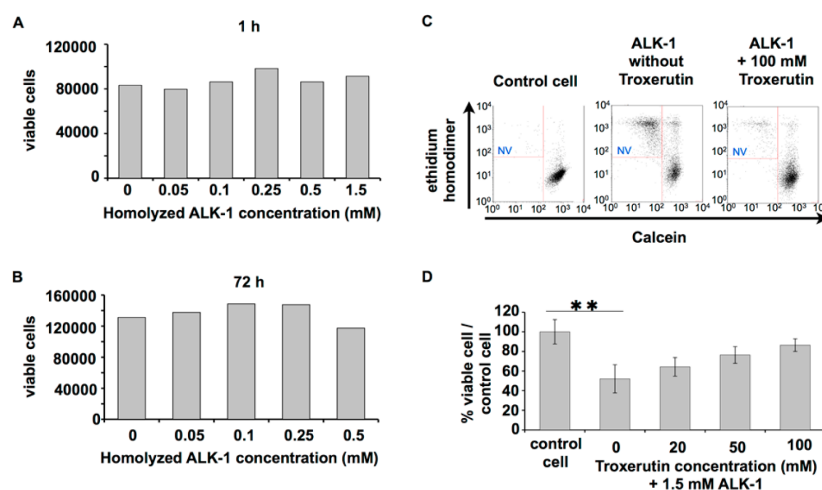


Figure 2. ALK-1 was left to homolyze in complete culture medium for 72 h and then applied to U87 cells (A and B). No effect on cell viability was visible by flow cytometry after incubation for 1 h (A) or 72 h (B) with identical ranges of concentrations as in Figure 1 of beforehand homolyzed ALK-1. The contribution of the alkyl radical was confirmed using troxerutin, an alkyl radical scavenger (C and D). Cells were incubated 1 h with 1.5 mM ALK-1 and increasing troxerutin concentrations. A typical representation of viability results obtained by flow cytometry (C) showed the decrease of the nonviable cell population (NV, left upper gate) in the presence of troxerutin. The analysis confirmed the protective effect of troxerutin (D). For these experiments ($n = 3$), statistical analyses were performed using one-way Anova followed by Tukey's multiple comparison test. The result (**) was significantly different with $p < 0.01$.

h (Figure 2A) and from 0.05 to 0.5 mM for 72 h (Figure 2B). U87 cell viability was not significantly altered at any concentration or any time of incubation. Thus, homolysis products deprived of the short-lived alkyl radicals are devoid of any toxicity (Figures 2A and 2B). The same experiment was also conducted using ALK-1 homolyzed beforehand during only 10 h (corresponding to ca. ten half-lives of the ALK-1) in order to probe the hypothesis of more stable oxidized derivatives acting as a reservoir that would explain the delayed toxicity until 72 h. The viability tests (not shown) did not reveal any significant effect up to 0.25 mM confirming that cell death is the consequence of the direct effect of the short-lived radicals. Nonetheless, at 0.5 mM a minor effect on the viability (15% loss, not shown) is visible which may contribute to the massive effect at 72 h. Moreover, 1 or 72 h incubation with either the nitroxide or the tosylate counterion at 1.5 mM did not display any effect on cell viability (not shown). In order to confirm the role of the alkyl radical on cell toxicity, U87 cells were incubated with 1.5 mM ALK-1 for 1 h in the presence of increasing concentrations of troxerutin, an alkyl radical scavenger (Figures 2C, 2D). With increasing concentrations of the scavenger the ALK-1 toxic effect on U87 cells was progressively suppressed until reaching the viability level of untreated cells. These results strongly support the major role for the alkyl radical in the ALK-1 toxicity with a potential minor contribution of derived oxidized species.

Oxidative Stress Induced by ALK-1. Since alkyl radicals are known to generate oxidative stress, the ALK-1 effect on the intracellular oxidative stress in the U87 cells was probed. Cells were incubated with H_2DCFDA probe and treated for 1 h with or without ALK-1 at 1.5 mM in the presence or not of troxerutin at 50 mM (Figure 3). The intracellular oxidation of H_2DCFDA has been increased 3.4-fold after ALK-1 treatment supporting increased oxidative stress level. Upon addition of

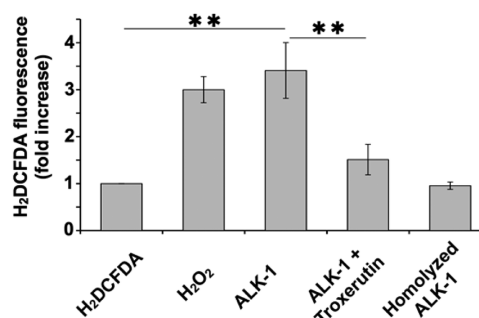


Figure 3. Oxidative stress induced by ALK-1. Oxidative stress produced through ALK-1 treatment was measured by flow cytometry using H_2DCFDA probe. Treatment with H_2O_2 was the positive control. U87 cells were incubated with H_2DCFDA and treated with 1.5 mM ALK-1 with or without 50 mM troxerutin. Flow cytometry data were expressed in fold increase of the mean fluorescent intensity obtained with the cells treated only with the H_2DCFDA probe. For these experiments ($n = 5$), statistical analyses were performed using one-way Anova followed by Tukey's multiple comparison test. The results (**) were significantly different with $p < 0.01$.

troxerutin, the probe oxidation level decreased more than 2-fold. With a beforehand homolyzed ALK-1 treatment, no probe oxidation was induced. Hence, ALK-1 induced an oxidative stress in the U87 cells through the alkyl radical release. Knowing that mitochondria alterations are involved in oxidative stress and also in cell death,¹⁸ mitochondria perturbations were investigated.

Mitochondria Modifications. To address the ALK-1 effect on mitochondria, the mitochondrial potential was monitored using tetramethylrhodamine ester (TMRE). In addition, the

mitochondrial morphology changes were observed through cardiolipin accessibility by nonyl acridine orange (NAO) staining. For all the tested times of incubation, the CCCP (carbonyl cyanide 3-chlorophenylhydrazone) uncoupling agent generated the expected drop of the mitochondrial potential (Figure 4). Independently of the incubation time the effect of

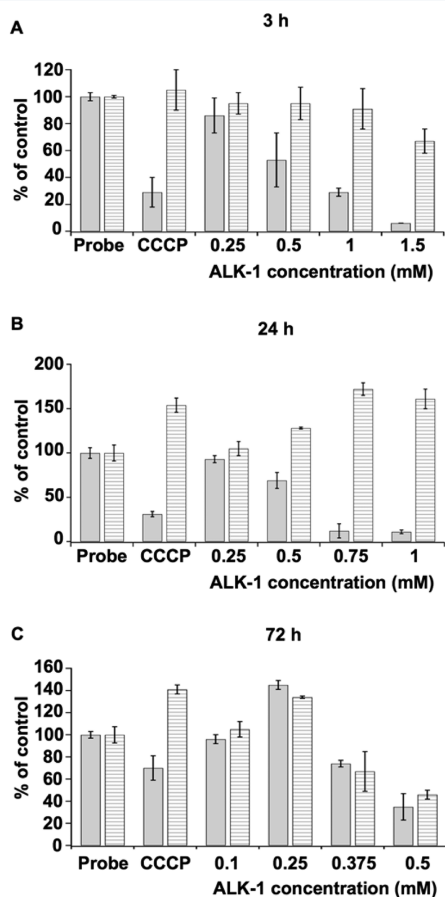


Figure 4. Mitochondria perturbations induced by ALK-1. ALK-1 effects on the mitochondria were measured using TMRE (gray bars) and NAO (dashed bars). U87 cells were incubated with concentrations of ALK-1 between 0.1 and 1.5 mM, and mitochondria perturbations were observed by flow cytometry at 3 h (A), 24 h (B), or 72 h (C) observation times ($n = 3$).

CCCP on the accessibility of the cardiolipins to the NAO appeared either neutral or positive. Starting from 0.5 mM ALK-1, the mitochondrial potential drops for all times of observation (Figure 4A–C). Nevertheless, NAO staining displays diverging evolutions as a function of ALK-1 concentration at 24 h (Figure 4B) and 72 h (Figure 4C) of incubation. Indeed at 24 h, NAO staining increased for ALK-1 concentrations greater than 0.5 mM while the potential dropped. At 72 h, NAO staining evolution correlates with the mitochondrial potential variations. Commonly, the cardiolipin labeling is described as a mitochondrial mass marker. However, it also depends on the

cardiolipin accessibility; therefore, it reflects the mitochondria morphology.¹⁹ A drop of both cardiolipin labeling and the mitochondrial potential suggests a loss of the mitochondrial content as observed after 72 h incubation in the presence of 0.375 to 0.5 mM (Figure 4C). An increase of NAO staining associated with a decrease of the mitochondrial potential is better discussed as a change in the mitochondrial morphology as seen at 24 h between 0.5 and 1 mM (Figure 4B). This is consistent with the fact that the mitochondrial content could not increase within 24 h especially in a stressful situation. A simultaneous increase of both parameters at 72 h and 0.25 mM reveals a transient growth of the mitochondrial mass compatible with the observation time (Figure 4C).

Apoptosis Induction by ALK-1. U87 cells were treated with ALK-1 at various concentrations and observed at 3, 24, and 72 h. Then, cell apoptosis was studied looking at propidium iodide membrane permeability (PI), phosphatidyl serine translocation by annexin-V (AV) staining, and caspase-3 and -7 activation (Figure 5). PI and annexin-V staining discriminate the early apoptotic cells (PI⁻/AV⁺) from the late apoptotic/necrotic cells (PI⁺/AV⁺). Caspase activation would discriminate the necrotic cells (caspase⁻) from the apoptotic cells (caspase⁺). At 3 h (Figure 5A), the percentage of PI⁻/AV⁺ cells increased until 1 mM of alkoxyamine treatment. At 1.5 mM most cells were necrotic or apoptotic cells (PI⁺/AV⁺). Percentage of cells carrying activated caspases reached 92% at 1.5 mM ALK-1. At 24 h (Figure 5B), the percentage of PI⁻/AV⁺ cells increases from 0.5 mM to 0.75 mM ALK-1. At 1 mM, 94% of the cells were necrotic or apoptotic cells (PI⁺/AV⁺). Simultaneously, 88% of the cells were caspase positive. At 72 h (Figure 5C), a slight rise in the level of PI⁻/AV⁺ cells was observed at 0.25 mM and 0.375 mM of ALK-1. At 0.5 mM, most cells were PI⁺/AV⁺. At this observation time, the number of caspase positive cells varies almost linearly from the lowest ALK-1 concentration of 0.1 mM to reach 80% at 0.5 mM. From the time dependent study, two ALK-1 concentrations appeared noticeable. At 0.25 mM for the 24 h observation time cells did not seem to enter the apoptotic pathway (most cells are PI⁻/AV⁻ and caspase⁻). However, at 72 h, cells displayed early apoptotic properties and were more than 40% caspase⁺. At 0.5 mM, cells entered into apoptosis no later than 24 h and after 72 h the remaining cells were massively in late apoptotic state with 80% of the cells being caspase⁺. These results demonstrated that ALK-1 induced the U87 cells death through apoptosis. It is worth noting that ALK-1 action ended after 5 times the half-life of homolysis, namely, 5 h. However, apoptosis appeared much later for the lowest concentrations. This strongly suggests that some irreversible alterations occurred within 5 h which were able to trigger apoptosis between 24 and 72 h after the beginning of alkoxyamine treatment.

Imaging of ALK-1 Homolysis by OMRI. The homolysis of ALK-1 was followed by OMRI at 0.8 mM in culture cell medium at 37 °C. The signal enhancement due to the generated nitroxide radical was monitored for 47 h (Figure 6). The signal amplification exhibited a 6-fold increase from 5 min to 2825 min after the beginning of ALK-1 homolysis. The signal displays an asymptotic exponential growth as expected from the first order kinetics of homolysis and was thus fitted to eq 1:

$$y = y_0 - A \times e^{-kt} \quad (1)$$

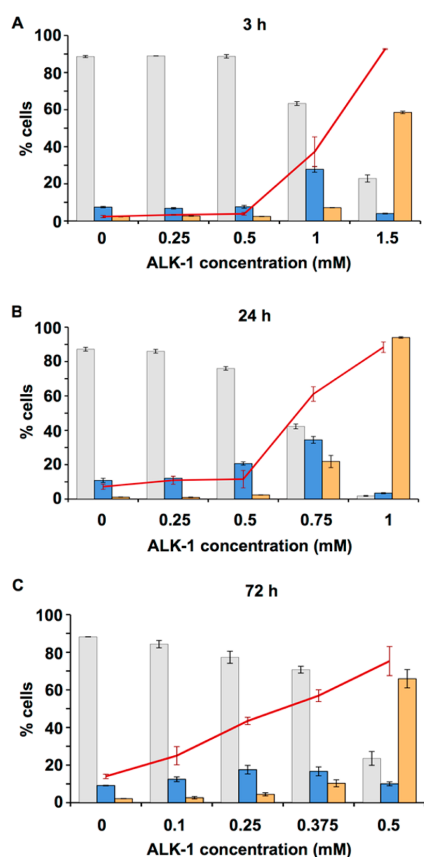


Figure 5. Quantitative analysis of cell apoptosis induced by ALK-1 given as the percentage of U87 cells in different stages against concentrations of ALK-1 at 3 h (A), 24 h (B), and 72 h (C). Percentages of U87 cells stages were determined by PI and annexin-V staining (viable cells, PI-/AV-, gray bars; early apoptotic cells, PI-/AV+, blue bars; and late apoptotic/necrotic cells, PI+/AV+, orange bars). The percentages of positive cells for caspase activity (caspase+) were represented by the superimposed red line.

with $y_0 = 5.9 \pm 0.2$, $A = 5.3 \pm 0.3$, and $k = 5.6 \times 10^{-3} \text{ min}^{-1}$. The experimental $t_{1/2}$ was approximately 125 min. This $t_{1/2}$ was fairly close to the value calculated from the homolysis activation energy. It afforded $E_a = 109 \text{ kJ/mol}$, very close to the 106 kJ/mol value reported, taking into account the inaccuracy of the technique. The 2.5 times discrepancy is easily accounted for by the nonlinear response of the whole OMRI process due to the nonlinear effect of the concentration of the nitroxide on the Overhauser enhancement and due to the lack of stability of the actual setup over 48 h. These results demonstrated that the released nitroxide can be used as a reporter of the radical alkyl owing to the one-to-one stoichiometry.

DISCUSSION AND CONCLUSION

Although alkoxyamine ALK-1 was only an unrefined lead compound, it displays a dose-dependent cytotoxic effect. This effect occurs through its homolysis, and we showed that an *in situ* released alkyl radical was required to induce cell death.

Indeed, when the alkyl radical was scavenged, cell viability turned back to normal level. Several effects of alkoxyamines on cells that could lead to cell death were investigated. ALK-1 induced a strong oxidative stress which was also suppressed upon alkyl radical scavenging. Even at low concentrations persistent changes in the mitochondrial potential, mass, and/or morphology were observed. Ultimately, as shown by the caspase-3 and -7 activation, membrane integrity alteration and phosphatidyl serine translocation cell death occurred by the apoptotic pathway.

The observation of the viability versus the time after exposition to ALK-1 revealed a delayed toxicity, as compared with the completion of homolysis (about 5 h) and the lifetime of the alkyl radical (a few milliseconds). This suggests that the released alkyl radical promptly induced cell alterations that committed the cells into an irreversible cell death process. The various time scales observed for oxidative stress, mitochondrial alterations, and the development of cell apoptosis suggest the absence of a single sequential link between these phenomena. It rather indicates a direct action from the alkyl radical on each effect without excluding interactions. A better understanding of these effects would help to design more efficient alkyl radical moieties in the alkoxyamine.

It has been shown here that the nitroxide radical released from the alkoxyamine homolysis could be efficiently detected by OMRI. This method is currently developed in order to enhance MRI specificity.^{14–16,20} The nitroxide stability would allow the monitoring of alkoxyamine homolysis *in vivo*, with an accurate real-time localization in 3D. Moreover, a longitudinal follow-up of the treatment could be achieved through standard MRI modality.

Perspectives of Improvements. The lead compound alkoxyamine used in this study has a homolysis half-time of *ca.* 50 min. Consequently, the instantaneous alkyl radical concentration remains low due to the first order rate of homolysis and the short lifetime of the alkyl radical itself. Hence, a higher local alkyl radical concentration could be obtained by employing alkoxyamines with shortened homolysis half-life time. This will be possible by varying the R^1 , R^2 , and R^3 substituents due to the flexibility of the alkoxyamine structure (Scheme 1A).⁷

The alkoxyamine LC_{50} may also be greatly improved by grafting more toxic alkyl radicals. Although such a property is difficult to predict, many highly toxic alkyl radical delivering molecules for chemotherapy are already reported.²¹

In this work, the nitroxide displayed six lines instead of three in its EPR spectrum due to the hyperfine coupling of the electron with the β -phosphorus atom. This has the consequence of decreasing the maximum Overhauser enhancement by half. Moreover the EPR line width was 2.5 G, much greater than those observed with nitroxides so far used for *in vivo* OMRI experiments (0.8–1.2 G). This prevented a complete saturation of the unpaired electron and an optimal Overhauser enhancement.²² The detection of alkoxyamine homolysis can thus be readily improved by changing the nitroxide moiety. This can be achieved in reducing the line width and the number of EPR lines. For instance, an alkoxyamine with a three-line nitroxide could be synthesized. Many alkoxyamines carrying nitroxyl fragments without phosphorus group at the β -position exhibit kinetic properties very close to those observed with SG1-based alkoxyamines.²³ The line number could be further reduced to two by introducing a ^{15}N -labeled atom. Interestingly, most three-line nitroxides currently used in OMRI have

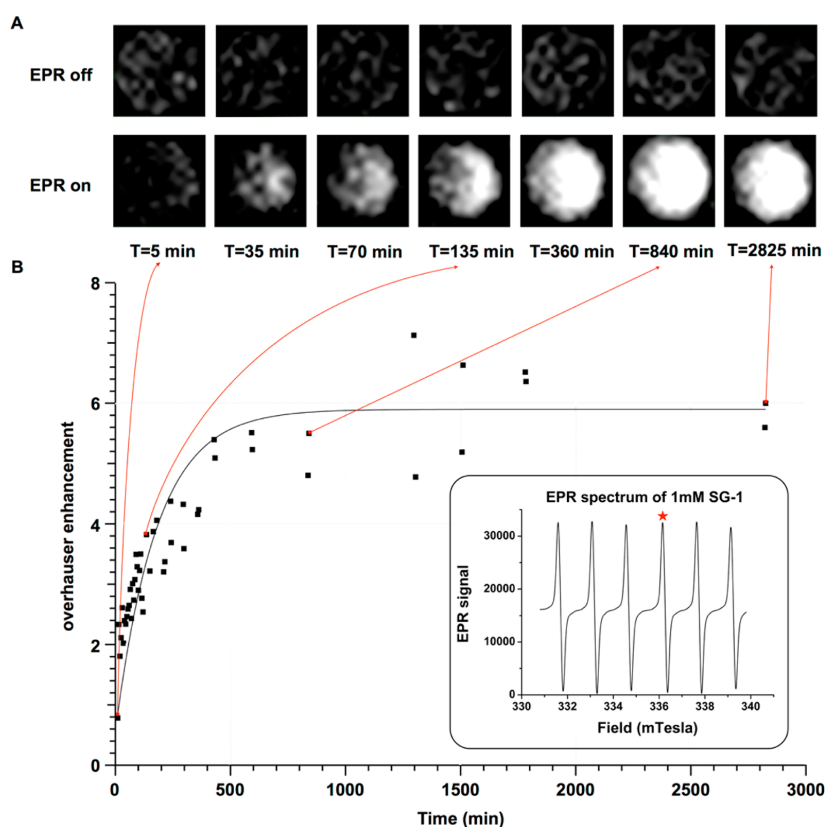


Figure 6. Monitoring the ALK-1 homolysis by OMRI. The release of SG1 nitroxide free radical upon 0.8 mM ALK-1 homolysis at 37 °C was monitored by Overhauser-enhanced magnetic resonance imaging. (A) MRI of ALK-1 homolysis in the absence (top) or presence (bottom) of EPR irradiation. (B) Overhauser enhancement (signal with EPR on/signal with EPR off) over time. The inset shows the EPR spectrum of SG1. The red star indicates the frequency used for EPR irradiation.

narrower line widths.²⁴ Moreover some three-line nitroxides have shown high resistance to reduction *in vivo* as exemplified in a murine model of glioma.¹⁶

A Possible Targeting Strategy. An alkoxyamine with a low $t_{1/2}$ for homolysis will release highly reactive alkyl radicals that will randomly alter lipids, proteins, and nucleic acids of the cells in the vicinity. Without targeting, such an unspecific action would be poorly efficient against cancer cells. Thus, for safety and efficiency the homolysis process has to occur at the tumor site exclusively (*vide supra*).

The tumor microenvironment is remodeled in many ways. One of them is the overexpression and the persistent activation of proteases, mostly matrix metalloproteinases (MMP) and/or cathepsin B. Targeting this activity would add a true specificity because healthy tissues are devoid of such an activity. Indeed physiological proteolysis is tightly controlled by high concentrations of protease inhibitors and is thus kept to a transient and localized event. Consequently, tumor targeting through its associated persistent protease activity has been proposed.^{25–28}

We recently described a theranostic approach for the treatment of solid tumors by alkoxyamines.⁶ We proposed to synthesize alkoxyamine-based prodrugs. The principle is to

design an alkoxyamine that is spontaneously protonated at physiological pH. The protonation has been shown to greatly lower the activation energy thus “activating” the alkoxyamine and triggering the homolysis.^{9–11} A primary amine function can play this role: indeed, by grafting a specific peptide on the amine, the protonation ability of the nitrogen atom is suppressed. Thus, the alkoxyamine is stabilized until a specific protease (such as MMP or cathepsin B) removes the peptide and thus regenerates the amine, which is immediately protonated at physiological pH, leading to an activated labile alkoxyamine. Such a prodrug by selecting a specific peptide could thus be tuned to be activated in the tumor environment where persistent proteolytic activity is present.

■ AUTHOR INFORMATION

Corresponding Authors

*E-mail: pierre.voisin@rmsb.u-bordeaux2.fr.

*E-mail: paul.bremond@univ-amu.fr.

*E-mail: philippe.mellet@rmsb.u-bordeaux2.fr.

Notes

The authors declare no competing financial interest.

ACKNOWLEDGMENTS

The authors thank the French National Research Agency (grants NITROMRI ANR-09-BLAN-0017-01 and SonRadls ANR-11-JS07-002-01), Université Victor Segalen Bordeaux 2, Aix-Marseille Université, CNRS, and INSERM for funding. This study, carried out in the frame of LabEx TRAIL (ANR-10-LABX-57), has received financial support from the French State, managed by the French National Research Agency (ANR) in the "Investments for the future" program IdEx Bordeaux (ANR-10-IDEX-03-02).

REFERENCES

- (1) Trachootham, D.; Alexandre, J.; Huang, P. Targeting cancer cells by ROS-mediated mechanisms: a radical therapeutic approach? *Nat. Rev. Drug Discovery* **2009**, *8*, 579–591.
- (2) Ozben, T. Oxidative stress and apoptosis: impact on cancer therapy. *J. Pharm. Sci.* **2007**, *96*, 2181–2196.
- (3) Davies, K. J. The broad spectrum of responses to oxidants in proliferating cells: a new paradigm for oxidative stress. *IUBMB Life* **1999**, *48*, 41–47.
- (4) Suntharalingam, K.; Johnstone, T. C.; Bruno, P. M.; Lin, W.; Hemann, M. T.; Lippard, S. J. Bidentate ligands on osmium(VI) nitrido complexes control intracellular targeting and cell death pathways. *J. Am. Chem. Soc.* **2013**, *135*, 14060–14063.
- (5) Singh, J.; Petteer, R. C.; Baillie, T. A.; Whitty, A. The resurgence of covalent drugs. *Nat. Rev. Drug Discovery* **2011**, *10*, 307–317.
- (6) Audran, G.; Brémond, P.; Franconi, J.-M.; Marque, S. R. A.; Massot, P.; Mellet, P.; Parzy, E.; Thiaudière, E. Alkoxyamines: a new family of pro-drugs against cancer. Concept for theranostics. *Org. Biomol. Chem.* **2014**, *12*, 719–723.
- (7) Bertin, D.; Gignes, D.; Marque, S. R. A.; Tordo, P. Kinetic subtleties of nitroxide mediated polymerization. *Chem. Soc. Rev.* **2011**, *40*, 2189–2198.
- (8) Chauvin, F.; Dufils, P.-E.; Gignes, D.; Guillaneuf, Y.; Marque, S. R. A.; Tordo, P.; Bertin, D. Nitroxide-mediated polymerization: the pivotal role of the k_d value of the initiating alkoxyamine and the importance of the experimental conditions. *Macromolecules* **2006**, *39*, 5238–5250.
- (9) Brémond, P.; Marque, S. R. A. First proton triggered C–ON bond homolysis in alkoxyamines. *Chem. Commun.* **2011**, *47*, 4291–4293.
- (10) Brémond, P.; Koita, A.; Marque, S. R. A.; Pesce, V.; Roubaud, V.; Siri, D. Chemically triggered C–ON bond homolysis of alkoxyamines. Quaternization of the alkyl fragment. *Org. Lett.* **2012**, *14*, 358–361.
- (11) Audran, G.; Brémond, P.; Marque, S. R. A.; Obame, G. Chemically triggered C–ON bond homolysis of alkoxyamines. 5. Cybotactic effect. *J. Org. Chem.* **2012**, *77*, 9634–9640.
- (12) Johnson, D. H.; Ahmad, R.; He, G.; Samouilov, A.; Zweier, J. L. Compressed sensing of spatial electron paramagnetic resonance imaging. *Magn. Res. Med.* **2013**, DOI: 10.1002/mrm.24966.
- (13) Lurie, D. J.; Bussell, D. M.; Bell, L. H.; Mallard, J. R. Proton electron double magnetic resonance imaging of free radical solutions. *J. Magn. Reson.* **1988**, *76*, 366–370.
- (14) Matsumoto, K.; Hyodo, F.; Anzai, K.; Utsumi, H.; Mitchell, J. B.; Krishna, M. C. Brain redox imaging. *Methods in molecular biology. Methods Mol. Biol.* **2011**, *711*, 397–419.
- (15) Koonjoo, N.; Parzy, E.; Massot, P.; Lepetit-Coiffé, M.; Marque, S. R. A.; Franconi, J.-M.; Thiaudière, E.; Mellet, P. In vivo Overhauser-enhanced MRI of proteolytic activity. *Contrast Media Mol. Imaging* **2014**, DOI: 10.1002/cmml.1586.
- (16) Massot, P.; Parzy, E.; Pourtau, L.; Mellet, P.; Madelin, G.; Marque, S.; Franconi, J.-M.; Thiaudière, E. In vivo high-resolution 3D overhauser-enhanced MRI in mice at 0.2 T. *Contrast Media Mol. Imaging* **2012**, *7*, 45–50.
- (17) Parzy, E.; Bouchaud, V.; Massot, P.; Voisin, P.; Koonjoo, N.; Moncelet, D.; Franconi, J.-M.; Thiaudière, E.; Mellet, P. Overhauser-enhanced MRI of elastase activity from in vitro human neutrophil degranulation. *PLoS One* **2013**, *8*, e57946.
- (18) Sinha, K.; Das, J.; Pal, P. B.; Sil, P. C. Oxidative stress: the mitochondria-dependent and mitochondria-independent pathways of apoptosis. *Arch. Toxicol.* **2013**, *87*, 1157–1180.
- (19) Van Ruijsssevelt, L.; Smirnov, P.; Yudina, A.; Bouchaud, V.; Voisin, P.; Moonen, C. Observations on the viability of C6-glioma cells after sonoporation with low-intensity ultrasound and microbubbles. *IEEE Trans. Ultrason., Ferroelectr., Freq. Control* **2013**, *60*, 34–45.
- (20) Shet, K.; Caia, G. L.; Kesselring, E.; Samouilov, A.; Petryakov, S.; Lurie, D. J.; Zweier, J. L. A novel variable field system for field-cycled dynamic nuclear polarization spectroscopy. *J. Magn. Reson.* **2010**, *205*, 202–208.
- (21) Fu, D.; Calvo, J. A.; Samson, L. D. Balancing repair and tolerance of DNA damage caused by alkylating agents. *Nat. Rev. Cancer* **2012**, *12*, 104–120.
- (22) Mellet, P.; Massot, P.; Madelin, G.; Marque, S. R. A.; Harte, E.; Franconi, J.-M.; Thiaudière, E. New concepts in molecular imaging: non-invasive MRI spotting of proteolysis using an Overhauser effect switch. *PLoS One* **2009**, *4*, e5244.
- (23) Bertin, D.; Gignes, D.; Marque, S. R. A.; Tordo, P. Polar, steric, and stabilization effects in alkoxyamines C–ON bond homolysis: a multiparameter analysis. *Macromolecules* **2005**, *38*, 2638–2650.
- (24) Grucker, D.; Guiberteau, T.; Eclancher, E.; Chambon, J.; Chiarelli, R.; Rassat, A.; Subra, G.; Gallez, B. Dynamic nuclear polarization with nitroxides dissolved in biological fluids. *J. Magn. Reson.* **1995**, *106*, 101–109.
- (25) Overall, C. M.; Kleinfeld, O. Tumour microenvironment - opinion: validating matrix metalloproteinases as drug targets and anti-targets for cancer therapy. *Nat. Rev. Cancer* **2006**, *6*, 227–239.
- (26) Atkinson, J. M.; Siller, C. S.; Gill, J. H. Tumour endoproteases: the cutting edge of cancer drug delivery? *Br. J. Pharmacol.* **2008**, *153*, 1344–1352.
- (27) Law, B.; Tung, C. H. Proteolysis: a biological process adapted in drug delivery, therapy, and imaging. *Bioconjugate Chem.* **2009**, *20*, 1683–1695.
- (28) Choi, K. Y.; Swierczewska, M.; Lee, S.; Chen, X. Protease-activated drug development. *Theranostics* **2012**, *2*, 156–178.